Unusual Near-Horizon Cosmic-Ray-Like Events Observed by the Fourth Flight of ANITA

Remy L. Prechelt

December 2022

Committee

Peter W. Gorham, *Chairperson*
Gary S. Varner
John G. Learned
Phillip Von Doentichem
David Sanders, *University Representative*

A dissertation presented for the degree of Doctor of Philosophy

in the

Department of Physics and Astronomy
University of Hawai'i at Mānoa
Honolulu, Hawai'i

Abstract

Despite decades of experimental observations, the astrophysical sources producing the measured flux of ultrahigh energy cosmic rays (UHECRs) have yet to be identified. Neutrinos, extremely weakly interacting neutral particles, are expected to be produced inside the astrophysical accelerators responsible for the production of UHECRs, and during the propagation of UHECRs to Earth. As neutral weakly-interacting particles, ultrahigh energy neutrinos are perhaps the best probe of the hadronic and leptonic processes governing these extreme astrophysical environments beyond the local universe. Yet, despite two decades of experimental searches, ultrahigh energy neutrinos have never been *definitively* detected.

ANITA-IV, the fourth flight of the ANtarctic Impulsive Transient Antenna (ANITA), observed four anomalous events extremely close to the horizon. In this dissertation, I present the possibility that one or more of these anomalous "near horizon" events are indeed ultrahigh energy *tau* neutrinos detected via the unique Earth-skimming "τ air shower channel". I develop the first "end-to-end" simulation of ANITA-IV's sensitivity to these unique events and I use this simulation to determine whether these events are *observationally* consistent with τ-induced extensive air showers and, if they are, what are the constraints on the implied flux from populations of diffuse and point-like neutrino sources. Finally, I perform a blind search for any statistically significant associations between these four anomalous events and catalogs of astrophysical sources that are considered to be possible ultrahigh-energy neutrino and cosmic ray emitters.

I find that these events are *not* observationally *inconsistent* with ultrahigh energy tau neutrinos, but that the implied (diffuse) flux and (point-like) fluence necessary to explain these events is in strong tension with limits set by other observatories, such as the Pierre Auger Observatory and IceCube. After unblinding the results of my search for associations between these events and catalog neutrino sources, I find *no statistically significant* associations with any of the considered sources.

Contents

List of Figures

List of Tables

I Searching for the Unknown Sources of Ultrahigh Energy Cosmic Rays

Conventional photon-based astronomy covers more than 20 orders of magnitude in photon wavelength: from 10^{5} cm radio waves to 10^{-16} cm gamma rays. Visible light, the original purview of classical astronomy, spans just a single octave above 10^{-5} cm. This dramatic range of wavelengths, more than 70 octaves, has been the primary tool for developing our understanding of the universe since the invention of the first telescopes. Photons are not, however, the only messengers of astrophysical processes. Victor Hess' 1912 balloon flight pioneered the detection of baryonic particles from the universe [1], now known as *cosmic rays*. In 2017, the Advanced Ligo and Advanced Virgo detectors announced the first detection of *gravitational waves* (in this case, from a binary neutron star merger) , which was simultaneously observed across the entire electromagnetic spectrum [2]. Also in 2017, the blazar TXS 0506+056 was simultaneously detected in both *high-energy neutrinos* (by the IceCube experiment) and *photons* across multiple wavelengths by several different instruments [3].

These discoveries have been heralded as the dawn of multi-messenger astrophysics. As we will see later in this chapter, the universe is *not* transparent to photons, especially above TeV energies. Therefore, if we are to probe distant high energy astrophysical processes *at all*, we *must* turn to these other messengers: neutrinos, cosmic rays, and gravitational waves.

This dissertation is focused on the intersection of ultrahigh energy cosmic ray (UHECR) and ultrahigh energy neutrino astrophysics performed with the Antarctic Impulsive Transient Antenna (ANITA) neutrino experiment. In the remainder of this chapter, I present an introduction to cosmic ray and neutrino astrophysics at the highest energies, discuss some of the most important open research questions and challenges in particle astro-

physics, and motivate the science of the simulations and analyses presented later in this dissertation.

1.1 Cosmic Ray Astrophysics

Cosmic rays, a flux of protons, electrons, and light nuclei from solar system, galactic, and extra-galactic sources, have been studied for more than a century since Victor Hess' flight [1] with a number of detection techniques and experiments. Non-solar cosmic rays have been observed over more than twelve orders of magnitude in primary energy, from $\sim$100 MeV (10^8 eV) to nearly $\sim$1 ZeV (10^{21} eV), using more than a dozen dedicated cosmic ray observatories (below $\sim$100 MeV the cosmic ray flux begins to be dominated by solar cosmic rays, known as *solar energetic particles* which are not relevant to the work in this dissertation [4, 5]). A recent compilation of measured cosmic ray fluxes over this energy span, by several observatories, is shown in Figure 1.1. Along with this large span in energy, the cosmic ray flux, with its strongly falling power-law-like behavior, varies over more than sixteen orders of magnitude over this same range in energy; from $\sim 1\,\mathrm{m}^{-2}\,\mathrm{s}^{-1}$ at GeV energies, to $\sim 1\,\mathrm{m}^{-2}\,\mathrm{yr}^{-1}$ at PeV energies, and to $\lesssim 1\,\mathrm{km}^{-2}\,\mathrm{yr}^{-1}$ at EeV energies [5].

Along with these extreme ranges in energy and flux, the major challenge of cosmic ray astronomy is, since cosmic rays are *charged* particles, they are "scrambled" by galactic and extra-galactic magnetic fields during their propagation to Earth and, as such, their observed arrival directions are typically uncorrelated with the direction of their original production environments or sources [6]. Therefore, traditional "*astronomy*", where the observed direction of incident particles is highly aligned with the sky location of the source, is not typically possible. However, at the highest rigidities (energy over charge), above $\sim$40 EV, the trajectory of most cosmic rays becomes magnetically rigid enough that their arrival directions could become correlated with the direction of their production and acceleration environments [7]; however, this energy scale coincides with the cosmic ray flux becoming small enough, $\ll 1\,\mathrm{km}^{-2}\,\mathrm{yr}^{-1}$, that even the largest current-generation experiments struggle with obtaining the necessary statistics for *discovery*-level analyses of cosmic ray arrival directions [8, 9, 7].

Since the observed direction of the cosmic ray is not useful across the vast majority of the cosmic ray energy spectrum, the two primary observables used are the *energy spectrum* and *mass composition* of the measured cosmic ray flux. In the following sections, we

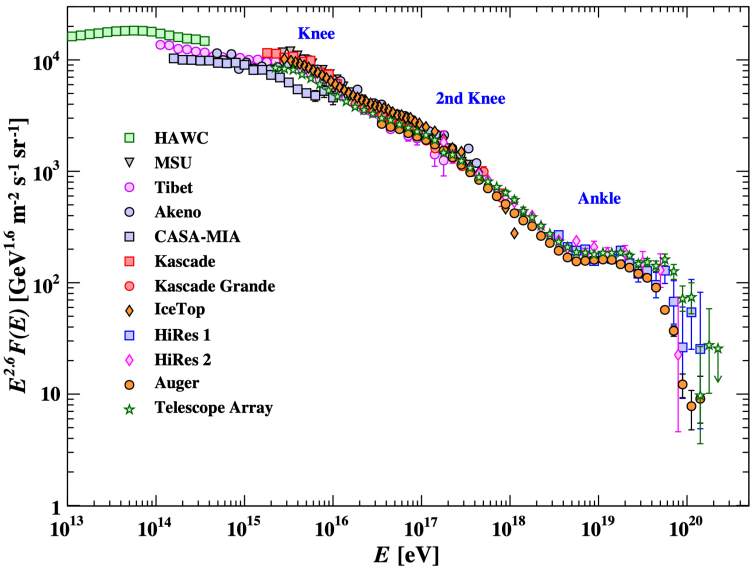

Figure 1.1: The all-particle spectrum of cosmic rays observed at Earth as a function of primary particle energy per nucleon, E, from air shower measurements from nearly a dozen different cosmic ray experiments. The figure also labels several spectral breaks in the cosmic ray spectrum, the *"knee"*, *"second (iron) knee"*, and *"ankle"*; more details on these spectral features will be discussed later in this chapter. This dissertation will be focused on the region above 10^{18} eV, with so-called *ultrahigh energy cosmic rays*. Figure from [5].

present a review of the theory and measurements of the energy spectrum, mass composition, and anisotropy of the cosmic ray flux at Earth.

1.1.1 UHECR Energy Spectrum

Precise measurements of the energy spectrum of UHECRs encodes invaluable information about the origin and mechanisms of cosmic ray acceleration and propagation [10, 11, 12, 13]. The two most sensitive current observatories for measuring the UHECR flux are Telescope Array (TA) [14], located in Utah, and the Pierre Auger Observatory (Auger) located in Argentina [15]. However, despite Auger's $\sim 10^5$ km^2 sr yr of integrated exposure (as of the time of writing), the total number of events observed, particularly above 50 EeV, poses a significant statistical challenge (the flux at these energies is $\ll 1\,\mathrm{km}^{-2}\,\mathrm{yr}^{-1}$). A comparison between the UHECR flux as currently measured by TA and Auger is shown in Figure 1.2 [16].

While Auger and TA use very similar experimental techniques to detect UHECRs (as will be discussed in Chapter 2), there *are* differences between the respective instruments and the analysis methods used to reconstruct the properties of the parent cosmic ray which can lead to systematic uncertainties when comparing the absolute energy scale and flux reported by each collaboration [16]. This is clearly seen in Figure 1.2 where the absolute flux reported by Auger and TA disagree within reported uncertainties across the energy range above 1 EeV. Above ∼40 EeV, the reported fluxes begin to disagree both in magnitude *and* in spectral shape. This is worsened by the increasingly limited statistics available at these extreme energies (note the size of the error bars at ∼100 EeV) as the cosmic ray flux begins to rapidly cutoff above ∼40 EeV.

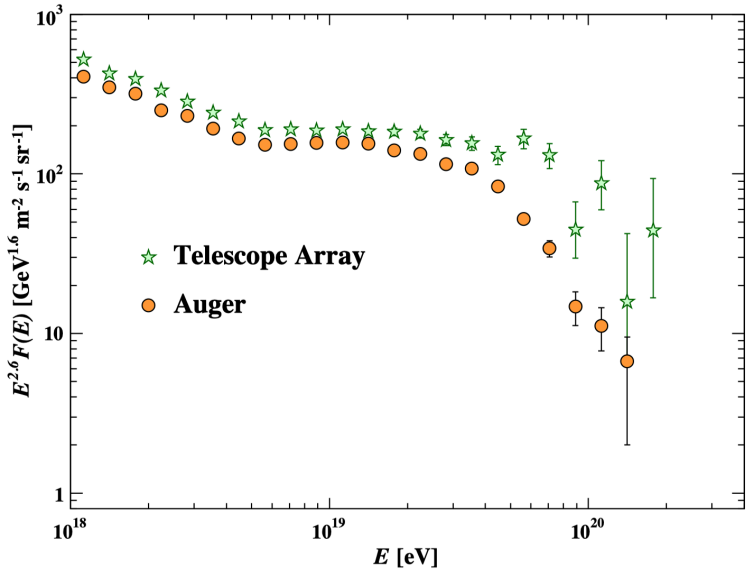

Figure 1.2: The UHECR energy spectrum above 1 EeV as measured by Auger and Telescope Array. The disagreement between these measurements is most significant above 40 EeV where the two flux measurements start to diverge significantly. Note that the units of this plot are $E^{2.6}F(E)$ in order to emphasize the changes in spectral slope on what would otherwise be a very steeply falling power-law-like spectral plot. Figure from [5].

An analysis and remeasurement performed by a joint Auger-TA working group found that applying systematic corrections to the energy and exposure calculations, as well as compensating for the different sky coverage of each observatory can significantly improve the agreement between the two observatories up to ∼60 EeV [16, 17, 18]. The reconstructed flux after correction is shown in the right panel of Figure 1.3. However,

the Auger-TA flux cross-calibration of Figure 1.3 still cannot account for the differences observed at the highest energies where the experiments still disagree [16].

In addition to the discrepancy between Auger and TA at the highest energies, the full cosmic ray energy spectrum (Figure 1.1 and 1.2) shows three distinct spectral breaks between 1 PeV and 1 EeV that are known as the *"knee"*, *"second-knee"*, and the *"ankle"*. The origin of these features is currently contested. In the following sections, we present a brief discussion of possible origins for the knee, second knee, and ankle of the cosmic ray spectrum.

There are currently two competing hypotheses for the origin of *"knee"* at 4 PeV and "second knee" at 200 PeV shown in Figure 1.1. The lack of galactic-plane-anisotropy in cosmic rays observed *above* the knee place strong limits on the contribution from galactic sources and therefore suggesting that galactic cosmic ray sources dominate the spectrum up to the knee, above which it is likely that the flux shifts to extra-galactic sources (the knee should therefore correspond to the start of the galactic to extra-galactic transition) [8, 19].

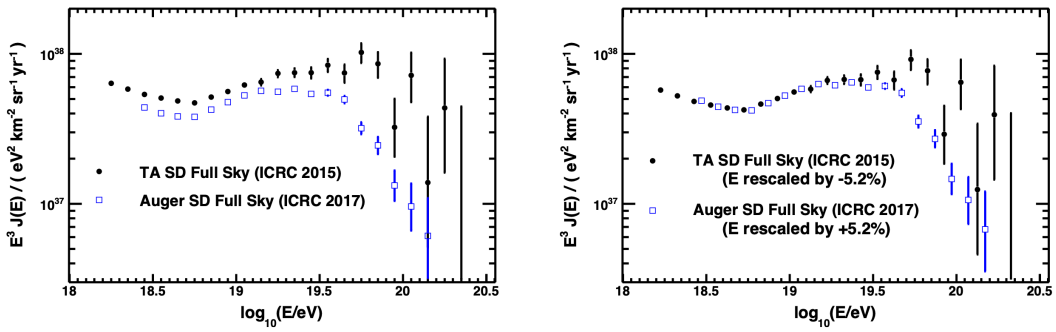

Figure 1.3: *Left*: A comparison of the UHECR energy spectrum as measured by Auger and TA. *Right*: The same flux comparison after rescaling the energies of Auger by +5.2% (red) and that of TA by -5.2% (black) to account for detector cross-calibration uncertainties [16, 20, 21]. Figure from [18].

Galactic cosmic rays

The first hypothesis for the origin of the knee assumes that cosmic ray accelerators exist within our galaxy capable of accelerating cosmic rays to super-knee energies. These accelerated cosmic rays will then propagate and diffuse within the turbulent galactic magnetic fields [22]. PeV cosmic ray protons in typical μG galactic magnetic fields possess

a Larmor radius that approaches the maximum turbulent wavelength of current galactic magneto-hydrodynamic (MHD) models [22]. When this occurs, the confinement of cosmic rays at super-knee energies becomes rapidly less efficient potentially allowing super-knee cosmic rays to escape the galactic disk, propagate into the extra-galactic medium, and therefore no longer be detected at Earth [23]. This model is one of a more general class of hypotheses where any change in cosmic ray diffusion and transport that leads to inefficient confinement around the energy of the knee could explain the steepening of the cosmic ray flux at the knee [24] as more cosmic rays begin to leave the galaxy.

These *confinement*-based models implicitly assume the presence of efficient cosmic ray accelerators in the galaxy capable of *accelerating cosmic rays to super-knee energies*. This is a challenge for many astrophysical source models as most galactic sources are not expected to have the conditions necessary to accelerate cosmic rays to energies at or above the knee. The one source class within the galaxy that may have this potential, up to the energy of the knee, are supernova remnants (SNR) but even SNR acceleration models disagree on their ability to act as cosmic ray PeVatrons [25, 26]. The only galactic source currently *known* to be capable of accelerating cosmic rays to the PeV scale is the galactic nucleus, Sgr A* [27], whose hadronic luminosity is too small to replicate the entire observed flux at Earth [28] and as such cannot explain the origin of the knee.

Therefore, an alternative hypothesis is that the knee could correspond to the *maximum cosmic energy produced by galactic sources*; i.e. galactic sources are unable to accelerate nuclei to more than several PeV per nucleon. The most theoretically supported PeVatron candidates are currently supernova remnants (SNR) which accelerate cosmic rays via magnetic diffuse shock acceleration [29, 30]. However, current SNR acceleration models still require significant magnetic field enhancement to act as efficient cosmic ray PeVatrons [29, 31]. An application of the Hillas criterion, which will be discussed in more detail in section 1.3, predicts that SNR can efficiently accelerate cosmic rays to an energy E_{max} given by,

$$E_{\text{max}} = \eta^{-1}\beta_{sh}eBR = \left(\frac{\eta}{10}\right)^{-1}\left(\frac{B}{3\,\mu\text{G}}\right)\left(\frac{R}{10\,\text{pc}}\right)\,\text{TeV}$$

where η parameterizes the efficiency of diffusion in the source, β_{sh} is the shock velocity, B is the magnetic field in the acceleration region, and R is the characteristic size of the acceleration region. The values chosen for each scaling term (in parenthesis) are typical values for SNR under current models [29]. The characteristic size of typical SNR are

well known, so in order for E_{max}∼PeV, there must be a process for significant magnetic field enhancement in SNR to produce PeV energy cosmic rays. Several different models have been proposed to create this additional magnetic field enhancement necessary for PeV cosmic ray acceleration in typical SNR, such as the cosmic ray current driven *Bell acceleration*, but none have been experimentally confirmed [32, 33] so it remains phenomenologically challenging for SNR to be the sole class of cosmic ray PeVatrons in our galaxy.

Both confinement or maximum accelerated energy hypotheses for the origin of the knee naturally predict corresponding "knees" for the different nuclear cosmic ray species (as both processes directly depend on the rigidity, E/Z, of the particle species). Therefore, if the knee is indeed a proton cutoff like current measurements indicate, then the "second knee", often called the "iron knee", corresponds to the energy at which iron nuclei are no longer confined or accelerated within the galaxy [34]. The energy of the second knee measured by Auger [35, 36], KASCADE-Grande [37], and TA [38, 39] are all experimentally consistent with this rigidity-dependent origin for several nuclei species.

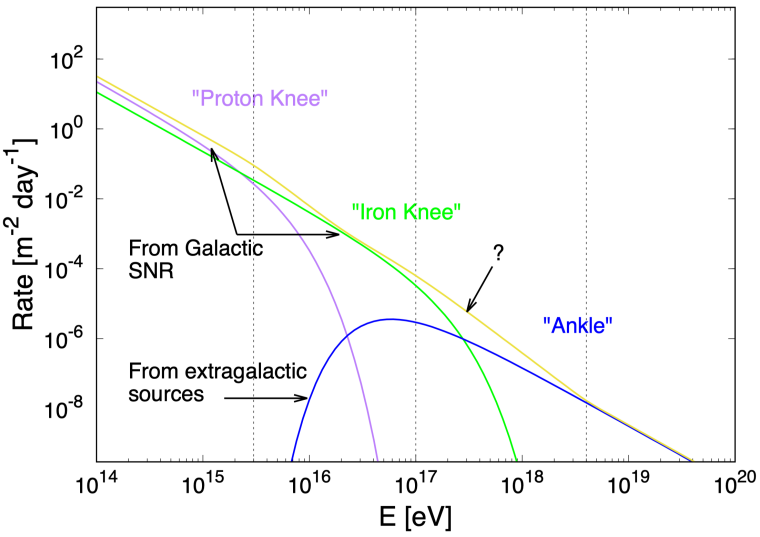

Figure 1.4: A well-supported theoretical model for the origin of the *"knee"*, *"second (iron) knee"*, and *"ankle"* as the transition between galactic and extragalactic sources under a *maximum energy model* (where the knee is due to an upper energy per nucleon limit of galactic cosmic ray accelerators). Under this model, the *"knee"* is due to the maximum energy of accelerated protons produced in galactic sources such as SNR, the *"second knee"* is the same feature but for iron, and the "ankle" is the transition to extragalactic UHECR sources. Figure from [31].

The most important spectral feature for this dissertation is the *cutoff* or *suppression* of the UHECR spectrum near the upper end of the spectrum at ∼40 EeV (Figure 1.2) with a significance (from Auger) of more than 6σ [40]. Since the (already small) flux begins to decrease even more rapidly at these energies, this coincides with even the largest (current generation) observatories, like Auger and TA, becoming statistics limited (note the size of the error bars at 100 EeV in Figure 1.2).

Extragalactic cosmic rays

There are currently two hypotheses compatible with measurements but current experimental constraints do not currently have the discovery power to distinguish between them [31], they are: 1) accelerators exist that *do* accelerate UHECRs to above the cutoff, but that these UHECRs are suppressed during *propagation* to Earth and are therefore unobserved; or 2) that the cutoff is simply the maximum energy that *can* be accelerated by the (currently unknown) UHECR sources (i.e. galactic and extragalactic sources cannot efficiently accelerate UHECRs to above the cut-off).

The likely process by which the UHECR flux could be suppressed during propagation is via interactions with extragalactic background photons, including the cosmic microwave background (CMB), via the long-predicted *Greisen-Zatsepin-Kuz'min* (GZK) effect, converting UHECRs into a flux of neutral secondaries including photons and neutrinos [41, 42]. The threshold energy of the GZK process, which occurs via the Δ^+-resonance with CMB photons at ∼60 EeV, is experimentally consistent with the cutoff energy observed by both Auger and TA [20, 43, 44]. A major prediction of a GZK-based-suppression hypothesis is that UHECRs should only be observed from sources within ∼100 Mpc of Earth, as cosmic rays from beyond this distance will be strongly attenuated by the GZK process; this is the so-called *"GZK sphere"* or *"GZK horizon"*. While the sources of observed UHECRs may therefore be limited to the local universe by the GZK effect, this does allow for the detection of these (also) ultrahigh-energy neutral secondaries, potentially from beyond the GZK horizon; the neutrino fluxes predicted by a GZK hypotheses will be discussed in more detail in section 1.2.

Under a *maximum energy hypothesis*, idealized models of populations of astrophysical UHECR accelerators distributed within ∼100 Mpc are able to nominally reproduce the observed UHECR spectrum and composition measurements of both TA and Auger within large experimental and model uncertainties [45, 46, 47]. However, uncertainties related to the identification, distribution, and environments of potential UHECR

sources, do not rule out a GZK-origin for the cut-off [48]. A detailed discussion on possible astrophysical environments that potentially have the ability to accelerate cosmic rays to ultrahigh energies will be discussed in section 1.3.

Reconstructing the origin of UHECRs under both hypotheses is currently challenging [46, 49, 47]. To forward model a single source or propagation hypothesis, a detailed source model for the UHECR spectrum and composition *at the source* is needed, generated from a detailed acceleration model. This must then be propagated through extragalactic and galactic environments to Earth with computationally expensive tools like CRPropa [50, 51, 52]. The simulated spectrum and composition must then be simultaneously fit to not only the energy spectrum and mass composition data from Auger & TA, but also to the reported anisotropy at ultrahigh energies reported by each experiment without violating other multi-messenger bounds (often gamma-ray, X-ray, and radio measurements) [46]. In additional to phenomenological uncertainties related to the source environment and acceleration mechanism [53, 54, 55, 56, 57, 48], extragalactic and galactic propagation environments [47, 22], and (often) statistics-limited measurements on Earth [58, 59, 60, 61], these simulation can be computationally challenging, even with modern tools like CRPropa, due to the high-dimensional parameter space (source models, propagation, air shower physics, etc.) that needs to be reconstructed only from observables *on Earth*.

Unfortunately, at this point in time, the statistics provided by Auger and TA are not sufficient to confidently disentangle these two potential hypotheses [31]. Future observatories like POEMMA [62] and EUSO [63], with extremely high UHECR sensitivities, may be able to provide invaluable information for understanding the origin of this UHECR cutoff by significantly increasing the available statistics (due to their high expected event rate).

1.1.2 UHECR Composition

In addition to the energy spectrum, another major observable for UHECR astronomy is the mass composition spectrum i.e. the energy spectra of each individual nuclei species that comprises the cosmic ray flux. The primary technique used to measure the mass composition is via simultaneous measurement of the depth, X_{max}, at which the total number of particles in an extensive air shower reaches its maximum, and the total energy, E, of the shower [61, 15]. Showers initiated by different primary particles have statistically differ-

ent distributions of the depth of $X_{\max}$ over energy. Monte Carlo simulations, with tools like AIRES [64] and CORSIKA [65, 66] (which each use several different hadronic and electromagnetic interaction models such as SIBYLL [67], QGS-JET-II [68], or EPOS-LHC [69]) can be used to perform detailed simulations of extensive air showers, which can then be used to reconstruct the incident mass compositions of the flux that are consistent with the observed distribution of $X_{\max}$ observed by the experiment. The average and standard deviation of the distribution of $X_{\max}$ measured by both Auger and TA is shown in Figure 1.5, along with predictions for pure-proton and pure-iron fluxes. From Figure 1.5, it is clear that neither a pure-iron or pure-proton flux can explain the observed distribution of $X_{\max}$, and that the composition of the flux must be changing as the energy increases.

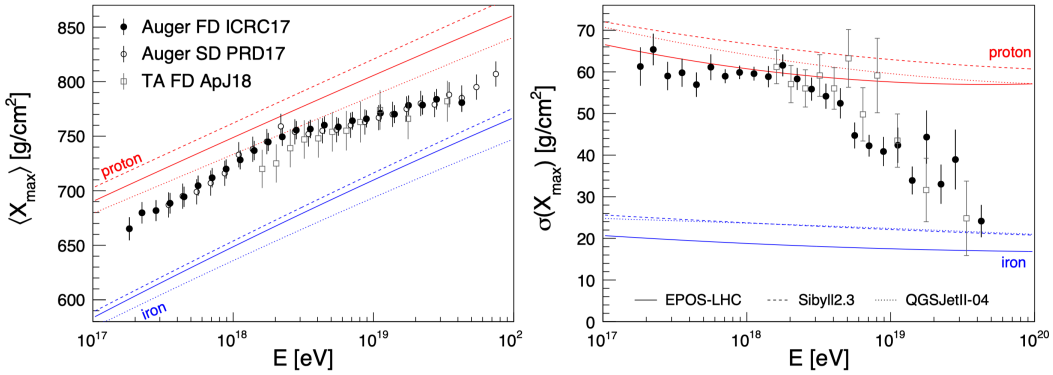

Figure 1.5: Measurements [70, 71, 72] of the mean (left) and standard deviation (right) of the distribution of shower maximum grammage (in g cm^{-2}) as a function of energy for both the Auger surface detectors (SD) and fluorescence detectors (FD) and the TA fluorescence detectors (FD). The data from the Telescope Array has been calibrated and adjusted by [31] to try and account for uncertainties from the detector and non-overlapping sky regions. The energy evolution of the shower maximum for pure iron and pure proton fluxes are shown in the blue and red lines respectively for various hadronic interaction models (line style). The changing shower maximum grammage as a function of energy is evidence that the composition of the cosmic ray flux is both *mixed* and energy dependent. Figure from [31].

For current ground based observatories like TA and Auger, the best $X_{\max}$ resolution is achieved with fluorescence telescopes (FDs) that can directly observe the longitudinal shower profile of each shower [73, 74]. Particle detector arrays, like the *surface detectors* (SDs) at Auger and TA, can also reconstruct the energy and composition of shower by measuring the fluence of particle species at the ground (most of the reconstruction power

comes from muons [73]) but this has significantly worse resolution than the fluorescence measurements [75] and suffers from theoretical uncertainties due to the hadronic interaction models used to simulate extensive air shower development and the so-called "muon problem" [60, 76, 77].

The measurements shown in Figure 1.5 suggest that the composition of UHECRs becomes lighter (i.e. more proton-dominated) as the primary energy increases from 10^{17} eV towards the ankle at 3×10^{18} eV but then starts to become heavier again as the energy approaches the observed UHECR cutoff.

Comparing these distributions against those simulated by Monte Carlo tools allow for reconstructing the incident mass compositions consistent with experiment. One particular reconstruction using four primary mass groups (p, He, N, Fe), performed by Auger, is shown in Figure 1.6 [70, 78]. *According to this model*, there are hints for a rapidly disappearing contribution of iron above the *knee* at $10^{16.9}$ eV followed by a decrease in the proton component around $10^{18.8}$ eV. The decrease in the *modeled* proton component is compensated for by an increase in the prevalence of light nuclei (He) and medium-mass nuclei (N) at the maximum reconstructed energies (under *this* reconstruction).

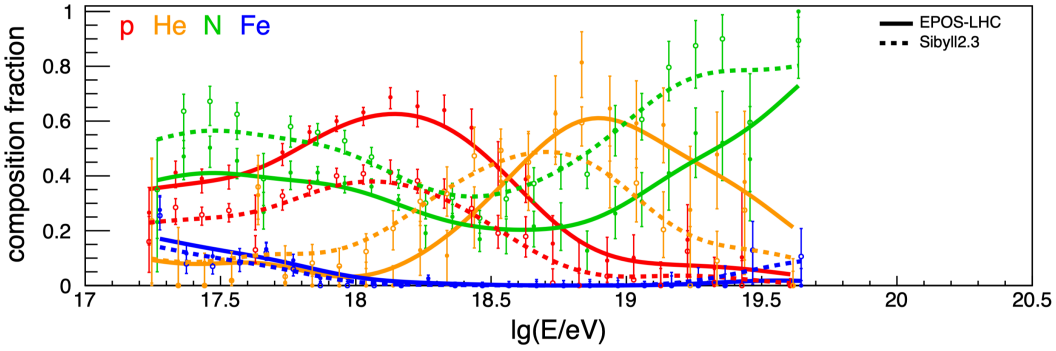

Figure 1.6: Composition fractions arriving at Earth derived from forward modeling templates of four mass groups to the $X_{\max}$ distribution observed by Auger reconstructed using two different hadronic interaction models (solid line vs. dashed line). Errors bar in this case are purely statistical. Composition reconstruction above $\sim 10^{20}$ eV is challenging due to the limited statistics at these high energies. Figure from [31] but originally adapted from [70].

Due to the large uncertainties involved in this process, this is not the only flux model that may be consistent with Auger measurements [31]. In particular, the limited statistics above $10^{19.6}$ eV are a major obstacle for accurate reconstructions of the mass composition [71, 73]. Furthermore, Figure 1.6 shows predictions for two different hadronic

interaction models, EPOS-LHC [69] and SIBYLL 2.3d [67], which are *not consistent* within uncertainties at most energy scales. This illustrates one of the major theoretical challenges of these measurements; since the center of mass energies in the early part of the shower can be more than an order of magnitude above the reach of current terrestrial accelerators, hadronic interaction models must be extrapolated and used in a regime where there are no direct terrestrial measurements [69]. This results in not only differences between reconstructed measurements using different hadronic and electromagnetic models, but also issues related to the accuracy of Monte Carlo simulations compared to direct observations, such as the *"muon excess"* where current hadronic interaction models predict significantly fewer muons in extensive air showers than are currently observed (i.e. showers are observed to have an "excess" of muons) [76].

This section has presented some of the major open questions in UHECR astronomy and has identified some of the challenges of both UHECR theory and the interpretation of measurements from the current generation of UHECR experiments. Some of these questions may be resolved by larger, *more sensitive* UHECR observatories, but others may only be able to be resolved using a multi-messenger approach. In particular, the neutral secondaries that could be produced, both in hadronic or leptonic astrophysical accelerators, or those that should be produced during GZK interactions between UHECRs and extragalactic background photons during propagation, could provide clear signatures for both identifying the currently unknown UHECR sources and the origin, composition, and nature of the UHECR spectral cutoff.

1.2 Ultrahigh Energy Neutrinos

In this section, we present a review of neutrino astrophysics at ultrahigh energies, how it relates to the open questions of ultrahigh energy *cosmic ray* astronomy, and motivate the science goals of current and next generation neutrino observatories.

1.2.1 Cosmogenic Neutrinos

As discussed in section 1.1.1, the GZK effect, first theorized in the 1960's, is the predicted suppression of UHECRs via interactions with extragalactic background photons. Above ∼40 EeV, UHECR protons can interact with cosmic microwave background (CMB)

photons via the Δ^+-resonance to produce secondary neutrinos and photons - these are referred to as *cosmogenic* secondaries [42, 41].

A branching diagram of the Δ^+-resonance interaction between UHECRs and extra-galactic background photons is shown in Figure 1.7 [41, 42]. Regardless of the branch taken by the original interaction, at least one UHE neutrino *or* photon will be produced, with the produced neutrinos typically carrying away ~5% of the incident proton energy, on average [41]. Both top level branches of this interaction will also produce secondary *protons*, albeit at a lower energy, which can contribute to the lower energy observed cosmic ray flux at Earth (and therefore changing the observed mass distribution at ultrahigh energies).

The flux of cosmogenic particles expected at Earth depends on the energy spectrum and mass composition of the UHECR flux at creation [79, 80], the redshift evolution for the currently unknown UHECR source population [81, 82], and the galactic and extra-galactic environments through the initial primary UHECRs and secondary particles propagate [46, 83]. As discussed in section 1.1.2, the GZK interaction is expected to strongly suppress UHECR fluxes from distances beyond ∼100 Mpc (the exact distance depends on the nuclei species). Therefore, UHECRs observed at Earth by terrestrial observatories like Auger and TA are expected to be from sources within a few hundred Mpc of Earth - the so-called *"GZK sphere"* or *"GZK horizon"* [41].

Fortunately, ultrahigh-energy neutrinos, as extremely weakly-interacting *neutral* particles, could be produced in the GZK interactions of UHECRs *outside* the GZK sphere and still propagate to Earth to be detected by terrestrial neutrino observatories [42, 46]. Therefore, ultrahigh energy neutrinos act as a *probe of hadronic UHECR physics beyond the horizon available to UHECR observatories*, like Auger. While also neutral, UHE photons have an interaction cross section that is orders of magnitude larger than an equivalent-energy neutrino and they therefore also possess a *"horizon"* beyond which they cannot be detected at Earth; at ultrahigh energies, this suppression is primarily due to pair production against infrared or CMB photons during propagation [84, 85, 86, 83].

The weakly interacting nature of the neutrino makes ultrahigh-energy neutrinos the *only* known technique able to probe extreme energy astrophysics outside the GZK cosmic ray and photon horizons. Unlike UHECRs, UHE neutrinos have not yet been conclusively observed despite extensive experimental searches [87]. A range of theoretical predictions for the expected cosmogenic neutrino fluxes due to the GZK process is shown in the yellow band of Figure 1.8 and in the grey band of Figure 1.9 along with limits from ex-

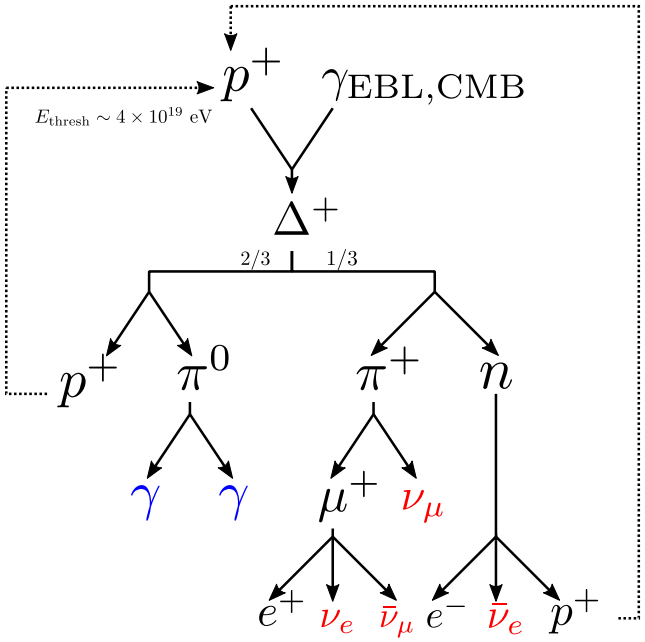

Figure 1.7: A branching diagram showing the production of UHE neutrinos from the Δ^+-resonance interaction between UHECRs and extragalactic background photons. The neutral secondaries produced are highlighted in red (neutrinos) and blue (photons). We have not shown any additional interactions or energy loss processes that could occur to the pions or neutrons before their respective decays.

isting UHE neutrino observatories. Detecting the UHE neutrino flux suffers from many of the same challenges faced by current UHECR observatories; primarily, the cosmogenic neutrino flux is predicted to be extremely small at these energies. In addition, the extremely small interaction cross section for the neutrino, $\sim 10^{-32}$ cm^2 to $\sim 10^{-30}$ cm^2 for the leading neutrino-nucleon deep inelastic scattering process at these energies [88], which in conjunction with the small flux, requires *huge* detectors [89] and/or long *exposures [90]* in order to be detected. The current best upper limits on the UHE neutrino flux are set by the IceCube Observatory [91], Pierre Auger Observatory [92, 93], and ANITA [87] and are shown in Figure 1.8 and Figure 1.9 along with *simulated* limits from a number of proposed next-generation neutrino observatories.

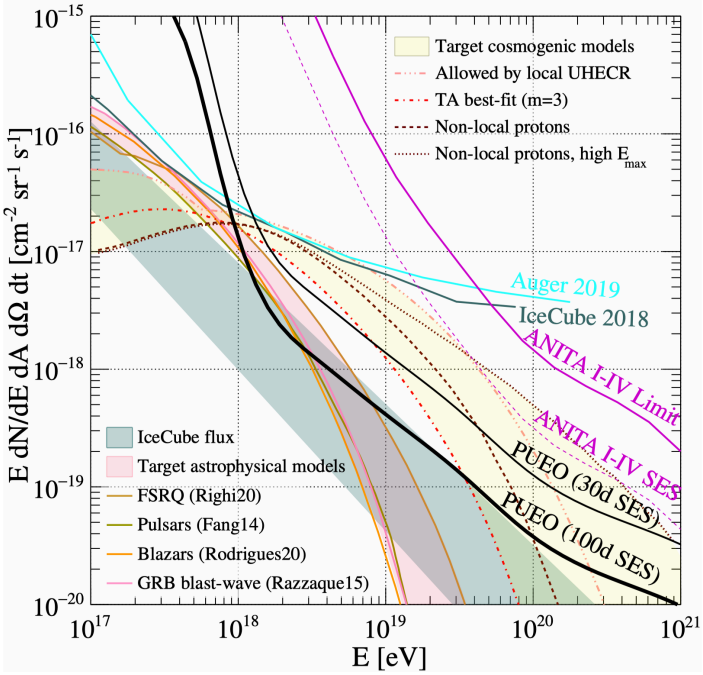

Figure 1.8: *Left:* Current limits on [91, 94, 87, 95] on cosmogenic neutrinos and other viable models. The models in this figure are source class fits to Auger data [95] and TA data [96] with a fixed source evolution model and subdominant all-proton models allowed by the measured proton fraction at Auger and TA [97]. This figure also shows the KKSS model from 2002 that was already previously ruled out by previous UHE neutrino experiments [98]. *Right:* The same experimental limits but instead against diffuse astrophysical neutrino flux models including FSRQs [99], AGN [100], GRBs [101], pulsars [102, 103], and an extrapolation of the IceCube neutrino flux [104].

These figures illustrate the large variation in predictions for the diffuse flux of UHE neutrinos which strongly depend upon assumptions about UHECR production and propagation models. Over the last ~15 years, as UHE neutrino limits from Auger [94], IceCube [91], and ANITA [87] have become more sensitive *without* the definitive discovery of an UHE neutrino, entire classes of models have been ruled out [105, 106, 107] and are no longer shown in plots like in Figure 1.8.

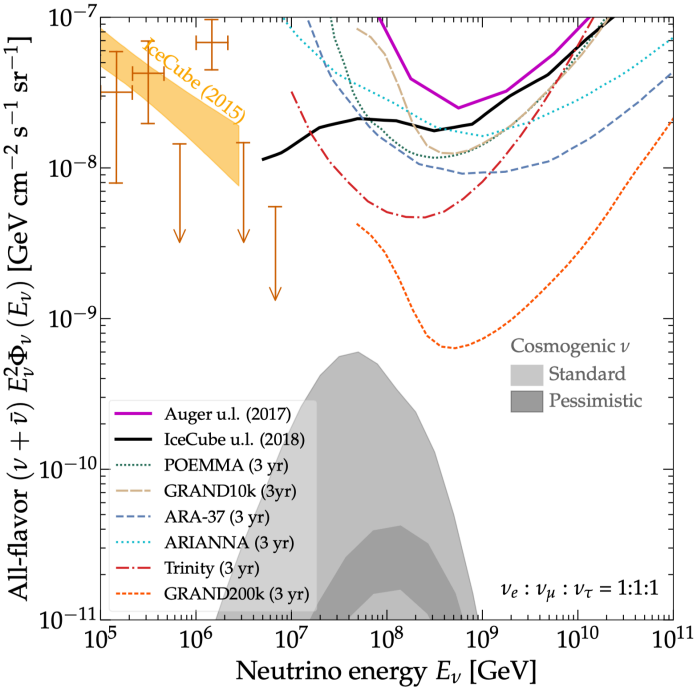

Figure 1.9: Similar UHE experimental neutrino limits as in Figure 1.8 but compared against an alternative set of models for the diffuse cosmogenic neutrino flux under different assumptions regarding the efficiency and redshift distribution of UHECR sources. Figure from [31].

The phenomenological challenge of predicting cosmogenic neutrino fluxes *on Earth* is also worsened by the additional degree of freedom introduced by the GZK horizon; UHECR measurements *on Earth* should only be able to probe hadronic accelerators in the very local universe, within the GZK horizon, but UHE neutrinos could propagate from significantly larger distances [108, 109, 110] Therefore, there is the possibility that the distribution of UHECR sources we observed with Auger, and the UHE neutrino sources we might observe with a neutrino observatory like ANITA, are fundamentally different source populations [111]. This decoupling between the constraints set by local

UHECR and photon measurements and cosmogenic neutrino production models significantly enhances the phase space for neutrino flux predictions [46]. One example of these models are the *"non-local proton"* models in Figure 1.8 (compared against predictions allowed by *local UHECR measurements* labeled as *"Allowed by local UHECR"*) and the variation between the light grey and dark grey bands in Figure 1.9.

Both Figure 1.8 and Figure 1.9 show *all-flavor* predictions for the UHE cosmogenic neutrino flux. As shown in Figure 1.7, the GZK process produces a flux of neutrinos, *at creation*, with a flavor composition of 1:1:0 (for flavor ratios in the form $\nu_e : \nu_\mu : \nu_\tau$, summing over both neutrinos and antineutrinos equally which are extremely hard to distinguish at ultrahigh energies above the Glashow resonance [112]) [41]. Typically, the electron neutrino produced by the neutron decay has a significantly lower energy compared to the neutrinos from the pion decay. This makes the flavor of the *ultrahigh energy* component of the flux closer to a 1:2:0 composition. However, neutrinos, even ultrahigh energy ones, *oscillate flavors* during propagation from creation to detection and as such can be observed to have a *different* flavor composition at Earth [113]. For an UHE 1:2:0 flux at an extremely large distance, current measurements of the neutrino oscillation matrix [114] predicts an approximately 1:1:1 flavor composition *at Earth*; i.e. *cosmogenic* neutrinos should be uniformly distributed among the three flavor by the time they reach Earth. As we will discuss in section 1.2.2, alternative sources of ultrahigh-energy neutrinos *not* from the GZK process can produce neutrino fluxes at Earth that are not 1:1:1. While the flux of UHE cosmogenic neutrinos is predicted to be uniform in flavor, the sensitivity and resolution of different neutrino observatories can vary significantly depending upon the specific neutrino flavor; this will be discussed in more detail in Chapter 2.

1.2.2 Astrophysical Neutrinos

Along with *cosmogenic neutrinos* produced by UHECRs during *propagation*, high energy astrophysical environments, such as blazars, hypernovae, or starbust galaxies (among others), that could themselves be UHECR accelerators, could also directly produce UHE neutrinos *within* the source environment [115, 116, 48]. These so-called *astrophysical* neutrinos provide an alternative messenger for understanding ultrahigh energy hadronic processes in extreme astrophysical environments. While there is still significant uncertainty around the exact mechanisms for astrophysical neutrino production, the most supported hypothesis is that accelerated cosmic ray protons undergo photo-hadronic interac-

tions against synchrotron photons from co-accelerated electrons or positrons within the same acceleration environment [117, 108, 118, 119] to produce charged pions and neutrons whose subsequent decays produce neutrinos (via the same decay channels shown in Figure 1.7 for the GZK process).

Astrophysical neutrino accelerators could be considered as individual "point-like" sources of UHE neutrinos, in which case we typically discuss the *fluence* (in $\mathrm{cm}^{-2}\,\mathrm{s}^{-1}$) produced by a single source. Alternatively, we can consider the total neutrino flux produced by the broader *population* of a specific source class (i.e. all AGN) which is typically described as a *diffuse astrophysical flux* (in $\mathrm{cm}^{-2}\,\mathrm{s}^{-1}\,\mathrm{sr}^{-1}$). A range of predictions for the neutrino flux from several different candidate source classes is shown in Figure 1.10.

The predictions for the *fluence* from individual objects is significantly more variable as many of the potential astrophysical neutrino sources are fundamentally transient (such as GRB [101] or neutron-neutron star merges [120]) and as such their fluence can vary by orders of magnitude depending upon the time-scale of detection [121].

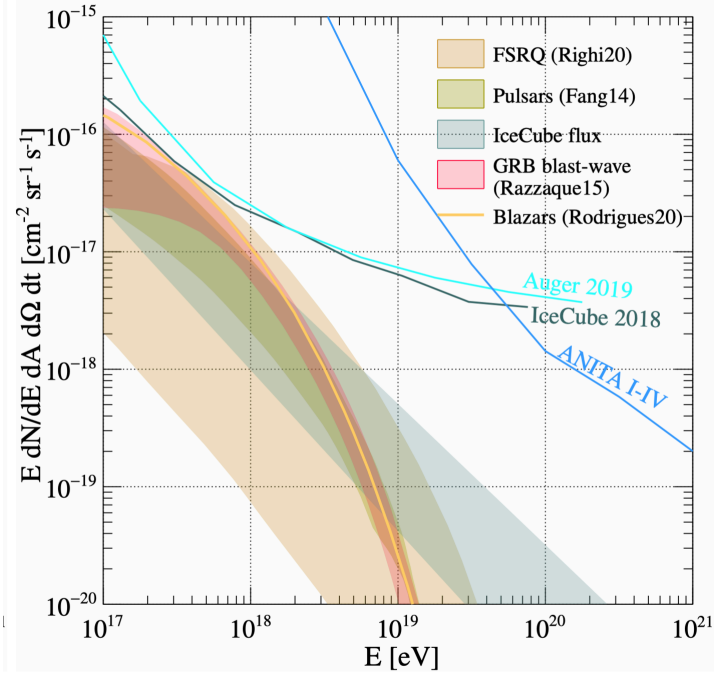

Figure 1.10: Predictions for the *diffuse* UHE astrophysical neutrino flux from several source models. FSRQs [99], pulsars [103, 102], GRBs [101], and blazars [122] along with limits from the IceCube [91], Auger [123], and ANITA [87] observatories Figure from [111].

A significant advantage of astrophysical neutrinos is that they may point *directly* back to their production environments as they can be produced within regions only tens of pc [124] or up to a few kpc in size [116] around the source, such that their parent particles do not undergo any significant deflection. Cosmogenic neutrinos, whose parent cosmic rays may have tens of Mpc of turbulent magnetic deflection before producing the cosmogenic, *may* have *less* correlation with their parent environment. However, since $\mathcal{O}(5\,\mathrm{EeV})$ neutrinos will nominally be produced by $\mathcal{O}(100\,\mathrm{EeV})$ UHECRs with high rigidity, and since cosmogenic neutrinos at this energy are more likely to be produced near the start of the UHECR trajectory, cosmogenic neutrinos should also still be significantly correlated with their parent UHECR source.

Since *astrophysical* neutrino production takes place inside high-energy astrophysical environments, a host of leptonic and hadronic processes can influence the parent processes of the neutrino, resulting in different energy spectra and flavor compositions compared to cosmogenic neutrino fluxes. The standard photo-hadronic interactions that are expected to dominate astrophysical neutrino production are

$$p + \gamma \rightarrow \pi^+ + n$$

The photon here is likely a synchrotron photon (as opposed to a CMB photon) produced by coaccelerated leptons. The π^+ and μ^+ then subsequently decay via

$$\pi^+ \rightarrow \mu^+ + \nu_\mu$$

,

$$\mu^+ \rightarrow e^+ + \nu_e \bar{\nu}_\mu$$

, while the neutron decays via

$$n \rightarrow e^- + \bar{\nu}_e + p^+$$

. The production of a charged kaon via

$$p + \gamma \rightarrow K^+ + \Lambda/\Sigma$$

which subsequently decays, producing neutrinos directly and via the corresponding muon decay,

$$K^+ \rightarrow \mu^+ + \nu_\mu$$

can contribute to the fluence depending upon the environment of the source but is typically subdominant to the pion-neutron contributions [117, 125].

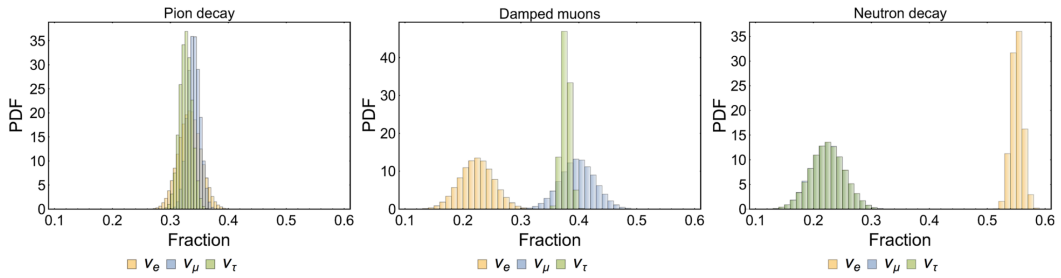

Figure 1.11: Predicted flavor compositions of high energy *astrophysical* neutrinos *at Earth*, including neutrino oscillations and model uncertainties, assuming that they are produced by three different production mechanisms at the source: pion decay (left); damped muons (center); and neutron decay (right). Note in the neutron decay figure, the predicted distributions of ν_μ and ν_τ overlap almost exactly and are not distinguishable in the figure. Figure from [126].

As discussed in section 1.2.1, the production of UHE neutrinos via photo-hadronic pion production (in isolation) produces a 1:1:0 or 1:2:0 flavor composition *at the source* (depending upon whether the lower energy neutrino from the neutron decay is included in the energy range of interest) that then oscillates to a 1:1:1 by the time it is observed at Earth. However, under the conditions present *inside* these high energy astrophysical environments, it is possible to suppress particular branches of these photo-hadronic interactions and subsequent decays and therefore change the flavor composition at the source and therefore also at Earth. The three most commonly proposed scenarios for ultrahigh-energy astrophysical neutrino production are referred to as:

1. **Pion Decay** In this model, the primary UHE neutrino flux comes from decay of charged pions that have undergone little to no energy loss. This results in an UHE flavor composition $\nu_e : \nu_\mu : \nu_\tau$ of 1:2:0, similar to the GZK process (since the neutrino from the corresponding neutron usually carries an order of magnitude less energy) [117]. Similar to the cosmogenic case, a "pion beam" source is expected to produce a 1:1:1 flavor ratio at Earth after neutrino oscillation [126, 127].

2. **Damped Muon Decay** Ultrahigh energy astrophysical accelerators typically require strong magnetic fields in order to be able to contain and accelerate UHE particles. If the magnetic fields of the environment are large enough such that the synchrotron loss time scale for the muons is shorter than the (dilated) muon lifetime, then the muons lose almost all of their energy before decaying. Therefore, the resulting neutrinos are no longer UHE and wouldn't contribute to the observed flux [117]. A *"damped muon decay"* source should have a 0:1:0 ultrahigh energy flavor ratio at the source which corresponds to a 1:2:2 flavor ratio at Earth [126, 127].

3. **Neutron Beam** Lastly, for sources with even larger magnetic fields, such that the synchrotron loss time for the muons *and* the charged pions is shorted than their corresponding lifetimes, than the anti-electron neutrinos produced by the neutron decay (assuming a source environment that is optically thin to neutrons) is the dominant contribution to the flux [117]. In this case, the neutrino flavor composition at the source should be 1:0:0, albeit at significantly lower energies than a pion decay or damped muon decay source model. This corresponds to a 3:1:1 composition at Earth [126, 127]. There are also additional processes that could occur in these environments that could further increase the neutron production (and the corresponding neutrino flux) such as photo-dissociation of heavier cosmic ray nuclei [128, 129].

A distribution of the expected flavor compositions *at Earth* for the three source models described above is shown in Figure 1.11. Currently, the latest IceCube constraints on the flavor of astrophysical neutrinos at the TeV $\rightarrow$ PeV scale are more consistent with a *neutron beam* source model and disfavor the pion beam and damped muon scenarios at 2σ and 2.6σ, respectively. While this is below the threshold of "ultrahigh energy" neutrino astrophysics relevant to most of this work, these are the (current) highest energy measurement of neutrino flavor and can help constrain theoretical predictions at even higher energies.

The flavor ratios from an astrophysical source are strongly influenced by the magnetic environment of the source (as this determines the synchrotron loss time scale). An example of one possible Hillas-like diagram showing the different source models (which determines the source flavor composition and spectra as above) as a function of the characteristic size, R, and magnetic field, B, of the source is shown in Figure 1.12. Figure 1.11 and Figure 1.12 highlight the physics reach of detailed measurements of astrophys-

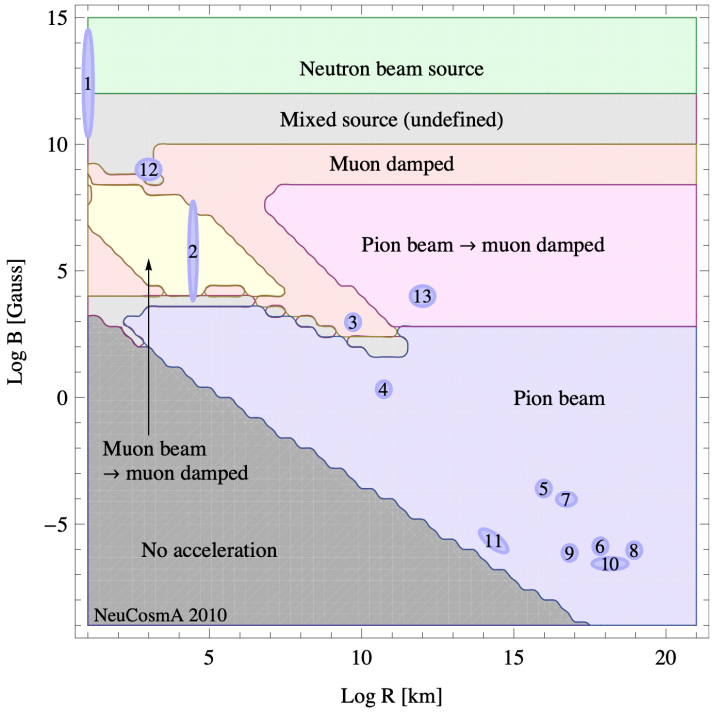

Figure 1.12: A Hillas-like flavor diagram classifying the acceleration environment (and therefore the corresponding flavor ratio at the source) for a variety of astrophysical conditions and neutrino production scenarios under specific assumptions for the underlying hadronic injection spectrum. See the text for descriptions of the different source models shown here. Figure from [117].

ical UHE neutrino flavor *at Earth*; they can provide invaluable information about the environment in which the neutrinos, and parent particles, are produced [109, 130, 131, 132, 133].

These benefits make *both* astrophysical and cosmogenic neutrinos extremely powerful messengers of astrophysical processes over cosmological distances, allowing us to explore the UHE hadronic universe outside the limitations of the GZK horizon. Therefore, many experiments have been constructed in the last two decades that aimed or aim to make the first detection of an UHE neutrino. More details on the detection techniques for observing UHE neutrinos will be discussed in Chapter 2.

After this brief review of UHECR and neutrino astronomy, we continue by discussing the phenomenology of astrophysical accelerators that may be capable of producing UHECRs and neutrinos, and discuss the specific models for some of the most likely astrophysical sources (under current theories).

1.3 Possible Sources of Ultrahigh Energy Particles

Despite significant theoretical advances in our understanding of cosmic ray propagation and acceleration, the sources of the observed UHECR flux remain *unresolved*. In this section, we present a review of the current theory of the production and propagation of UHECRs and UHE neutrinos. In particular, we discuss several proposed astrophysical objects and environments that could be responsible for the observed UHECR flux, and that may also be sources of UHE neutrinos, and how current theoretical predictions relate to the observations of current generation experiments.

The challenge of accelerating cosmic rays up to a given energy is often presented as the *"Hillas criterion"*, a minimum requirement for any source to be an accelerator for cosmic rays of a given energy [134]. The Hillas criterion states that a *necessary* (but not *sufficient*) condition to accelerate particles to a given energy is that the source environment can *confine* the particles in the acceleration environment up to the required energy (as they become increasingly rigid at higher energies) in order to *actually accelerate* them. After acceleration up to some maximum energy, at which the confinement power of the acceleration regime is insufficient to contain the particles, the cosmic rays will then leave the accelerator and (potentially) propagate to Earth. This is expressed as a requirement

on the Larmor radius of the particle in the acceleration region: to first order, a particle can stay in the *acceleration region* as long as its Larmor radius is smaller than the characteristic size of the acceleration environment.

Under this model, the maximum energy achievable, E_{max}, by a cosmic ray source with a characteristic size, R, and magnetic field strength, B, is approximately

$$E_{\text{max}} \sim \frac{\beta_{\text{sh}}}{\eta} eBR\Gamma \tag{1.1}$$

where β_{sh} is the velocity of the accelerating shock front in units of the speed of light, η parameterizes the efficiency of the acceleration relative to the Bohm limit [135], Γ is the Lorentz factor of the acceleration process, and e is the charge of the electron [134].

This condition is not *sufficient* to guarantee the acceleration of cosmic rays to a given energy, as details of the acceleration and energy loss mechanisms are important [135], but it does allow us to identify sources that have the *potential* to be UHECR accelerators. A Hillas diagram, that compares the characteristic size and magnetic field strength of an accelerator, is shown in Figure 1.13 with colored regions delineating a variety of sources that could satisfy the Hillas condition for producing UHECR protons and iron nuclei with energy 10^{20} eV.

Classes of objects to the *left of and below* the diagonal lines in Figure 1.13 do not satisfy the Hillas criterion and are unlikely to be significant sites of UHECR acceleration under *current* models for the source environments [31]; this currently excludes Wolf-Rayet-like stars [136], and typical supernovae [137, 138]. Source classes that are currently candidates for UHECR acceleration include magnetars [139, 120], active galactic nuclei (AGN) [124, 140, 141], gamma-ray bursts (GRBs) [142, 101, 54, 143], starburst galaxies [144, 116], and tidal disruption events (TDEs) [145, 146, 147, 148].

The standard formalism for hadronic acceleration in high energy sources is *diffusive shock*, or *first-order Fermi*, acceleration (DSA) [149, 150, 32, 33] where charged particles are repeatedly accelerated as they cross magnetic shock fronts found within astrophysical accelerators. One of the main strengths of diffusive shock acceleration-like models are that they can also easily predict falling power-law energy spectra (as observed across the entire cosmic energy spectrum) for parameters that are consistent with estimates for cosmic ray accelerators [151].

Along with the properties of individual astrophysical sources and environments, similar constraints can be placed on the *number density of sources* or *total effective luminosity*

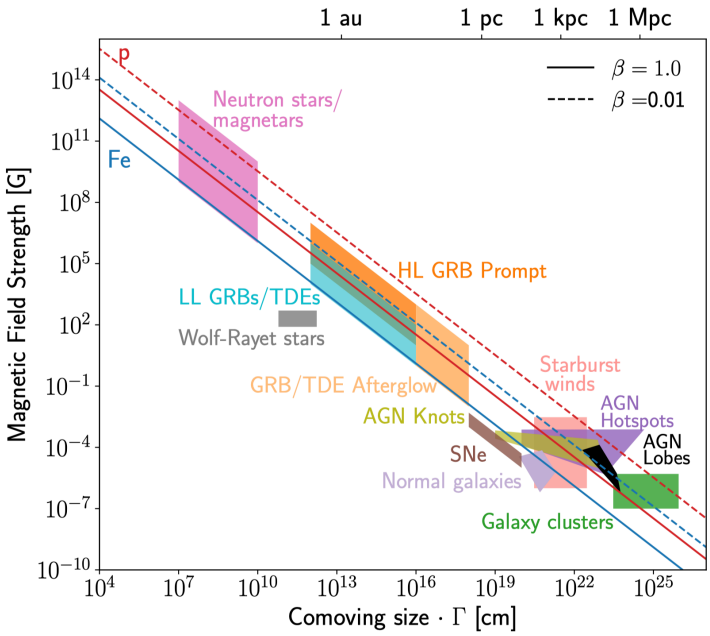

Figure 1.13: A Hillas diagram showing a variety of sources classes as a function of their characteristic comoving size, Γ, and their magnetic field strength, B, in the ideal Bohm limit (where the mean free path is assumed to be equal to the Larmor radius) where $\eta = 1$ (note the Γ in this equation is not the same Γ in Equation 1.1. Γ in this figure is comparable to R in Equation 1.1). Solid (dashed) lines indicate the region beyond which confinement of protons (red) or iron nuclei (blue) with energy 10^{20} eV are possible for outflows with shock velocities of $\beta_{\rm sh} = 1$ (solid) and $\beta_{\rm sh} = 0.01$ (dashed). Figure from [31].

of each source class. This constraint can be inferred both from the total incident energy and *anisotropy* of UHECRs measured at Earth (i.e. a very small number of high-luminosity sources is *too anisotropic* to be compatible with constraints from Auger and TA). A similar Hillas-like diagram for source luminosity versus number density for a variety of UHECR production models is shown in Figure 1.14. This provides additional information in the search for the unknown cosmic ray accelerators; for example, while high-luminosity gamma-ray bursts (HL-GRBs) might *individually* have the capability to accelerate UHECRs (see the Hillas diagram in 1.13), current measurements of the source evolution and number density of HL-GRBs make them an unlikely candidate for being the dominant contributor to the measured diffuse UHECR flux at Earth (Figure 1.14).

It is also possible that multiple source classes play significant roles in producing the observed UHECR flux (as opposed to one source class dominating the observed flux which is assumed in Figure 1.13 and Figure 1.14). These scenarios have been explored in [122, 13, 49], and can be used to reduce potentially tension with some single source class models but significantly more theoretical study is needed.

Under the simple constraints of Figure 1.13 and Figure 1.14, we proceed to outline the source acceleration mechanisms for several potential UHECR accelerators, and therefore potentially UHE neutrino sources, and discuss current experimental constraints and searches.

1.3.1 Gamma-ray Bursts (GRBs)

Gamma-ray bursts have been a likely candidate for UHECR acceleration for nearly three decades [56, 55]. The standard model for UHECR production in GRB is the so-called *"Fireball"* model where blobs of plasma (*"fireballs"*) emitted from and accelerated within the central engine, collide within the relativistic jet (in the case of short sGRBs) or in the halo around the central engine (in the case of a longer non-short GRBs) to form magnetic shocks, that can then accelerate charged particles via a diffusive shock acceleration mechanism (so-called *"internal"* models). Alternative models involving forward and reverse shocks created by the interaction between the *"fireball"* and the surrounding circumburst medium also exist (so-called *"external"* models) [153, 154].

GRBs are typically sub-divided into two categories: *high-luminosity GRBs* (HL-GRB) ($L \gtrsim 10^{49}$ ergs s^{-1}) and *low-luminosity GRBs* (LL-GRBs) ($L \lesssim 10^{49}$ ergs s^{-1}). Both HL-GRB and LL-GRB meet the Hillas criterion for accelerating UHECRs to 10^{20} eV (Figure 1.13)

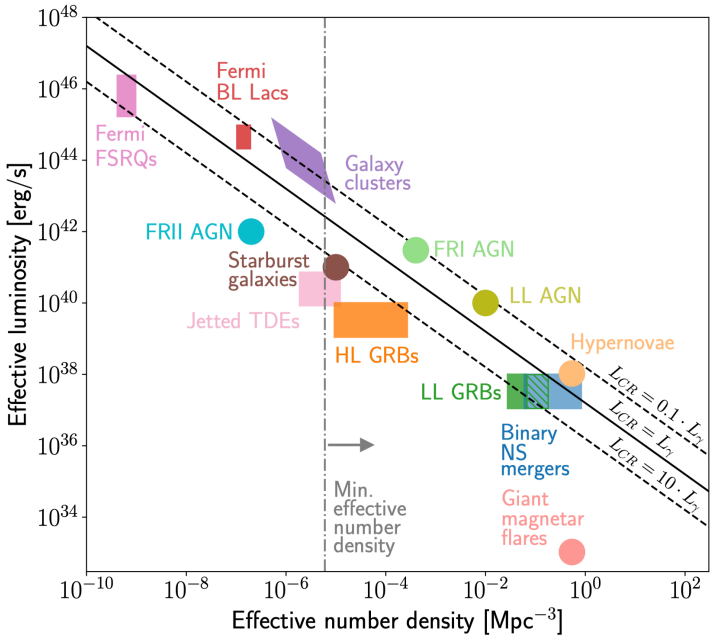

Figure 1.14: Characteristic source luminosity versus source number density for steady sources, and effective luminosity versus effective number density for transient sources assuming a characteristic diffusion time spread of $\tau = 3 \times 10^5$ yr (this constant depends upon assumptions about galactic and extra-galactic magnetic field strengths). The black solid (diagonal) line gives the best-fit UHECR energy production rate, derived in [59], which corresponds to 5×10^{44} erg Mpc^{-3} yr^{-1} under the assumption that the UHECR luminosity is equal to the photon luminosity of each source class, L_γ. The two dashed lines above and below indicate different assumptions about the efficiency of UHECR production which is converted to different scalings between L_{cr} and L_γ. The vertical dashed line is a separate estimate of the required number density from Auger [152]. Figure from [31]. References for the models used for each source class are also available in [31].

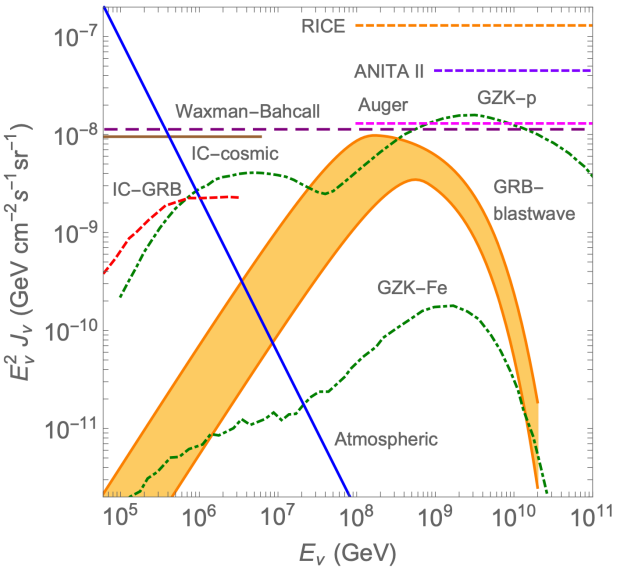

Figure 1.15: Models of diffuse muon neutrino fluxes from one model of neutrino production in GRB blast-waves (shaded orange), atmospheric (solid blue) [155], GZK p-dominated (upper dot-dashed green) and GZK Fe-dominated (lower dot-dashed green) [81]. Also shown are the best-fit flux for the IceCube detected events (solid brown) [156], Waxman- Bahcall theoretical upper limit on the GZK flux [156, 110], Ice-Cube upper limit on the prompt GRB flux [157]. Also shown are upper limits on diffuse $\propto E^{-2}$ flux from the Pierre AugerObservatory [123], ANITA-II [158] and RICE [159] experiments.

but the number density of HL-GRBs poses some phenomenological challenges (Figure 1.14). LL-GRBs are the most luminous objects observed within ∼100 Mpc (the horizon distance of UHECRs) and easily exceed the minimum source number density requirement (Figure 1.14) necessary to replicate the observed flux [54, 143].

GRBs are also expected to be efficient producers of ultrahigh-energy neutrinos via the photo-meson production process discussed in section 1.2.2 against the intense γ-ray fluxes produced by synchrotron or inverse-Compton radiation from (shock)-accelerated electrons and positrons [160]. A range of predictions for the diffuse flux from GRBs is shown in Figure 1.15 and Figure 1.8. The *top* of the yellow shaded region in Figure 1.15 was explicitly designed to saturate available bounds (at the time of publication) and is now in tension with new limits. The transient nature of gamma ray bursts, with time scales that vary from hundreds of milliseconds to several hours, requires that the observatory be active and sensitive to a burst that may only be seconds in duration.

1.3.2 Hypernovae (HNe)

As suggested by the Hillas condition in Figure 1.13, the typical supernova is not expected to be able to accelerate cosmic rays to ultrahigh energies, however the ejecta of rarer trans-relativistic and engine-driven supernovae (i.e. hypernova), whose kinetic energy is more than an order of magnitude larger than normal supernovae at $\gtrsim 10^{52}$ erg, *may* be able to accelerate and produce UHECRs [115, 161, 162]. The UHE cosmic ray and neutrino flux predicted by a recent model of hypernovae (trans-relativistic supernovae (TRSN)) is shown in Figure 1.16 [163] along with a prediction for cosmogenic neutrinos (green dashed line). Interestingly, one possible model where the UHECR flux is due *primarily* to a combination of GRBs and hypernovae can reproduce the UHECR composition data observed by Auger and TA, within experimental and generous model uncertainties [162].

1.3.3 Active Galactic Nuclei (AGN) and Blazars

Active galactic nuclei (AGN), extremely luminous compact regions at the cores of active galaxies, often accompanied by powerful relativistic *"jets"* or outflows, are promising candidates for UHECR acceleration [53, 57, 48], with likely acceleration signatures observable in the gamma ray spectrum [165, 166, 167]. In particular, much phenomenological study has been devoted to *radio-loud* AGN with jets closely aligned with the observation direction from Earth, known as *blazars*, that can easily meet the Hillas criterion (Fig-

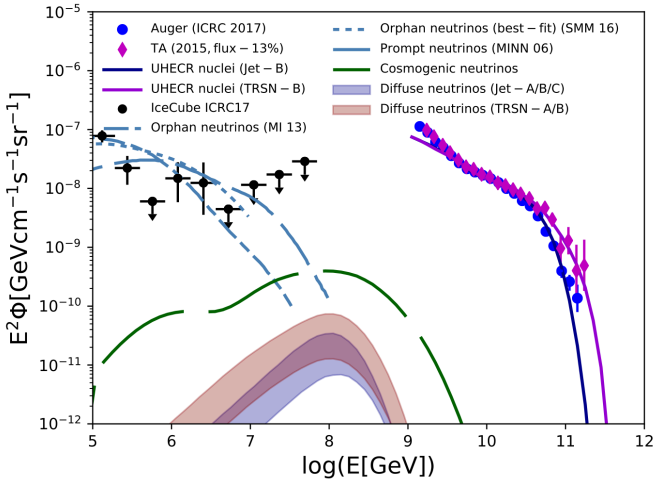

Figure 1.16: The predicted diffuse energy spectra of UHECR nuclei and neutrinos from hypernovae (trans-relativistic supernovae (TRSN)) and hypernovae associated with low-luminosity GRBs ("Jet"). Also shown are the diffuse neutrinos in the case of choked jets (dot-dashed line) [164], and LL-GRB prompt neutrinos (dashed line) [143]. Figure from [163].

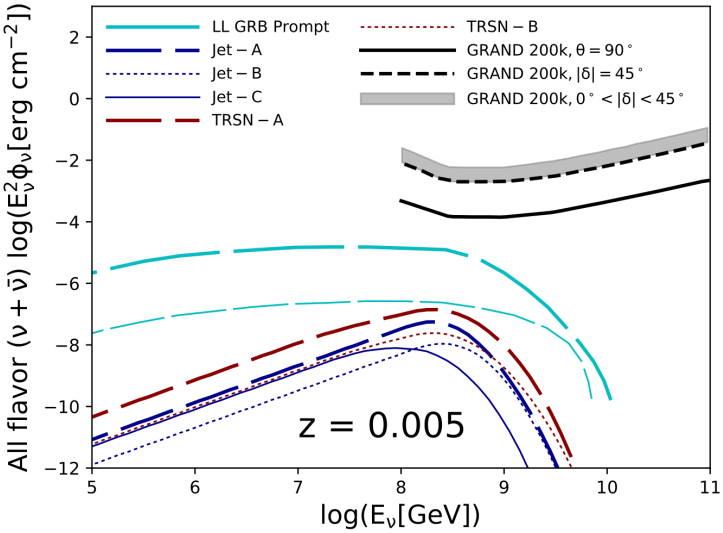

Figure 1.17: The all-flavor neutrino fluence from a *single* hypernovae located at redshift $z = 0.005$. The various thick, thin, and dashed lines indicate different assumptions regarding the acceleration environment of hypernovae (TSRN) and hypernovae associated with a LL-GRB ("Jet"). Figure from [163].

ure 1.13) for UHECR acceleration up to $\sim 10^{20}$ eV. There is significant interest in this source model, especially after the recent discovery of a high energy astrophysical neutrino coincident with a flaring blazar, TXS 0506+056, by the IceCube Observatory, that was simultaneously observed across the entire electromagnetic spectrum [118, 3] as well as evidence of correlation between observed AGN sky coordinates and Auger cosmic ray events [57, 9].

There are several models for UHECR acceleration in the jets of blazars including *shear reacceleration* [168, 169], non-ballistic acceleration [170], and *one-shot "ESPRESSO"* acceleration [171]; these are generally all based on the principle of diffusive shock acceleration (DSA) discussed in section 1.3 with different models for the origin and location of the accelerating shocks. Furthermore, many of these acceleration models, including *shear* and *"ESPRESSO"* acceleration, are able to reproduce the spectral shape and composition observations of Auger and TA [140, 171, 168], but different analyses disagree on whether the known population of blazars can reproduce the *total* observed UHECR luminosity at Earth [140, 31]. Detailed *"bottom-up"* simulations of UHECR acceleration in blazars, needed to generate accurate predictions for the flux and composition for a given phenomenological model, are computationally challenging and typically involve expensive magneto-hydrodynamic (MHD) simulations of the conditions inside blazar jets and their effect on injected cosmic rays; an example of such a simulation is shown in Figure 1.18 for the *"ESPRESSO"*, or *one-shot*, model [171].

The *one-shot acceleration* model involves high energy cosmic ray *"seeds"* accelerated up to PeV energies by supernova remnants (see the discussion of the origin of the knee in section 1.1.1) in the AGN's host galaxy that penetrate into the relativistic jet and receive a single boost (or "shot") of a factor of $\sim\Gamma^2$ in energy, where Γ is the Lorentz factor of the relativistic AGN jet outflow. One *"ESPRESSO"* shot can therefore boost the energy of galactic CRs by a factor of $\Gamma^2 \sim 10^3$, boosting 10^{17} eV cosmic rays to UHECRs at 10^{20} eV, assuming a Lorentz factor of $\Gamma \sim 30$, which is supported by multi-wavelength observations of AGN [173, 174]. The method of acceleration, determined by the AGN environment and conditions within the jet, determines the flux of cosmic rays *and* UHE neutrinos observed at Earth and therefore these models are crucial in determining whether AGN are indeed the sources of observed UHECRs.

The known population of blazars is divided into several subclasses, including high- and low-luminosity BL Lacertae objects (HL-BL Lacs and LL-BL Lacs, respectively), and flat spectrum radio quasars (FSRQs) [177]. These different blazar subclasses are identified

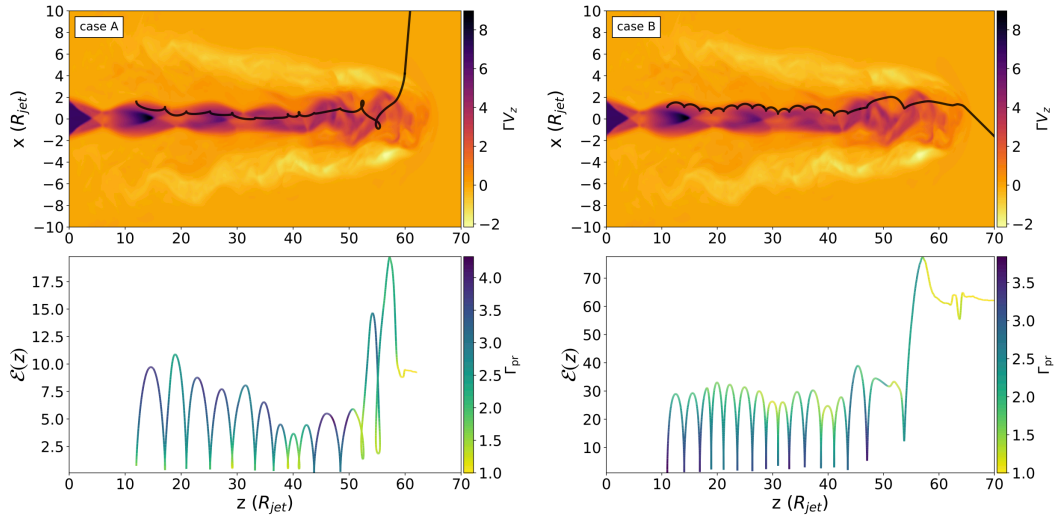

Figure 1.18: Top: Two example cosmic ray trajectories (black) calculated using the ESPRESSO AGN model using the PLUTO MHD code [172] plotted over the 4-velocity component Γv_z (colormap) of the jet flow. Bottom: The energy gain for each particle as it is boosted in the jet. Both particles are initialized with gyroradii smaller than the jet radius and both gain energy in excess of Γ^2. Figure from [171].

by multi-wavelength observations across the electromagnetic spectrum, which provide insight into the different astrophysical environments at the source, as well as different underlying redshift source evolutions for each subclass [177, 140]. A diagram of the measured (white background) and extrapolated (yellow background) redshift evolution for these different blazar subclasses, under one evolution model, is shown in Figure 1.19, along with the integrated redshift distribution (bottom).

The differences in the source environments between these different blazar subclasses are expected to produce significant differences in the fluxes of UHECRs, UHE astrophysical neutrinos, and γ-rays from each source population [140]. UHE neutrino production in blazars and AGN is expected via the same photo-disintegration and photo-pion production discussed in section 1.2.2, but the photon luminosity and energy spectra are expected to be different across the different blazar subclasses. In particular, the high energy, high luminosity photon fluxes in high-luminosity FSRQs are currently expected to lead to extremely efficient photo-hadronic neutrino production at the cost of attenuating the source UHECR spectrum. Alternatively, *low-luminosity* BL Lacs, with their (relatively) lower photon luminosities are expected to have minimal neutrino production while being optically thin for UHECRs produced within the jet. Therefore, current

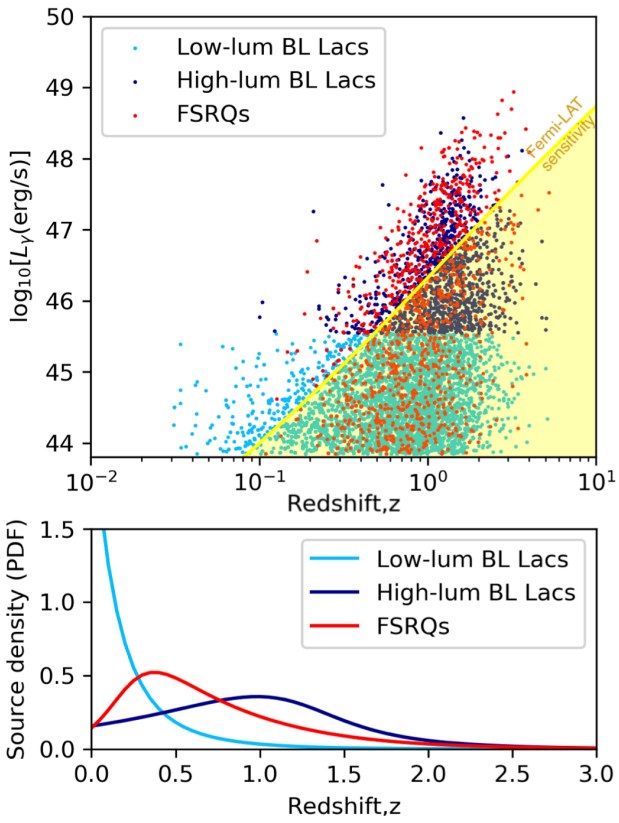

Figure 1.19: Measured and simulated distributions of the redshift evolution of different blazar subclasses according to the model of Ajello et al. [175, 176] as function of luminosity and redshift. The yellow region represents the simulated phase space that falls below the sensitivity of Fermi calculated using this model. The lower panel shows the same distribution but integrated over luminosity to indicate the different expected redshift evolution of these different subclasses; in particular, the strongly negative evolution of LL-BL Lac compared to the high-luminosity AGN (BL Lacs and FSRQs) allows for each source class to have different relative contributions to either the cosmic ray or neutrino flux (see the text for more details). Figure from [140].

models predict that observed UHECR and neutrino fluxes may be produced by different sub-populations of blazars; with LL-BL Lacs being efficient UHECR sources but poor neutrino sources, while HL-BL Lacs and FSRQs are expected to be poor UHECR sources but extremely efficient neutrino sources [48, 140].

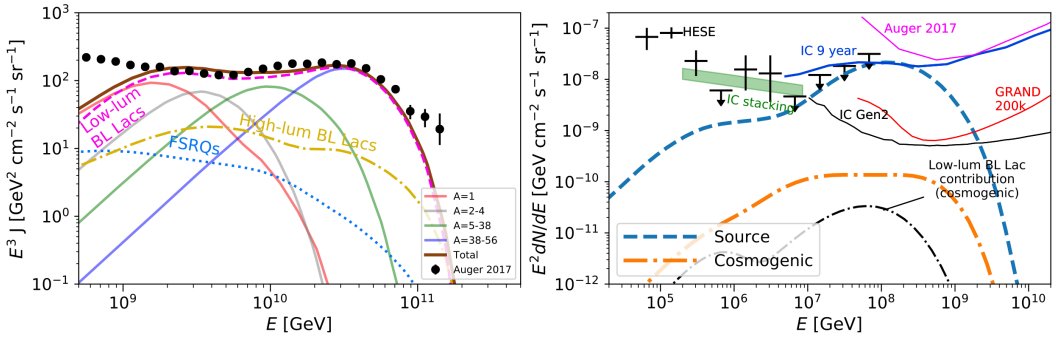

Figure 1.20: *Left:* A prediction for the UHECR flux from the reconstructed population of blazars shown in Figure 1.19. *Right:* The *maximum* all-flavor neutrino flux allowed by this same population of blazars without exceeding current limits. In this model, the UHECR spectrum is dominated by low-luminosity BL Lacs (due to the negative source evolution and efficient cosmic ray production) while the maximum of the neutrino flux is achieved by efficient neutrino in the population of FSRQs outside the GZK horizon. Figure from [140].

One model prediction for the UHECR and neutrino flux from the population of blazars shown in Figure 1.19 is shown in Figure 1.20. The redshift evolution for the different blazar subclasses shown in Figure 1.19 also adds an additional degree of freedom when reconstructing populations of sources that can produce the observed UHECR flux. Since there are no known FSRQs within the GZK horizon, the efficient neutrino production of FSRQs can be used to produce large neutrino fluxes without exceeding UHECR bounds set by Auger [140] and the strongly negative source evolution of LL-BL Lacs (almost all known LL-BL Lacs are within $z < 0.5$), combined with their efficient UHECR acceleration and inefficient neutrino production, allows them to be the dominant UHECR source for measurements from Auger and TA without exceeding neutrino bounds by IceCube [91], ANITA [87], and Auger [123].

1.3.4 Starburst Galaxies (SB)

Starburst galaxies (SBG) - galaxies undergoing intense star-formation activity - are observed to drive powerful galactic-scale "superwinds" which could be highly efficient cos-

mic ray accelerators [116] via shock acceleration-like processes. However, different acceleration models have come to different conclusions on whether starburst galaxies exceed the Hillas criterion at 10^{20} eV and could produce the upper end of the cosmic ray spectrum [116, 144, 178, 179].

In particular, one model for the source of the accelerating shocks are so-called "termination shocks" created when the *supersonic* jet no longer has sufficient pressure to remain supersonic and abruptly becomes a *subsonic* jet, creating a steady-state "termination shock" [179, 144]. This source class is of particular importance as Auger has observed an excess in the UHECR flux ($\gtrsim$40 EeV) in the direction of starburst galaxies with 4.0σ post-trial significance [9]. However, a corresponding search by TA is consistent with *both* the Auger starburst result (within 1.4σ) and with *isotropy* (within 1.1σ) [180]. Furthermore, several starburst galaxies, NGC 4945 and M 83, lie within the most significant UHECR excess in the southern sky observed by Auger and M 82 is spatially consistent with the TA UHECR hotspot [181, 182].

The low-γ-ray luminosity associated with most starburst galaxies - only a dozen SBGs have been cataloged by Fermi as point-like γ-ray sources [183] - sets strong constraints on their role as astrophysical neutrino producers [184]. Theoretical models that satisfy all current bounds can still vary in their predictions of the diffuse and point-like neutrino fluxes from SBGs by more than order of magnitude [185]. Analyses performed on IceCube neutrino observations claim that SBGs cannot be the sole astrophysical neutrino contributor to IceCube's astrophysical neutrino flux measurement [186, 187]. However, IceCube has reported a 2.9σ excess of neutrino events coming from NGC 1068, one of the few SBGs that has been resolved by Fermi-LAT [188]. Yet, an additional analysis of the IceCube high energy starting events (HESE) sample, not by the IceCube collaboration, found that neutrino directions were consistent with no causal correlation, or at most, 10% of the observed neutrino events [189]. However, a different analysis of the same IceCube HESE sample suggests that under alternative starburst models, SBGs could explain up to 40% of IceCube's events at the hundreds of TeV energy scale [190]. The variation between these analyses, and corresponding models for SBG neutrino production, demonstrates the significant phenomenological uncertainty in modeling SBGs, and other astrophysical objects, as the sources of astrophysical neutrinos, given current model freedom and experimental uncertainties.

Chapter Summary

1. Ultrahigh energy cosmic rays (UHECRs) with energies $\gtrsim$ 1 EeV have been observed by multiple terrestrial observatories for more than three decades.

2. As charged particles, most cosmic rays are significantly deflected in galactic and extra-galactic magnetic fields during propagation and therefore do not point back to their origin. At the very highest energies, where the cosmic ray rigidity is largest, there is the possibility for correlation between sources on the sky and cosmic ray arrival directions but current measurements have been unable to make any definitive identification.

3. The astrophysical environments that accelerate and produce these particles, likely to be extra-galactic objects, are currently *unknown*.

4. A cutoff is observed in the UHECR spectrum at $\sim$100 EeV. It is unknown whether this corresponds to the maximum energy that *can* be accelerated by UHECR sources, or the suppression of the cosmic ray flux during *propagation* via the GZK effect (photo-pion production between UHECRs and the cosmic microwave background) to produce *cosmogenic* neutrinos.

5. UHECRs are thought to be accelerated by diffusive shock acceleration-like processes in extreme astrophysical environments. Some of the likely candidates for ultrahigh energy cosmic ray acceleration include blazars, starburst galaxies, hypernovae, and gamma ray bursts.

6. UHECR acceleration is often theorized to be accompanied by ultrahigh energy (UHE) *astrophysical* neutrino and photon production due to photohadronic interactions between accelerated cosmic rays and the synchrotron radiation from co-accelerated leptons.

7. UHE neutrinos, both cosmogenic and astrophysical, have the potential to point directly back to their production environments, as well as constrain the conditions of their acceleration environments via their flavor composition, and as such are potentially a powerful multi-messenger tool for identifying the unknown UHECR sources.

2 Detecting Ultrahigh Energy Cosmic Rays and Neutrinos

In this chapter, we present an introduction to the current methods used to detect ultrahigh energy cosmic rays and neutrinos with a particular focus on detection via secondary *radio emission*. In section 2.1, we introduce the concept of particle cascades at ultrahigh energies, in air and in dense media, section 2.2 presents methods of *directly* detecting UHE cascades, section 2.3 present optical methods, and section 2.4 discusses the detection of these cascades using passive radio techniques.

2.1 Ultrahigh Energy Particle Cascades

When ultrahigh energy particles enter a medium (even one as rareified as the Earth's atmosphere), they will eventually interact with the medium, creating additional high energy secondary particles that are mostly collimated in the direction of the primary's momentum; these secondary particles will typically interact again themselves, producing additional particles, that will themselves interact, and so on. This *cascade* of secondary particles continues until the particles are sufficiently low energy to be below the production threshold of new particles, or when their interaction cross-sections are too small to contribute to the development of the shower (i.e. neutrinos). In air, these cascades are referred to as *extensive air showers* as they can extend for many tens of kilometers in longitudinal length (due to the low density of the atmosphere) and may have footprints on the ground in excess of one kilometer in diameter [21]. In denser media, such as ice or the lunar regolith, these are typically referred to just as *showers* or *cascades* and can be several meters to several tens of meters in lengths with lateral sizes on the order of a few millimeters to centimeters, depending upon the density of the medium in which they are developing [191].

The initial interaction that starts the shower development depends upon the species of the primary particle and leads to particle cascades that are typically divided into two categories: *hadronic* and *electromagnetic* showers. In both shower types, the shower development is a highly complex process, for several reasons: (1) they are fundamentally stochastic and as such no two showers are identical: (2) a multitude of particle species can be involved, from electrons to charmed η mesons; (3) energy scales from keV to many EeV are relevant; (4) interactions via the strong, weak, and electromagnetic forces can all contribute; and (5) many of these processes depend upon the medium in which the shower is developing [192, 76].

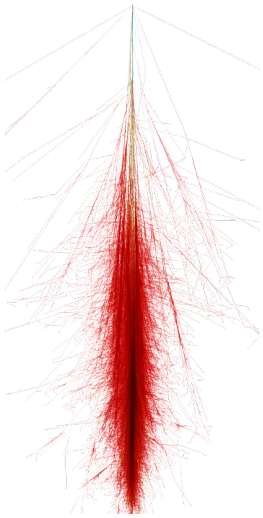

Figure 2.1: A simulation of a typical extensive air shower, initiated by a vertical proton in this case, calculated using the CORSIKA 8 shower simulation code. Depending upon the energy of such a shower, the total length can be up to a few tens of kilometers, with a total lateral footprint on the ground with a diameter of a $\mathcal{O}(1\,\mathrm{km})$. The majority of the shower is longitudinally aligned along the shower axis but particles do pick up transverse momentum due to multiple scattering as they propagate within the atmosphere. Figure from [66].

Due to the high energies involved in these showers, high energy cascades develop mainly *longitudinally* along the direction of the primary particle [192]. The (imaginary) straight line that continues the trajectory of the primary particle is called the *shower axis* and the distribution of particles over *longitudinal* distance (or grammage) *along* the shower axis is known as the *longitudinal* profile. Cascades also develop a *lateral* width as they develop (in the directions transverse to the shower axis) due to transverse multiple scattering, and (in some cases) geomagnetic deflection, but this is typically much smaller than the longitudinal extent for all high energy showers; this distribution of particles is known as the *lateral* profile.

2.1.1 Hadronic Cascades

High energy cosmic rays, such as protons or light nuclei, will typically *inelastically* scatter off a nucleus in the medium creating secondary particles in the interaction; such an interaction starts a *hadronic* shower, as they are initiated by *hadrons*. These are the most common primary shower type for cosmic ray astrophysics detectors, and have been the focus of decades of experimental study, yet, there are still significant theoretical uncertainties in our knowledge of the development of hadronic showers at ultrahigh energies [76].

For (lab-frame) energies above 10^{17} eV, the center-of-mass energy per nucleon, $\sqrt{s} \sim \sqrt{2m_p E}$, exceeds that of the Large Hadron Collider (LHC) at its current maximum energy of 14 TeV [193]. By 10^{19} eV, $\sqrt{s}$ exceeds ∼140 TeV, well above the maximum proposed center-of-mass energy, 100 TeV, of the Future Circular Collider (FCC-hh), which is not planned to turn on until the 2050s-2060s [194]. Therefore, many of the physics processes that determine the evolution of UHECR-induced showers, with energies reaching $\sim 6 \times 10^{20}$ eV, occur above the energies available in terrestrial accelerators and must be extrapolated from lower energy measurements [95, 60]. Therefore, hadrons and their interactions are among the most complex and least well understood aspects of ultrahigh energy particle cascades. This is made even more challenging as hadrons are typically not detected directly in particle cascades and are only observed *indirectly* via their production of muons and electromagnetic particles [195].

The current theoretical understanding of the strong interaction also makes it challenging to construct accurate predictions for the cross sections at ultrahigh energies with *ab initio* calculations. The standard framework for the theory of strong interactions at high energies, perturbative quantum chromodynamics (QCD) under the *parton* model [196], is only possible for interactions between single partons and where the coupling constant is small [197]. Since hadrons are always composite objects formed of many partons, modeling hadronic interactions in particle cascades requires phenomenological modeling to go from hadrons to individual partons, so that it is possible to calculate the strong scattering interaction of the individual partons with perturbative QCD; one must then *hadronize* the resulting parton distributions to determine the final state particles produced by the interaction [197].

These steps are complex and have significant phenomenological uncertainty. Therefore, there are several independent high-energy *hadronic interaction models* that each make different assumptions about the hadron-to-parton-to-hadron process and each give

different predictions for the cross sections and final state hadrons of different processes. Therefore, hadronic showers simulated using different interaction models often produce different predictions for shower features and behaviors. The three most used are SIBYLL [67], QGS-JET-II [68], and EPOS-LHC [69]. A figure showing the flux of muons at the ground, one feature where these models disagree significantly, calculated using these three different nuclear interaction models is shown in Figure 2.2 along with measurements by the Pierre Auger Observatory. As mentioned in section 1.1.2, air showers are observed to have significantly more muons than predicted by all *three* interaction models, and even then, the models disagree with each other.

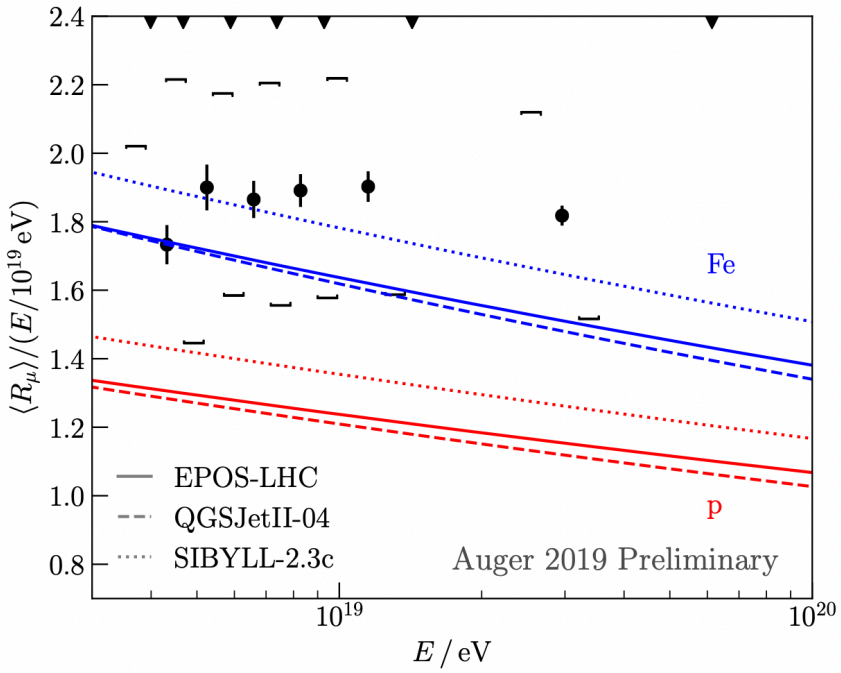

Figure 2.2: The average number of muons in extensive air showers as a function of primary energy as measured by the Pierre Auger Observatory. The error bars represent the statistical uncertainty and the square brackets indicate the systematic uncertainty. Predictions are shown for a pure proton (red) and pure iron (blue) flux from three different hadronic interaction models (linestyles). Figure from [77].

However, these high-energy hadronic interaction models, based on the parton model, are not suited to describing hadronic interactions at low energies, typically below $\sqrt{s} \lesssim 10\,\mathrm{GeV}$. While the first few generations of particles in an ultrahigh energy hadronic shower might predominantly be in the energy range accessible to these parton-based models, many later generations can be dominated by these low energy secondary particles.

Therefore, accurate modeling of high energy particle cascades also requires specialized low energy interaction models, not based off parton physics, that typically extend the hadronic interaction threshold down to ∼100 MeV. The most common of these low energy models are FLUKA [198], UrQMD [199], and HSA [64]. While there is significantly less phenomenological uncertainty compared to the high energy models, since there is extensive terrestrial collider data to help validate these models, there still exists minor differences in the predictions from each simulation code [200].

2.1.2 Electromagnetic Cascades

Alternatively, showers initiated by particles that primarily interact electromagnetically (i.e. electrons, positrons, and photons) initiate *electromagnetic* showers. At ultrahigh energies, the dominant processes in electromagnetic showers are pair production, where a photon converts to an $e^{\pm}$ pair, and the bremsstrahlung emission of a photon by a high energy $e^{\pm}$. Unlike hadronic interactions, these electromagnetic processes can be calculated under standard quantum electrodynamics (QED) with high precision and these calculations agree well with experimental measurements [201]. The cross sections for pair production and bremsstrahlung were first calculated by Bethe and Heitler in 1934 [202] and are still accurate across a wide range of energies.

The characteristic scale of electromagnetic processes is the *radiation length*, X_{rad}, which is dependent upon the medium, with a value of $X_{\text{rad}} \sim 37\,\text{g}\,\text{cm}^{-2}$ in air. Much of the behavior of shower development in different media can parameterized or discussed in a media-independent way by expressing the shower in units of radiation lengths, X_{rad}.

While bremsstrahlung and pair production can be well calculated for a wide range of energies, there is an additional process, the Landau-Pomeranchuk-Migdal (LPM) effect, that can alter the development of electromagnetic showers at the highest energies. At high energies, the formation zone of the interaction for bremsstrahlung and pair production can approach the inter-atomic spacing. When this occurs, the Bethe-Heitler model fails as successive interactions *interfere* with each other (a fundamental assumption of the Bethe-Heitler calculations for the cross section is that each successive interaction is independent [202]). When this occurs, the cross sections from bremsstrahlung and pair production are suppressed, compared to the standard Bethe-Heitler model. Since the inter-atomic spacing depends upon the density and composition of the medium, the LPM effect introduces a *density* dependence on the cross sections and therefore the de-

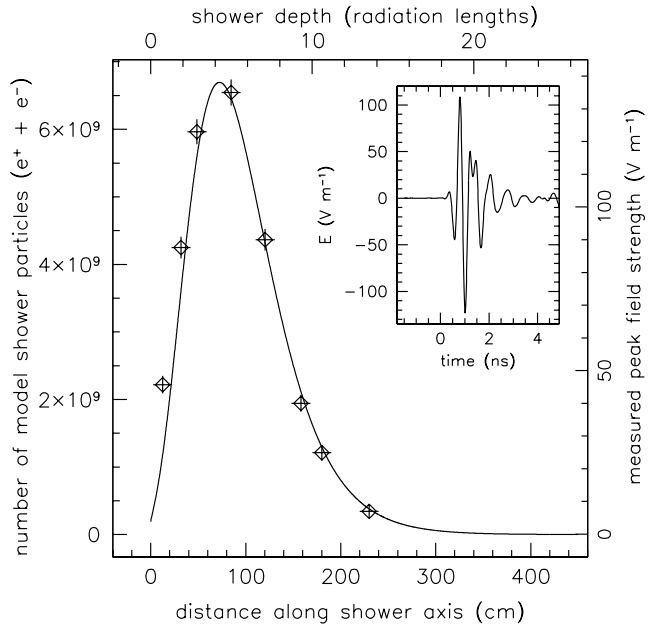

Figure 2.3: An example of the longitudinal profile of electrons and positrons in an electromagnetic shower in silica sand measured both in distance (bottom axis) and radiation lengths (top axis). The inset shows the radio pulse created by this charged particle profile and will be discussed in more detail in section 2.4.1. Figure from [203].

velopment of electromagnetic cascades. The energy at which the LPM effect becomes significant, E_{LPM}, is given by

$$E_{\mathrm{LPM}} \sim \left(\frac{4mc^2}{E}\right)^2 \left(\frac{mc}{2\hbar}\right) Lmc^2 \sim 60\,\frac{L}{1\,\mathrm{cm}}\,\mathrm{TeV}$$

As the cross section for both processes is suppressed, electromagnetic cascades above E_{LPM} are *elongated* compared to non-LPM cascades and show *long tails* in the longitudinal profile due to the suppressed cross sections [204, 205].

2.1.3 Realistic Particle Cascades

While cosmic rays are typically considered to initiate *hadronic* showers, hadronic showers can still have significant muonic and electromagnetic components, created *initially* by hadrons that decay into electromagnetic (i.e. π^0) or muonic (i.e. $\pi^{\pm}$) particles. A schematic diagram showing how an initial cosmic ray hadron initiates different "subshower" types is shown in Figure 2.4. After several generations of particle creation in an

extensive air shower, the electromagnetic component dominates the total particle profile and by the time the shower reaches the ground, most of the shower energy has been converted into either electromagnetic particles or muons, which can be used for the experimental detection of these showers. Since the hadron fluxes on the ground are typically small, understanding the development of muons and electromagnetic particles inside hadronic showers is crucial in order to understand and reconstruct information about the cosmic ray primary from measurements of these non-hadronic particles at the ground.

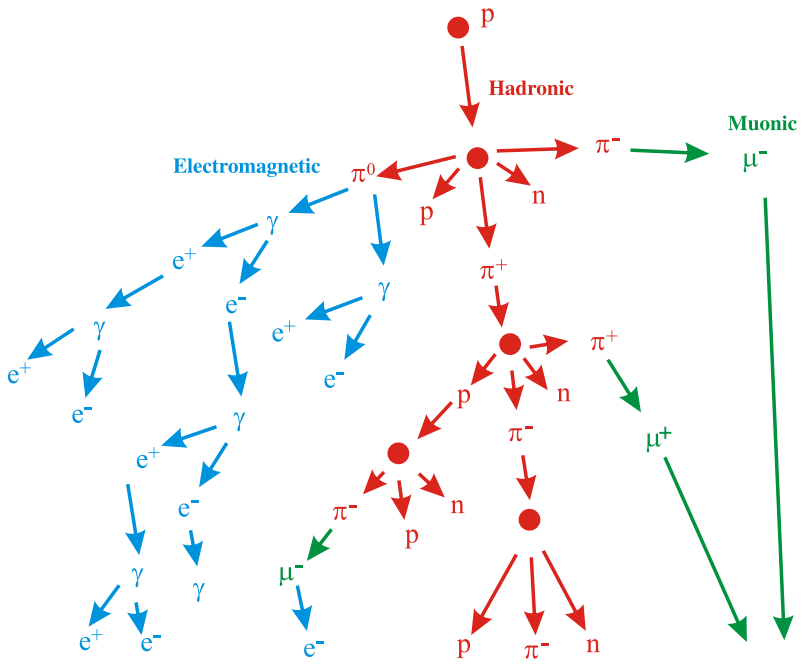

Figure 2.4: A diagram of the key processes involved in the evolution of particle cascades initiated by a cosmic ray proton: the three sub-components of a typical cascade, the *electromagnetic*, *hadronic*, *muonic* showers.

While the LPM effect is a purely electromagnetic effect, hadronic showers, with their large electromagnetic components, can have significantly different profiles at energies where the LPM effect is important. In addition, as the LPM effect occurs at high or ultrahigh energies depending upon the medium, it is often in the regime where many short-lived resonances that decay into electromagnetic particles, such as η or η' which have rest-frame life times of 10^{-21} s to 10^{-19} s, can travel significant distances before decaying; this can create multiple elongated electromagnetic *sub-showers* inside UHE hadronic showers [191]. An example of several hadronic showers with energies above E_{LPM} demon-

strating the multiple sub-showers created at different depths within the shower is shown in Figure 2.5a and Figure 2.5b.

2.1.4 Neutrino-induced Cascades

At ultrahigh energies, the dominant interaction process for neutrinos in dense matter, like ice or rock, is deep inelastic scattering (DIS) between neutrinos and nucleons (neutrino-nucleon DIS) [206]. This scattering process can be mediated by a W^+ or W^- boson in a so-called *charged current* (CC) interaction, or via the electrically neutral Z boson in a so-called *neutral* current (NC) interaction. These interactions take the form: $\nu + N \rightarrow l + X$ for charged current where l is a lepton and X are a collection of other particles (i.e. the rest of the nucleus) or $\nu + N \rightarrow \nu + X$ for neutral current interactions. A Feynman diagram showing both NC and CC neutrino-nucleon interactions is shown in Figure 2.6a.

Charged and neutral current interactions can both initiate hadronic particle cascades while only charged current interactions can initiate electromagnetic showers [208, 206, 209, 208, 210]. All current methods to detect ultrahigh energy neutrinos rely on the direct or indirect detection of these showers via secondary emission or secondary particles (such as the tracks left by through-going muons produced in high energy ν_μ charged-current interactions).

There are additional sub-dominant interactions of UHE energy neutrinos that are often ignored due to their small(er) cross section; in decreasing order of cross section magnitude, they are: (1) the Glashow resonance of electron neutrino and anti-neutrinos at 6.3 PeV [112]); (2) elastic and inelastic neutrino scattering off the photon field of individual nucleons; and (3) coherent neutrino scattering off the photon field of entire nuclei [207]. The Feynman diagram for one of these subdominant processes, the scattering of a neutrino of the photon field of the nucleus, is shown in Figure 2.6b.

2.2 Direct Detection of Particle Cascades

The primary method for detecting UHECRs is through "direct detection" of the secondary particles produced in the shower; this is the core technique used by the Pierre Auger, Telescope Array, and HAWC observatories (although they also employ other techniques that will be discussed in sections 2.3 and 2.4).

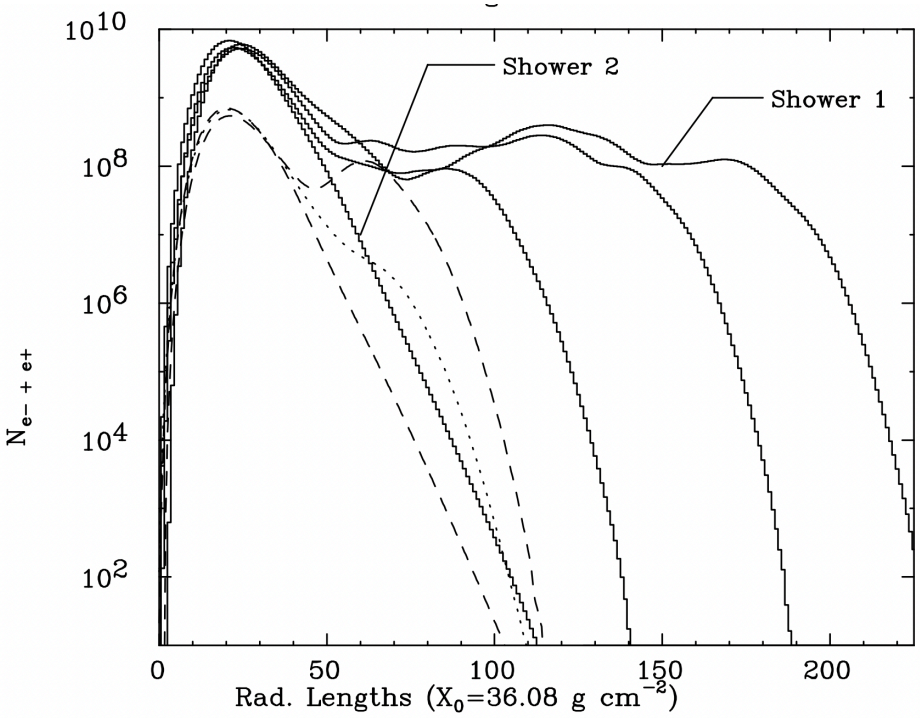

(a) A sampling of hadronic showers in ice showing the influence of the LPM effect. Above $E_{\mathrm{LPM}} = 2\,\mathrm{PeV}$ in ice, the LPM effect starts to create multiple elongated sub-showers at various depths within the shower; this effect, is however, stochastic as not all showers show the characteristic "humps" in the profile.

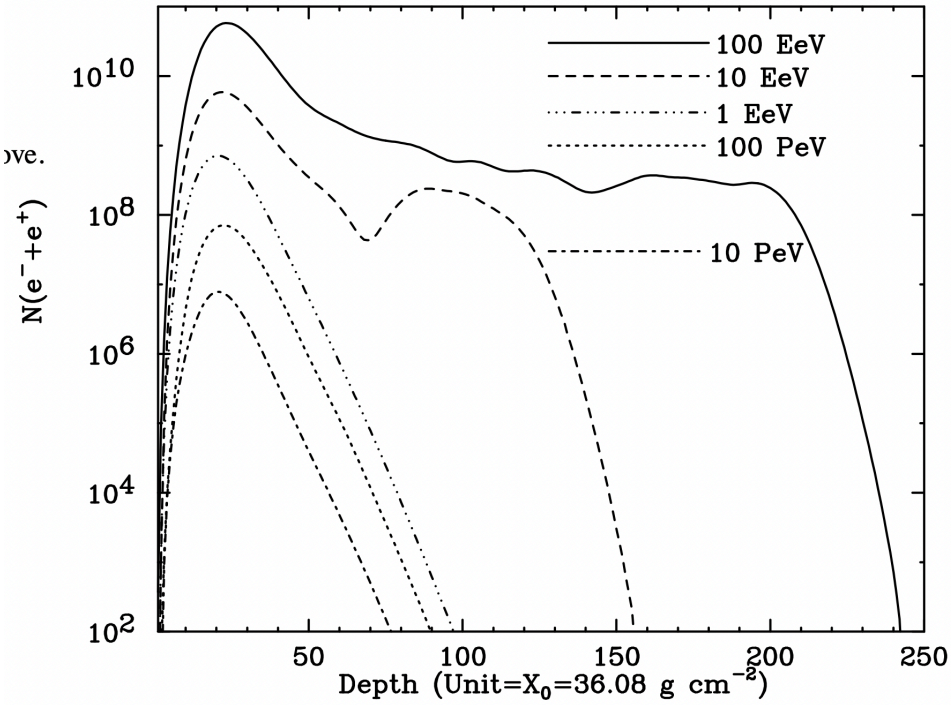

(b) A sampling of showers at a *fixed energy* above E_{LPM} showing that the formation of these elongated sub-showers is a stochastic process. Some of the showers have standard shower profiles that rise and fall uniformly, whereas other showers, initiated by the same primary in the same medium, show significant evidence of LPM-effected electromagnetic sub-showers. Figure from [191].

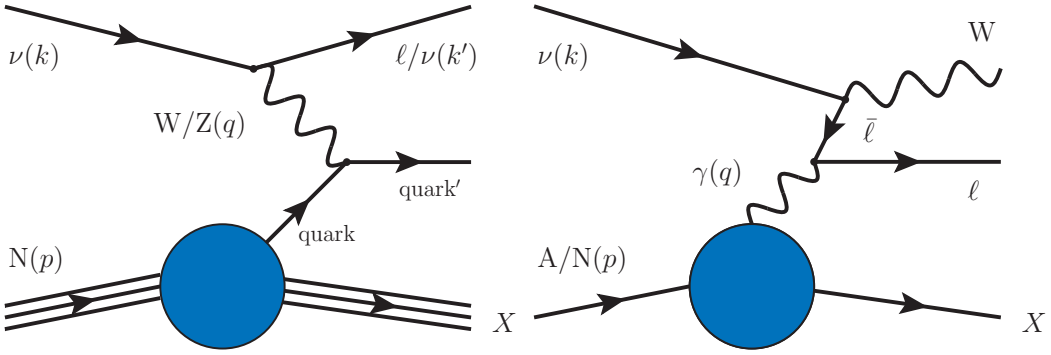

(a) A Feynman diagram for both charged and neutral current neutrino-nucleon deep-inelastic scattering. Figure from [207].

(b) A Feynman diagram for the coherent scattering of an ultrahigh energy neutrino off the photon field of a nucleus. Figure from [207].

Most of the hadrons produced in UHECRs do not make it to the surface, except at the highest energies close to the zenith, so the shower is primarily detected at the surface by the muonic and electromagnetic components. This is typically done using so-called "surface detectors" (SDs). At Auger, the surface detectors are large tanks, filled with pure water, and instrumented with several photomultiplier tubes (PMTs); Auger currently employs more than 1600 SDs covering more than 3000 km^2. When muons or other charged particles transit the tank, they emit optical Cherenkov light that can be detected using the PMTs. The absolute amplitude and timing delays of the PMT signals observed across the collection of SDs allows for estimating the energy and incident direction of the primary cosmic ray [211]. An annotated photo of one of the Auger surface detectors is shown in Figure 2.7.

The two primary disadvantages of surface detectors are as follows: a) the number of particles at the ground is a stochastic process and is affected by fundamental shower-to-shower fluctuations; and b) the area covered by the surface water tanks is only a small fraction of the total area of the shower footprint and as such suffers from sampling uncertainties. For example, a relatively low energy primary cosmic ray that interacts deep in the atmosphere can create a extensive air showers which has the same footprint on the ground as one produced by a more energetic primary that interacts higher in the atmosphere [211]. Therefore, the two largest ground-based cosmic ray observatories, Auger and Telescope Array, are *hybrid* observatories that supplement direct particle detection with other techniques to help compensate for the inherent uncertainties of this technique.

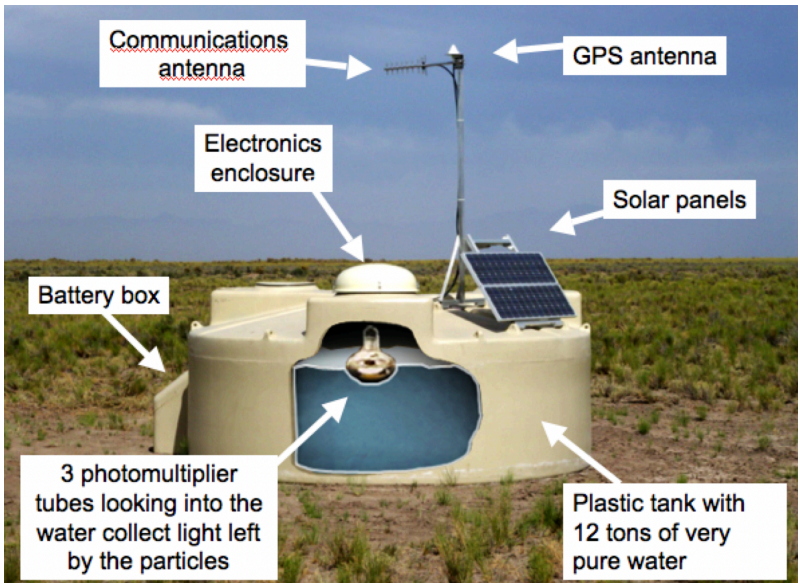

Figure 2.7: An annotated image of one of the water Cherenkov surface detectors (SDs) at the Pierre Auger Observatory. Figure from [211].

2.3 Optical Detection of Particle Cascades

In addition to the direct detection of the particles produced in cascades, it is possible to detect and reconstruct extensive air showers based on secondary optical fluorescence emission.

When extensive air showers develop in the atmosphere, they excite nitrogen molecules which emit fluorescence photons, with wavelengths typically between 280 nm and 450 nm as the molecules relax back to the ground state. This technique is not typically applied for showers in media other than air due to the reduced fluorescent photon yields in other media compared to molecular nitrogen in air [74]. These photons are emitted across a wide range of solid angle and can therefore be detected by optical fluorescence telescopes from *outside* of the shower footprint, including from orbital instruments [212].

An advantage of this technique is that the longitudinal profile of charged particles can be measured *directly* as it creates a similar longitudinal profile in the fluorescence photon distribution as the number of fluorescence photons emitted is proportional to the total electromagnetic energy lost by the particles in the shower. The brightness of this profile allows for an accurate measurement of the energy of the cosmic ray that initiated it, and as discussed in section 1.1.2, measurements of the longitudinal profile allows for a statistical measurement of the composition of the cosmic ray flux. A diagram illustrating

the observation of the fluorescence emission of a cosmic ray shower with a fluorescence telescope is shown in Figure 2.8.

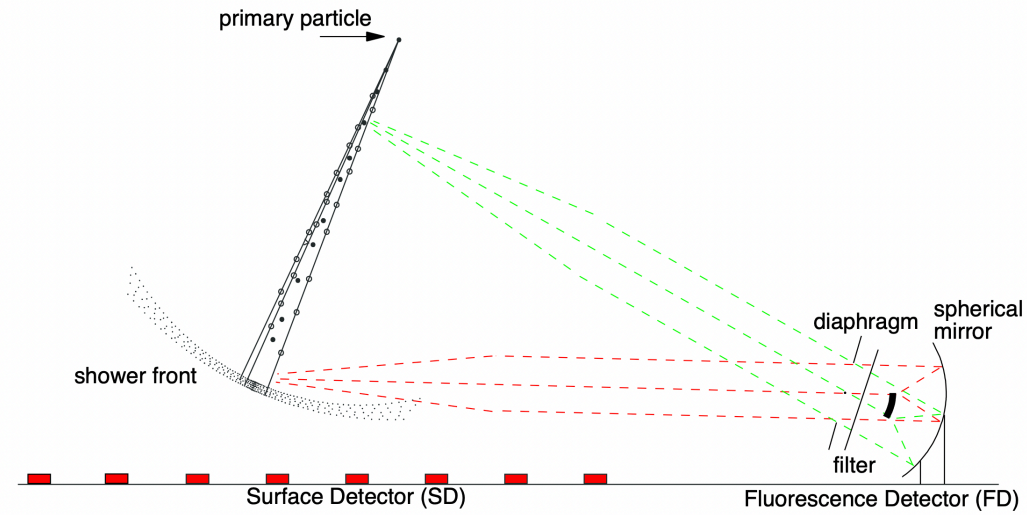

Figure 2.8: A schematic of the detection of the fluorescence emission from an extensive air shower as detected by the fluorescence detectors (FDs) of the Pierre Auger observatory. Figure from [74].

This technique was first pioneered in the 1960's with the Volcano Ranch Observatory in Utah [213] and achieved significant success with the Fly's Eye [214] and HiRes (High Resolution Fly's Eye) [215] observatories in the 1980's through to the early 2000's. The Fly's Eye observatory is of note for detecting the so-called "Oh My God Particle" which was an ultrahigh energy cosmic ray with an estimated energy of 3×10^{20} eV, which at the time was the highest energy cosmic ray ever observed and challenged existing models for the maximum energy of the cosmic ray flux [216]. The Pierre Auger Observatory also employs several fluorescence telescope stations (known as "Fluorescence Detectors", or FDs, in Auger parlance); this makes Auger a *hybrid* observatory as it uses both direct particle detection with water Cherenkov tanks and indirect detection with fluorescence [74, 20].

The disadvantage of the fluorescence technique is its low duty cycle. Due to the low fluorescent photon yields from cosmic ray induced air showers, these detectors require dark skies in order to observe the shower above atmospheric sky backgrounds. Therefore, the observatories cannot operate while the moon is visible in the sky or close to dusk or dawn. Therefore, the fluorescence telescopes at Auger only have a 10%-15% duty cy-

cle [74] which significantly limits their use compared to the surface detectors that have 100% duty cycle[211].

2.4 Radio Detection of Particle Cascades

Another important method for the *indirect* detection of high energy particle cascades, both in air and in dense media, is the *radio emission* produced by the shower as it develops within the medium. This radio emission propagates away from the shower over a range of solid angles and can therefore be used to detect showers from large distances using radio antennas that do not need to be *inside* the actual particle cascade, similar to the fluorescence technique. The two primary mechanisms for radio emissions from particle cascades are the *Askaryan* effect, and *geomagnetic* emission [217].

Radiation from particle cascades in air, *extensive air showers*, was first observed in 1964 [218] and subsequently by other experiments in the 1960s [219, 220], but the measured radiation was inconsistent with the phenomenology at the time (that predicted only Askaryan radiation). Subsequent to these measurements, new theoretical work first proposed the geomagnetic radiation process [221] in 1967 that is now known to account for $\sim$90% of the radio emission from extensive air showers.

Due to the ever-present thermal noise in the radio and microwave spectrum, detecting showers via their secondary radio emission requires shower energies and distances such that the emission is above the thermal and background noise floor; this *typically* limits the radio technique to particle cascades above $\mathcal{O}(1\,\text{PeV})$ depending upon the geometry of the experiment and the proximity of the detection to the neutrino-induced shower.

2.4.1 The Askaryan Effect

When high energy particle showers develop in dielectric media (such as air or ice), they develop a compact negative charge excess along the *front* of the shower that is typically $\mathcal{O}(\text{cm})$ thick. This negative charge excess, with a magnitude of roughly $\sim$20% of the *total* charge in the shower, forms as atomic electrons are preferentially upscattered into the shower (due to Compton, Bhaba, and Møller scattering) while positrons are annihilated against the same population of atomic electrons [222]. For an external observer, this negative charge excess is observed as a compact net negative bunch charge moving along the longitudinal axis of the shower at close to the speed of light.

For high energy showers, many of the particles in this charge excess are traveling faster than the phase velocity, (c/n), of light in the medium and therefore emit Vavilov-Cherenkov, or Cherenkov, radiation [223].

Vavilov-Cherenkov radiation is emitted whenever a charged particle travels faster than the phase speed, (c/n), of light in a given medium. As the *charged* particle travels through the medium, it polarizes molecules in the medium which emit photons along spherical wavefronts upon returning to the ground state. When the particle's velocity is greater than the phase velocity, the spherical wavefronts emitted along the particle's path become coherent at an angle of θ_c, with respect to the direction of the particle's motion, given by

$$\cos\theta_c = \frac{1}{n\beta}$$

As Cherenkov radiation is emitted uniformly in azimuthal angles and at only a fixed angle θ_c, it is observed to emit a "cone" of emission as the particle propagates through the medium [223, 224]. A diagram of the Cherenkov radio emission process is shown in Figure 2.9.

The energy spectrum of Cherenkov radiation by a particle traveling a distance dx emitted in a frequency range $d\omega$ is given by the Frank-Tamm formula:

$$\frac{d^2E}{dxd\omega} = \frac{q^2}{4\pi}\mu(\omega)\omega\left(1 - \frac{1}{\beta^2 n^2(\omega)}\right) \tag{2.1}$$

for a particle of charge q traveling at a speed β in a medium with magnetic permeability $\mu(\omega)$ and refractive index $n(\omega)$. This demonstrates the characteristic *linear* rise in power over frequency, ω, of Cherenkov radiation, for a medium with n and μ constant over frequency [224]. While Cherenkov radiation is most commonly used in the optical and near-ultraviolet, the spectrum does extend down to radio and microwave frequencies, although the dependence on frequency implies that there is significantly less emitted power than in the optical and ultraviolet for a *single* charged particle.

When the charge excess bunch that develops at the front of a high energy particle cascade is observed at wavelengths larger than the lateral scale of this charge excess (related to the Moliére radius of the medium), typically a few MHz to a few GHz depending upon the medium (i.e. radio to microwave frequencies), it is impossible to *resolve* the Cherenkov radiation of each individual charged particle and the *entire* charge excess bunch at the front of the shower is *observed* as a *single charged particle* with an effective

charge of 20%-25% of the total charge contained in the shower emitting Cherenkov radiation; this is *coherent Cherenkov radiation* or *Askaryan radiation*. The *individually* weak radio Cherenkov emission from each particle in the shower is adding *constructively* at the observer. The coherent radio or microwave Cherenkov emission from the negative charge excess in a particle cascade in dense media is known as the *Askaryan effect* and the radiation is known as *Askaryan radiation*.

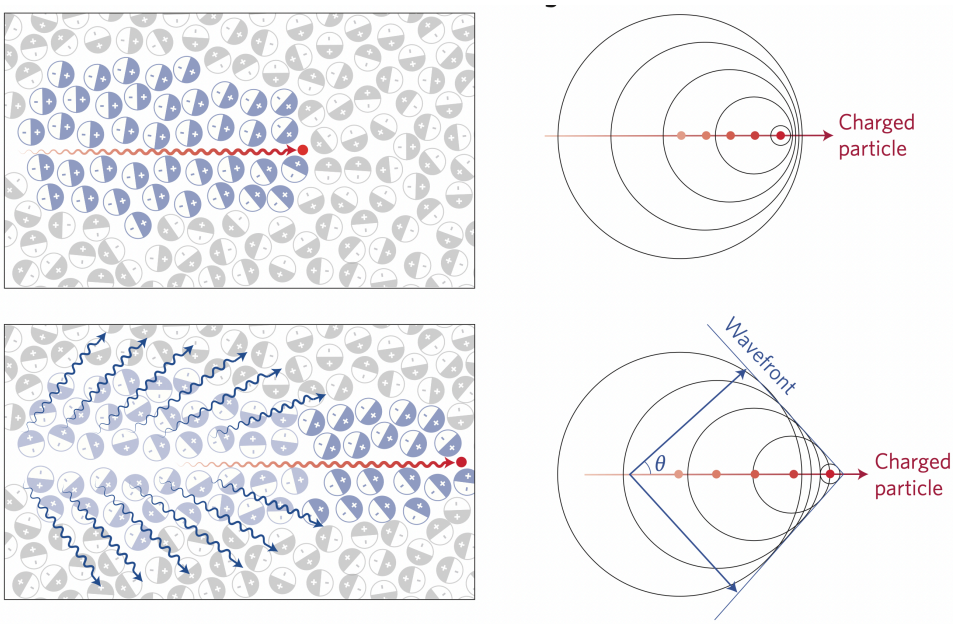

Figure 2.9: A schematic diagram of the emission of Cherenkov radiation from the polarization of molecules in the medium as a charged particle moves through. The top pane shows a particle that is traveling slower than the phase speed of the medium; the wavefronts from each medium particle do not combine coherently and no Cherenkov radiation is observed. The bottom pane shows the same charged particle moving faster than the phase speed of the medium. In this case, the wavefronts from each medium particle combine coherently as the superluminal particle overtakes each successive wavefront as they are emitted. This emission becomes coherent at the Cherenkov angle, θ_c. Figure from [225].

Via the Askaryan effect, high energy particle cascades in dielectric media emit 100% linearly polarized, wide-bandwidth, impulsive radio emission with a similar conical beam pattern as regular incoherent Cherenkov radiation. The emission from the Askaryan effect is radially polarized (due to the underlying Cherenkov emission) and the power spectrum rises linearly with frequency until the coherence condition is no longer satisfied; this depends upon the compactness of the charge excess, which depends on the medium, as

well as the location of the observer, but extends to $\gtrsim$1 GHz in ice for observers near the Cherenkov angle. Within the range of frequencies where the emission is coherent, the power emitted via the Askaryan effect scales quadratically with the total shower energy as can be seen in Equation 2.1 and Figure 2.10a.

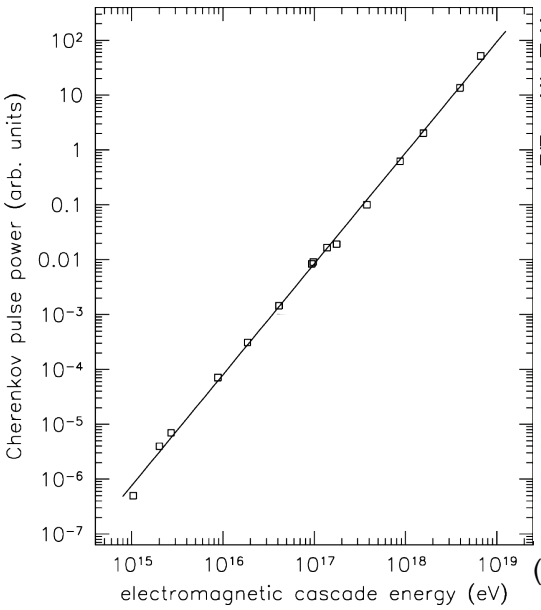

(a) A measurement of the Cherenkov pulse power vs. the total electromagnetic shower energy measured showing the characteristic q^2 dependence of radio power on charge expected from the Frank-Tamm formalism. Figure from [226].

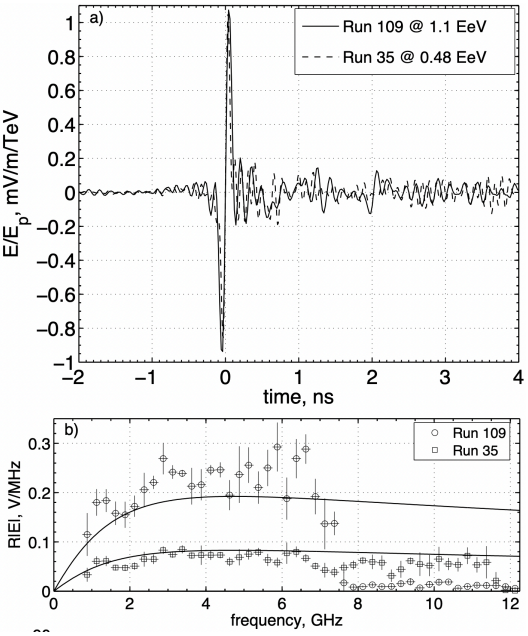

(b) A measurement of the pulse and spectral power of an Askaryan pulse measured in salt using wide-bandwidth antennas with the measured electric field coherence extending up to in excess of 6 GHz. Both figures were produced using data from the T460 experiment at SLAC. Figure from [227].

This effect was first predicted by Gurgen Askaryan in 1962 [222] and was experimentally confirmed in 2001 by Saltzberg & Gorham [203] in a silica sand target. It has since been measured in terrestrial accelerator experiments in a variety of other media including ice [228], salt [226], and alumina [229], and it has also been observed in extensive air shower experiments [230]. Several measurements of the Askaryan effect are shown in Figure 2.10a and Figure 2.10b taken at the SLAC National Accelerator Laboratory, including the dependence on shower energy, as well as a broadband waveform and spectra.

Akin to classical *optical* Cherenkov, Askaryan radiation is emitted on a cone with the opening angle of peak power given by the Cherenkov angle, θ_c. The wavelengths involved here can be 10^6 to 10^7 times longer than used in the optical and can be a significant frac-

tion of the longitudinal and lateral width of the charge excess. Therefore, the angular spectrum, which is highly peaked at θ_c in the optical, is significantly broader in the radio with extended emission away from the Cherenkov angle.

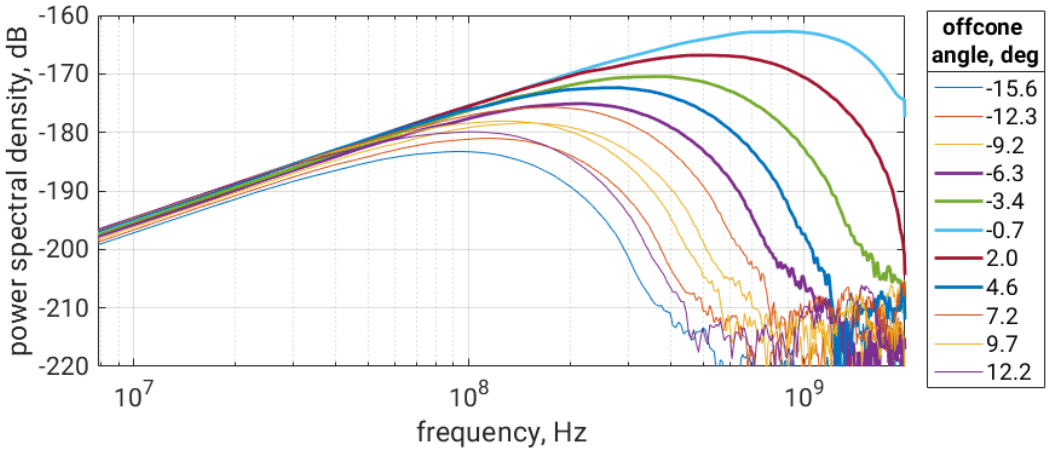

Figure 2.11: A simulation of the power emitted via Askaryan radiation as a function of off-axis angle for various upper frequency limits calculated with the ZHAireS code [231]. *Right:* The spectra of Askaryan radiation for a shower in lunar regolith at various off-cone angles. The most "on-cone" simulation, only 0.7° away from the Cherenkov axis, has the highest coherence frequency (where the spectra starts to roll over and decrease with frequency). Figure by Peter Gorham with data produced by Remy Prechelt.

This effect is frequency dependent as it forms due to the projected charge excess size at the observer and the wavelength of observation. For high frequencies (i.e. approaching the maximum coherence frequency), the majority of the emitted power is focused in a "finite-width beam" around the Cherenkov angle with a width of typically a few degrees (i.e. a cone with "angular width"). However, at lower frequencies, where the wavelengths can become several orders of magnitude larger than the projected size of the charge excess, the emission broadens until the angular spectrum extends over a significant fraction of polar angle [191]. As the viewing angle, θ, moves away from θ_c and becomes more "off-cone", the radiation becomes less coherent at high frequencies, as the projected thickness of the shower front becomes larger, and so the overall emitted power per solid angle decreases and the spectrum's upper frequency limit moves down [232]. This is demonstrated in Figure 2.11 for an UHE cosmic-ray-induced shower in the lunar regolith.

The Askaryan effect has, is, and will be used by a number of ultrahigh energy neutrino experiments to explore the neutrino flux above $\mathcal{O}(1\,\mathrm{EeV})$. In order to maximize the ra-

dio signal arriving at the detector, these experiments require target volumes for neutrino-nucleon interactions that also possess low dielectric loss tangents so that the radio emission suffers less attenuation as it propagates from the neutrino-induced shower to the radio antennas. However, the extremely low fluxes of UHE neutrinos, $\lesssim 1\,\mathrm{km}^2\,\mathrm{yr}^{-1}$, (Figure 1.8) also requires a large volume of the medium to be available. The (current) candidate is the large volumes of extremely pure ice in Antarctica or in the Greenland ice sheet. Both of these large volumes of ice are extremely radio transparent with attenuation lengths of $\mathcal{O}(1\,\mathrm{km})$.

The principle of all of these detectors is the same: an ultrahigh energy neutrino-nucleon interaction in the ice (potentially up to $\sim$3 km below the surface) creates a hadronic or electromagnetic shower that generates an impulsive radio signal via the Askaryan effect. The radio emission is then detected with an array of radio antennas at distances ranging from $\mathcal{O}(1\,\mathrm{km})$ to $\mathcal{O}(600\,\mathrm{km})$. The relative time delays across the collection of antennas, along with the observed power spectra, can be used to reconstruct the direction and energy of the incident neutrino [233, 89, 159]. These detectors can be broadly split into two categories: *in-ice* and sub-orbital/orbital experiments.

In-ice neutrino observatories use arrays of radio antennas *buried* deep in the Antarctic ice in boreholes up to 200 m below the surface. This depth is chosen to avoid the $\lesssim \mathcal{O}(100\,\mathrm{m})$ of *firn*, snow deposited on the surface that is still being compacted, where the index of refraction is strongly depth dependent and is therefore a potential source of reconstruction error. This technique was first deployed on a large scale by the Radio Ice Cherenkov Experiment (RICE) [159], and later by the current Askaryan Radio Array (ARA) [234] and Antarctic Ross Ice-Shelf Antenna Neutrino Array (ARIANNA) [235] observatories, and is one of the major detectors for the *proposed* IceCube-Gen2 observatory [236]. ARIANNA is unique in this group in that it uses antennas located *at the surface* instead of buried deep in the ice. Alternative bodies of ice, such as the Greenland ice sheet, are also current targets for radio detection of Askaryan radiation with the experiments like the Radio Neutrino Observatory in Greenland (RNO-G) [237]. A diagram showing the design and detection geometry of in-ice radio arrays is shown in Figure 2.12a and Figure 2.12b.

Alternatively, the radio emission generated by the neutrino-induced cascade can be detected from *outside* the ice (i.e. in the *air*). This technique was pioneered by the ANtarctic Impulsive Transient Antenna (ANITA), the subject of this dissertation, which was designed to detect the Askaryan emission from orbit on a long-duration balloon (LDB)

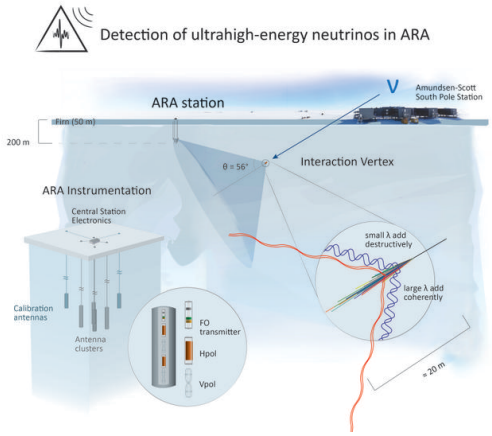

(a) A diagram showing the detection methodology of the Askaryan Radio Array (ARA) experiment located at the South Pole. Ultrahigh energy neutrinos undergo neutrino-nucleon interactions in the ice and generate Askaryan emission that is detected by an array of radio antennas. These signals are then used to reconstruct the direction and energy of the incident neutrino. Figure from [234].

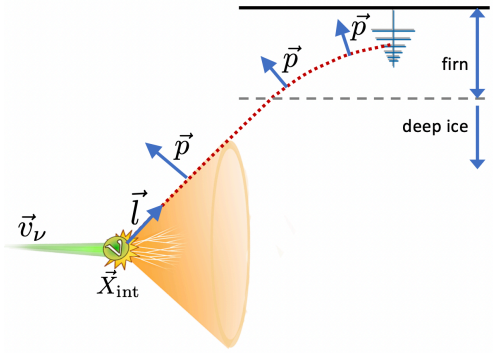

(b) A diagram of how an buried or near-surface radio antenna observes the coherent radio emission, including ray curvature effects from the depth-dependent refractive index of the ice. Figure from [238].

at an altitude of ∼37 km [89] (and therefore a payload-neutrino distance that can be in the hundreds of kilometers). The neutrino interaction is still in the located within the ice; the radio emission propagates from the interaction to the surface, refracts out, and then propagates through the air to the payload. The increased distance between the interaction vertex and the detector in sub-orbital (or orbital) detectors enforces a higher neutrino energy threshold, typically $\mathcal{O}(1\,\text{EeV})$ for current sub-orbital detectors.

The limited duration of long duration balloon flights, typically ∼1 month for the standard zero pressure balloon (ZPB) currently used for most of these experiments, is compensated by the extremely large volume of ice they are sensitive to due to their unique observing location at high altitudes [89, 239]. This allows these experiments to set the most stringent UHE neutrino limits above ∼10 EeV in only ∼30 days of exposure, even when compared against ground-based observatories with nearly a decade of livetime [240]. The forthcoming super pressure balloon (SPB) technology, currently undergoing testing for NASA's LDB program, could increase the flight duration to $\gtrsim$ 100 days, significantly increasing the exposure that can be collected by these sub-orbital balloon instruments in a single flight [239, 241].

2.4.2 Geomagnetic Emission

High energy particle cascades produce large numbers of electrons and positrons, as well as other less numerous charged particles. In the presence of a magnetic field, all of the charged particles in the shower undergo acceleration via the Lorentz force and emit radio synchrotron radiation as they accelerate in the direction transverse to the shower axis. Extensive air showers, which develop in the Earth's geomagnetic field, are therefore said to emit *geomagnetic* or *geosynchrotron* radio emission as they develop [221]. Due to their low mass and high number density in extensive air showers, the electrons and positrons are the dominant contributor to the observed geomagnetic radiation (although other charged particle species in the shower still do emit and contribute synchrotron power).

Under the Lorentz force, the charged particles in the shower begin to *split* and propagate laterally away from the shower axis in opposite directions based upon the sign of their charge. Due to the high energies involved, this divergence is typically small and the shower still remains mostly directed longitudinally along the shower axis (Figure 2.1a). This splitting of the positive and negative charge in the shower acts to create a net "transverse current", along the $\hat{v} \times \hat{B}$ direction, that is moving longitudinally along the shower axis at close to c, growing in magnitude along with the total number of particles (i.e. the longitudinal profile). Due to the different fundamental mechanism of emission from the charged particles in the shower, geomagnetic radiation has a different spectrum and polarization than Askaryan radiation [242].

Geomagnetic radiation is *nominally* polarized along the $\hat{v} \times \hat{B}$ direction, where $\hat{v}$ is the (vector) direction of the shower axis and $\hat{B}$ is the direction of the local geomagnetic field vector, since *most* particles are closely aligned with the shower axis for realistic values of the geomagnetic field. However, the true observed electric field polarization is the convolution of the true distribution of particle velocities, $\vec{v}$, and the magnetic field, $\vec{B}$.

To accurately calculate the electric field magnitude and polarization at a given observer position, detailed shower simulation codes must be used that calculate the (vector) electric field contribution from each individual particle in the shower (which have been slightly deflected away from the shower axis due to both multiple scattering and the transverse acceleration provided by the Lorentz force) and sum them, with correct propagation delays, at the observer [65, 66, 64]. Since calculating the radio emission requires a knowledge of the direction, charge, and energy of all the particles in the shower, the most accurate radio simulations are integrated with air shower or cascade simulation

codes. The AIRES [64] shower toolkit has a radio extension known as ZHAireS (using the ZHS algorithm [231]), CORSIKA 7 [65] has a similar extension known as CoREAS (using the "endpoint" formalism [243]), and CORSIKA 8 has new implementations of both the ZHS and "endpoint" formalisms [66].

Furthermore, for extremely long showers, like high zenith angle showers that develop near horizontally over long distances, or Earth-skimming "stratospheric" cosmic rays whose shower axis would otherwise never intersect the ground, the exact electric field at the observer must also use accurate models for the full geomagnetic field, as the true observed field depends on $\hat{v} \times \hat{B}(\vec{r})$, where $\hat{B}(\vec{r})$ is the *varying* magnetic field vector that the shower observes over its long propagation distance [244].

While geomagnetic radiation is fundamentally different than the Askaryan effect, built from coherent Cherenkov radiation which naturally preserves the conical emission pattern characteristic of Cherenkov radiation, geomagnetic radiation from an extensive air shower does also possess a "conical" emission pattern with the same opening angle, θ_c, as expected from Askaryan and Cherenkov radiation [242].

The origin of this effect can be shown using the simple model of geomagnetic radiation as a transverse current moving at the speed of light along the longitudinal axis of the shower. For an observer *inside* the Cherenkov angle, the emission from the particles at the *end* of the shower, typically moving (at c) faster than the radio emission from the start of the shower traveling at (c/n), is observed *earlier* than the emission from the start of the shower. Conversely, for an observer *outside* the Cherenkov angle, the emission from the particles at the start of the shower is observed *before* the emission from the latter end of the shower. However, *at* the Cherenkov angle, the time delay between the start and end of the shower are equal and the *entire shower* is observed *coherently*, significantly boosting the observed power. This coherence creates Cherenkov-like ring in the observed footprint of geomagnetic radiation with an opening angle of θ_c [245, 242].

Similarly to Askaryan radiation, as we consider lower frequencies, the different time delays from the start and end of the shower become significantly less than a wavelength, and so the emission no longer shows the characteristic cone like behavior [242]. The off-axis angular and frequency spectra for simulations of the geomagnetic radiation from an UHECR-induced air shower is shown in Figure 2.13.

The spectrum of geomagnetic radiation rises with frequency until a characteristic turnover frequency, $\mathcal{O}(100\,\text{MHz to } 200\,\text{MHz})$ in air, above which it has an *exponentially* falling power spectrum (Figure 2.13). For air, this implies that geomagnetic radiation has a sig-

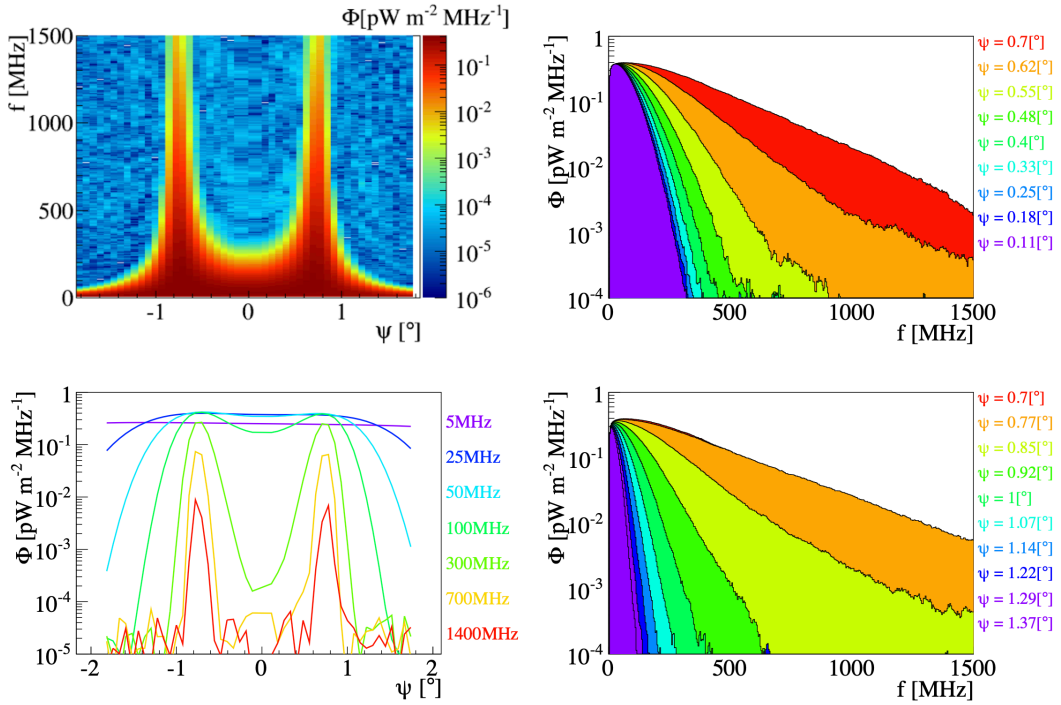

Figure 2.13: The distribution of the geomagnetic radio emission for an $10^{18.4}$ eV proton shower with a zenith angle of $\theta = 71°$ as a function of off-axis angle, ψ, and frequency, f. The top and bottom right panels shows the spectra *inside* and *outside* the Cherenkov angle, $\theta_c = 0.7°$ for this simulation. Figure from [231].

nificantly lower-frequency weighted spectrum compared to Askaryan radiation that rises linearly with frequency the same frequency band. The different polarizations and spectra of Askaryan and geomagnetic radiation allows for separating the relative contributions of geomagnetic and Askaryan emission in air showers observed in the radio with ground arrays such as LOFAR [230].

For extensive *air* showers, that develop in a low density medium like air (i.e. compared to an in-ice shower), the *geomagnetic* emission is typically an order of magnitude stronger than the Askaryan [242, 230]. However, in dense media like ice, the charge bunch is significantly more compact and the showers are significantly shorter, so the transverse current induced by the Lorentz force is of overall smaller magnitude, reducing the total power emitted via the geomagnetic process. Therefore, for showers in dense media, like ice, the Askaryan effect is the dominant radio emission process [208, 242].

The radio emission from cosmic-ray induced extensive air showers is used as a standalone detector for high energy cosmic rays (HECRs), with experiments like LOFAR [230, 246, 247] as well as only one detection technique in larger *hybrid* observatories such as Auger (with the Auger Engineering Radio Array, or AERA) [248]. Much like in-ice neutrino detectors that utilize the Askaryan effect, these detectors are comprised of large arrays of radio antennas. However, due to the difference in spectrum, cosmic ray-focused radio arrays looking for extensive air showers typically focus on lower frequency ranges, typically in the 30 MHz to 300 MHz range. Also, similar to in-ice Askaryan detectors, measurements of the power, spectrum, and polarization at each antenna in the array can be used to estimate the incoming direction and energy of the primary cosmic ray. Naively, the technique does not allow for estimating the depth of X_{max}, and therefore estimating the nuclear species of the primary cosmic ray, but advances in interferometry and detector array design has recently made this possible for appropriately designed arrays [249].

Therefore, detecting ultrahigh energy particle cascades *on Earth*, whether they be initiated by cosmic rays or neutrinos, via radio emission depends upon the medium in which the particle cascade is created; in dense media, the observed signal is typically dominated by Askaryan emission, while in rare media, like air, the signal is typically dominated by geomagnetic radiation.

2.5 The Tau Detection Channel

An alternative detection channel that has been of significant experimental interest in the last two decades is the so-called "tau air shower channel". This is in some sense a hybrid method between neutrino and cosmic ray detection methodologies and is depicted in Figure 2.14.

An Earth-skimming UHE tau neutrino has the possibility of undergoing a charged current deep-inelastic scatter interaction *inside the Earth* (most likely in rock, water, or ice) to produce a τ-lepton. If the τ-lepton is produced relatively close to the surface (the τ decay length is 47 km at 1 EeV and increasing linearly with energy so, relatively "close" here typically means hundreds of kilometers), the tau may leave the Earth and then *decay* in the *air*. This decay, which can be either hadronic or leptonic, will initiate an *extensive air shower* similar to those produced by ultrahigh energy cosmic rays [240]. However, unlike the *downgoing* geometries of UHECR-induced EAS, these *Earth-skimming* τ-leptons produce EASs that are near horizontal or upgoing with respect to the surface of the Earth. For detectors that are at high-altitudes, such that the horizon is noticeably below the horizontal, these showers are observed to be *upgoing* and can therefore occur in a range of solid angle

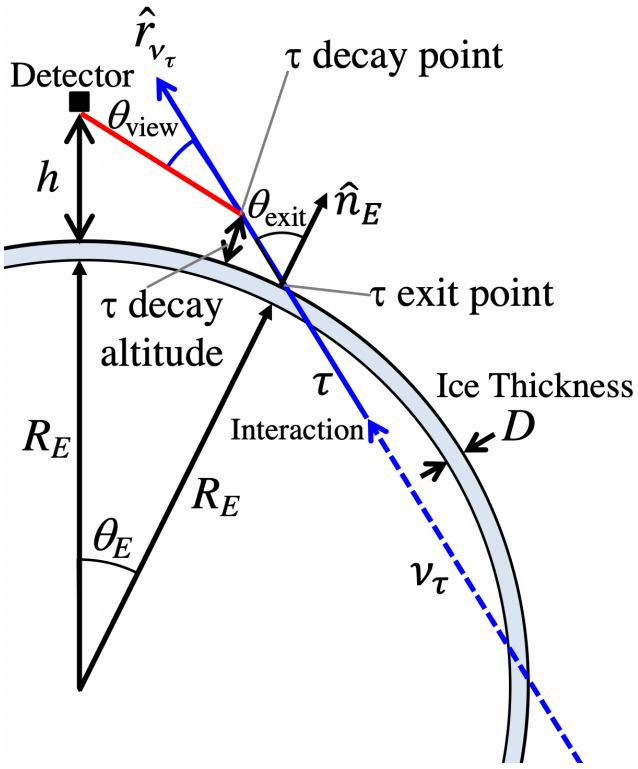

Figure 2.14: A diagram of the detection of an atmospheric τ-lepton decay produced via an Earth-skimming ν_τ that undergoes a charged-current neutrino-nucleon interaction within the Earth. Figure from [250].

where we do not expect any UHECR background (i.e. below the horizon for suborbital detectors like ANITA or high-altitude detectors like BEACON [251]).

These showers behave similarly to those produced by UHECRs although their evolution can be altered as they experience a different density profile along the shower axis as they showers develop *upwards* into a more-rareified atmosphere (whereas a downgoing UHECR is developing *downwards* into a denser atmosphere) [252]. The same techniques that are used to detect downgoing UHECR-initiated showers can also be used to detect upgoing tau-induced showers including direct, optical, and radio detection [93, 240]. In the case of ground-based observatories, direct particle detection with "surface detectors" typically require near horizontal showers, with zenith angles $\theta \sim 90^\circ$ such that the outer halo of scattered particles skims, almost horizontally, through the surface detectors; this is the primary technique that Auger uses to search for Earth-skimming τ extensive air showers [93].

While experiments like Auger that focus on the detection of downgoing UHECRs can *also* detect upgoing tau showers, there are a host of other experiments that are dedicated, and optimized for, detecting upgoing or Earth-skimming τ-induced showers [251, 252, 253, 254]. To optimize for this channel, the observatories are typically suborbital or orbital instruments, or ground detectors located at high elevations [251, 253], or on the side of large valleys [254], such that the observed direction for Earth-skimming τ showers is *below* the apparent horizon, looking through some amount of rock or ice, significantly reducing cosmic ray backgrounds. The detection techniques used by these "high-altitude tau neutrino observatories" span the full range of particle detection techniques: direct particle detection [254], optical Cherenkov [253], fluorescence [252], and radio [251].

2.5.1 Tau Regeneration

This channel is enhanced by a process known as *tau regeneration*. Consider an UHE tau neutrino incident upon the Earth as in Figure 2.14. Eventually, this ν_τ will undergo a neutrino-nucleon deep inelastic scatter interaction (section 2.1.4), ignoring subdominant neutrino-photon interactions, with two possible outcomes: a) if it was a neutral current interaction, a shower will be created, and a lower energy tau neutrino will leave the interaction vertex and continue propagating along the direction of the original ν_τ (at these energies, the deflection during a DIS interaction is negligible); b) if it was

a charged current interaction, a shower will also be created, and an UHE τ-lepton will *always* be produced (or a τ^+ in the case of a $\bar{\nu}_\tau$) [207].

τ-leptons have extremely short lifetimes, $\mathcal{O}(0.3\,\text{ps})$ in the rest frame of the τ, and can therefore decay before losing a significant fraction of their energy in τ-medium energy loss processes including bremsstrahlung, ionization, and photo-hadronic interactions [250]. When a τ-lepton decays, whether it be a hadronic (with 65% probability) or leptonic (with 35% probability) decay, it will *always* produce a new tau neutrino. Therefore, an incident flux of UHE tau neutrinos can be *regenerated* as it propagates through the Earth: as $\nu_\tau \rightarrow \tau$ in a charged current DIS; $\nu_\tau \rightarrow \nu_\tau$ in a neutral current DIS; and $\tau \rightarrow \nu_\tau$ during a τ decay. This allows for *tau regeneration* chains, such as $\nu_\tau \rightarrow \tau \rightarrow \nu_\tau$ or $\nu_\tau \rightarrow \nu_\tau \rightarrow \tau \rightarrow \nu_\tau$, with only moderate reduction in the original ν_τ energy at each stage [250].

This is in contrast to muon neutrinos, ν_μ, and electron neutrinos, ν_e. When electron neutrinos interact via a charged current interaction to produce an UHE electron, that electron will almost immediately initiate a shower and rapidly lose energy via bremsstrahlung (and, of course, the electron cannot decay under the Standard Model). While a ν_μ will produce a muon in a charged current deep inelastic scatter just as in the ν_τ case, the muon has: a) significantly larger energy loss per unit grammage than a τ; and b), the lifetime of the muon, 2.2 μs, is seven orders of magnitude larger than that of the τ, implying that the typical muon will lose a significant fraction of its energy before decaying back into a muon neutrino (especially as it will typically be propagating in dense media like *rock* where energy losses are high). Therefore, an UHE ν_μ neutrino flux is quickly downconverted to significantly lower energies, below the threshold of ultrahigh energy neutrino detectors, and at energy ranges that can have significant atmospheric neutrino backgrounds [252, 155].

The tau channel, like the regular UHE Askaryan channel, has never before been definitively observed at ultrahigh energies. However, the IceCube Observatory has reported on the apparent detection of two $\mathcal{O}(\text{PeV})$ tau neutrinos, colloquially known as "Double Double" and "Big Bird" with an IceCube "tauness" measure of $\sim$97% and $\sim$76%, respectively, which are incompatible with a non-tau flux at 2.8σ [255]. These events were not Earth-skimming, and were detected *in ice*, not in air, where there are significant backgrounds and as such does not represent as pure a detection channel as the in-air tau channel discussed above.

Chapter Summary

1. When high energy particles impact a medium, they initiate a particle cascade or shower either via a nuclear scattering, in the case of most cosmic rays hadrons, or via bremsstrahlung or pair production in the case of electromagnetic particles.

2. The shower continues to grow, producing new particles in each generation, until the energy loss to the medium starts to exceed the production rate of new particles, and the shower begins to diminish in number.

3. These showers are typically divided into hadronic, electromagnetic, and muon components which are dominated by different particles and processes. UHECR showers are at energy scales unavailable to terrestrial colliders and must therefore be extrapolated, introducing significant theoretical uncertainties.

4. There are many methods of detecting these particles including the direct detection of particles produced in the shower, the detection of fluorescent light produced by the excitation of molecular nitrogen, and the detection of secondary radio emission.

5. The secondary radio emission is produced via either: a) the Askaryan effect, the coherent radio Cherenkov from the compact negative charge excess on the front of the shower; or b) geomagnetic radiation, whereby particles in the shower are accelerated under the Lorentz force in the Earth's geomagnetic field and produce radio synchrotron radiation.

6. Earth-skimming ν_τ can produce τ-leptons that can later decay in the *air*, producing an extensive air shower that can be detected. This process is enhanced by *tau regeneration*: since a ν_τ is always produced in a τ-lepton decay, regeneration chains can be built where a ν_τ flux is regenerated via $\nu_\tau \to \tau \to \nu_\tau$ and $\nu_\tau \to \nu_\tau \to \tau \to \nu_\tau$ chains.

3 Antarctic Impulsive Transient Antenna (ANITA)

This chapter presents an introduction to the Antarctic Impulsive Transient ANtenna (ANITA) instrument, an ultrahigh energy sub-orbital neutrino observatory. This chapter is split into three parts: section 3.1 presents an overview of ANITA's detection methodology; section 3.2 presents a detailed walkthrough of the hardware of the fourth flight of the ANITA instrument, ANITA-IV, including a description of the signal chain, trigger logic, attitude determination, and a review of the flight; and section 3.3 presents a review of the major scientific results of the four successful flights of the ANITA instrument (from 2006 to 2016) with a particular focus on the anomalous and near-horizon events that will be the focus of the rest of this dissertation.

3.1 Detection Methodology

ANITA was originally conceived as a sub-orbital long-duration balloon payload that aimed to detect the Askaryan radiation from neutrino interactions in the Antarctica ice (see section 2.4.1). However, after the analysis of the first flight, and again after subsequent flights, additional detection channels were identified, some of which are (currently) unique to the ANITA instrument [256, 257, 258]. A diagram of the four primary detection channels of the ANITA instrument, each of which will be discussed in the following subsections, is shown in Figure 3.1.

3.1.1 In-Ice Askaryan Neutrino Detection

The original detection channel for ANITA was the in-ice Askaryan channel described in section 2.4.1. In this model, an ultrahigh-energy neutrino undergoes a neutrino-nucleon deep inelastic scatter in the ice, initiating an ultrahigh energy cascade. The Askaryan

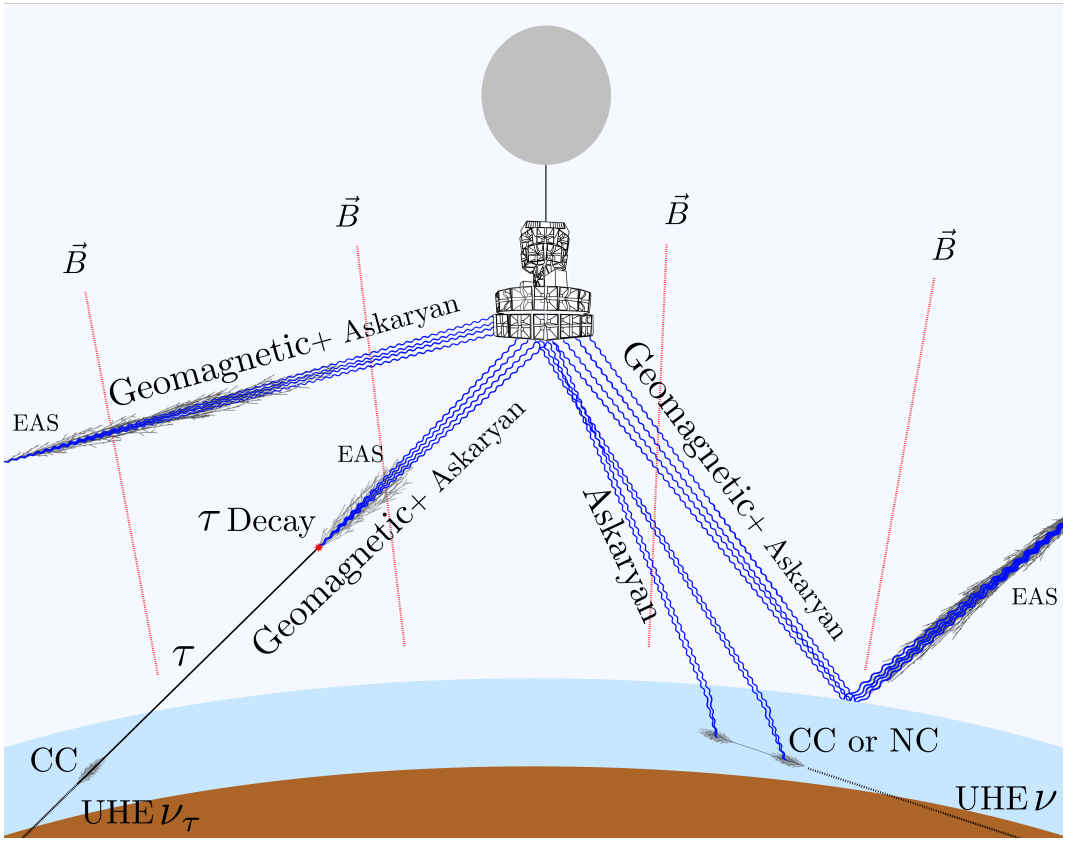

Figure 3.1: A diagram showing the four primary detection channels of the ANITA instrument: (1) the original in-ice Askaryan channel; (2) the detection of *stratospheric* cosmic rays that do not intersect the surface; (3) the detection of cosmic rays from the geomagnetic radio emission after it *reflects* off the ice surface; and (4) the detection of Earth-skimming tau neutrinos from the in-air decays of tau leptons.

emission generated by this cascade propagates up to the surface, refracts out, and propagates up the payload. Due to the expected geometry of in-ice neutrino events, as well as the Fresnel coefficient of the ice-air boundary, we expect most Askaryan neutrino events to be predominantly *vertically-polarized* (although the exact polarization angle can be tens of degrees away from pure vertical depending upon the event). Due to the large neutrino-payload distance, ANITA's Askaryan neutrino sensitivity begins to turn on above $\mathcal{O}(1\,\mathrm{EeV})$. This is ANITA's primary detection channel and is its most sensitive for the detection of UHE neutrinos.

3.1.2 Reflected UHECR Detection

ANITA is also sensitive to the geomagnetic radio emission from *downgoing* (normal) UHECRs; in ANITA's case, the radio emission from the cosmic ray *reflects off* the Antarctic ice surface, before propagating back *up* to the payload. From ANITA's perspective at $\sim$37 km, these events are observed to be *upgoing* from *below* the horizon.

Due to the predominantly vertical magnetic field in Antarctica, the $\hat{v} \times \hat{B}$ polarization of the geomagnetic emission implies that UHECRs observed by ANITA should be predominantly *horizontally polarized*. The observed polarization of impulsive radio events is therefore a powerful discriminator between neutrino events (that are predominantly vertically polarized) and cosmic ray or extensive air shower events (that are predominantly horizontally polarized). In addition, the Fresnel *reflection* coefficient for the air-ice interface forces a *polarity inversion* on the horizontally polarized geomagnetic signal; this, in effect, *flips the sign* of the instantaneous time-domain electric field. Therefore, the presence of a *polarity inversion* allows ANITA to discriminate between *reflected* cosmic ray events and *above-horizon non*-reflected UHECRs [257].

3.1.3 Stratospheric UHECR Detection

While *most* of ANITA's cosmic ray detections are *reflected* events from *below* the horizon, each flight of ANITA has also detected a population of *above*-horizon UHECRs that ANITA observes *directly* without reflection. These so-called *stratospheric* UHECRs are on Earth-skimming trajectories that do not ever intersect the ground. Due to the rarefied atmosphere at these Earth-skimming altitudes, these showers can extend for hundreds of kilometers in length and can be initiated by cosmic ray primaries beyond the horizon (from ANITA's perspective). ANITA was the first experiment to detect these

stratospheric cosmic rays although later experiments have since also detected these unique events [241].

3.1.4 Earth-skimming Tau Neutrino Detection

ANITA was one of the first experiments to be significantly sensitive to the Earth-skimming ν_τ air shower technique described in section 2.5. Due to ANITA's unique observing location at an altitude of $\sim$37 km, ANITA is sensitive to τ-lepton air showers over a wide range of angles, but the attenuation of the neutrino flux with increasing angle below the horizon (at ultrahigh energies) suggests that the direction of peak sensitivity should be close to the horizon. A very preliminary simulation of ANITA's sensitivity to this channel was presented in [259], which concluded that despite having a large instantaneous effective area, the total integrated of exposure of ANITA to a *diffuse* ν_τ neutrino flux was, via the τ-lepton decay channel, was at least an order of magnitude smaller than Auger and IceCube.

3.2 Instrument Description

This section presents an overview of the hardware and flight of the *fourth* flight of ANITA.

3.2.1 Antennas

All four ANITA flights have used the same nominal antenna design, although it has been slightly modified over the span of the four flights. These main antennas are quad-ridged "Seavey" horn antennas from Antenna Research Associates (ARA, Inc.). They are dual-polarized (both horizontal and vertical polarization), high-gain (with a peak gain of $\sim$10 dBi and a full-width half-maximum beamwidth of $\sim 60^\circ$), and broadband (with a nominal bandwidth, for ANITA-IV, of 180 MHz to 1200 MHz). These antennas are highly directional, with their boresight pointed -10° below the horizontal (which is $\sim 4^\circ$ below the horizon at $\sim -6^\circ$), and are designed to focus ANITA's sensitivity towards directions where we are likely to detect ultrahigh energy neutrinos, while reducing the influence of background sources outside of this angular range. A photo of ANITA-IV before launch from McMurdo Station is shown in Figure 3.2; the white square quad-ridged antennas can been covering most of the available payload surface area.

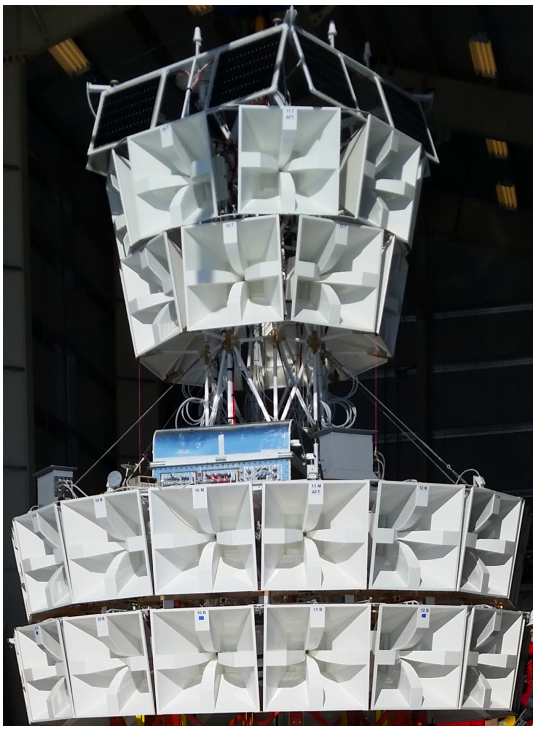

Figure 3.2: A photo of the fourth flight of ANITA, ANITA-IV, outside the launch hangar at McMurdo Station prior to launch in 2016. Photo courtesy of Christian Miki.

The total number of antennas on each payload has increased between ANITA-I and ANITA-IV. ANITA-IV flew 48 quad-ridged antennas, arranged vertically into three rings known as the *top* (T), *middle* (M), and *bottom* (B) rings. Each column of antennas, covering 22.5° of azimuth, is known as a *phi-sector* (ϕ-sector), and identified with a number between 1 and 16 ($22.5^\circ \times 16 = 360^\circ$). Therefore, each channel on the payload can be identified by combining a phi-sector, a ring, and a polarization, i.e. 16TH, 01BV, 07MH. With 48 dual-polarization antennas, ANITA-IV had a total of 96 radio-frequency channels. This arrangement of antennas allows for between 9 and 15 antennas, each dual polarization, to potentially observe a single radio-frequency plane-wave-like signal, as might be emitted by an ultrahigh energy neutrino-induced shower.

ANITA interferometrically combines these signals, with appropriate delay corrections to account for their physical offsets, to create a *coherently summed* signal. By performing interferometry, ANITA gains a $\sim\sqrt{N}$ increase in signal-to-noise ratio (SNR), and can identify the incident direction of the radio signal (if it is roughly a plane wave). An example *interferometric map* created by ANITA-IV showing the *coherently summed peak* indicating the incident direction of the radio signal is shown in Figure 3.3.

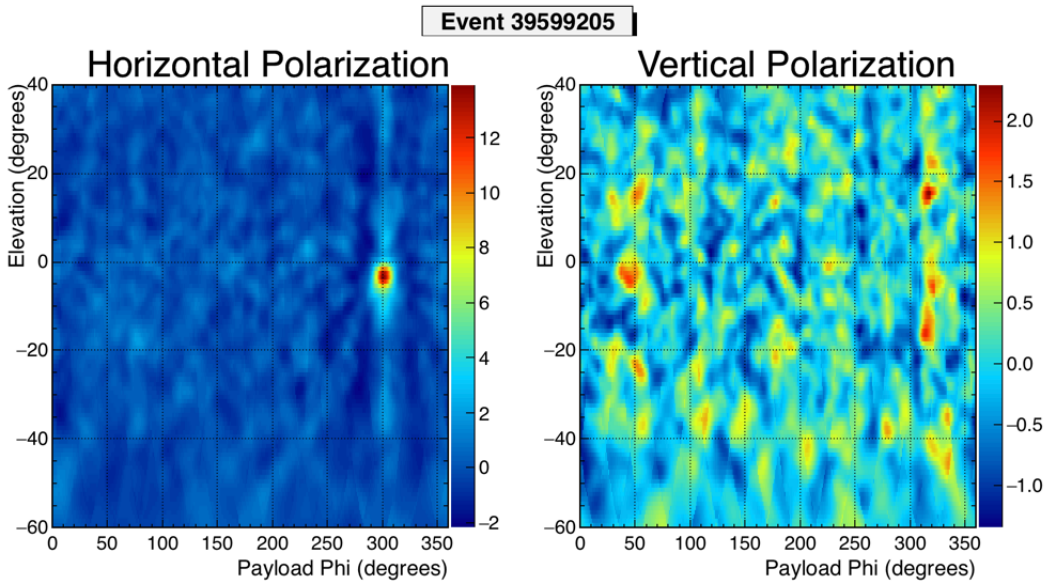

Figure 3.3: An example interferometric map of a *horizontally* polarized event from ANITA-IV. Each map shows the interferometric combination of antenna signals, with appropriate delays, for signals coming from different directions in elevation and azimuth angle. The horizontally-polarized map shows a clear coherent peak, with a coherent map peak in excess of 12, indicating the incoming direction of the radio pulse (in this case, a UHECR likely air shower). The map on the right has a different color scale, for vertical polarization, and shows no clear preferred direction since there is no significant signal in this channel, with a map peak of 2.0. Figure from [260].

Since ANITA is a dual polarization instrument, it can reconstruct the full set of Stokes parameters for the incoming signal. As discussed in section 3.1, reconstructing the polarization of the incoming signal is a powerful discriminator between in-ice Askaryan neutrinos, cosmic rays, and anthropogenic backgrounds (which are expected to be elliptically polarized) The reconstruction of the Stokes parameters must be done carefully as, while ANITA's antennas are dual-polarized, there is a phase offset between the two polarizations that must be measured and calibrated as the physical antenna feeds cannot physically occupy the same space in the antenna. This appears as a difference in the *phase centers* of each polarization of the antenna. This is shown in Figure 3.4.

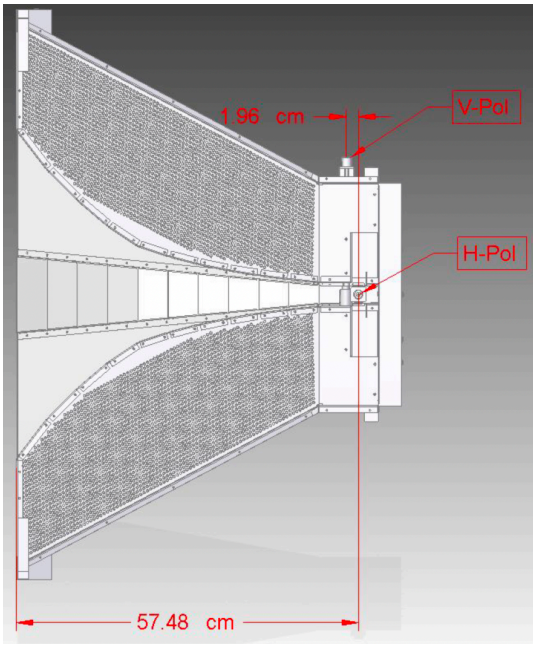

Figure 3.4: A diagram showing the location of the feeds for the ANITA-IV "Seavey" quad-ridged antennas; the physical offset between the two feeds appears as an offset in the phase centers of the horizontal and vertical polarizations. Diagram courtesy of Christian Miki.

The antenna temperature, which was 110 K to 130 K for ANITA-IV, is the single largest contributor to ANITA's system temperature, and therefore ANITA's overall neutrino sensitivity. The largest contributor to the antenna temperature is the beam-weighted brightness temperature of the objects in the antenna's field-of-view (FoV).

It is possible to estimate this to first-order before proceeding with a detailed calculation. For ANITA, at a ∼37 km altitude, the Antarctic ice occupies roughly 60% of the antenna's main beam lobe (since the antenna is pointed below the horizon) with the sky occupying the remaining 40%. At these frequencies, the brightness temperature of the ice is ∼240 K and the sky is roughly ∼3 K across much of ANITA's frequency band. An

arithmetic average, assuming constant gain over the main beam lobe, predicts an overall antenna temperature of ∼145 K.

However, the sky is not exactly 3 K; at the lower end of ANITA's frequency range, the galactic and extra-galactic radio backgrounds are rapidly decreasing and can be ∼1000 K at ∼180 MHz, the nominal high-pass cutoff of the ANITA-IV antennas [261]. In addition, the ice surface is reflective at angles close to the horizon, so ANITA's antennas also observe the *reflection* of the sky *off* the ice surface (with an appropriate Fresnel coefficient) that acts to cool the apparent brightness temperature of the ice near the horizon. A full simulation of the brightness temperature observed by an ANITA antenna, as well as the integrated antenna temperature, is shown in Figure 3.5. When including these effects, ANITA-IV's nominal antenna temperature is 112 K for horizontal polarization and 127 K for vertical polarization, compared against the first-order estimate of 145 K, (the polarization dependence is introduced by the polarization-dependent Fresnel reflection coefficient at the air-ice boundary).

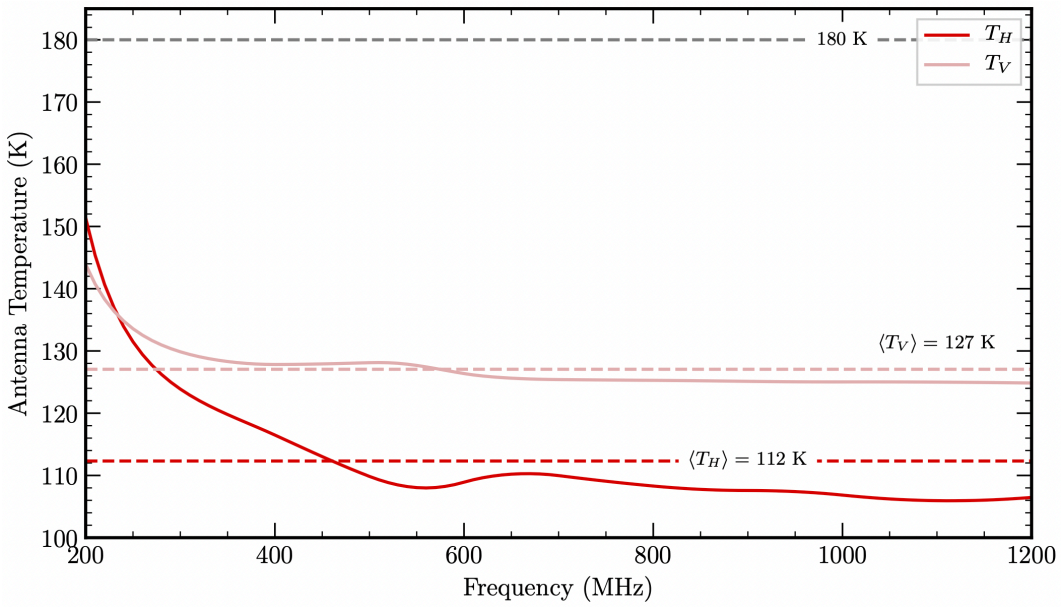

Figure 3.5: The differential antenna temperature as a function of frequency for an ANITA-IV quad-ridged antenna for both horizontal and vertical polarizations. This takes into account the solid angle covered by the sky and ice, the antenna beamwidth, the frequency dependent average sky brightness temperature (the reason for the strong increase at low frequencies), and the Fresnel reflection coefficient for the air-ice reflection. The total antenna temperature, integrated over frequency, is shown with the dashed lines for each polarization.

3.2.2 Signal Processing

Each ANITA-IV channel, 96 in total, is functionally identical from antenna to digitizer. A diagram of the overall ANITA-IV system and signal chain is shown in Figure 3.6.

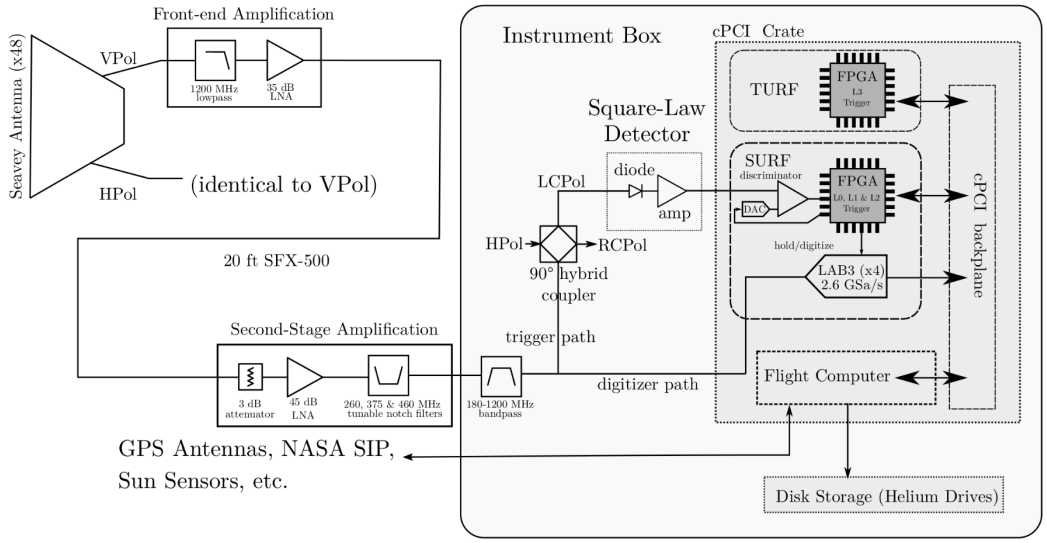

Figure 3.6: A diagram of the ANITA-IV signal chain from the amplifiers all the way through to the digitizers, flight computer, and data storage. See the text for details on each component in this diagram. Figure from [262].

The signal from the antennas is immediately sent through front-end amplification close to the antenna, and then sent through coaxial cable to the main instrument box. Here, the signal undergoes a second stage of amplification and notch and bandpass filtering before being split into *trigger* and *digitizer* paths. The digitizer-copy of the signal is sent straight to the digitizers, while the trigger path is further processed before being connected to an adjustable comparator to determine whether the payload should trigger. If the trigger logic determines that a trigger condition has occurred, the copy of the signal stored in the digitizer is read out and saved to disk. Each of these stages and components are described in detail in the following sections.

AMPAs

The primary front-end amplification is performed by a custom assembly known as an Antenna Mounted Pre-Amplifier (AMPA). A photo of an open AMPA enclosure is shown

in Figure 3.7. Each AMPA contains 1200 MHz low-pass filters and a 35 dB low-noise amplifier (LNA) designed by National Taiwan University (NTU).

The motivation for the AMPAs is three-fold: (1) to amplify the radio signals from the antenna so that they are significantly above the background system noise for transmission over the *lossy* cable to the payload; (2) there are strong anthropogenic radio signals above our band, such as the Iridium satellite constellation at ∼1625 MHz, that could easily *saturate* our LNAs, rendering them useless, and these signals must be removed before the first and second stage amplifiers; and (3) regions above and below our useful science band (180 MHz to 1200 MHz) contribute unnecessary thermal noise unless removed via filtering at an early stage. Much of the AMPA design is focused on low-pass filtering as the antenna gain provides a natural intrinsic high-pass to our observed signals. To maximize the efficiency of transmission from the antenna to the AMPA, each AMPA is directly attached to the LNA's N-type coaxial port (see Figure 3.7). A measurement of the gain and noise temperature of all 96 AMPAs used in ANITA-IV is shown in Figure 3.8.

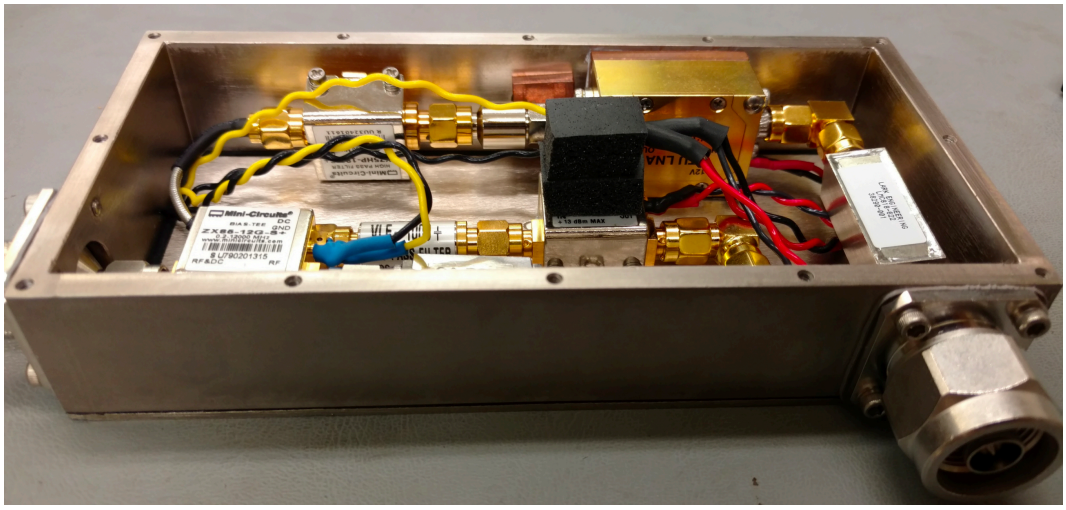

Figure 3.7: A photo of the inside of one of the AMPA enclosures used in ANITA-IV showing the combination of filters, bias tees, and a custom LNA designed by NTU. The male N-type coaxial connector shown in the photo is directly attached to the corresponding female N-type connector on the antenna. Photo courtesy of John Russell.

IRFCM & TUFFs

After the AMPAs, each signal is connected to the main "instrument box" via ∼20 ft of SFX-500 coaxial cable; the connection in the instrument box is to the Internal Radio

Frequency Conditioning Modules (IRFCMs). There were four IRFCMs in ANITA-IV, each of which consisted of a second-stage of amplification with 45 dB LNAs, and a set of three tunable notch filters *per* channel. The tunable notch filter stage used on ANITA-IV was called the Tunable Universal Filter Frontend (TUFF) [262].

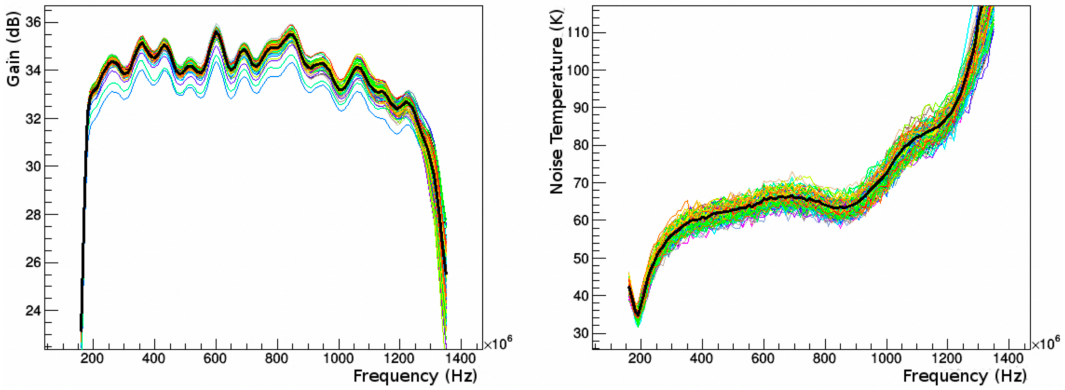

Figure 3.8: The measured gain and noise temperature of each AMPA used in ANITA-IV (colored lines) along with the average (black). Figure from [260].

These set of notch filters were added in ANITA-IV to counter continuous-wave (CW) satellite interference that significantly impacted the effective livetime of the ANITA-III flight [263, 262]. Even when away from Antarctic bases with radio-loud environments, ANITA-III consistently observed CW contamination from a population of satellites not previously observed in ANITA-I and ANITA-II. In ANITA-III, this satellite interference was compensated by *masking* particular phi-sectors so that they did not contribute to the trigger logic. Since many of these satellites were geosynchronous and therefore almost always in view of ANITA-III, the north-facing half of the payload was almost always masked throughout the ANITA-III flight. The design goal of the TUFF filters was to use narrow notch filters to remove the CW frequencies used by these satellites so that the entire payload could be "unmasked" and operate at maximum sensitivity.

The three notch filters on each channel were programmed with default center frequencies of 260 MHz, 375 MHz, and 460 MHz. Informed by the ANITA-III analysis, these frequencies were chosen to combat the origins of the worst CW contamination: 260 MHz and 375 MHz for geosynchronous Department of Defense satellites, and 460 MHz for specific communications systems used by Antarctic bases [263]. Each notch filter can be switched on and off, as well as retuned to different center frequencies as needed throughout the flight. Notches 1 and 2 (260 MHz and 375 MHz) were turned

on, in some capacity, for most of the flight, but notch 2 was occasionally retuned ± 10 MHz to combat specific CW interference. Due to its effect on ANITA-IV's sensitivity, notch 3 (460 MHz) was only turned on when necessary, primarily in view of large Antarctic bases. The addition of the TUFFs decreased the fraction of the payload that had to be masked from $\gtrsim 50\%$ to $\lesssim 30\%$, while keeping the deadtime relatively low ($\sim$7% when averaged over the entire flight). A plot of the noise spectral density measured throughout the flight, clearly showing the effect of the three notches, as they turn on and off throughout the flight, is shown in Figure 3.9.

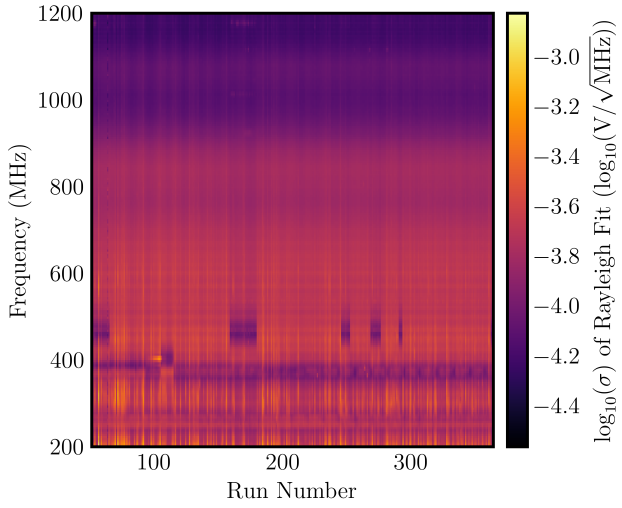

Figure 3.9: The base-10 logarithm of the average noise spectral density in $V/\sqrt{MHz}$ for each run in the ANITA-IV flight starting at the first science run. The two horizontal lines are notches 1 and 2 at roughly 260 MHz and 375 MHz respectively that were on throughout most of the flight. The effect of the third notch filter, at roughly 460 MHz, can be seen as it is turned on and off throughout the flight.

While improving on the pure-masking system used by ANITA-III, the presence of the notch filters did still reduce ANITA-IV's overall sensitivity and, together with the AMPAs, introduced significant group delay into the impulse response of the system that caused complications in the post-flight analysis. The design of the AMPAs was optimized for noise figure, not impedance matching, and the design used in ANITA-IV introduced an impedance mismatch between the antenna, AMPA, and TUFFs below $\sim$300 MHz; this acted to create a long long-frequency tail in the impulse response that was not properly simulated during the initial analysis. A comparison between the predicted impulse response used in the ANITA-IV analysis (which assumed perfect impedance matching) and the *actual* measured impulse response is shown in Figure 3.10.

After the IRFCMs, the signal is band-pass filtered *again* to 180 MHz to 1200 MHz using Lark Engineering filters, to filter out any additional out-of-band noise or signals before

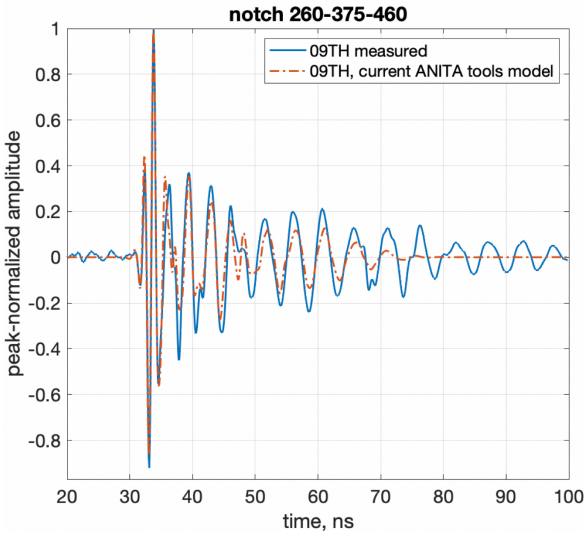

Figure 3.10: A comparison between the predicted (simulated) impulse response for one channel on ANITA-IV, assuming perfect impedance matching between the various components, and the actual *measured* impulse response. The simulated impulse response was what was used in the initial ANITA-IV analysis; this was then redone using the new set of measured impulse responses. Figure by Peter Gorham.

the digitizer (the effective Nyquist sampling rate for ANITA-IV's digitizer is 1.3 GSa/s). After these last stage filters, the signal is split into *trigger* and *digitizer* paths.

3.2.3 Trigger Path Signal Chain

ANITA-IV had a maximum sustainable trigger rate of 50 Hz, where each trigger *event* consists of a 100 ns long snapshot of the time domain voltage in each channel, along with housekeeping and attitude information. When combined, the $\mathcal{O}(10^8)$ events recorded by ANITA-IV only samples 0.0005% of the total flight time. Therefore, the ANITA-IV payload must decide in real time which 0.0005% of the total flight should be saved for later analysis; this is done by only saving waveforms that *trigger*. The following sections detail the signal chain for the *trigger path* that decides, in real time, whether a *trigger* should be issued, saving the current set of waveforms. A photo of the trigger path assembly is shown in Figure 3.11.

Hybrids

While ANITA's quad-ridged horn antennas fundamentally measure *horizontal* and *vertical* polarization, it is actually advantageous for ANITA to trigger on *left-circular* (LCP) and *right-circular* polarization (RCP).

ANITA's science signals, both Askaryan and geomagnetic in origin, are expected to be *linearly* polarized, although the *axis* of polarization varies depending upon the event location and detection channel. Furthermore, the polarization axis of the electric field

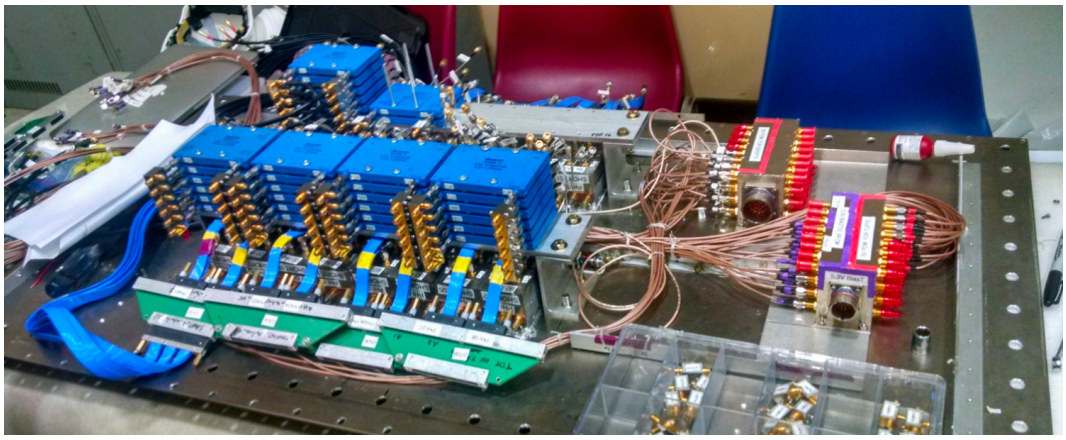

Figure 3.11: A photo of the trigger path assembly used in ANITA-IV including the hybrids and SHORTs (see text for details). Photo courtesy of John Russell.

is not guaranteed to be aligned exactly with the horizontal or vertical polarization axes of the antenna. A *linearly* polarized signal decomposes into *equal* magnitudes of left-circular and right-circular polarization, regardless of the axis of the linear polarization. In addition, thermal noise is expected to be largely unpolarized, and the CW contamination from satellites is largely elliptically polarized, so by triggering on equal amounts of LCP and RCP, ANITA-IV's trigger can isolate events that are linearly polarized while rejecting a whole class of background events. After splitting the signals into the trigger and digitizer path, the trigger path signals are sent through 90° *hybrid couplers*, or "hybrids", that convert the pair of horizontal and vertical polarization signals coming from a single antenna to left-circular and right-circular polarizations.

L0 Trigger

To detect impulsive signals, ANITA used a square-law power detector with a specific time constant designed to respond to signals with durations similar to those expected from ultrahigh energy neutrinos; this power detector is implemented with a tunnel diode. The time domain response of this tunnel diode is shown in Figure 3.12.

The output of the tunnel diode is amplified, transformed into a differential pair, and fed to a comparator that is read out by a Field-Programmable Gate Array (FPGA). The combination of the tunnel diode, amplifier, and differential transformer is known as the SURF High-Occupancy RF Trigger (SHORT). The SHORTs can also be seen in Figure 3.11. If any of the comparators exceed their threshold, which is set by digital-to-analog

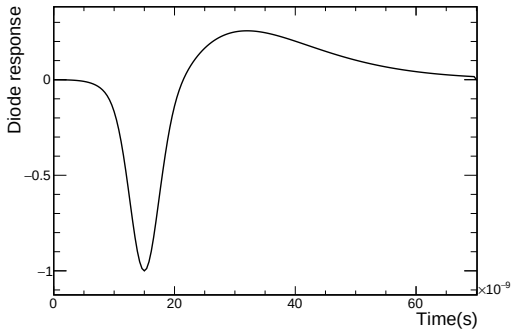

Figure 3.12: The normalized time-domain response of the tunnel diodes used in the ANITA-IV L0 trigger designed to maximize our sensitivity to impulsive signals with durations of a few tens of nanoseconds. Figure from [264].

converters (DACs) controlled by the FPGA, then a zeroth-level (L0) trigger is issued. The L0 trigger thresholds are adjusted in real time to keep the final global (L3) trigger rate at 50 Hz; for ANITA-IV, this typically put the L0 trigger rate between 5 MHz and 6 MHz.

L1 Trigger

Whenever a zeroth-level trigger is issued, the Triggering Unit for Radio Frequencies (TURF) checks for a first-level (L1) trigger. An L1 trigger is issued if both the LCP and RCP channels from a *single antenna* fire within 4 ns of each other. This is motivated by the use of LCP & RCP since a perfectly linearly polarized signal, along *any axis*, should be equal magnitude in both channels (and therefore meet the requirements for an L0 trigger in both channels).

L2 Trigger

A second-level (L2) trigger relies on the coincidence of at least two L1 triggers within a single phi-sector. With three antennas in each phi-sector, there are three possible combinations of coincidences: top-middle, top-bottom, and middle-bottom. Before checking for a coincidence, the TURF delays the signals from the middle and bottom rings by 4 ns in order to bias *against* triggering on plane waves coming from above the payload (that would trigger the top and middle rings first), and are not expected to be science signals. The temporal width of the allowed coincidence window is different for each antenna-pair: it is 12 ns wide for a top-bottom trigger, 8 ns wide for a middle-top trigger, and 4 ns wide for a middle-bottom trigger. The motivation for these time delays is shown in Figure 3.13. These different window lengths and delays are chosen in order to preferen-

tially trigger on signals that are incident from below the payload, where we expect all of ANITA's science signals to be located.

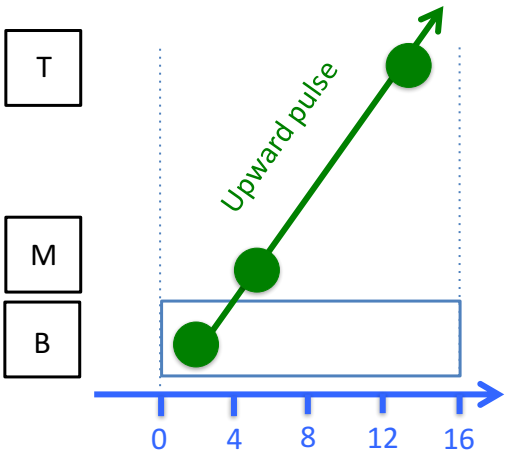

Figure 3.13: A diagram demonstrating the origin of the different time delays for top-middle, middle-bottom, and top-bottom triggers to preferentially trigger on signals that are coming from *below* the horizon. [264].

L3 Trigger

A top-level (L3), or *global*, trigger is issued if two L2 triggers are issued in *adjacent* phi-sectors within 10 ns. If an L3 trigger is issued, the digitized signal for all 96 channels is read out and processed as an *event*, unless all four storage buffers of the digitizers are full.

If that occurs, the event cannot be stored and the payload has a period of *dead time* where no further triggers can be processed until the digitizer buffers are no longer full. As discussed in 3.2.3, the maximum sustainable global trigger rate for ANITA-IV was 50 Hz. Therefore, the L0 trigger thresholds are continually adjusted so that the global L3 trigger rate does not exceed 50 Hz in order to prevent completely filling the digitizer buffers and incurring deadtime (when a potential science signal may be received and then *lost*).

Minimum-bias Triggers

The L0-L1-L2-L3 trigger logic preferentially selects signals that are similar to those expected from ultrahigh energy neutrinos and extensive air showers. However, during post-flight analysis, an accurate sample of the background radio environment is needed in order to understand the possibility for anthropogenic backgrounds to "replicate" science signals. Therefore, each flight of ANITA has taken a set of "minimum-bias" triggers that

aim to provide an unbiased sample of the background radio environment. These samples, that contain mostly thermal noise, with some anthropogenic background, act as our analysis sample of the background noise environment. This is done by triggering the payload at a fixed rate, roughly 3 Hz, consistently throughout the flight without applying *any* trigger condition; these triggers are derived from the GPS PPS signal from ANITA-IV's navigational systems. These minimum-bias triggers were used to construct the 2D noise histogram in Figure 3.9.

3.2.4 Digitizer Path Signal Chain

Since the amount of data stored by ANITA is too large to be telemetered to the ground during the flight, the time-domain voltage of each channel must be digitized and saved to disk for post-flight analysis. The trigger logic, described in section 3.2.3, determines whether the current set of waveforms needs to be saved, but the *digitizer signal chain* is responsible for performing the digitization and saving the signals to disk. The signal from the digitizer-trigger split, shown in Figure 3.6, is connected directly to the ANITA-IV digitizers.

The sampling is done by custom Application Specific Integrated Circuits (ASICs), designed specifically for the ANITA instrument. ANITA-IV used the Large Analog Bandwidth Recorder and Digital Order Readout (LABRADOR) design; specifically, the LAB3 ASICs. Each LAB3 ASIC digitizes eight analog channels with an array of 260 sample long switched-capacitor array (SCA) analog-to-digital conveters (ADCs), which at a nominal sample rate of 2.6 GSa/s, can store a 100 ns long waveform per-channel. The LAB3 ADC samples each channel with 12 bits of resolution (although the bottom bit is almost immediately discarded). Due to the fundamental design of switched-capacitor array ADCs, the timing between subsequent samples is uneven, which imparts a frequency response to the ADC that must be corrected in calibration. Unfortunately, the LAB3 ADCs have a smaller bandwidth compared to the overall 180 MHz to 1200 MHz bandwidth of the ANITA signal chain. The LAB3 digitizers are therefore the dominant source of high-frequency attenuation within the main frequency band, other than intentional low-pass filters in the signal chain. the LAB3 has a 3 dB point at $\sim$900 MHz, and therefore attenuates signals in the top $\sim 1/3$ of the ANITA-IV frequency band. A plot of the frequency response of the LAB3 ASICs, along with the magnitude of the transfer function, is shown in Figure 3.14.

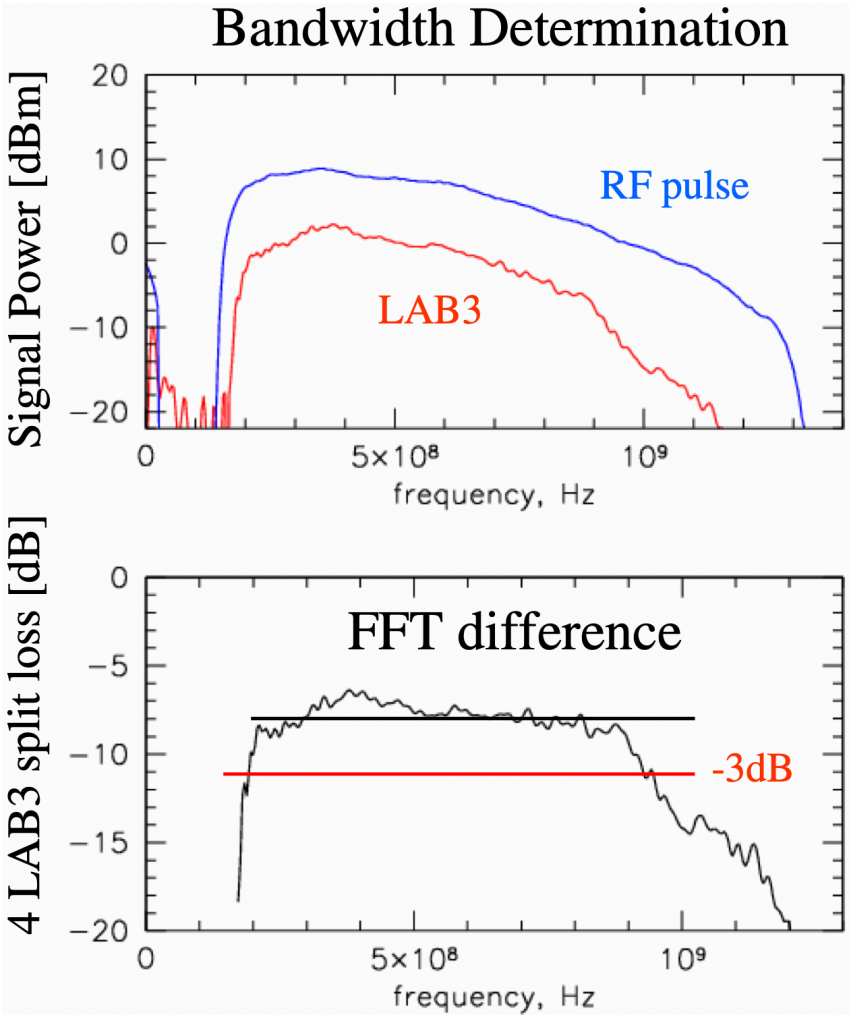

Figure 3.14: The measured response of the LABRADOR (LAB3) ASIC used as the primary digitizer for ANITA-IV. This was measured by sending a high-bandwidth pulse (blue) through a 4-way split and reading it out on the LAB3 (red). The difference between these two pulses is shown in the bottom pane. As the signal is sent through a 4-way split, a perfect digitizer would reproduce a flat −6 dB attenuation. Figure from [265].

Four LAB3 chips are combined on a single board to form the Sampling Unit for Radio Frequencies (SURF) board. The SURF coordinates the control of each of the LAB3 ASICs and distributes a 33.3 MHz clock to each LAB (on a ninth ADC channel) that can be used to correct for timing jitter between each LAB3 ASIC on every SURF.

3.2.5 Attitude Determination

Like previous ANITA flights, the ANITA-IV payload is free-floating and free-rotating, and as such the altitude and heading of the payload varies throughout the flight due to changes in wind speed, atmospheric pressure, temperature, etc. ANITA requires precise attitude information so that: (1) we can point back the observed radio signals to locations on the sky to search for astrophysical sources; (2) we can identify signals that come from the direction of active bases on the continent and are likely to be of anthropogenic origin; (3) to discriminate other sources of backgrounds (such as the sun); and (4) to constrain potential events to different detection channels that may produce a *science* signal as they can occur from different regions of ANITA's field of view (i.e. extensive air showers vs. in-ice neutrino signals)

Due to the importance of having accurate attitude and heading information, ANITA-IV flew multiple redundant attitude determination systems.

GPS

ANITA-IV flew three *independent* GPS systems, two ADU5s and one G12, that were designed to be the primary attitude system for the flight. Each ADU5 GPS unit had its own array of four antennas, with an additional antenna for the G12, for a total of nine GPS antennas. These systems provided an attitude update at roughly 1 Hz throughout the flight. The ADU5s were the primary attitude system and were used in the ANITA-IV post-flight analysis: they each independently report latitude, longitude, heading, altitude, pitch, and roll. The G12, with its single antenna, only reported position and velocity information.

Due to their resolution and accuracy, the GPS systems were intended to be the primary attitude system in the absence of any backups. However, in case the GPS units failed, ANITA-IV flew two backup systems: sun sensors, and a magnetometer.

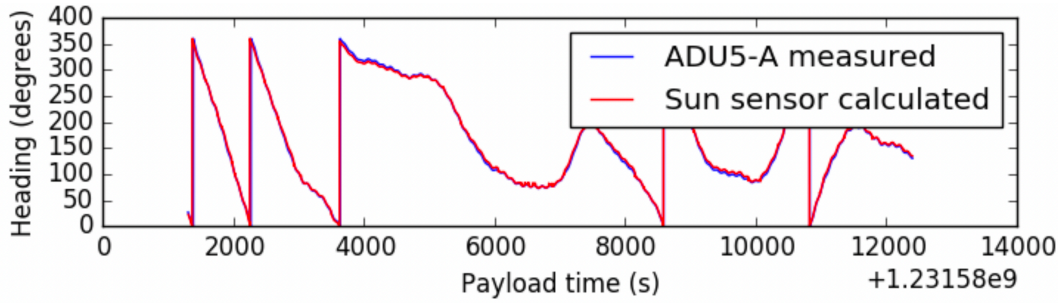

Figure 3.15: A plot of the payload heading reconstructed using one of the two ADU5 GPS units, ADU5-A, and the suite of sun sensors on ANITA-IV. While the sun sensors were not used in the analysis since the GPS units did not fail, they did accurately reconstruct the heading of the payload. Figure from [260].

Sun Sensors

As ANITA flies in the Austral summer, the sun is always above the horizon and in view of the payload. With accurate ephemerides for the sun, the *relative* location of the sun on the sky, measured by the sun sensors, can be used to reconstruct the heading of the payload. Unlike the GPS systems that provided full attitude information, the sun sensors can only accurately be used to measure the heading. Since the GPS units did not fail for ANITA-IV, the sun sensor data was not used in the post-flight analysis. However, a reconstruction of payload heading from the sun sensors compared against data from one GPS system, which agree remarkably well, is shown in Figure 3.15.

Magnetometer

In addition to the sun sensors, ANITA-IV flew a magnetometer that measured the instantaneous three-vector of the local magnetic field. With an accurate model of the geomagnetic field, it is possible to reconstruct the location of the payload with coarse accuracy; this requires an altitude in order to provide a unique solution, which must either be assumed, or provided from another subsystem (such as the G12 single-antenna GPS). Similar to the sun sensors, since the GPS antennas did not fail for ANITA-IV, the magnetometer data was not employed for any analyses.

3.2.6 Flight Computer

The ANITA-IV flight computer coordinated the operation of the payload, and was responsible for gathering data from the various subsystems, writing that data to disk or telemetry, and responding to commands from ANITA-IV's ground staff. The ANITA-IV flight computer was a Compact-PCI (cPCI) single-board-computer, running Fedora Linux, and mounted in the same cPCI crate as the SURF and TURF boards (so that they all shared low-latency communication via the cPCI backplane). The flight software, with lineage from the first flight of ANITA in 2006, is comprised of multiple *daemons* that are responsible for different subsystems in the payload: `Acqd` gathered data from the SURF and TURF boards and used that data to update thresholds and phi masking settings; `GPSd` managed the GPS systems and communicated attitude information to `Acqd`; `Monitord` managed the data storage subsystems and ensured data was written to disk; `Prioritizerd` controlled the GPU-based prioritizer; etc.

Telemetry

ANITA-IV had several different telemetry links to provide downlink & uplink between the payload and the ANITA-IV ground crew, with different available rates. The five different telemetry subsystems flown by ANITA-IV were, in order of decreasing data rate:

1. The Line-of-Sight (LOS) transmitter was used when the payload was in direct view of McMurdo Station just after launched and had the highest overall data rate.
2. Iridium OpenPort is a satellite telemetry system with data rates up to 128 kbps.
3. NASA Tracking and Data Relay Satellite System (TDRSS)—*fast* subsystem.
4. NASA Tracking and Data Relay Satellite System (TDRSS)—*slow* subsystem.
5. Iridium low-rate satellite telemetry.

Prioritizer

Due to the amount of data stored by ANITA-IV, it was impossible to telemeter it down to the ground during the flight; therefore, the storage disks must ideally be recovered. However, if the payload landed somewhere unrecoverable, such as the ocean, or if the drives were destroyed or failed during impact with the ground, the data may be have been

unrecoverable. To mitigate the *scientific* damage of this happening, a *prioritizer* was running continuously throughout the flight, processing events in real-time to determine if they were likely to be high-quality science events. High-priority events were prioritized for downlink via telemetry so that they could be backed up on the ground in the case of full flight data loss.

The prioritizer ran on a Graphical Processing Unit (GPU) and performed a suite of interferometry on each event to determine the peak coherent interferometric image peaks and coherent Hilbert envelopes. Each event was given an integer priority between 1 and 9 (inclusive), where 1 was the highest priority: a priority of 1-6 was used for normal science events; 7 indicated the prioritizer event buffer was close to full; 8 indicated a event with strong (apparent) continuous-wave interference, and 9 indicated that there was saturation in the SURF digitizers. Since ANITA-IV was successfully recovered, the downlinked data from the prioritizer was not used in any ANITA-IV analyses.

Figure 3.16: A photo of the ANITA-IV payload after crashing on the continent near the South Pole. The bottom and middle ring are "sacrificial" and were designed to crumple on landing to reduce damage to the main instrument box and payload (shown in the photo). Photo provided by Christian Miki.

Data Storage

ANITA-IV recorded $\mathcal{O}(10^8)$ events during the flight which required $\mathcal{O}(4\,\mathrm{TB})$ of data storage. Since the exact flight time was not known in advance, the storage system for flight data was sized to store data from the longest possible flight ($\mathcal{O}(60\,\mathrm{days})$, nearly twice as

long as the actual flight). In addition, since recovering a full science data set from the payload was an essential requirement for maximizing science reach, the storage systems on ANITA-IV were redundant. The primary system was a pair of 8 TB helium-filled spinning disk drives in a RAID 1 configuration (where the data was duplicated 1-to-1 on both disks simultaneously). In addition, a RAID-0 array of six 1 TB solid state drives, designed by National Taiwan University (NTU), was accessible via Ethernet and was used to store a complete backup of the flight data from the helium drives. Both storage systems survived the flight and were successfully recovered.

3.2.7 Balloon & Flight

ANITA-IV used a 34H ("34 heavy") balloon provided by the Columbia Scientific Balloon Facility (CSBF). For an instrument with the mass of ANITA-IV, this provided a nominal float altitude of $\sim$37 km, decreasing slowly over the flight, using approximately 34 million cubic liters of helium. While the balloon was rated for a maximum nominal flight duration of 60 days, most Antarctic long-duration balloon payloads have flight times in the 20-30 day range; all ANITA flights have been in this range, with ANITA-IV lasting for 28 days.

During the austral summer, a circumpolar wind is present on the Antarctic continent, so long-duration balloon payloads in Antarctica follow roughly circumpolar orbits (although their latitude can change throughout the orbit). This has the advantage of allowing long duration flights around the South Pole where the payload stays *above the ice* (since the payload and science data is not recoverable if it lands in the ocean). When the decision to terminate a flight is made, the payload detaches from the balloon, ejects a parachute, and (hopefully) lands with minimal damage to the main payload. However, the bottom two rings of antennas were designed to crumple during landing and help protect the rest of the payload from significant impact damage. The complete flight path of ANITA-IV, which completed nearly three loops around the continent is shown in Figure 3.17 and a photo of the crashed ANITA-IV, showing the crumpled "sacrificial" antennas, is shown in Figure 3.16.

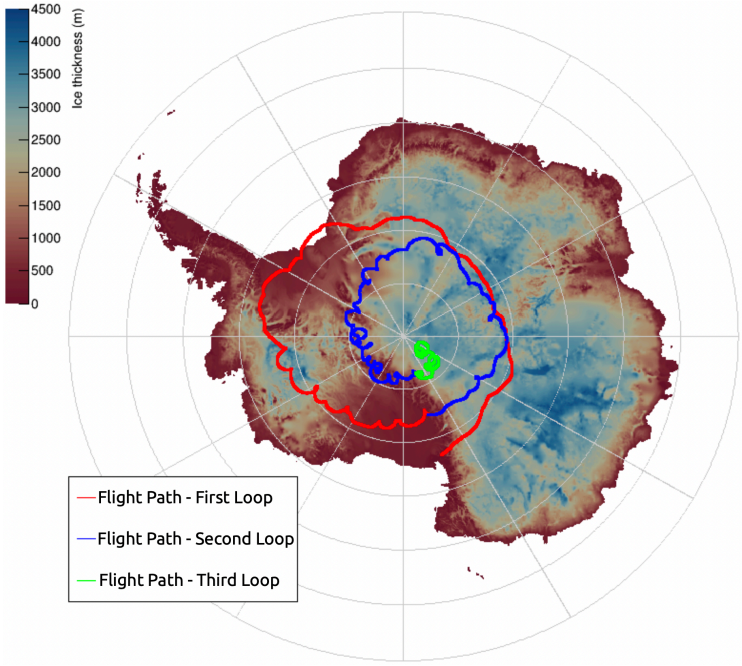

Figure 3.17: The flight path taken by ANITA-IV during its 28 day flight. Each successive loop around the continent is drawn in a different color. Figure taken from [260].

3.3 Scientific Results

During its four successful flights, ANITA performed a variety of science investigations, beyond its origin goal of searching for ultrahigh energy neutrinos via the Askaryan effect. section 3.3.1 presents ANITA's diffuse ultrahigh energy neutrino limits, section 3.3.2 presents ANITA's measurements of the diffuse UHECR flux, and section 3.3.3 reviews several anomalous and near horizon events observed by ANITA, which will be the focus of much of this dissertation.

3.3.1 Limits on the Diffuse Neutrino Flux

ANITA has not definitively discovered a flux of ultrahigh energy neutrinos (i.e. a 5σ significance) but each flight of ANITA has set increasingly stronger limits on the diffuse ultrahigh energy neutrino flux, ANITA's original science goal.

The *prototype* flight of ANITA, ANITA-lite, lasting 18.4 days, was able to immediately rule out several classes of neutrino production models [266, 267, 268]. In particular, the *Z-burst process* was completely ruled out. In this process, ultrahigh energy ($\gtrsim 10^{22}$ eV)

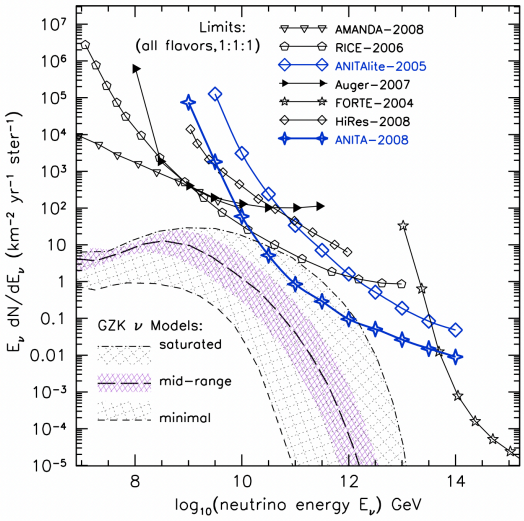

Figure 3.18: The differential limit on the ultra-high energy neutrino flux set by the ANITA prototype, ANITA-lite, and the first full flight, ANITA-I. Even with its original 18 day, ANITA-lite and ANITA-I were able to rule out a whole class of models, including a range of GZK ν models (shown in the figure). Figure from [266, 107]

neutrinos annihilate with cosmic background antineutrinos ($T_\nu \sim 1.9\,\mathrm{K}$) to generate a Z^0 vector boson, via $\nu\bar{\nu} \rightarrow Z^0$, that will then decay to produce UHECRs within the GZK horizon of Earth [268].

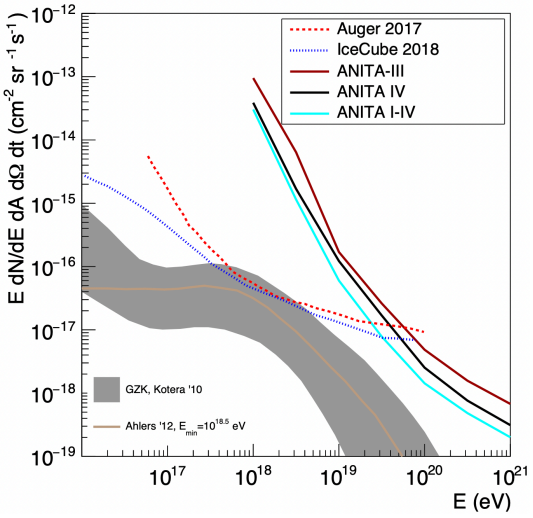

Figure 3.19: The differential limit on the ultra-high energy neutrino flux set by the latest ANITA flight, ANITA-IV, along with the combined ANITA limit from all four flights, along with limits from the IceCube and Auger observatories. Also shown are predictions for the GZK neutrino flux (grey band). Figure from [87].

The differential limit on the diffuse flux set by the first flight of ANITA, ANITA-I, is shown in Figure 3.18. ANITA-I, with only a 18 day flight, set the strongest limits on this flux, at the time, from 3×10^{18} eV (below which RICE set a stronger limit [159]) up to $\sim 10^{23}$ eV (above which FORTE set a stronger limit [269]) [107].

In one 18 day flight, ANITA-I was also able to rule out a variety of *strong source evolution* models, including models that saturate all bounds, that predicted between 1 and 10

events for ANITA-I's sensitivity [270, 271, 272]. Each successive flight has continually set a stronger limit on the ultrahigh energy neutrino flux, and ruled out additional neutrino production models. The latest limit, set by ANITA-IV, is shown in Figure 3.19. As of the ANITA-IV flight, the combined ANITA limit is the strongest above 4×10^{19} eV below which the long livetimes of the IceCube and Auger observatories set a stronger limit [87, 240].

3.3.2 Measurements of the Diffuse UHECR Flux

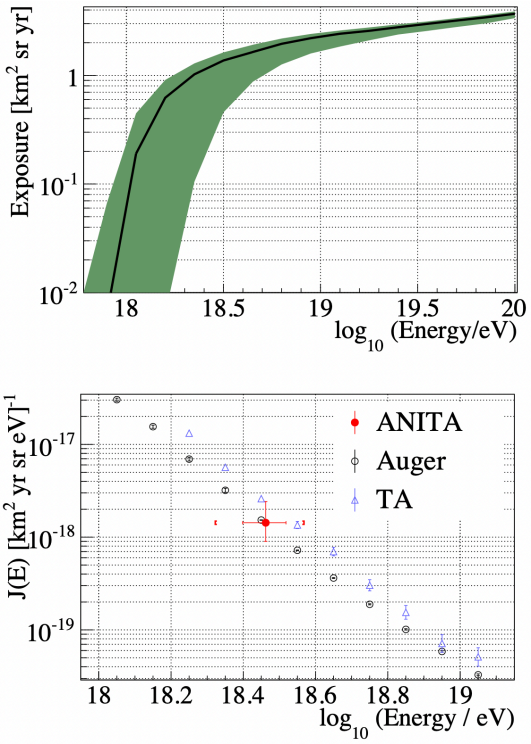

Figure 3.20: *Top:* The exposure of ANITA-I to reflected UHECRs (black) with the range given by model uncertainties in green. *Bottom:* The UHECR flux measured by ANITA-I (red) compared against measurements from Auger and Telescope Array. ANITA-I's first measurement, using *reflected* UHECRs, is completely consistent with other measurements of the flux. Figure from [273].

The first flight of ANITA observed a population (16) of horizontally-polarized impulsive radio signals distributed across the continent away from known sources of anthropogenic radio signals. As discussed in section 3.1.2, the geomagnetic radio emission from UHECRs should be strongly horizontally polarized due to the mostly vertical orientation

of the geomagnetic field near the poles. A later analysis of these events by the ANITA collaboration determined that they are consistent with UHECRs reflecting off the ice surface. This was the first direct detection of *reflected* cosmic ray radio signals [273].

This post-flight analysis by the ANITA collaboration, including detailed cosmic ray simulations, used this sample of UHECRs to calculate the exposure of ANITA to UHECRs and perform a measurement of the UHECR flux between 1 EeV and 10 EeV. The exposure of ANITA to UHECRs is shown in Figure 3.20a while the flux estimate, compared against measurements by TA and Auger, is shown in Figure 3.20b. While ANITA's exposure to UHECRs is dwarfed by experiments like Auger, ANITA's UHECR flux measurement was consistent with that of Auger within experimental uncertainties [273].

3.3.3 Anomalous & Near Horizon Events

ANITA-I & ANITA-III Anomalous Events

ANITA-I and ANITA-III observed a pair of impulsive horizontally polarized signals, typical of extensive air showers, but with an inverted polarity compared to the broader sample of normal cosmic ray events [258]. As discussed in section 3.1.2, down-going UHECRs, whose geomagnetic emission reflects off the ice surface and appear to be incident from below the horizon, pick up a *polarity reversal* due to the air-ice Fresnel coefficient for horizontally polarized signals. The polarity reversal provides a unique method for distinguishing reflected radio signals from those created by *upgoing* extensive air showers. The two events, one observed in ANITA-I, and one observed in ANITA-III, each had polarity consistent with an *upgoing* extensive air shower. The waveforms for the ANITA-III anomalous event, Event 15717147, is shown in Figure 3.21 along with the waveform from a normal *above*-horizon UHECR (Event 39599205).

As discussed in section 3.1.4, *upgoing* extensive air showers are expected from Earth-skimming ν_τ's that produce τ-leptons that then decay in the air; this was initially proposed as a physical explanation for these two *non-inverted* cosmic ray-like events. However, both of these events were observed at steep angles below the horizontal, -36° and -27° respectively, where the ν_τ flux is expected to be strongly suppressed due to the large Earth-crossing grammage at these angles [258]. An initial analysis of these events under a ν_τ hypothesis found that they were in strong tension with tau neutrino flux limits set by IceCube and Auger; the implied flux necessary to create these events, given the strong attenuation at these steep emergence angles, is two orders of magnitude above current

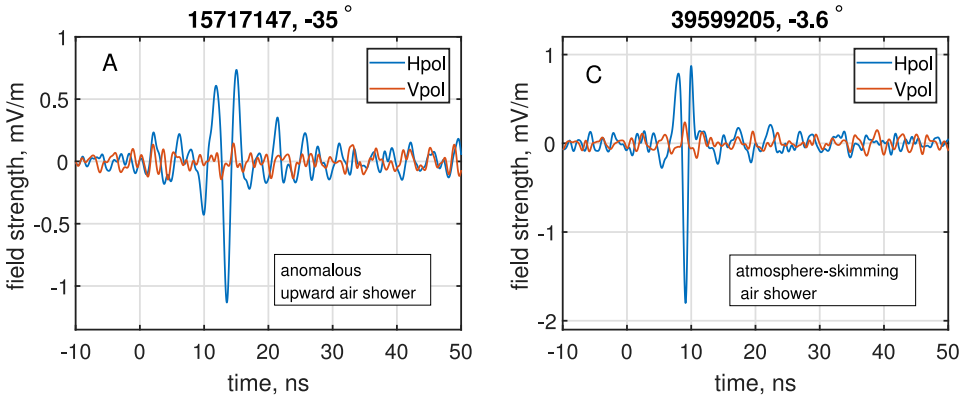

Figure 3.21: The waveform for the anomalous steeply upgoing event from ANITA-III, Event 15717147, compared against a regular *above*-horizon UHECR from the same flight, Event 39599205. Despite the left event being from $-30°$ below the horizon, and the right event being from $\sim 3°$ above the horizon, they have the same polarity (*negative* in this representation). Figure from [258].

neutrino limits [259]. The exposure of ANITA-I and ANITA-III to a ν_τ flux compared against neutrino limits set by Auger, IceCube, and ANITA's Askaryan channel is shown in Figure 4.1.

A range of alternative explanations have been proposed for these events; some of which are "Standard Model"-compatible (SM) hypotheses while others are "Beyond Standard Model" (BSM). For Standard Model-compatible hypotheses, Shoemaker et al. recently proposed that subsurface ice reflectors may be able to reflect the cosmic ray signal without the corresponding polarity inversion [274]. However, a follow-up analysis by the ANITA collaboration, with detailed finite-difference time-domain (FDTD) electromagnetic simulations based on ANITA and HiCal measurements, disfavors the subsurface reflector hypothesis [275]. In addition, it was recently shown that the coherent transition radiation from the otherwise electrically neutral transverse geomagnetic current passing from air into the ice can *potentially* produce impulsive radio signals with the same polarity as upgoing extensive air showers. However, further work is needed to determine whether this process can reproduce the cosmic ray-like signals observed for each of these events [276]. There have also been a host of BSM theories, including: non-thermal dark matter [277]; leptoquarks [278]; R-parity violating supersymmetry [279]; dark axions [280]; and others [281, 282, 283, 284, 285]; but significantly more evidence is needed for *any* of these hypothesis to become significant.

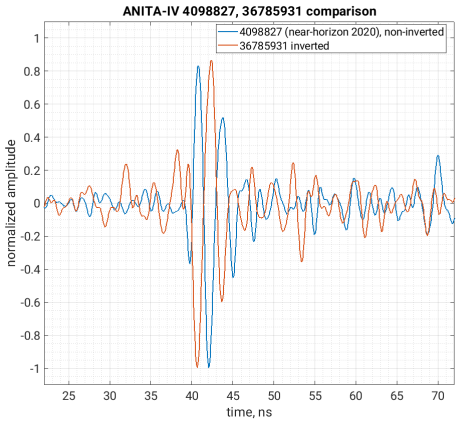

Figure 3.22: A comparison between the deconvolved electric-field waveform of an anomalous horizontally-polarized cosmic ray-like event, Event 4098827, and a similar *reflected* UHECR event, Event 36785931. Despite Event 4098827 also coming from *below* the horizon, it has an *inverted* polarity compared to Event 36785931. Figure from [257].

ANITA-IV Near Horizon Events

event #	mm dd hh mm ss UTC 2016	Apparent source location Lat.°,Lon.°, alt., m	elev. angle[a] degrees	horizon angle[a] degrees	azimuth degrees	Payload location Lat.°, Lon.°, alt., km	Type[c]	Energy[d] EeV
4098827	12 03 10 03 27	-75.71, 123.99, 3184	-6.17 ± 0.21	-5.92 ± 0.020	337.70	-80.157, 131.210, 38.86	NI	1.5 ± 0.7
9734523	12 05 12 55 40	-71.862, 32.61, 19000[b]	-5.64 ± 0.20	-5.95 ± 0.020	2.01	-80.9, 31.6, 39.25	AH	...
19848917	12 08 11 44 54	-80.818 , -79.87, 758	-6.71 ± 0.20	-6.06 ± 0.020	194.34	-76.66, -72.86, 38.97	NI	0.9 ± 0.5
50549772	12 16 15 03 19	-83.483, 14.73, 2572	-6.73 ± 0.20	-5.92 ± 0.020	234.08	-81.95, 47.29, 38.52	NI	0.8 ± 0.3
51293223	12 16 19 08 08	-74.800, 11.43, 18600[b]	-5.38 ± 0.24	-5.85 ± 0.020	306.45	-81.7, 39.2, 37.53	AH	...
72164985	12 22 06 28 14	-86.598, 0.35, 2589	-6.12 ± 0.10	-5.93 ± 0.020	140.03	-86.93, -104.29, 38.58	NI	3.9 ± 2.5

Figure 3.23: The parameters of the four anomalous near-horizon events, as well as two above-horizon stratospheric cosmic-ray-like events, observed by the fourth flight of ANITA.

In addition to the steep events observed in ANITA-I and ANITA-III, ANITA-IV observed *four* extensive air showers, from below the horizon, with polarity consistent with *upgoing* extensive air showers [257]. However, unlike the ANITA-I and ANITA-III events, these were observed very close to the horizon, $\lesssim 1^\circ$, where the attenuation of the ν_τ flux is small and we expect ANITA's ν_τ sensitivity to be maximized (to first order). The parameters of these events, along with two *above* horizon stratospheric UHECRs also detected by ANITA-IV, are shown in Figure 3.23. Events 4098827, 19848917, 505498772, and 72164985 are the "near-horizon events" that reconstruct *below* the apparent horizon but do not show any evidence of a polarity flip due to a surface reflection. The waveform of one of the ANITA-IV near horizon events, Event 4098827, compared against a regular inverted cosmic ray, Event 36785931, is shown in Figure 3.22.

These new events, very close to the horizon, have the *potential* to be the first experimental detection of ultrahigh energy tau neutrinos or an entire new class of currently unknown events for ANITA. The remainder of this dissertation presents a simulation

and analysis of these four near horizon events to determine if they are consistent with a ν_τ hypothesis, and identify what claims ANITA can make given the detection of these four events in ANITA-IV.

Chapter Summary

1. ANITA is an Antarctic long-duration balloon radio neutrino telescope.

2. ANITA is primarily sensitive to four distinct sources of radio emission from astrophysical particles: (1) the (original) in-ice Askaryan channel from UHE neutrinos; (2) the *reflected* emission from down-going UHECRs; (3) the *direct* emission from atmosphere-skimming stratospheric UHECRs; and (4) the upgoing emission from extensive air showers produced by the decay of a τ-lepton from an Earth-skimming tau neutrino.

3. ANITA detects these radio signals using an array of 48 dual-polarization quad-ridged horn antennas with a nominal bandwidth of 180 MHz to 1200 MHz.

4. Each flight of ANITA has set progressively stronger limits on the diffuse ultrahigh energy neutrino flux and ruled out a variety of neutrino production models. As of the last flight, ANITA sets the strongest limit on the UHE neutrino flux above 19.4 eV up to $\mathcal{O}(10^{22}\,\mathrm{eV})$ where lunar neutrino experiments become more sensitive.

5. ANITA has also collected a sample of more than 60 UHECRs and has used these to perform a measurement of the UHECR flux between 1 EeV and 10 EeV, although ANITA's overall exposure is not competitive to that of Auger or Telescope Array.

6. ANITA-I and ANITA-III each observed a pair of steeply upgoing extensive air shower events with polarity consistent with an *above*-horizon extensive air shower. While originally hypothesized to be τ-lepton induced air showers, the steep emergence angles of these events strongly disfavors a tau neutrino hypothesis.

7. ANITA-IV also observed four cosmic ray-like events with polarity consistent with an *upgoing* extensive air shower; however, unlike the steep events in ANITA-I and ANITA-III, these events were observed very close to, but *below*, the horizon. As these events are observed close to the horizon, where the attenuation of the neutrino flux is small, they have the *potential* to be the first experimental detection of ultrahigh energy *tau neutrinos*.

4 Simulating the Sensitivity of ANITA to τ-induced Extensive Air Shower

The fourth flight of ANITA (ANITA-IV) observed four below-horizon cosmic ray-like events that have non-inverted polarity - a 3.2 σ fluctuation if due to background [257] (Figure 4.2). Unlike the steeply-upcoming anomalous events of this type reported in two previous ANITA flights ($\sim 30^\circ$ below the radio horizon) [258, 286], all of the ANITA-IV anomalous events were observed at angles close to the horizon ($\lesssim 1^\circ$ below the horizon).

A Standard Model explanation originally proposed for the steeply upcoming events from the first and third ANITA flights (ANITA-I and ANITA-III, respectively) was skimming ν_τ interactions in the Earth producing τ leptons that escape into the atmosphere, subsequently decaying and producing an upgoing extensive air shower (EAS) mimicking the signal of a cosmic ray. While this origin was initially considered to be unlikely due to the attenuation of neutrinos across the long chord lengths through Earth at these steep angles, several analyses have studied the ν_τ-origin hypothesis for these steeply upgoing events [258, 287].

These analyses have studied two different astrophysical assumptions, with varying degrees of accuracy: (1) that the events were due to a diffuse isotropic flux of ultra-high energy (UHE) neutrinos; and (2) that the events were from transient UHE neutrino point sources that were active or flaring during each flight (using a toy simulation).

Under the diffuse hypothesis for the ANITA-I & ANITA-III anomalous events, a prior analysis by the ANITA collaboration [259, 288] implied a diffuse neutrino flux limit that is in strong tension with the limits imposed by the IceCube [289] and Pierre Auger [123] observatories (Auger). A figure comparing the exposure of ANITA-IV against Auger and IceCube from one of these earlier preliminary analyses is shown in Figure 4.1. This discrepancy is strongly influenced by the large attenuation experienced by any UHE

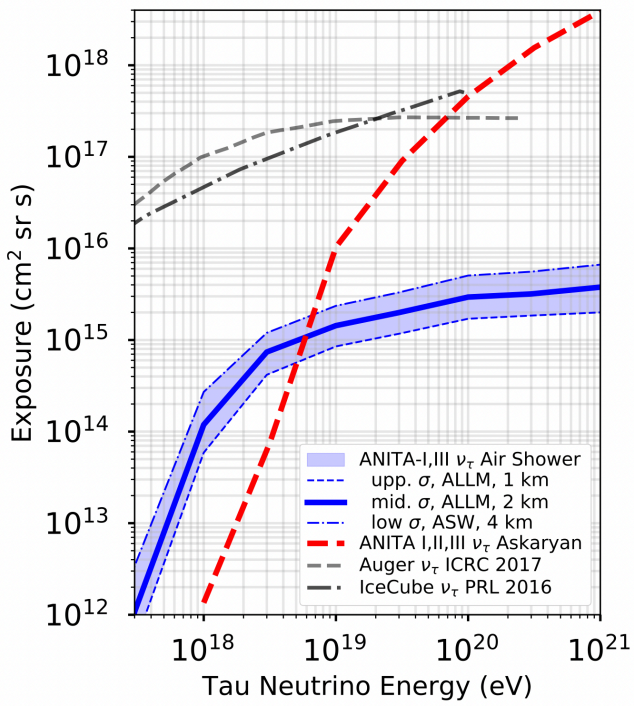

Figure 4.1: The bounds set on ANITA-III's exposure to a diffuse and isotropic flux of ultrahigh-energy tau neutrinos using an earlier preliminary analysis of the steeply upgoing events observed in ANITA-I and ANITA-III. Figure from [259, 288].

neutrino flux at these steep emergence angles (i.e. a large Earth crossing chord length), driving up the flux necessary for ANITA to have seen two events across two cosmic-ray-sensitive flights (as mentioned in Chapter 3, ANITA-II had limited sensitivity to air showers).

A preliminary follow-up analysis by the ANITA collaboration *estimated* the sensitivity of ANITA to ν_τ point sources in the direction of the ANITA-I and ANITA-III anomalous events to investigate the possibility that a point-like neutrino source could be responsible for these events. This analysis *bounded* the *instantaneous* point source effective area to $\lesssim 2.2$ m^2 for the ANITA-I event and $\lesssim 0.3$ m^2 for the ANITA-III event [290], but this calculation was done using a simple preliminary simulation, and was not extended to cover ANITA's full field of view (i.e. they were only calculated for the directions of the specific events in question) These values are significantly smaller than Auger's ν_τ point source peak effective area to ν_τ of 1×10^4 to 3×10^5 m^2 for energies above 10^{17} eV and are also in strong tension with point-like neutrino limits set by Auger [93].

A number of alternative hypothesis have been proposed to explain the ANITA-I and ANITA-III anomalous events. These range from Beyond Standard Model (BSM) physics [277, 278, 279, 281, 280, 282, 283, 284, 285] to more mundane effects such as transition ra-

diation of cosmic ray air showers piercing the Antarctic ice sheet [276] and subsurface reflections due to anomalous ice features [274], although the latter has recently been experimentally constrained by the ANITA collaboration [275].

ANITA's sensitivity to the τ EAS channel is highly directional and is expected to be maximal near the horizon where it is likely to be orders of magnitude larger than for the steeply upgoing angles of the ANITA-I and ANITA-III events due to the significantly reduced flux attenuation at the shallow skimming angles near the horizon. This opens the possibility for an Earth-skimming ν_τ explanation for the ANITA-IV events (that occur extremely close to the horizon) while potentially significantly reducing the tension with limits set by Auger and IceCube for the ANITA-I and ANITA-III events [287].

The previous simulations of ANITA sensitivity to the tau air shower channel focused on diffuse fluxes and suffered from limitations in the accuracy of some of the models used in each simulation [259, 288]. For this reason, the ANITA collaboration used these tools to report upper bounds or estimates on sensitivity, as opposed to a full calculation.

In this chapter, we present the development of a completely new simulation toolchain, TAPIOCA, to more accurately estimate ANITA's sensitivity to diffuse and transient point source fluxes of UHE neutrinos. This simulation improves on almost all aspects of the previous "upper-bound" simulations while also acting as a completely independent cross-check of these earlier results. We use this simulation toolchain in the next chapter, Chapter 5, to investigate the near horizon events as potential tau neutrino detections, and again in Chapter 6 to search for potential associations between these events and astrophysical neutrino point sources. The work contained in these two chapters was originally published in Physical Review D, as the paper *"Analysis of a tau neutrino origin for the near-horizon air shower events observed by the fourth flight of the Antarctic Impulsive Transient Antenna"*, but has been expanded upon and revised for this dissertation.

4.1 ANITA-IV Anomalous Events

While ANITA was originally designed to detect the Askaryan emission from in-ice UHE neutrino interactions, ANITA is also sensitive to the geomagnetic radiation emitted by ultrahigh-energy cosmic ray (UHECR) induced extensive air showers (EAS) as they develop in the atmosphere. As an extensive air shower evolves in the presence of the Earth's magnetic field, charged particles in the shower are accelerated via the Lorentz force, creating a time-varying transverse current within the shower. This transverse current generates

an impulsive electric field whose polarization is transversely aligned with the orientation of the Earth's magnetic field. Over Antarctica, the Earth's magnetic field is primarily vertical, resulting in predominately horizontally-polarized emission from an EAS [291].

Typical air shower events observed by ANITA are classified into two categories: (1) *direct* UHECR events that reconstruct above the radio horizon (i.e. ANITA observes the emission directly from the shower at it develops in the atmosphere); and (2) *reflected* UHECR events where ANITA observes the radio emission from air showers after the radio emission *has reflected off the surface of Antarctica* (these must therefore reconstruct *below* the horizon).

Along with their reconstructed direction, events are also typically classified as direct or reflected by the polarity of the received electric field. For a unipolar waveform, the polarity is determined by the sign ($\pm$) of the impulse. For bipolar waveforms, the polarity is typically indicated by the order of the two primary poles (i.e. $+,-$ or $-,+$). Due to the Fresnel reflection coefficient at the air-ice boundary, reflected EAS signals have an inverted polarity with respect to the signals observed directly from an EAS without reflection [273]. *Polarity*, which is related to the *sign* of the electric field impulse, is distinct from *polarization*, which describes the *geometric orientation of the electric field* and is used to separate EAS events from in-ice Askaryan neutrino events. Over its four flights, ANITA has observed seven direct events and 64 reflected UHECR events [256, 273, 257].

ANITA-IV also observed four extensive air shower-like events that have the same polarity as the direct events (i.e. non-inverted $\implies$ non-reflected), but reconstruct below the horizon. These four events therefore appear to be upward-going air showers emerging from the surface of the Earth, but unlike the ANITA-I and ANITA-III anomalous events, the ANITA-IV events reconstruct near to, but below the horizon ($\lesssim 1^\circ$) [257]. As shown in Table 4.1, ANITA's angular uncertainty for these events is $\sim 0.2^\circ$, placing these events typically $\gtrsim 1\sigma$ to 4σ below the horizon.

The significance of finding 4 events with a polarity inconsistent with their geometry out of the 27 air shower events with a well-determined polarity is estimated to be greater than 3σ, when considering the possibilities that: the events could be an anthropogenic background; that there might be an error in the reconstructed arrival direction; and that the polarity might be misidentified [257]. The probability distribution of the true number of non-inverted EAS-like events from one of the two Monte Carlo simulations used to evaluate the above significance is shown in Table 4.2. The most probable number of

true signal events, under the above background possibilities, is *3* with total probability density of 0.7 (against the probability of observing 0, 1, 2, or 4 signal events mixed with anthropogenic or cosmic ray backgrounds).

4.1.1 Calculation of Event Significance

The calculation of the significance of observing these four events, reported in [257] as $(3.3 \pm 0.5)\sigma$, was first performed in [257], but was reproduced as part of this analysis. This calculation was performed using a toy Monte Carlo simulation that allowed these events to come from three possible sources of background: (1) an anthropogenic background event that leaked into our signal sample; (2) an above horizon cosmic ray that has been reconstructed to below the horizon; and (3), that this an inverted (reflected) cosmic ray whose polarity has been misidentified. The method of this simulation is presented below.

For each Monte Carlo trial, we:

1. Throw for a random chance that the event is actually an inverted event with a misidentified polarity. The chance of polarity flipping was studied during the initial ANITA-IV analysis by a careful study of our signal processing and deconvolution methods [257].

2. Throw for a chance that the event is actually from above the horizon, assuming a normal distribution of probabilities given the pointing uncertainty on each specific event.

3. Draw for a random chance that this event is one of our anthropogenic background events, using a Poisson-like distribution of the background leakage into the cosmic ray sample calculated by one of the ANITA-IV search analysts.

4. Combine these three background sources and calculate the number of these four near horizon events that survive as "non-background".

Repeating this process many times, storing the signal event count at each trial, results in the distribution shown in Figure 4.2.

While the significance of the observed anomalies do not clearly distinguish these events from possible backgrounds, in this study we consider the hypothesis that these events may

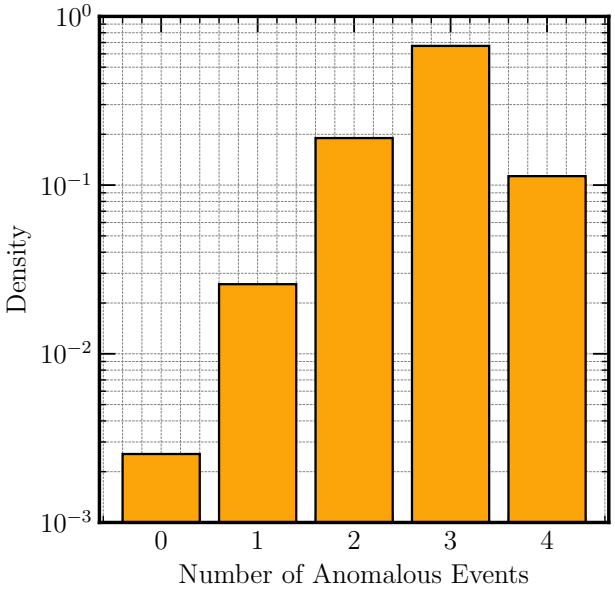

Figure 4.2: The probability density distribution (i.e. normalized event density) for the true number of near-horizon anomalous events observed by ANITA-IV under the assumptions of the toy Monte Carlo simulations described in [257]

Event	Time (ISO 8601)	$(\theta - \theta_H)$ (deg.)
4098827	2016-12-03T10:03:27Z	-0.25±0.21°
19848917	2016-12-08T11:44:54Z	-0.65±0.20°
50549772	2016-12-16T15:03:19Z	-0.81±0.20°
72164985	2016-12-22T06:28:14Z	-0.19±0.10°

Table 4.1: The time of each observed event along with the reconstructed elevation angle of the shower, θ, below the radio horizon, θ_H. All events are observed within 1° of the radio horizon and are all greater than 1σ from the horizon.

be due to a tau neutrino interaction inside the Earth that creates an exiting τ lepton and analyze these events under this hypothesis.

The observed event parameters for the ANITA-IV anomalous events, reported in [257], are shown in Table 4.1 where θ is the elevation angle of the observed radio-frequency direction and θ_H is the elevation angle of the radio horizon. To delineate each event in the remainder of this dissertation, without repeating the full event numbers, we will often refer to each event using its unique three number prefix followed by "xx", (i.e. 409xx, 198xx, 505xx, and 721xx).

4.2 Theory of Particle Telescopes

In this section, we present the theory of the sensitivity and acceptance of particle telescopes to both diffuse and point source fluxes of particles.

The number of events detected by a particle telescope can be as expressed as [292]:

$$N = \int_{t_0}^{t_0+T} dt \int_S d\vec{\sigma} \cdot \hat{r}_\omega \int_\Omega d\omega \int_0^\infty dE \, P_{\text{obs}}(E, \vec{\sigma}, \hat{r}_\omega, t) \, \mathcal{F}(E, \vec{\sigma}, \hat{r}_\omega, t) \tag{4.1}$$

N = the total number of particles detected by the telescope,
t = time,
t_0 = the starting observation time,
T = the total observation time,
S = a *reference* surface through which all particles *detectable* by this telescope must pass through,
$d\vec{\sigma}$ = a differential element of surface area on S,
$\hat{r}_\omega$ = a unit vector pointing in the direction of the normal to $d\omega$
Ω = the total domain of incident solid angle seen by the reference surface,
$d\omega$ = a different element of solid angle seen from the reference surface,
E = the energy of the incident particle,
P_{obs} = the probability of detecting a particle with the given parameters,
$\mathcal{F}$ = the spectral intensity of particles (eV^{-1} $\text{cm}^{-2}\text{sr}^{-1}$ s^{-1}),
$d\vec{\sigma} \cdot \hat{r}_\omega$ = the projected element of area looking along ω.

The energy spectrum of detected events is therefore

$$\frac{dN}{dE} = \int_{t_0}^{t_0+T} dt \int_S d\vec{\sigma} \cdot \hat{r}_\omega \int_\Omega d\omega \, P_{\text{obs}}(E, \vec{\sigma}, \hat{r}_\omega, t) \, \mathcal{F}(E, \vec{\sigma}, \hat{r}_\omega, t) \tag{4.2}$$

and the corresponding *rate of detected events* per unit energy as:

$$\frac{d^2N}{dEdt} = \int_S d\vec{\sigma} \cdot \hat{r}_\omega \int_\Omega d\omega \, P_{\text{obs}}(E, \vec{\sigma}, \hat{r}_\omega, t) \, \mathcal{F}(E, \vec{\sigma}, \hat{r}_\omega, t) \tag{4.3}$$

4.2.1 Diffuse & Isotropic Flux

For an *isotropic time-independent* particle flux, $\mathcal{F}(E)$, this is typically separated into two components: the *acceptance* (expressed in units of cm^2 sr) of the particle telescope and the *spectral intensity* of the flux:

$$\frac{d^2N}{dEdt} = \mathcal{F}(E) \underbrace{\int_S d\vec{\sigma}\cdot\hat{r}_\omega \int_\Omega d\omega\, P_{\text{obs}}(E,\vec{\sigma},\hat{r}_\omega,t)}_{\text{Acceptance}} = \mathcal{F}(E)\langle\mathcal{A}\Omega\rangle(E,\,t) \tag{4.4}$$

where $\langle\mathcal{A}\Omega\rangle(E,\,t)$ is the acceptance of the particle telescope. The first term in the acceptance is calculating the effective flux of particles through the reference surface, while the second captures the probability that these particles are *detected* by the telescope. By separating out the acceptance integral (which is often computationally expensive to calculate), we can easily evaluate the differential event rate efficiently for arbitrarily many $\mathcal{F}(E)$.

4.2.2 Point Source Flux

For a flux of particles that can be treated as a *point source* with respect to the particle telescope, we express the flux from a fixed sky direction, $\hat{r}_\star$, as

$$\mathcal{F}(t,E,\hat{r}_\star) = \int d\Omega\, \delta(\hat{r}-\hat{r}_\star)\, F(t,E,\hat{r}), \tag{4.5}$$

where $\delta(\hat{r}-\hat{r}_\star)$ is a Dirac δ-function on a spherical surface with units of inverse steradians. In this case, F has units of eV^{-1} cm^{-2} s^{-1} (note the missing *steradian* compared to $\mathcal{F}$. Many likely candidates for astrophysical point sources are also not expected to be time-*independent* so we explicitly include the time-dependence that was dropped in Equation 4.4. This results in a differential event rate of

$$\frac{d^2N}{dEdt} = \mathcal{F}(t,E_\nu,\hat{r}_\star) \underbrace{\int_S d\vec{\sigma}\cdot\hat{r}_\omega\;\; P_{\text{obs}}(E,\vec{\sigma},\hat{r}_\omega,t)}_{\text{Effective Area}} = F(t,E,\hat{r}_\star)\mathcal{A}(E,\,t,\hat{r}_\star) \tag{4.6}$$

where $\mathcal{A}(E,\ t, \hat{r}_\star)$ is known as the *effective area* of the particle telescope and has units of *area* (as opposed to area-steradians for the diffuse *acceptance*). Since the acceptance, $\langle \mathcal{A}\Omega \rangle$, can be calculated, a posteriori, by numerically integrating the effective area direction, $\hat{r}_\star$, over solid angle, it is common to directly evaluate, and *save*, the effective area (as opposed to bypassing the effective area and directly calculating the acceptance).

Given an astrophysical model for the incident particle flux, the total spectral rate of events can easily be calculated if the effective area, $\mathcal{A}(E, t, \hat{r}_\star)$, or acceptance, $\langle \mathcal{A}\Omega \rangle (E,\ t)$, is known (for point source and diffuse fluxes, respectively). Typically, the effective area of a particle telescope can only be analytically calculated for the simplest geometries and so requires numerical evaluation. Furthermore, due to the complexity and (almost always) stochastic nature of the sensitivity of most particle telescopes to *individual* particles, performing a direct numerical integration is computationally intractable, so the effective area is almost exclusively calculated using *Monte Carlo integration techniques*.

4.2.3 Monte Carlo Evaluation of the Effective Area

For Monte Carlo evaluation, we consider a *differential element* of the effective area integral:

$$d\mathcal{A} = dA\, \hat{n} \cdot \hat{r}_\omega\, P_{\text{obs}}(E, \hat{n}, \hat{r}_\star, t) \tag{4.7}$$

This can be easily evaluated with a standard Monte Carlo integration technique using the following algorithm:

1. Choose a random point on the *reference surface*, S. We take $\hat{n}$ as the unit-length normal vector to the surface at this point.

2. Choose a random particle direction, $\hat{r}_\omega$, from the range of solid angle that is detectable by the particle telescope. $\hat{r}_\omega$ must be sampled such that equal solid angle has equal probability.

3. Calculate the observation probability, P_{obs}, for this combination of $\hat{n}$ and $\hat{r}_\omega$. This typically requires simulating the detector response to the given input particle, and is almost always a stochastic function of the particle type and $\hat{n}$ and $\hat{r}_\omega$. Therefore, we typically approximate P_{obs} with a binary function such that the *average* over many Monte Carlo trials converges to the true value of P_{obs}.

4. Evaluate $\hat{n} \cdot \hat{r}_\omega \, P_{\text{obs}}$.

5. Repeat, sum the results, and divide by the total number of trials.

In this case, P_{obs} is calculated implicitly from the average over repeated Monte Carlo trials by checking for a trigger in step (3) during each trial. For the simple case where incident particle directions are chosen from the full 4π steradians over a surface with geometric area A, this Monte Carlo evaluation using M trials can be expressed as:

$$\mathcal{A}(E,t) \simeq \frac{4\pi A}{M} \sum_{i}^{M} \hat{r}_i \cdot \hat{n}_i \, P_{\text{obs}}(E_i, \hat{n}_i, \hat{r}_i, t) \tag{4.8}$$

For many particle telescopes, particles are only incident from one side of the reference surface, in which case trajectories are drawn only from 2π in solid angle. In this case, Equation (4.8) can be written as

$$\mathcal{A}(E,t) \simeq \frac{2\pi A}{M} \sum_{i}^{M} \hat{r}_i \cdot \hat{n}_i \, P_{\text{obs}}(E_i, \hat{n}_i, \hat{r}_i, t) \tag{4.9}$$

Lastly, for many experiments, the integral (in this case, the sum) over $r_i \cdot \hat{n}_i$ can be performed analytically, *before* the Monte Carlo evaluation. Ignoring this projection factor, incident particle trajectories must be sampled uniformly in solid angle i.e. $\propto \cos\theta$, where θ is a spherical coordinate system centered at the differential area element, $d\vec{\sigma}$, in question. Now, consider the integral over $d\sigma$ in Equation 4.6. The contribution of incident directions at the differential element is weighted by $\mathcal{F}(\omega)$, but also by the $\cos\theta$ factor from $d\vec{\sigma} \cdot \hat{r} = \cos\theta d\sigma$. The *weighted* distribution of particle trajectories, in spherical coordinates, therefore becomes

$$\cos\theta \mathcal{F}(\omega) d\cos\theta d\phi = \frac{1}{2}\mathcal{F}(\omega) d\cos^2\theta d\phi \tag{4.10}$$

Therefore, the distribution of trajectories sampled during the Monte Carlo evaluation can be improved: if $\mathcal{F}(\omega) \propto 1$, i.e. an isotropic flux, we choose random particle trajectories in $\cos^2\theta$; if $\mathcal{F}(\omega) \propto \cos^n\theta$, then choose random trajectories according to $\cos^{2+n}\theta$ [292].

This allows us to rewrite Equation 4.9 as

$$\mathcal{A}(E,t) \simeq \frac{\pi A}{M} \sum_{i}^{M} P_{\text{obs}}(E_i, \hat{n}_i, \hat{r}_i, t) \tag{4.11}$$

Where, unlike Equation 4.11, trajectories must be sampled uniformly in $\cos^2\theta$, unlike the traditional $\cos\theta$ for sampling uniformly in solid angle. This is an extremely simplified form of importance sampling where more trajectories are sampled that would have a higher *weight* in the Monte Carlo sum, $r_i \cdot \hat{n}_i$, allowing the simulation to more accurately capture the distribution (given the same number of samples). Where P_{obs} is complicated or expensive to evaluate (as is often the case), changing the sampling strategy in this way can significantly speed up evaluation of the integral.

4.2.4 Geometric Effective Area and Geometric Acceptance

To assist in understanding the different contributions to $\mathcal{A}$, the effective area (or acceptance) of a particle telescope is sometimes separated into a *geometric* component and an *efficiency*. The geometric component is calculated using a simple model for the efficiency, P_{obs}, such that:

$$D(\hat{r},\hat{n}) = \begin{cases} 0 & \text{, the particle is not detectable.} \\ 1 & \text{, the particle is } \textit{potentially} \text{ detectable.} \end{cases}$$

where the condition for *detectability* is chosen such that *all* events that *could* have a non-zero P_{obs} pass the *detectability* cut. The geometric acceptance is therefore the acceptance of a *perfect* particle detector from the *detector geometry*, alone.

For a full 4π sensitive particle telescope without the $\cos^2\theta$ importance sampling desribed in the previous section, the *geometric acceptance*, calculated using Monte Carlo integration, is

$$\mathcal{A}_g \simeq \frac{4\pi A}{M} \sum_{i}^{M} \hat{r}_i \cdot \hat{n}_i \, D(\hat{r}_i, \hat{n}_i) = \frac{4\pi A}{M} \sum_{i,\text{detectable}} \hat{r}_i \cdot \hat{n}_i = 2\pi A \tag{4.12}$$

Sometimes additional geometric cuts are made to the geometric acceptance in order to better approximate the *effective* area or acceptance. An example of this for ANITA is described later in this chapter.

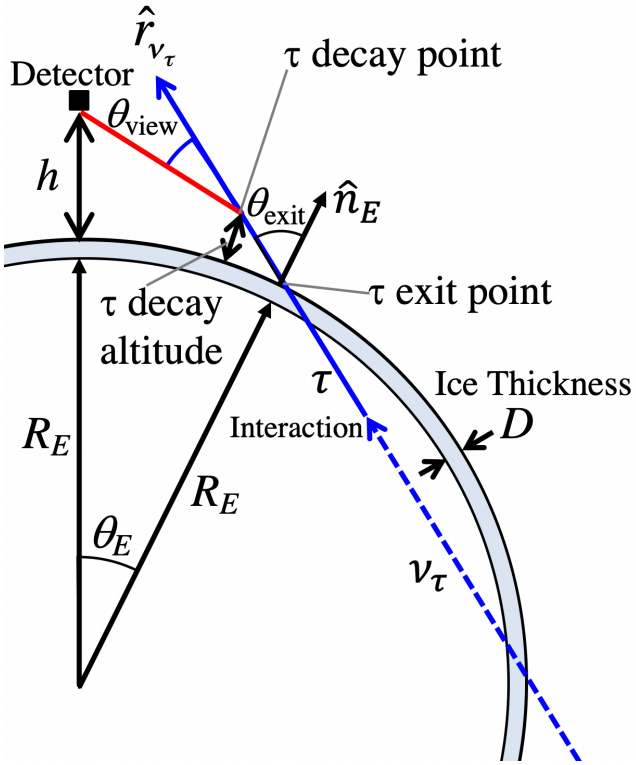

Figure 4.3: A diagram of the geometry and key variables needed to understand and evaluate ANITA's sensitivity to Earth-skimming ν_τ. Here "Detector" is the location of ANITA at some point during the flight. This is also the geometry assumed by NuTauSim for propagating and calculating the exit τ-lepton fluxes as a function of angle. Figure from [259, 288].

4.2.5 Effective Area Integral for ANITA-IV's Sensitivity to Tau Air Showers

For an accurate evaluation of $\mathcal{A}$ or $\langle \mathcal{A}\Omega \rangle$, an accurate detection simulation must be provided to calculate P_{obs} for each trial. The remainder of this chapter details the detection model used in evaluating the above Monte Carlo integral for ANITA's sensitivity to Earth-skimming nν_τ events. The geometry used for this detection channel was previously shown in Figure 2.14 but is repeated in Figure 4.3 for clarity and easier reference during the following discussion.

The behavior specific to the observatory is encoded in the function $P_{obs}(t, E_\nu, \vec{x}_E, \hat{r})$, which in this case, is the probability that a tau neutrino with energy E_ν coming from sky direction $\hat{r}$, whose axis of propagation intersects a point $\vec{x}_E$ on the surface of integration A (the surface of the Earth for ANITA), at time t is detected by ANITA. The dot product $\hat{r} \cdot \hat{x}_E$ accounts for the projected area element in the direction of $\hat{r}$ and $\Theta(\hat{r} \cdot \hat{x}_E)$ accounts for the fact that we only consider neutrinos propagation axes that exit the Earth in the observing regions of interest (i.e. no *down-going* Earth-skimming tau neutrinos).

A description of the function P_{obs} for ANITA was first derived for a diffuse flux in [259, 288] and is extended for neutrino point sources in Equation 4.13. The probability of observation is decomposed into a convolution of probabilities summarized as follows:

1. The probability, P_{exit}, that a ν_τ with original energy E_ν undergoes a sequence of interactions inside the Earth that results in a τ lepton leaving the Earth.

2. The probability, P_{decay}, that the τ lepton subsequently propagates in the atmosphere and decays before reaching ANITA [290].

3. The probability that the τ decay creates a shower with sufficient energy to be detectable by ANITA and that the decay point is far away enough from ANITA that the shower can fully develop before passing ANITA (during the calculation, this is folded into the next probability below).

4. The probability, P_{trig}, that the radio emission from this particular shower is sufficiently strong enough to trigger ANITA (and be detected) [293, 259, 288].

All of these factors are combined later in this dissertation (and in the corresponding simulation) to calculate ANITA's *effective area* to τ-induced extensive air showers (Equation 4.13) given a ν_τ of energy E_ν coming from direction $\hat{r}_\nu$ at time t with the τ exiting the earth at $\vec{x}_E$.

$$\begin{aligned} P_{obs}(t, E_\nu, \hat{r}, \vec{x}_E) = & \int dE_\tau \; P_{exit}(E_\tau \mid E_\nu, \theta_{em}) \\ & \int ds_{decay} \; P_{decay}(s_{decay} \mid E_\tau) \\ & \int dE_{EAS} \; P_{EAS}(E_{EAS} \mid E_\tau) \\ & \int d\mathcal{E} \; P_{\mathcal{E}}(\mathcal{E} \mid E_{EAS}, s_{decay}, \hat{r}_\nu,) \\ & \quad P_{trig}(\vec{x}_{\text{ANITA}} \mid \mathcal{E}, s_{decay}, \hat{r}_\nu) \end{aligned} \tag{4.13}$$

where:

E_τ = the energy of the exiting τ,
θ_{em} = the emergence angle of τ at the surface,
s_{decay} = the decay length of the τ,
E_{EAS} = the energy of the extensive air shower,
$\mathcal{E}$ = the electric field at the payload,
$\vec{x}_{\text{ANITA}}$ = the location of ANITA,
$\hat{r}_\nu$ = the incident direction of the neutrino and τ,

Due to the stochastic nature of many of these variables, we use a Monte Carlo approach to evaluating these various probabilities. In the following sections, we present the various models that are used to evaluate the various contributions to these integrals. Some of the terms in Equation 4.13 are computationally efficient and are evaluated on every trial (i.e. sampling the τ lepton decay range), while others are computationally expensive and would be intractable to (re)calculate for every Monte Carlo trial: for those, such as the calculation of the electric field from a given tau-decay, we pre-calculate values for the function over a fixed parameter space and develop parameterizations or lookup-tables of these terms that can then be used in the full Monte Carlo calculation.

4.3 Simulation Models

Some of the the models used to evaluate ANITA's acceptance to tau neutrinos via the extensive air shower channel were first developed in [259, 290] while others were first developed in this work. All of the models developed in [259, 290] have been redeveloped and rewritten as part of this work, in order to improve either their accuracy or computational efficiency, and to act as an *independent* cross-check of the earlier "upper-bound" results from [259, 290]. In the following sections, we present the various models used in this simulation, with a focus on the new developments that have been made since the earlier estimates.

4.3.1 Tau Lepton Exit Probability

The exit probability, $P_{\text{exit}}(E_{\nu_\tau}, E_\tau)$, defined as the probability that an incident tau neutrino with energy E_{ν_τ} undergoes a series of tau regeneration interactions that results in a τ-lepton with energy E_τ leaving the surface of the Earth on the *other* side. This is often

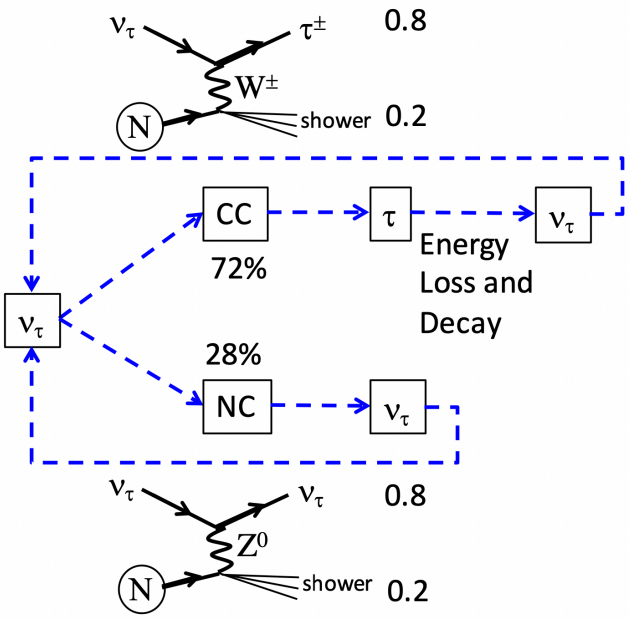

Figure 4.4: A diagram of the event loop and core logic of the NuTauSim code for propagating ultrahigh energy tau neutrinos through the Earth. The numbers represent the average values for the particular distributions used in each stage. Figure from [259, 288].

presented as the marginal distribution, $P_{\text{exit}}(E_{\nu_\tau})$, which has been integrated over the exit probability of the tau lepton, E_τ, above some typical threshold.

There are a variety of public Monte Carlo codes available to calculate $P_{\text{exit}}(E_{\nu_\tau}, E_\tau)$ including NuTauSim [250], NuPyProp [294], NuPropEarth [207], PROPOSAL [295], and others. In this work, we use the NuTauSim package, that this author has contributed to, as it captures the key behaviour of $P_{\text{exit}}(E_{\nu_\tau}, E_\tau)$ at the energies and angles relevant to ANITA, while being significantly faster than other available tools so that it is possible to generate sufficient Monte Carlo statistics at a range of energies (for reference, as of the time of writing, NuTauSim is approximately two *orders of magnitude* faster than NuPyProp).

We configured NuTauSim with the standard ("middle") UHE neutrino-nucleon cross section parametrization from [88] and the ALLM energy loss model [296] for the τ lepton (which are the defaults for this particular propagation code).

To evaluate the probability that a τ-lepton leaves the Earth and decays in the atmosphere, as well as the distribution of τ-lepton energies, for a given exit angle, θ, and neutrino energy, E_ν, the top-level flow of the simulation flow of NuTauSim is shown in Figure 4.4.

1. Throw for a (random) neutrino neutral current interaction length and charge current interaction length.

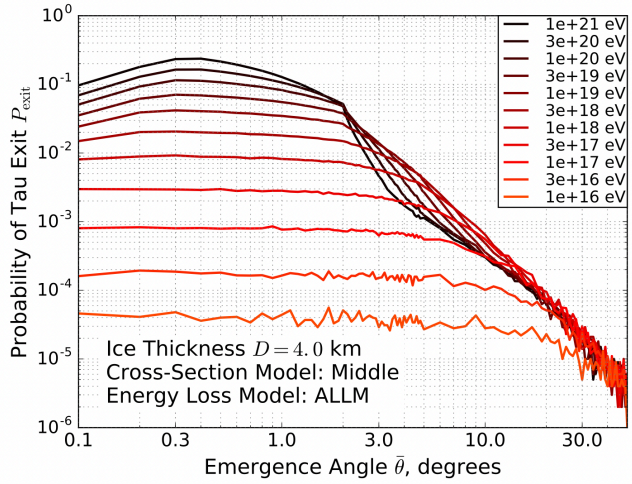

Figure 4.5: The probability for a τ-lepton to leave the Earth from an incident flux of ν_τ for various emergence angles given a 4 km thick ice layer with standard cross sections and energy loss models. Figure from [259, 288].

2. Propagate the ν_τ through the Preliminary Earth Reference Model (PREM [297] Earth density model until the neutrino interacts via a neutral current or charged current interaction.

3. Each interaction type is then handled separately:

   - If the interaction was a neutral current interaction, sample the CTEQ-5 inelasticity distribution [298] to calculate the energy of the outgoing ν_τ and repeat this procedure starting from 1.
   - If the interaction was a charged current interaction, sample the energy of the outgoing τ-lepton using the CTEQ-5 inelasticity distributions and move to 4.

4. Throw for a (random) τ-lepton decay time and continue propagation. At each propagation step, calculate the τ-lepton energy loss using the chosen continuous parameterization (in our case, ALLM).

5. If the τ-lepton leaves the Earth, save the τ energy and finish.

6. Otherwise, at the τ-lepton decay point, use distributions of τ-lepton decay produces produced using TAUOLA [299] to calculate the energy of the outgoing ν_τ. Restart this procedure from 1. with this new ν_τ.

A figure showing the tau exit probability at a variety of neutrino energies and emergence angles at the surface is shown in Figure 4.5. In the best case, the incident neutrino

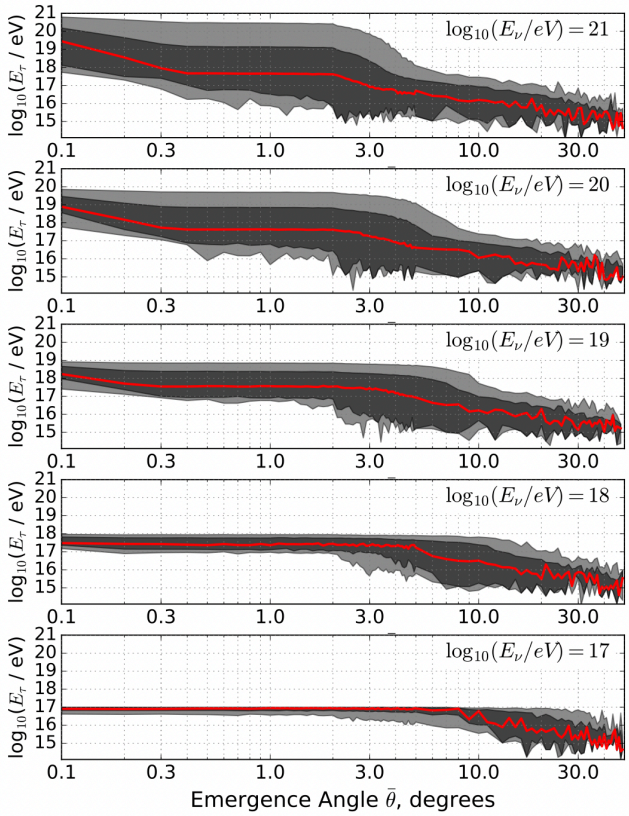

Figure 4.6: The average τ-lepton energy upon leaving the Earth (red), along with the 68% (95%) variation in light grey (dark grey) calculated with NuTauSim. Figure from [259, 288].

flux is reduced by a factor of 5x, but the typical reduction for the energies relevant to ANITA is closer to 50x.

Given a fixed incident neutrino energy, there is significant variation in the energy of the exiting τ-lepton; this is shown in Figure 4.6. As we will see in Chapter 5, this variation is directly convolved into the neutrino energy resolution of ANITA. Furthermore, as the emergence angle increases, the corresponding chord length through the Earth increases; this also increases the *average* number of regeneration interactions that a ν_τ-τ pair must undergo in order to successfully make it to the other side of the Earth. This causes the variation in τ-lepton energy to increase significantly as the emergence angle (i.e. steepness) increases.

Despite being orders of magnitude faster than similar public codes, NuTauSim is still not fast enough in order to be used directly for every tapioca simulation trial. Therefore, for a discrete number of incident neutrino energies, we propagate $\mathcal{O}$(500 M) incident neutrinos using NuTauSim to generate large lookup tables containing $\mathcal{O}$(100,000-1M) detectable τ-leptons per energy bin, while simultaneously calculating the marginal

distribution, $P_{\text{exit}}(E_{\nu_\tau})$. The distributions of exit probability and exit energy calculated from each of these large simulations are then sampled directly in TAPIOCA to produce an exit probability and τ energy for each Monte Carlo trial.

4.3.2 Tau Lepton Decays

In the ANITA tau neutrino acceptance bounds of [259, 288], a single τ decay was used ($\tau^- \rightarrow \pi^-\pi_0\nu_\tau$) with 99% of the energy of the τ assumed to be distributed across the showering particles (π^+ and π_0) to seed the air shower, with no stochastic variation in the neutrino energy to shower energy conversion.

Furthermore, for the prior analysis, a right-handed polarized (positive helicity) τ-lepton was used in the calculation of P_{exit} and in the decay simulations. Reference [288] identified that τ-leptons from astrophysical tau neutrinos are expected to have a left-handed polarization (negative helicity). For this work, we regenerated the NuTauSim distributions using the correct (negative helicity) polarization decay tables, in accordance with the strong theoretical motivation of [288]. After correcting the helicity, the distribution of energy among the τ-decay components, and the branching fraction among the second-order decay channels, was modified on the order of 10% [288]. In addition, to capture the stochastic variation in the fraction of τ's energy that goes into showering particles, and capture the rare electromagnetic τ-decays, we generated a large sample of τ^- decays with negative helicity using PYTHIA 8.244 [300]. For each sample, we estimated the total fraction of initial energy that goes into the EAS by excluding neutrinos and muons from the secondary particles; this is known as the "shower energy". The resulting fraction of the original τ energy transferred to the air shower is shown in Figure 4.7; on average, 40% of the tau's energy is transferred into showering particles. These stochastic shower energy distributions are individually sampled in TAPIOCA for *each* Monte Carlo trial.

We also store the average energy of the particles in the most common tau decay mode, ($\tau^- \rightarrow \pi^-\pi_0\nu_\tau$), so that we can use this later to capture the average electric field from a typical induced shower (however, as described later, the electric field is naturally scaled to the shower energy of a specific PYTHIA trial when used in the Monte Carlo).

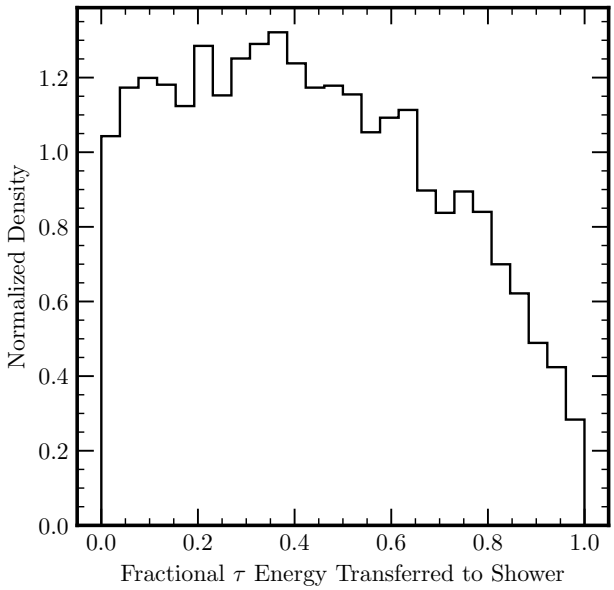

Figure 4.7: The relative fraction of the tau energy transferred to the shower in decays of ultrahigh-energy negative helicity τ-leptons simulated using PYTHIA 8.244 [300, 259, 288].

Air Shower Electric Field Model

One of the most significant improvements of this new simulation over previous ANITA ν_τ analyses has been a completely reworked electric field model for the geomagnetic emission from the τ-decay-induced extensive air showers.

The electric field of the τ decay cannot be simulated with standard ZHAireS [293] due to the unique geometry of the up-going τ channel and since standard ZHAireS can, by default, only simulate a single primary particle (and the decay of the τ typically produces multiple showering particles). A patch to the standard ZHAireS code was produced by the ANITA collaboration to calculate the associated electric field in this geometry [259].

However, since ZHAireS cannot simulate τ-lepton decays directly, we use TAUOLA [299] to calculate the decay products of a given τ-lepton decay. These products are then injected into the simulation using a *"special particle stack"*. The electric field calculation and shower simulation can then proceed as normal with no change to the radio emission code (once the above patch has been applied to convert ZHAireS to support the upgoing geometry).

Due to the *extremely-high* computation requirements for simulating the electric field (a single Earth-skimming shower at $\mathcal{O}(100\,\mathrm{PeV})$ with a few tens of radio antennas takes between one and three *weeks* to evaluate on modern processors), it infeasible to directly simulate every Monte Carlo trial with ZHAireS. Therefore, we use ZHAireS to produce

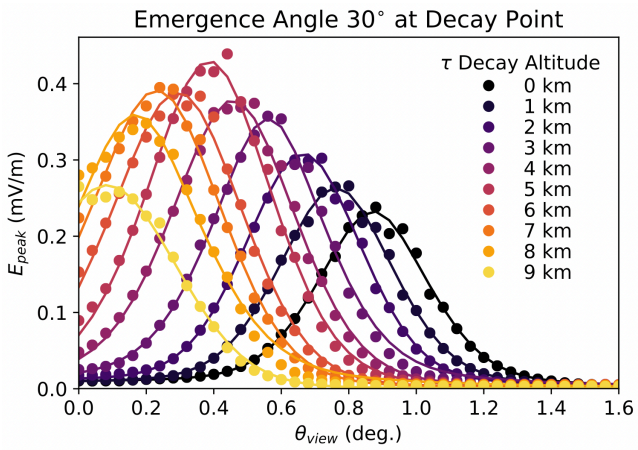

Figure 4.8: The variation in the peak electric field strength for a steeply inclined τ-lepton induced shower at various different τ decay altitudes as a function of off-axis angle (calculated using ZHAireS). The dots indicate the location of a ZHAireS simulation "field point" while the curves interpolate between the various simulation samples. Figure from [259].

a large lookup table (LUT) that is then interpolated to generate the electric field spectra of each trial.

The previous ANITA-I & ANITA-III ν_τ analyses used a simplified version of this electric field model that only stored the *peak* value of the electric field, as opposed to the full electric field waveform or spectrum [293] simulations. These were run at a range of decay altitude ($0-9$ km in 1 km steps), emergence angles ($1^\circ - 35^\circ$), and off-axis view angles, ψ ($0^\circ - 3^\circ$) completely covering the amplitude range expected to be detectable by ANITA. The variation of the peak electric field with off-axis angle and decay altitude used in this work is shown in Figure 4.8.

For this new work, this model was significantly improved by storing the complete time-domain electric field waveform instead of just storing the peak value of the electric field. This new ZHAIRES shower library was then used to produce a pair of 4D lookup-table (LUT) of electric field from the tau decay shower in terms of $(h_{decay}, \theta_{em}, \psi, f)$ or $(h_{decay}, \theta_{em}, \psi, t)$ where θ_{em} is the emergence angle of the τ at the exit location on the surface, f is the frequency, t is time, ψ is the off-axis angle of the observation direction, and h_{decay} is the altitude of the decay point. (see Figure 4.9 and Figure 4.10 for several slices of these simulations). The range of parameters for the lookup table were chosen to cover the entire parameter space that is expected to contribute to ANITA's effective area. The spacings of the sample points in the ψ, h_{decay}, and θ_{em} spaces were chosen such that quad-linear interpolation accurately captured the behavior of the function with relatively high accuracy. This field was then used as the primary input to the antenna and detector model with appropriate scaling to account for the specific shower energy and

decay-payload distance that was being simulated. We did implement several analytical scalings and parameterizations that extend the coverage of this lookup-table outside the range of our simulations, but these were rarely used in any of the simulations in this work.

All showers in the library were simulated with a shower energy of 100 PeV (distributed across the showering particles in the same ratio as predicted by the PYTHIA and TAUOLA simulations discussed in the previous section). The electric field amplitude for extensive air showers scale very close to linearly with shower energy across the energy and altitude range of interest [273, 293], and as such, the electric field for any particular shower energy can be accurately calculated by scaling the electric field of our 100 PeV simulations by $(E_{\text{shower}}/100\,\text{PeV})$.

For every Monte Carlo trial, we wish to evaluate the electric field from the tau decay at the location of ANITA. h_{decay}, θ_z, ψ, and E_{shower} are known a priori based upon the geometric properties of the specific Monte Carlo trial. These parameters are then used to perform a 4D quad-linear interpolation into the lookup-table to estimate the electric field at the payload.

4.3.3 Detector Model

The previous diffuse ν_τ analysis used a simple detector model that only used the *peak* electric field at the payload (with no detector model) and therefore only attempted to estimate or *bound* ANITA's ν_τ acceptance [259]. The most recent analysis used a frequency domain detector model with the following limitations [290]:

1. The beam width of ANITA's quad-ridge antennas was ignored and it was assumed that the antennas were uniformly sensitive across a wide range of ANITA's field of view.

2. The gain of ANITA's antennas was approximated as a constant 10 dBi; this is an overestimate compared to the actual gain of the antennas used in ANITA-IV, which is rising over much of ANITA's frequency band and only reaches 10 dBi towards the higher frequency portion of ANITA's band. Unfortunately, the discrepancy between this "constant-gain" model and the measured antenna gain is most significant where the electric field from extensive air showers (that peaks around 200 Mhz to 300 MHz) is largest.

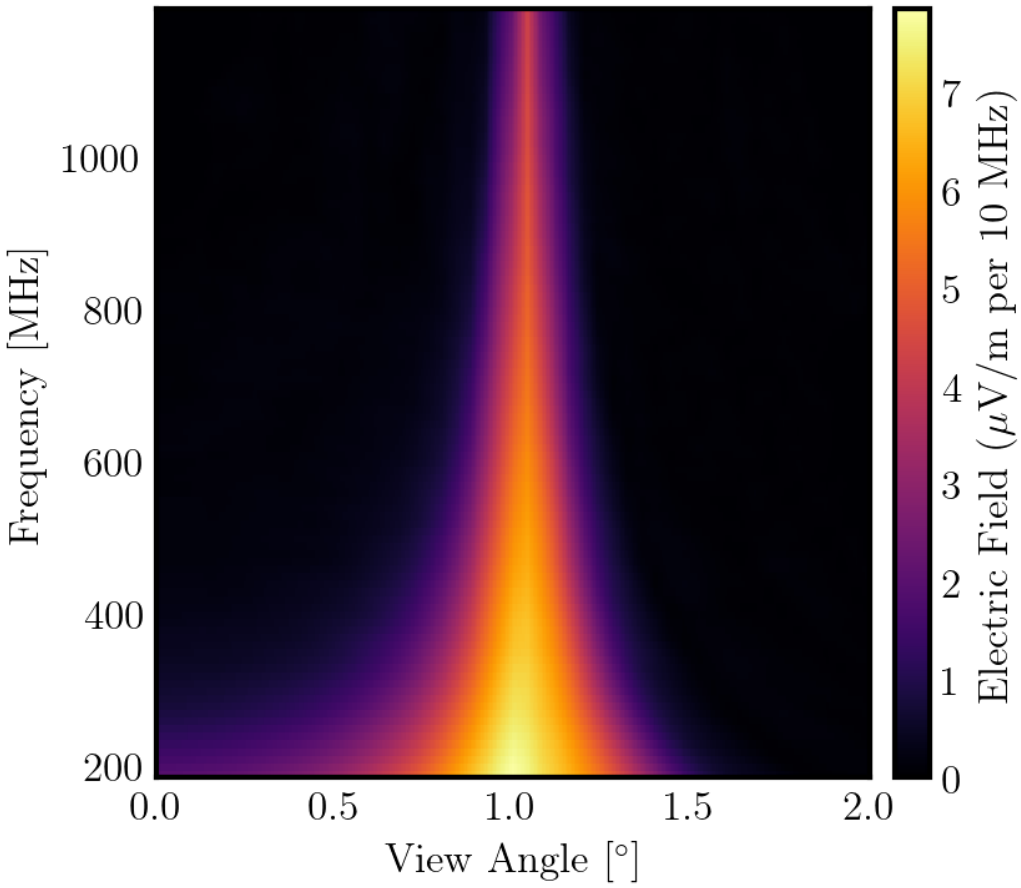

Figure 4.9: The electric field strength as a function of frequency and view angle with respect to the shower axis for a specific *slice* through the 4-D lookup table used to evaluate the electric field ($\theta_{\text{em}} = 5°$, $h_{\text{decay}} = 2$ km).

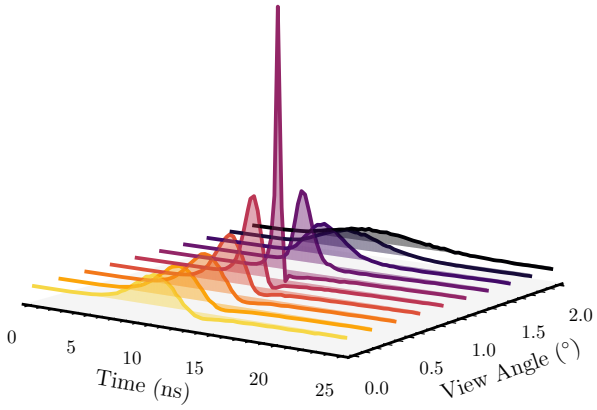

Figure 4.10: ZHAireS-simulated electric field waveforms for various view angles for a specific *slice* through the 4-D lookup table used to evaluate the electric field ($\theta_{\text{em}} = 5^\circ$, $h_{\text{decay}} = 2$ km).

3. An analytical estimate of the antenna temperature was performed that only accounted for thermal noise sources (the ice and sky); this is an underestimate compared to actual flight data that can contain significant anthropogenic contamination. This analytical antenna temperature estimate also ignored the Fresnel improvements discussed in Section 3.2.1.

4. As discussed in Section 3.2.2, ANITA-IV flew programmable notch filters whose center frequencies were changed throughout the flight. The earlier analyses did not include models for the TUFF responses and were therefore only able to simulate ANITA-I and ANITA-III. The TUFFs caused significant issues with the ANITA-IV analysis, and negatively impacted ANITA-IV's cosmic ray acceptance (as the 260 MHz and ∼375 MHz notches were located in a region with significant electric field spectral power from cosmic ray air showers).

For this work, we have developed a completely new *time-domain* detector model based on a recent (re)measurement of the impulse responses of all 96 channels in ANITA-IV [257]. This new detector model improves on all four of the aspects that limited the accuracy of previous simulations. In addition, this new *time-domain* detector model directly uses these post-flight calibration measurements, as well as a flight-data driven noise model, to more accurately simulate the response of ANITA-IV and, as such, is

expected to have significantly higher fidelity than the assumptions made in the simple model of [259].

ANITA-IV Impulse Response Measurements

During the ANITA-IV EAS and neutrino analysis presented in [257], a detailed calibration campaign was performed to measure the total time-domain transfer function (impulse response) of every channel and configuration of the ANITA-IV payload, in which the author of this dissertation was significantly involved, as well as two exceptional undergraduate students. ANITA-IV had 96 channels (48 antennas each with two polarizations per antenna) however, the TUFF notch filters were reconfigured several times during the flight to combat specific radio-frequency interference and therefore empart a flight-time dependence on the transfer function. These notch filters significantly change the amplitude and phase response of each individual channel; 6 different filter configurations were used throughout the flight for a total of $\sim$600 independent impulse responses that needed to be measured.

Each of these $\sim$600 independent impulse responses were measured in the University of Hawai'i anechoic chamber. A photo of one of the antennas used in this measurement is shown in Figure 4.11 inside the anechoic test chamber.

A high-quality "picosecond pulse generator" was connected to the input of a custom UH-designed and built transverse electromagnetic (TEM) horn antenna designed to have an impulsive high-quality wide-bandwidth impulse response. This antenna was placed at one end of the anechoic chamber, facing an ANITA-IV flight antenna recovered from the payload. This antenna was connected to the ANITA-IV payload (also inside the anechoic chamber, but hidden by radio-frequency absorbing pyramids) with an ANITA SFX-500 flight cable, also recovered from Antarctica. The waveforms were recovered using the ANITA data-acquisition system (DAQ) and processed using the standard ANITA flight data software.

The waveform that was measured by the payload was the convolution of the pulse shape of the "picosecond pulser", convolved with the impulse response of the test TEM horn, and convolved with ANITA's impulse response. To back out the contribution of the pulse generator and the test TEM horn, we built an identical TEM horn and performed separate measurement of the response of a TEM-to-TEM horn. This measurement allowed us to *deconvolve* the contribution of the pulse generator and the TEM horn out of the measured ANITA data and generate an estimate of the impulse response of *that*

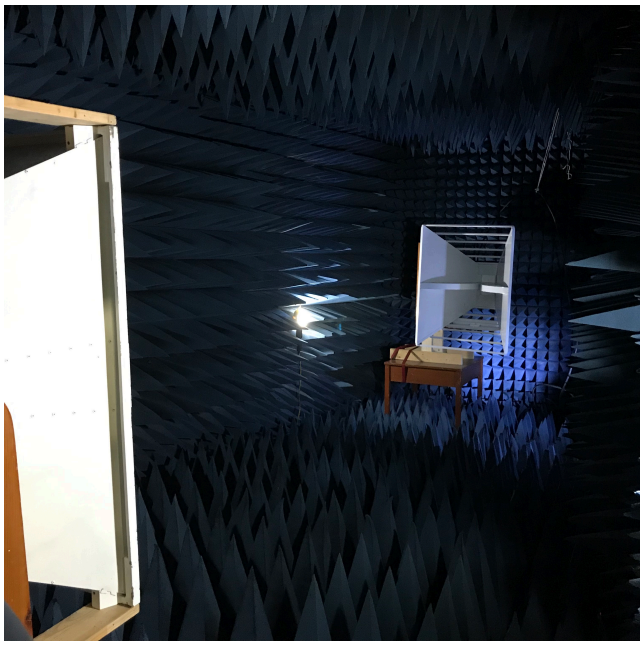

Figure 4.11: An image showing an ANITA flight antenna (left edge of the image) across from a dual-ridged Electrometrics 2 GHz test horn antenna used in early stages of the impulse response (re)measurement of ANITA-IV.

channel in *that* filter configuration. This process was repeated ∼600 times to individual capture the response of every channel and configuration on the payload.

The payload-wide average of these responses for each configuration is shown in Figure 4.12. These measurements provide the total time-domain transfer function of each channel (including antennas, front-end LNAs, bandpass filters, notch filters, and second-stage signal chain). Since the transfer-function, $\bar{h}(t)$, is a complete representation of the ANITA signal chain from the antenna to the digitizer, the incident electric field can be immediately converted into a voltage via

$$V(t) = \bar{h}(t) * \mathcal{E}(t) \tag{4.14}$$

where:

$V(t)$ = the time-domain voltage measured by ANITA (in V),
$\bar{h}(t)$ = the time-domain transfer function (in m/ns),
$\mathcal{E}(t)$ = the time-domain incident electric field (in V/m),
$*$ = represents linear convolution,

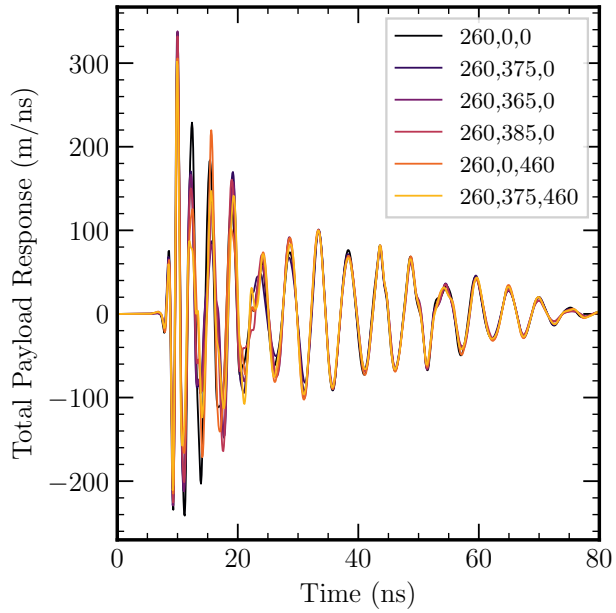

Figure 4.12: The *average* time-domain full signal chain transfer function for each notch filter configuration used in the ANITA-IV flight. The legend indicates the frequencies (in MHz) that each of the three filter notches were programmed to for each configuration.

Simulating the Observed Waveform from a τ Decay

To calculate the observed waveform for a given channel, we convolve the time-domain electric field from the 4D ZHAireS interpolation (described in section 4.3.2) with the specific time-domain response for that channel.

We replace the analytic noise generation model used in the previous ANITA ν_τ analysis with a model derived from actual GPS-triggered noise waveforms recorded during the ANITA-IV flight. We extracted a large sample of *"minimum-bias"* events from each of the ∼300 runs in the ANITA-IV flight dataset.

Since the bin-by-bin amplitude of random phasor noise in the frequency domain is expected to follow a Rayleigh distribution (since there is no signal present; in the presence of signal, we would expect a Rician distribution), we fit a Rayleigh probability density function to each 5 MHz bin in the distribution of amplitude spectral densities using a maximum-likelihood estimator (see [264] for more details on this process). The amplitude spectral density of background noise evolved significantly throughout the flight (Figure 4.13, and also shown in Figure 3.9), so this fitting process is done on a run-by-run basis.

Given a simulated extensive air shower signal waveform calculated using Equation 4.14 and a random noise waveform sampled from the inverse-Fourier transform Rayleigh dis-

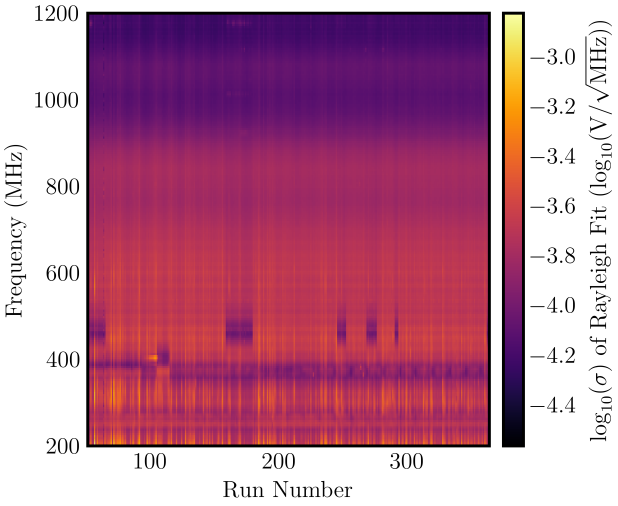

Figure 4.13: The average per-channel integrated noise power for each run of the ANITA-IV flight shown as the logarithm of the scale parameter, σ, of a Rayleigh distribution fit to the distribution of noise samples in a given frequency bin over a given run. The changing center frequency of the notch filters is clearly evident as changes in the location of the "horizontal" stripes in this figure.

tributions, the signal-to-noise ratio (SNR) of the combined waveform, $V(t) = V_s(t) + V_n(t)$, used in our trigger calculation, is calculated with Equation 4.15.

$$\begin{aligned} \text{SNR} &= \frac{\max V(t) - \min V(t)}{2\sigma} \\ &= \frac{\max V(t) - \min V(t)}{2\sqrt{\sum_t V_n(t)^2}} \end{aligned} \tag{4.15}$$

where:

SNR = signal-to-noise ratio,
$V(t)$ = the time-domain signal voltage,
σ = the standard deviation of the noise waveform,
$V_n(t)$ = the simulated noise waveform

4.3.4 Trigger Model

Due to the complexities of modeling ANITA-IV's multi-stage trigger logic, we use a simpler trigger system fitted to observed ANITA-IV data. Given the observed signal-to-noise ratio (SNR) of a particular simulated event, drawn from Rician statistics, we model ANITA's trigger using a Heaviside step-function where $P_{\text{trig}} = 100\%$ for any trial with SNR $>$ SNR$_{\text{trig}}$ and $P_{\text{trig}} = 0\%$ otherwise. The threshold signal-to-noise ratio, SNR$_{\text{trig}}$,

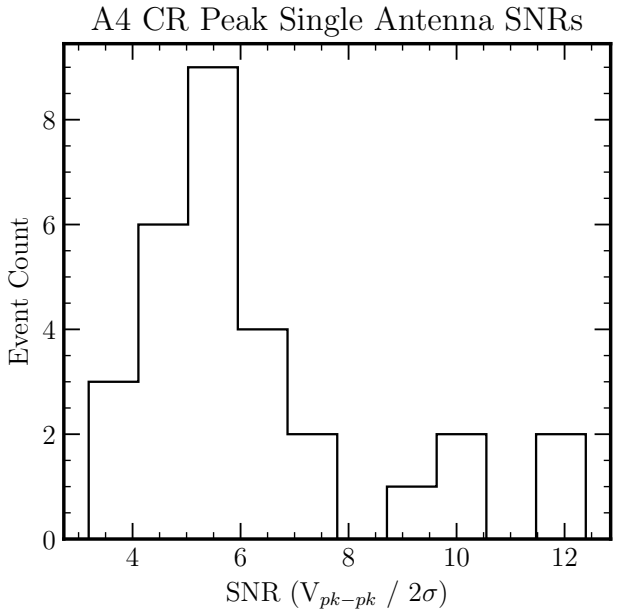

Figure 4.14: The peak single-antenna signal-to-noise ratio (SNR) for each of the 28 cosmic ray observed by ANITA-IV. σ is the RMS of thermal noise measured in the corresponding channel

is chosen as the minimum value of the distribution of "single-antenna" SNRs of the total population of extensive air shower observed by ANITA-IV during post-flight analysis (Figure 4.14). ANITA performs pulse-phase beamforming on the impulsive waveforms from the collection of antennas that observed each event so the final "post-beamforming" is significantly higher than shown in Figure 4.14. An additional advantage of deriving our trigger threshold from the post-flight analysis event list, is that the threshold atomatically emulates both the hardware trigger, as well as the analysis efficiency and any cuts employed by the ANITA-IV cosmic ray search analysts in order to isolate these UHECR signal events from background.

4.4 ANITA's Sensitivity to ν_τ Fluxes

This formalism is derived from the general formalism presented in Section 4.2.1 and Section 4.2.2, but is specialized to the detection of tau neutrinos with ANITA.

4.4.1 Acceptance to a Diffuse and Isotropic Flux

We model a diffuse, isotropic flux as independent of direction and time so that we may write $F(t, E_\nu, \hat{r}) \simeq F(E_\nu)$. Equation (4.4) then becomes

$$\frac{d^4 N_{obs}}{dt\, dE_\nu\, dA\, d\Omega} = (\hat{r}_\star \cdot \hat{x}_E)\, \Theta(\hat{r}_\star \cdot \hat{x}_E) \\ F(E_\nu)\, P_{obs}(t, E_\nu, \hat{r}_\star, \vec{x}), \tag{4.16}$$

where $\hat{r}_\star$ is a fixed direction on the sky. Since a diffuse isotropic flux, $F(E_\nu)$, does not explicitly depend on the differential area of integration dA or projected differential solid angle $d\Omega$, we may write

$$\frac{d^2 N_{obs}}{dt\, dE_\nu} = F(E_\nu)\, \langle A\Omega \rangle(t, E_\nu), \tag{4.17}$$

where the acceptance $A\Omega(t, E_\nu)$, averaged over the sky, is given by

$$\langle A\Omega \rangle(t, E_\nu) = \int_\Omega d\Omega \\ \int_A dA\, \hat{r}_\star \cdot \hat{x}_E\, \Theta(\hat{r} \cdot \hat{x}_E)\ P_{obs}(t, E_\nu, \hat{r}_\star, \vec{x}), \tag{4.18}$$

We note that while the flux is independent of time, ANITA's acceptance, $\langle A\Omega \rangle(t)$, still has an explicit time dependence due to variations in dA and P_{obs} throughout the $\sim$ 30-day ANITA flight (for example, as the payload filter configurations change, the altitude of the payload changes, and the noise environment increases near sources of increased anthropogenic activity).

4.4.2 Point Source Effective Area

We model a point source flux in a fixed sky direction $\hat{r}_\star$ as

$$S(t, E_\nu, \hat{r}_\star) = \int d\Omega\, \delta(\hat{r} - \hat{r}_\star)\, F(t, E_\nu, \hat{r}), \tag{4.19}$$

where $\delta(\hat{r} - \hat{r}_\star)$ is a Dirac δ-function on a spherical surface with units of inverse steradians. Unlike a diffuse and isotropic flux, point source flux is in units of number per unit

time per unit energy per unit area. Applying the integration over solid angle in Equation 4.6, the event rate for the point source is given by

$$\frac{d^3N_{obs}}{dt\,dE_\nu\,dA} = (\hat{r}_\star \cdot \hat{x}_E)\,\Theta(\hat{r}_\star \cdot \hat{x}_E) \\ S(t, E_\nu, \hat{r}_\star)\,P_{obs}(t, E_\nu, \hat{r}_\star, \vec{x}). \tag{4.20}$$

Since the point source flux, $S(t, E_\nu, \hat{r}_\star)$, itself also does not explicitly depend on the differential area of integration dA used for estimating the event rate, we may write

$$\frac{d^2N_{obs}}{dt\,dE_\nu} = S(t, E_\nu, \hat{r}_\star)\langle A\rangle(t, E_\nu, \hat{r}_\star), \tag{4.21}$$

where the point source effective area $\mathcal{A}(t, E_\nu, \hat{r}_\star)$ is given by

$$\mathcal{A}(t, E_\nu, \hat{r}_\star) = \int_{A_g} dA_g\,(\hat{r}_\star \cdot \hat{x}_E)\,\Theta(\hat{r}_\star \cdot \hat{x}_E) \\ P_{obs}(t, E_\nu, \hat{r}_\star, \vec{x}), \tag{4.22}$$

where A_g is the geometric area on the surface of the Earth that we integrate over (yellow spherical patch in Figure 4.15). For ANITA's ν_τ effective area, we define A_g as the ellipsoidal area on the surface from which the off-axis view angle at the surface, $\theta_{\text{view,exit}}$, is less than some predefined θ_{max}. In most cases, $\theta_{\text{max}} \sim 1 - 2^\circ$ (Figure 4.15).

TAPIOCA

To simulate ANITA's sensitivity to both diffuse and point sources of τ neutrinos using the formalism in Section 4.4.2, we have developed a new ν_τ simulation code, the **Ta**u **P**o**i**nt **S**o**u**rce **Ca**lculator, or TAPIOCA. TAPIOCA is publicly available and released under an open-source copy-left license.

In particular, TAPIOCA performs a Monte Carlo evaluation of the integrals shown in Equations 4.18 and 4.22 using the various simulation models described in the previous section. A flow chart showing the top-level logic of the TAPIOCA code, as well as the required inputs and data sources, is shown in Figure 4.16 and described in the remainder of this chapter. In addition to the simulation capabilities, TAPIOCA also integrates with the EMCEE Markov Chain Monte Carlo (MCMC) Bayesian inference engine to allow for reconstructing the full posterior distribution of neutrino parameters consistent with our observed events; this aspect of TAPIOCA will be discussed in Chapter 5.

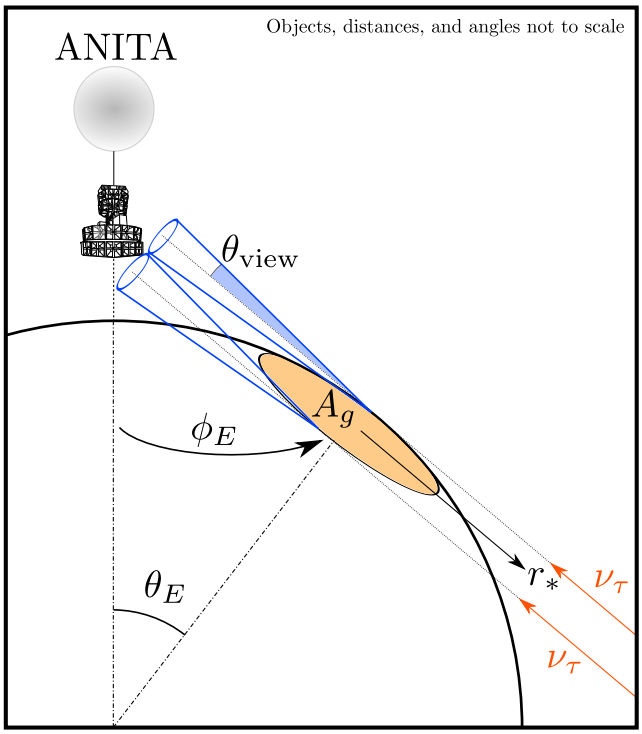

Figure 4.15: A diagram showing how this analysis defines the geometric area as the area on the surface of the Earth which ANITA observes with a view angle from the surface of less than $\theta_{\text{view,max}}$.

By default, TAPIOCA calculates the *effective area* as a function of elevation angle, azimuth angle, energy, and time. This can later be quickly converted to an acceptance for a diffuse and isotropic flux by integrating over time and solid angle as discussed in Section 4.2.3

Given the location of the payload (ϕ, λ, h, t), where ϕ, λ are latitude and longitude, h is the altitude above the reference Earth ellipsoid, and t is the observation, and the coordinates of a neutrino source (α, δ), we calculate the *geometric* area of *neutrino exit locations* that is potentially detectable by ANITA. This is done by setting a cut on the maximum

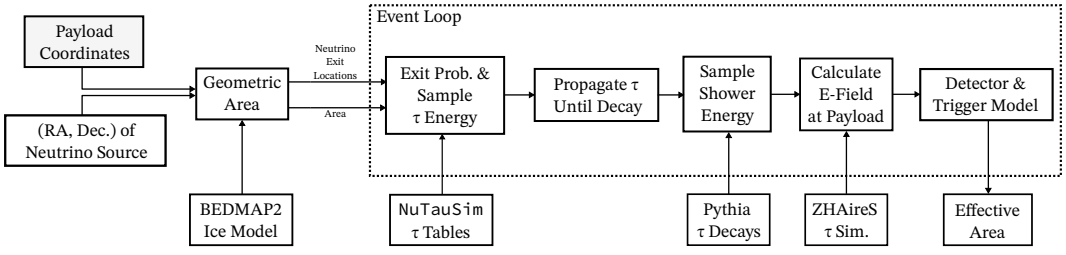

Figure 4.16: A flowchart showing the top-level logic and event loop of the TAPIOCA simulation code with the external data sources used at each stage. This logic is described in detail in Section 4.4.2 of the text.

view angle, $\theta_{\text{view,exit}}$, at the neutrino exit location on the surface as shown in Figure 4.15. Since the Cherenkov angle in air is $\sim$1°, and the radio emission from the Askaryan effect is closely beamed around the Cherenkov angle, we do not expect to see tau events more than $\sim$1.6° off axis.

Since the observed ANITA-IV events are extremely close to the horizon, we must also accurately take into account the altitude of the ice and curvature of the Earth at the observed location of each event. For each observed ANITA-IV event, we raytrace the observed radio-frequency event direction back to the continent and then use the BEDMAP2 [301] ice dataset to calculate the altitude of the ice surface in the region surrounding the exit location of our event in our 3D coordinate, and use that to calculate the geometric area.

The flowchart shown in Figure 4.16 outlines the core steps in TAPIOCA, and are described in more detail below:

1. Given the geometric area calculated in the previous step, TAPIOCA samples N (the number of desired Monte Carlo trials to evaluate the integral) neutrino exit locations within the area consistent with a neutrino source at (α, δ).

2. TAPIOCA then loops over each of these sampled neutrino locations and assigns an incident neutrino energy given by the simulation input parameters.

3. For each neutrino:

   a) We use the NuTauSim lookup-tables to sample the exit probability of a τ-lepton at this location given the incident neutrino energy. This step also randomly samples the energy of the τ-lepton from the `NuTauSim` distributions [250, 288]. This step gives us P_{exit}.

   b) We step this τ to its decay point in our full 3D coordinate system, under the assumption that the τ does not undergo significant energy loss in air. This step gives us P_{decay}.

   c) At the decay point, we sample the decay distributions generated by PYTHIA to get the fraction of the τ energy that was transferred into the extensive air shower.

   d) The ZHAireS electric field model described in section 4.3, in the frequency- or time-domains (depending upon the simulation configuration), is then used to calculate the incident electric field at the location of the payload.

e) The previously described detector model is then applied to determine whether this trial passed our trigger model (i.e. $P_{\text{trig}} = 1$ or $P_{\text{trig}} = 0$).

The total effective area, $\mathcal{A}(t, E_\nu, \alpha, \delta, \phi, \lambda, h)$, is then calculated as

$$A(t, E_\nu, \alpha, \delta, \phi, \lambda, h) \approx \frac{A_g}{N} \sum_{i=1}^{N} \hat{r}_{i,*} \cdot \hat{x}_{i,E}\, P_{i,\text{exit}} P_{i,\text{decay}} P_{i,\text{trig}} \tag{4.23}$$

For a typical run of TAPIOCA , $N \sim 10^8 - -10^9$ since our phase space cuts are generous to ensure that we accurately capture the tail of the integral being evaluated. When simulating ANITA, TAPIOCA can operate in two distinct modes:

1. Reconstructing the effective area associated with a specific *observed* ANITA-IV event using the run, geometry, and location of the event in question.

2. Calculate the effective area for every point on the sky by simulating the entire flight. While this is significantly slower than (1), TAPIOCA can still calculate the effective area for the entire flight in a few minutes on a laptop.

To illustrate the various contributions to ANITA-IV's effective area, we break down the effective area calculation for a neutrino energy of 10 EeV into the various sub-components of the Monte Carlo calculation (Equation 4.23) in Figure 4.17 as a function of the elevation angle of the neutrino source at the payload.

Due to its unique observing location at ∼37 km above the surface, ANITA's geometric area approaches 400 km^2 using the off-axis angle cut described previously. Near the horizon, the probability of an incident 10 EeV ν_τ generating a τ-lepton is approximately $\sim 1/50$ immediately reducing the maximum effective area to ∼8 km^2; below $\sim 8^\circ$, the exit probability for a τ-lepton falls drastically significantly reducing the maximum potential effective area; typically, the τ-lepton exit probability is the most relevant factor to ANITA's effective area. Since ANITA is $\lesssim$ 600 km from the horizon, the probability that a $\sim$ 10 EeV τ decays prior to reaching ANITA is still relatively high and is not a significant contributor to the effective area (as can be seen in Figure 4.17 as the magenta and purple lines overlap significantly).

ANITA's effective area to ν_τ sources extends above the horizon as ANITA observes the radio emission off-axis with respect to the neutrino propagation axis. Therefore, an

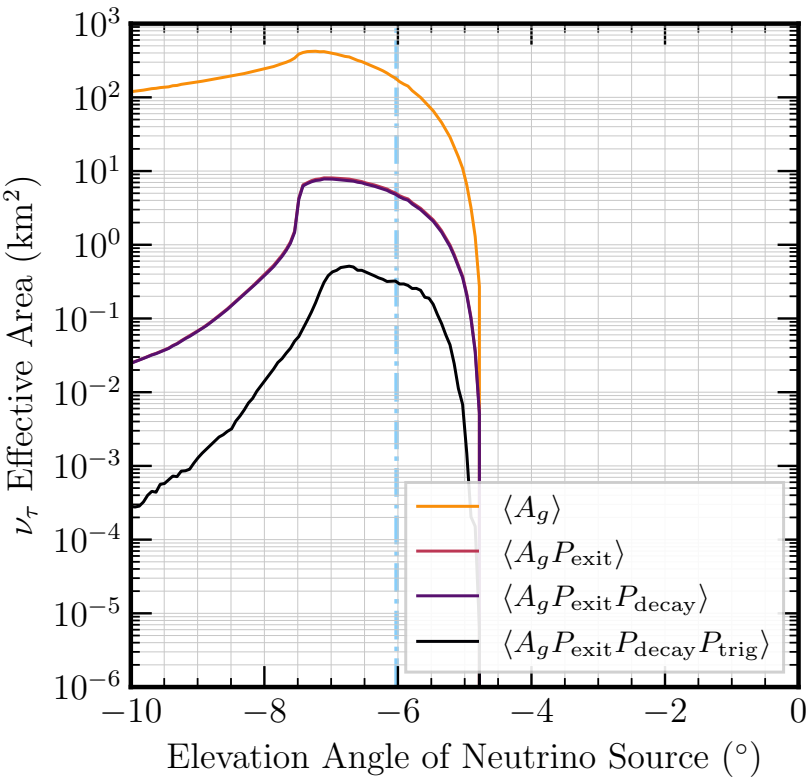

Figure 4.17: The effective area for $E_\nu = 10$ EeV for an average location and position in the flight broken down into the various components that are calculated by TAPIOCA as a function of the elevation angle of the neutrino source below ANITA's horizontal. The dashed line indicates the approximate location of the geometric horizon in ANITA's coordinate system. The actual location of the observed radio horizon differs from the geometric horizon due to refraction of the radio emission during the $\sim$ 600 km of propagation and depends on the payload's altitude, ice thickness near the horizon, and the instantaneous atmospheric conditions.

Earth-skimming neutrino from a source slightly above the horizon (*as seen by* ANITA), sampled from a plane-wave in directions with normal aligned with the observation vector from the source to ANITA, can still skim the Earth, decay in the air, and be observed $\gtrsim 1^\circ$ off-axis by ANITA.

ANITA is a broadband instrument and primarily designed for the detection of Askaryan emission which has significantly more high-frequency power than an in-air cosmic ray shower. Therefore, ANITA must typically observe an EAS fairly close to the Cherenkov angle in order to trigger, especially at lower energies near ANITA's threshold. This was worsened by the presence of the notch filters (described in Section 4.3.3) that preferentially removed low-frequencies (200 MHz - 500 MHz) where the spectrum of an EAS has maximum spectral power density within ANITA's band. This *on-cone* geometric factor in the detection model shows up in the trigger probability calculation and further reduces the effective area calculation by an order of magnitude.

In the following chapter, we use this new simulation of ANITA's effective area to Earth-skimming tau neutrinos to study the possibility that the four near-horizon events are, *in-fact*, Earth-skimming tau neutrinos.

Chapter Summary

1. We develop a new simulation code, known as `tapioca`, that can be used to calculate ANITA-IV's effective area to Earth-skimming ν_τ-induced air showers from point-like transient sources anywhere on the sky.
2. This code uses pre-calculated data tables from a variety of established codes including NuTauSim for ν_τ and τ propagation, PYTHIA and TAUOLA (for τ-decays), and ZHAireS for calculating the electric field from a τ-induced shower.
3. This simulation improves drastically on previous estimates by the ANITA collaboration and is the first ν_τ code for ANITA that utilizes an accurate detector model based upon empirical calibration measurements of the payload.
4. ANITA-IV's effective area to a pure ν_τ flux peaks at 1 km^2 between 1° and 2° below the horizon with the effective area falling rapidly below 1 EeV.

5 Analyzing the ANITA-IV Near-Horizon Events as Earth-skimming Tau Neutrinos

5.1 Interpreting ANITA events as upgoing tau neutrinos

In section 5.1, we consider the observational evidence that the four near horizon events originated from upgoing τ-neutrinos via the τ-induced EAS channel. This includes considering the implied neutrino source directions, energies, and a spectral analysis against simulations. We find that the events are not *inconsistent* with the tau neutrino hypothesis. In section 5.2 and section 5.3, we further consider the implications of the tau neutrino hypothesis by considering both an isotropic, diffuse flux of tau neutrinos and point sources—both steady and transient—of tau neutrinos. This includes comparisons to other experimental searches for ultrahigh-energy tau neutrinos.

Neutrino Source Parameters

Uncertainties in the location of the neutrino source on the sky with right-ascension (α) and declination (δ) are dominated by the cone-shaped beam of the upgoing air shower radio emission, which itself varies with the τ-lepton decay altitude and the zenith angle of the shower. This motivates the use of a forward modeling approach to reconstruct the location of the neutrino source and the corresponding energy of the neutrino that is most consistent with our observed events.

We developed a Markov Chain Monte Carlo simulation to reconstruct the posterior distributions of (E_ν, α, δ); in particular, we use the `emcee` package [302] that implements an affine-invariant ensemble MCMC sampler [303]. For this reconstruction, we use the following likelihood function, implemented in TAPIOCA, that captures the entire process of neutrino emission to the observed radio-frequency signal:

$$\mathcal{L}(E_\nu, \alpha, \delta, t) \quad \propto \quad A_g \, P_{\text{exit}} \, P_{\text{decay}} \, \mathcal{L}_\theta \, \mathcal{L}_\phi \, \mathcal{L}_{\text{waveform}} \tag{5.1}$$

where:

A_g = the geometric area for a given $(\alpha, \delta, t_{\text{event}}, \vec{x}_{\text{payload}})$,
P_{exit} = the probability that this neutrino generates a τ-lepton that leaves the Earth,
P_{decay} = the probability that the τ-lepton decayed before ANITA,
$\mathcal{L}_\theta$ = a Gaussian likelihood for the observed RF elevation angle,
$\mathcal{L}_\phi$ = a Gaussian likelihood for the observed RF azimuth angle,
$\mathcal{L}_{\text{waveform}}$ = a sample-by-sample Gaussian likelihood for the residuals between the simulated waveform and the observed waveform.

Since the neutrino flux distribution at these energies is unobserved, we repeat this likelihood optimization for different priors on the neutrino spectrum. We assume a generic power law neutrino flux distribution, E_ν^γ, between 0.1 EeV and 1000 EeV and reconstruct the neutrino parameters for discrete values $\gamma \in \{-3, -2, -1\}$ to accommodate a range of cosmogenic and astrophysical neutrino models, representing a generic power law extension to the observed diffuse neutrino flux and for comparison to similar analyses from other experiments [93]. For the second case, we estimate the sensitivity per bin, thereby placing no prior on the assumed flux, recognizing that the UHE neutrino spectrum can assume different spectral shapes. We use broad (6° wide) uniform (in solid angle) priors on α and δ centered around the sky location of the observed RF of each event. As an example, we consider the posterior distributions of (E_ν, α, δ) for Event 72164985 (Figure 5.1). The most likely neutrino energy depends strongly on the assumed neutrino spectral index, γ. A harder spectra ($\gamma \sim -1$) is more likely to generate higher energy neutrinos that have more phase space for producing a decaying τ with sufficient shower energy to trigger ANITA; equivalently, a softer spectrum ($\gamma \sim -3$) strongly disfavors the production of higher energy ν_τ's and therefore requires an upward fluctuation in the τ energy and shower fraction in order to be detected by ANITA. For $\gamma = -2$, the 50%

Event	$E_{\nu,\gamma=-1}$ (EeV)	$E_{\nu,\gamma=-2}$ (EeV)	$E_{\nu,\gamma=-3}$ (EeV)
4098827	$49.8^{+80.3}_{-37.7}$	$12.5^{+29.9}_{-7.4}$	$5.2^{+6.0}_{-2.5}$
19848917	$31.9^{+76.0}_{-24.5}$	$5.2^{+11.0}_{-2.9}$	$2.6^{+3.1}_{-1.1}$
50549772	$45.4^{+83.4}_{-34.4}$	$8.8^{+19.5}_{-4.9}$	$4.3^{+4.8}_{-2.1}$
72164985	$60.3^{+88.9}_{-38.2}$	$15.1^{+27.3}_{-7.6}$	$8.9^{+10.5}_{-4.5}$

Table 5.1: The most-likely reconstructed neutrino energies, using the MCMC approach described in section 5.1, for various priors on the neutrino flux.

quantile in reconstructed neutrino energy for Event 72164985 is 15.1 EeV with lower and upper 1-σ quantiles of 7.6 EeV and 42.4 EeV, respectively.

We note that the energies given in Table I of [257] are generic cosmic-ray shower energies (not neutrino energies) that were estimated using standard cosmic-ray shower models as opposed to the dedicated upward τ EAS simulations used in this work that take into account the tau regeneration and decay processes specific to this channel.

The reconstructed neutrino parameters for all of the four events are shown in Table 5.1 under the various assumptions for γ. This MCMC, which forward models the entire process from incident neutrino to detection by ANITA, includes uncertainties in the detector models as described in section 4.3, as well as the uncertainty in the observed event parameters. The observed electric field amplitude is a function of the broad distribution of exiting τ-lepton energies, the decay length of the τ, and the fraction of the τ's energy transferred to the shower.

Since ANITA orbits the South Pole, ANITA's elevation (azimuth) resolution is almost purely converted into declination (right-ascension) resolution. Figure 5.1 shows that the most likely neutrino source location α and δ is distributed as an annulus on the sky with an angular radius of $\sim 1^{\circ}$. This is due to the conically shaped radio emission from the EAS which has a Cherenkov angle of approximately 1° in air, displacing the neutrino source direction from the reconstructed direction of the radio-frequency signal at the payload.

Since ANITA only observes the radio emission at one *point* on the Cherenkov cone, the shower energy and the azimuthal angle around the shower axis (equivalently, *which* side of the cone you are observing) are degenerate. Higher-energy showers may be observed with less radio power if the Askaryan and geomagnetic components are anti-aligned. Equivalently, if the Askaryan and geomagnetic components are aligned, this will result in an increase in the observed RF emission. It may be possible for ANITA to break this

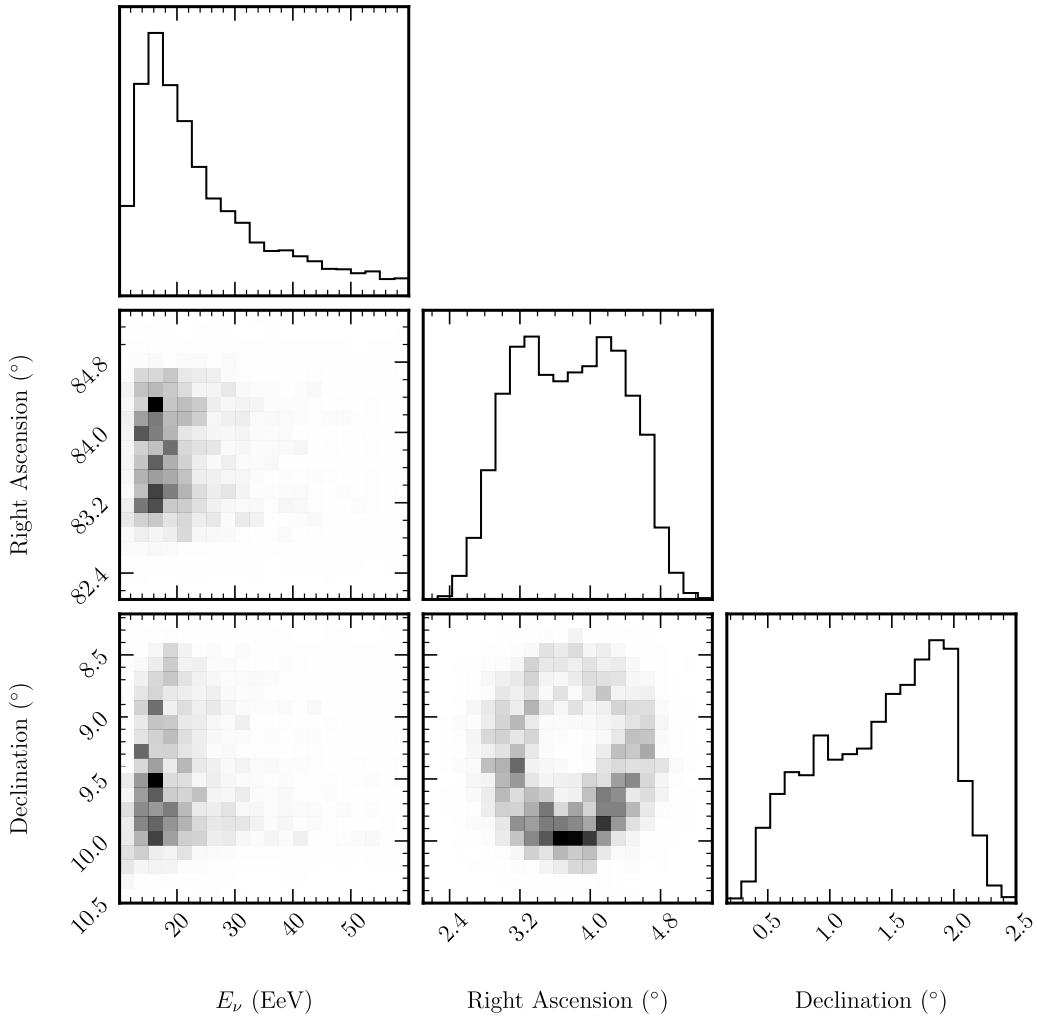

Figure 5.1: The posterior distributions of the neutrino energy and neutrino source locations, (E_ν, α, δ), for Event 72164985 under a $\gamma = -2$ hypothesis as reconstructed by the `emcee` [302] Markov Chain Monte Carlo using the likelihood function in Equation 5.1. We note that the right-ascension and declination have been shifted by a random (constant) offset for this publication. The true reconstructed sky coordinates will be published in a follow-up paper by the ANITA collaboration.

degeneracy through a detailed analysis of event polarization and the local geomagnetic field, but this is challenging to simulate due to the geometry of the near horizon events (see section 5.6). The results of the MCMC shown in Figure 5.1 and Table 5.1 indicate that ANITA has approximately $\pm 1^{\circ}$ resolution in right-ascension and $\pm 0.5^{\circ}$ resolution in declination for the τ-induced extensive air shower channel. We note that this is not ANITA's resolution for reconstructing the observed direction of the RF emission (which is typically $\sim 0.2^{\circ}$, see [257]); the additional uncertainty is due to the uncertainty for the azimuthal angle around the shower axis of the EAS as well as the reconstruction of the off-axis angle of observation.

Spectral Analysis

In this section, we compare the observed spectra against simulated spectra for upgoing τ-induced EAS produced using ZHAireS [293]. The spectral shape of an upgoing air shower radio pulse can be approximated as a falling exponential above ~ 300 MHz [256, 273, 245]. The amplitude and exponential constant are dependent on the shower energy, the off-axis angle, the decay altitude of the τ-lepton, and the zenith angle of the shower. The decay altitude and the zenith angle changes the atmospheric profile over which the shower develops, which affects the coherence of the radio emission, resulting in a different off-axis dependence as well as a lower required energy since the shower can develop closer to ANITA depending upon the decay length of the τ lepton.

Figure 5.2 shows the deconvolved electric field spectra for each event [257]. Since the spectrum of extensive air showers is well approximated by an exponential spectrum above 300 MHz, we also fit each deconvolved spectrum with an exponential function, $A(f) = A_{300}\, e^{\gamma(f-300)}$, with f in MHz where γ is the spectral index. We also show a range of electric field spectra simulated by ZHAireS to demonstrate the range of spectral indices observed in upgoing τ-induced air showers (light blue).

Event 72164985, which is closest to the horizon, is an excellent match to simulated upgoing EAS signals as well as the expected exponential spectral profile. Events 19848917 and 50549772 show a clear reduction in spectral power at low frequencies ($\lesssim 500$ MHz). It is possible that atmospheric effects due to the long distance propagation from close to the horizon could create anomalous spectra like is seen in these events. Possible physical explanations for this missing low-frequency power are discussed in section 5.5. For the purpose of our simulations, we do not include or model this low-frequency reduction and only fit the frequency range above the location of max spectral power (typically $300-$

500 MHz) for Events 19848917 and 50549772. Above $\sim$ 500 MHz, the events appear to agree with our simulations as well as with the expected exponential shape.

We use TAPIOCA to generate a sample of simulated τ-EAS events that passed ANITA's trigger so that we can compare these four events against the expected broader population of τ EAS. The spectral indices of each of the four near horizon events compared to the full population of normal (reflected and stratospheric) observed cosmic rays, as well as the simulated events, is shown in Figure 5.3. We do not necessarily expect that the spectral index of reflected UHECRs should match that of the simulated τ-induced EASs due to the different event geometries as well effects from the reflection of the radio emission off the ice.

We perform a Kolmogorov-Smirnov (KS) test to determine whether the spectral indices of the four near horizon events are consistent with the underlying population of *normal* UHECRs or the simulated τ distributions. The results of this test are shown in Table 5.2.

Test	p-value
Near horizon against regular UHECRs	0.48
Near horizon against simulated τ EAS (ZHAireS)	0.45

Table 5.2: The results of a Kolmogorov-Smirnov test on the spectral index, γ, of the near horizon events compared against the sample of regular UHECRs and simulated τ EAS.

In both cases, the KS test finds no evidence that the four near horizon events are not drawn from the underlying distribution. The p-value of both cases is approximately 0.5 which is an order of magnitude worse than would be needed to reject the hypothesis that the four NH events came from each underlying distribution at a 5% significance.

Considering both the implied neutrino parameters (E_ν, α, δ) and the spectral evidence, we conclude that these events are not *inconsistent* with τ-induced EAS, within model and simulation uncertainties.

5.2 Diffuse Flux Limits

Figure 5.4 shows the exposure of ANITA-IV to a diffuse ν_τ flux via both the Askaryan [87] and upgoing EAS channels (this work). The upgoing EAS channel dominates ANITA's ν_τ exposure at energies below $\sim 10^{19}$ eV above which the Askaryan channel dominates.

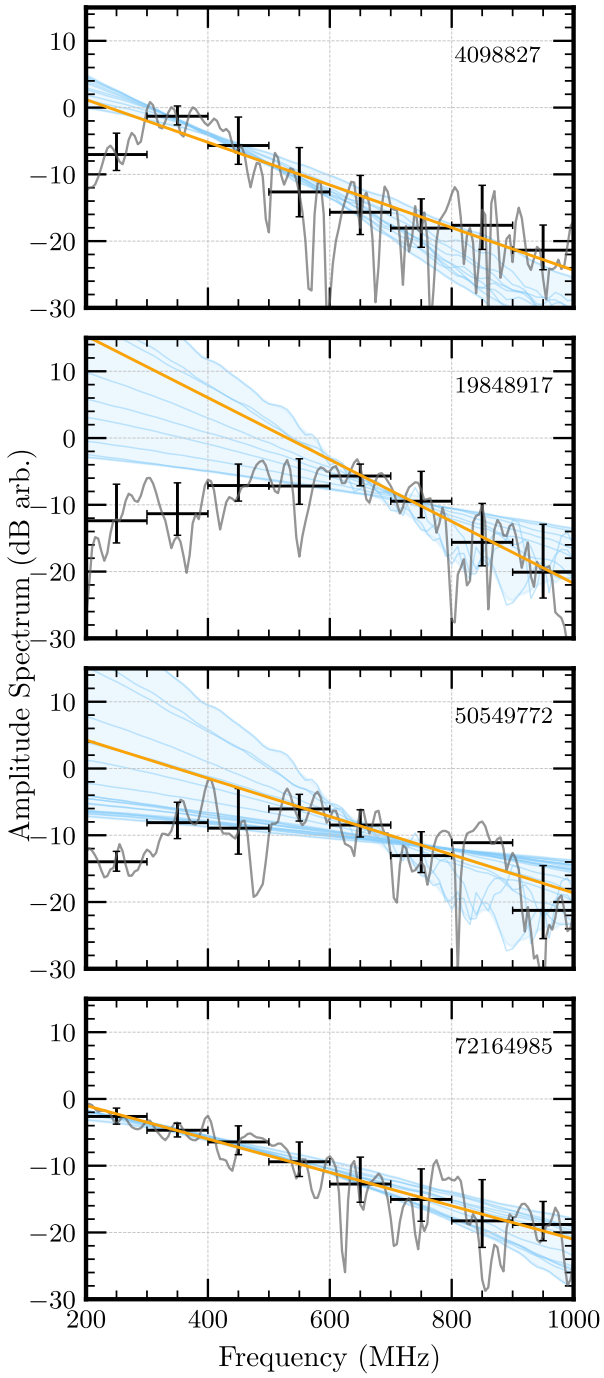

Figure 5.2: The deconvolved electric field amplitude spectrum for each event produced using the CLEAN deconvolution algorithm described in [257]. The amplitude spectrum (gray) is shown along with the average over consecutive independent 100 MHz bins (black). Each set of averages (black) was fit with an exponential form (orange), $A\exp(\gamma(f - 300))$. For 4098827 and 72164985, the fit was performed from 300 MHz up to 1000 MHz. For 19848917 and 50549772, the fit was performed over the frequency region above the peak "turnover" (typically 500-600 MHz). Several different ZHAireS simulated upgoing τ spectra are also shown (light blue) for a variety of decay altitudes and zenith angles that could be consistent with these events.

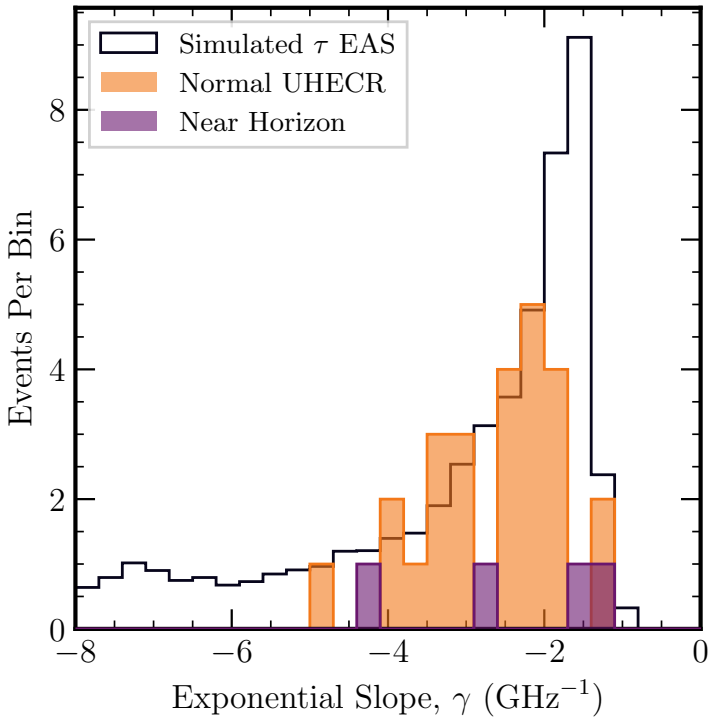

Figure 5.3: The exponential radio-frequency spectral slope distribution of the waveforms of the regular (reflected) cosmic rays (orange) observed by ANITA-IV compared against the spectral indices of the four near-horizon τ-like events (purple) compared to an arbitrary scaled distribution of τ events simulated with TAPIOCA. We note that to be consistent with previous ANITA publications, we have reused γ here as the spectral slope (with units of inverse frequency) of the radio-frequency waveform whereas early (to be consistent with other published work) we also used γ as the exponent in the power law neutrino flux distribution.

Due to the short flight of ANITA-IV ($\sim$ 28 days), neither the Askaryan or EAS ν_τ exposure is comparable with IceCube or Auger at energies below $\sim 10^{19.5}$ eV (the combined limit of ANITA I-IV sets a stronger limit than is shown in Figure 5.4). The significant discrepancy in the total exposure rules out a diffuse isotropic ν_τ flux origin for the four ANITA-IV near horizon events under the Standard Model. This is the same conclusion reached for the two *steeply upgoing* events observed in ANITA-I and ANITA-III [259, 288] and consistent with the expected sensitivity of the three flights [290].

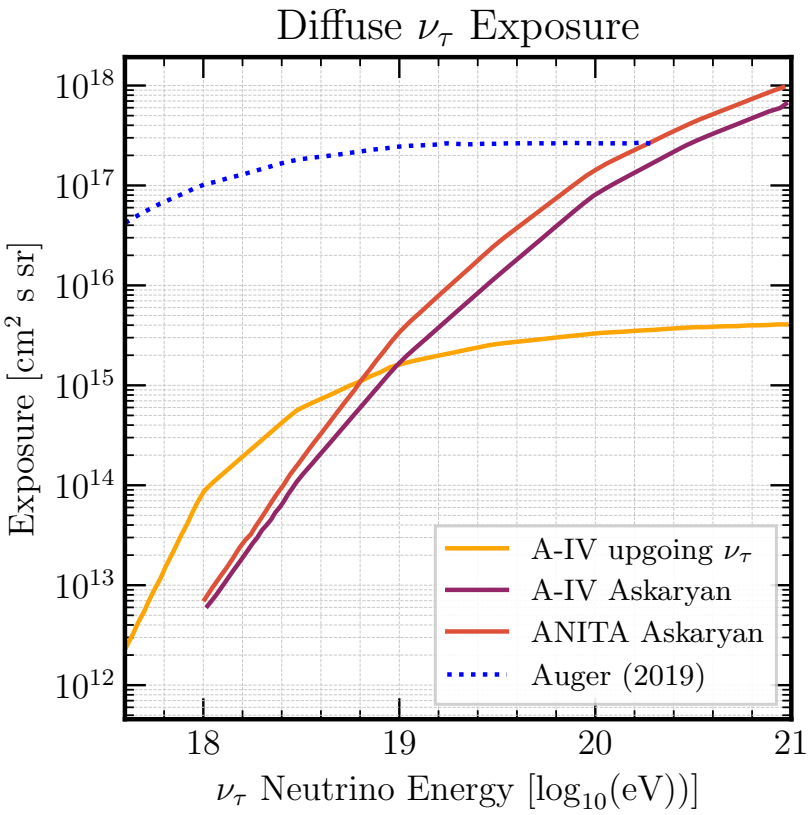

Figure 5.4: The (single-flavor) exposure to ν_τ for ANITA's EAS channel as well as its Askaryan in-ice detection channel [87] compared against ν_τ exposures from the Pierre Auger Observatory [90].

5.3 Point Sources

In this section, we present ANITA-IV's sensitivity to astrophysical neutrino point sources, including transient sources that may have only been active for extremely short durations.

Due to its unique viewing location in the stratosphere, ANITA typically has a large instantaneous effective area that partially compensates for its $\sim$ 30 day observing time.

The effective area as a function of the elevation angle of the neutrino source on the sky for a range of energies from 1 EeV to 1000 EeV is shown in Figure 5.5. ANITA's EAS sensitivity to ν_τ turns on at several hundred PeV with a peak effective area of $\mathcal{O}(1\,\mathrm{km}^2)$ at the highest energies. By $\sim$300 EeV, ANITA's effective area begins to saturate as the trigger probability tends to $\sim$ 1 for events at these energies. ANITA's peak sensitivity to neutrino sources occurs when the neutrino source is roughly $\sim$ 1° below the horizon since this allows for a larger geometric area of possible neutrino exit locations for neutrinos from that source to be geometrically visible by ANITA and observed close to the Cherenkov angle (Figure 4.17 and Figure 5.5).

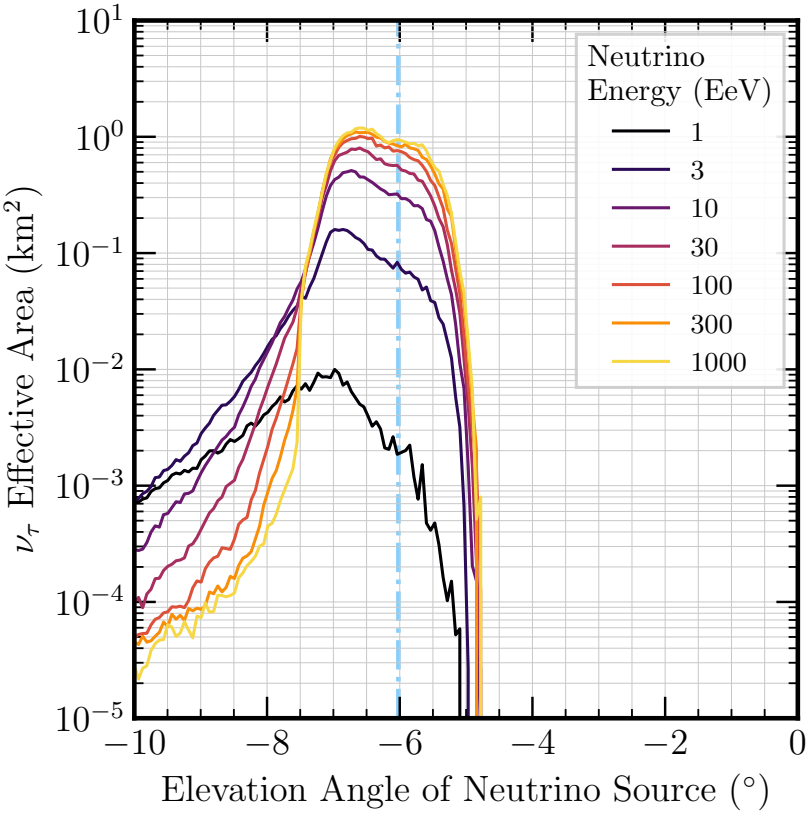

Figure 5.5: The effective area vs. neutrino source elevation angle for various tau neutrino energies from 1 EeV to 1000 EeV. The dashed blue line shows the approximate location of the geometric horizon (averaged over the flight).

The *peak* effective area of ANITA-IV as a function of incident neutrino energy for both the Askaryan channel (single-flavor effective area assuming a 1:1:1 flavor ratio) and the τ air shower channel is shown in Fig. 5.6. The effective area in the ν_τ EAS channel exceeds that of the Askaryan channel, below 10^{19} eV and significantly lowers ANITA's threshold energy for ν_τ detection down to $\sim$ 0.3 EeV. The sensitivity of the Askaryan channel exceeds the ν_τ EAS channel above 10^{19} eV and can approach $\sim$ 30 km^2 at the highest energies. We also show the Pierre Auger Observatory's upgoing ν_τ effective area over the same energy range using the published data from [93].

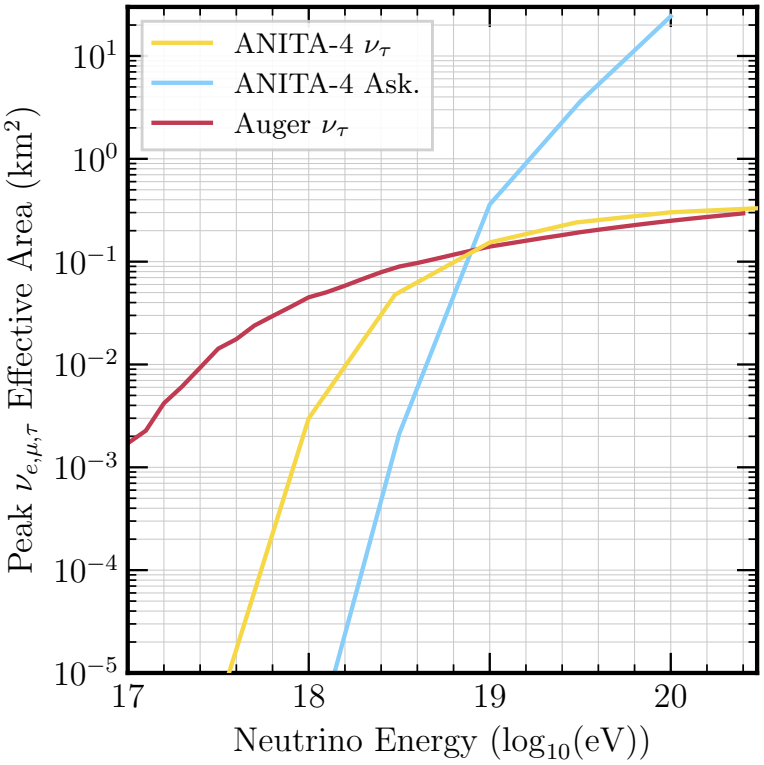

Figure 5.6: The peak *all-flavor* (1:1:1) effective area (over elevation angle) as a function of neutrino energy for the ANITA-IV air shower channel, the ANITA-IV Askaryan channel, and the Pierre Auger Observatory's upgoing ν_τ channel. The Auger curve was extracted using published data in [93].

Consistency with ν_τ

We compare where our four observed events occur within the expected distributions of the elevation angles of τ-induced EAS events as simulated by `tapioca`. Using the param-

eters (payload location, time, ice thickness, etc.) at the time of each observed near horizon event, we generate a large random sample of simulated ν_τ air shower events that would have been detected by ANITA by sampling the calculated effective area shown in Figure 5.5. We use the energy curve closest in energy to the reconstructed neutrino energies shown in Table 5.1 assuming a E^{-2} prior on the neutrino flux energy spectrum.

Given this distribution of elevation angles, we perform a series of Kolmogorov-Smirnov tests to determine if the observed events are consistent with the simulated event distributions; the p-values for the KS tests are shown in Table 5.3.

Event	KS p-value
4098872	0.95
19848917	0.60
50594772	0.72
72164985	0.85
All Events	0.19

Table 5.3: The p-value of a Kolmogorv-Smirnov test for rejecting the hypothesis that these events are drawn from the simulated distribution of events from TAPIOCA.

For each observed event, there is no evidence to reject the hypothesis that the observed events are taken from the simulated distribution of elevation angles of τ-induced EAS events. Under the model presented in this work, all four events taken together are observed at elevation angles that are *not inconsistent* with τ-induced EAS.

Field of View

ANITA has a relatively narrow instantaneous field-of-view on the sky (a $\sim 1^\circ$ wide band in elevation angle) for which it has a large effective area, so the effective area over time for a given sky coordinate is not constant due to the orbital movement of the payload and the sidereal motion of the source on the sky. The ANITA payload typically completes several full orbits around the geographic south pole (i.e. $\phi \in [-180, +180]$) with a latitude that varies between -90° and $\lesssim -75^\circ$

The instantaneous effective area at 1 EeV for a 5-day period encompassing the detection of Event 72164985 is shown in Figure 5.7 along with the effective area of the Pierre Auger Observatory [93]. As ANITA is also *orbiting* the continent, the shape and duration of each daily viewing period changes on a day-to-day basis. The time at which ANITA observed event 72164985 is shown with a blue vertical line. All four near hori-

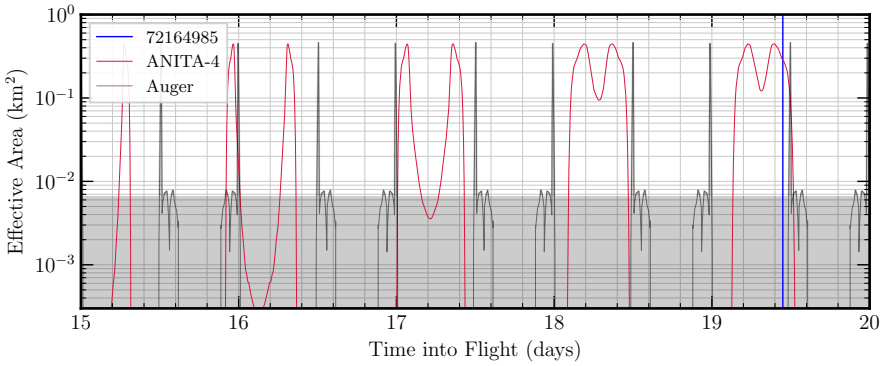

Figure 5.7: The time evolution of the effective area of ANITA-IV ν_τ (pink) and Auger (grey) [93] in the direction of the peak source location corresponding to event 72164985 (see Table 5.1). Event 72164985 occurred at the time indicated by the blue line at day $\sim$ 19.5. The Auger curves (simulated by us) were performed using the published curves in [93].

zon events were observed by ANITA during a window when they *were not* visible by Auger and occurred close to the daily peak in ν_τ effective area.

Since ANITA's sensitivity to τ-lepton induced EAS is large but transient, As shown in Figure 5.7, ANITA's effective area to a given neutrino source location on the sky can be large, but varies significantly as a function of time since the visible portion of the sky changes and ANITA's effective area depends strongly on elevation angle. Therefore, ANITA can set different sensitivity limits on the point source flux depending upon the duration of the transient source. The *instantaneous* single event sensitivity (SES) limit set by ANITA-IV for short-duration ($<$ 15 minute) and long duration ($>$ 1 day) transient neutrino sources occurring at the location of the four observed near-horizon events is shown in Figure 5.8 (this SES limit is estimated using the method in [304]). Since each event was observed at a different location on the $A_{\text{eff}}(\delta)$ curve, and since each of the sources moves in and out of ANITA's field of view with different transit rates, the strength of the SES is different for each neutrino candidate location and for different event durations. However, since each event was observed very close to the peak in ANITA's time-varying ν_τ effective area, the short-duration SES limits for each event are similar

Comparison with other Observation Channels

Under the assumption that ANITA-IV observed 3-4 ν_τ events (Figure 4.2) from a population of transient neutrino sources, we calculate the number of events that should

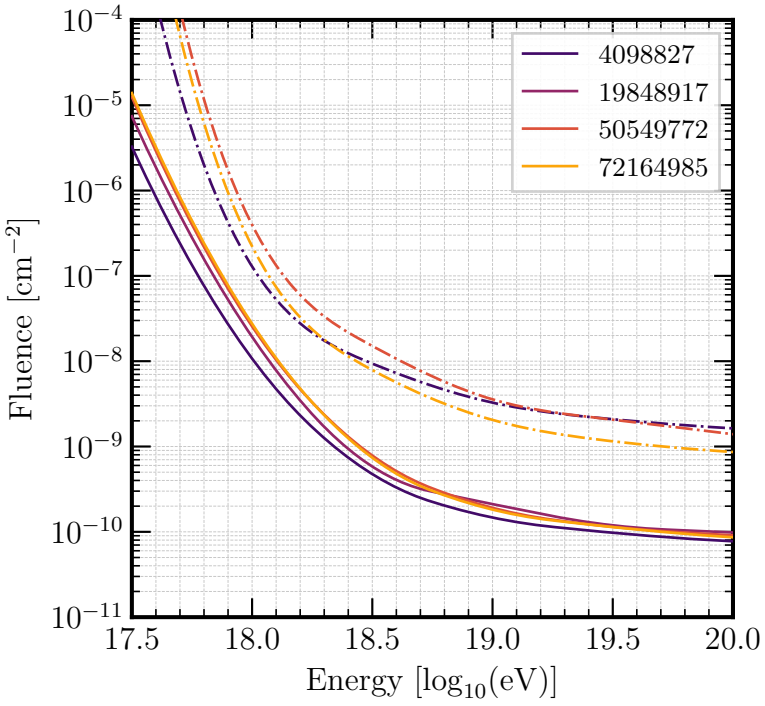

Figure 5.8: ANITA's sensitivity to short-duration ($<$ 15 minute) (solid) and long duration ($>$ 1 day) (dashed) transient neutrino sources at the location of each of the four near-horizon events observed in ANITA-IV.

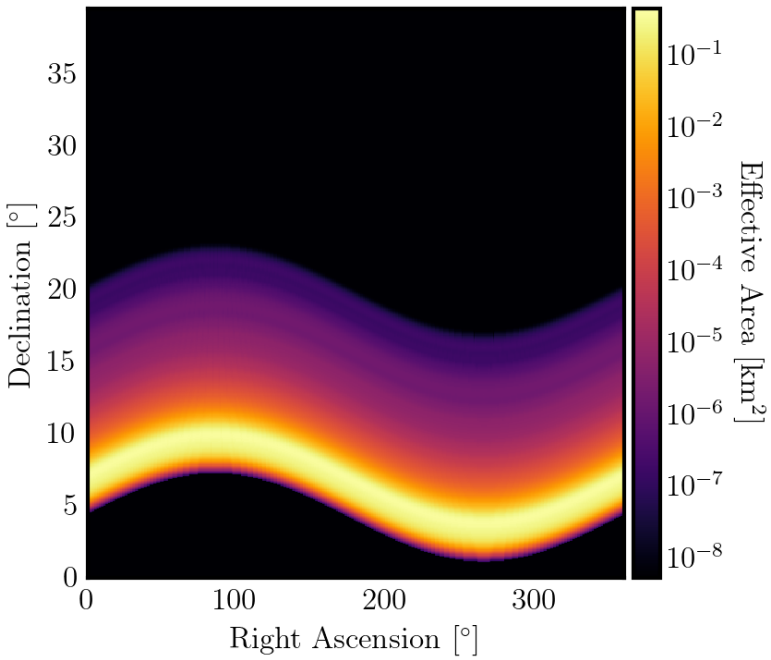

Figure 5.9: An instantaneous sky map of ANITA-IV's ν_τ effective area over right-ascension and declination at the time of observation of Event 72164985 for a neutrino energy of 100 EeV.

have been observed by the Pierre Auger Observatory (Auger) as well as ANITA-IV's Askaryan neutrino channel (which observed 1 candidate neutrino event consistent with background) [87]. We also show the estimated event counts for an integrated E^{-2} pure-ν_τ flux with a constant normalization, k_{ps}, with units of GeV cm^{-2} s^{-1}.

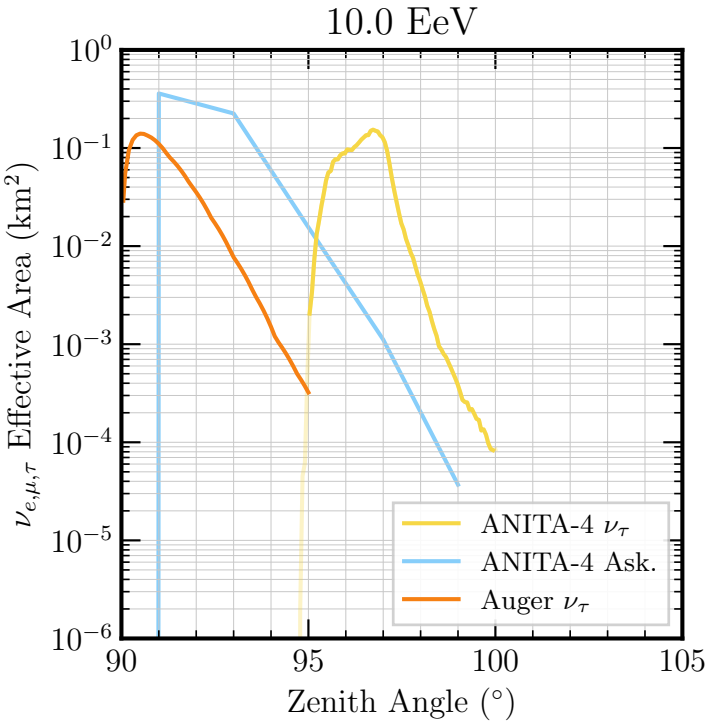

Figure 5.10: Single flavor effective area for the ANITA air shower channel (this work) and Askaryan channel [304] as well as the Auger Earth-skimming ν_τ channel. The Auger curve was produced using published data from [93].

The field of view (FoV) of ANITA's ν_τ EAS channel is compared to the ANITA Askaryan channel and Auger's ν_τ channel in Figure 5.10 and Figure 5.9. The FoV of both Earth-skimming ν_τ channels (ANITA and Auger) are both $\sim 5°$, as it is strongly driven by the exit probability of a τ-lepton from a ν_τ which is mostly independent of each detector. The peak effective area at 10 EeV is comparable for all three channels, with the Askaryan channel a factor of two higher than the two Earth-skimming ν_τ channels.

We compare ANITA and Auger's sensitivity to a population of transient neutrino sources using a flux-model independent approach. We calculate the sensitivity of ANITA's ν_τ and Askaryan channels, as well as those of Auger, in logarithmic energy bins between 0.1 EeV and 1000 EeV. We then compare the fluence sensitivity for transients of vari-

ous durations from 1 second to half-day timescales, as well as for different full-sky transient rates varying from 1 per-month to several thousand per day. While not an exhaustive search of the parameter space, this covers a representative sample of short- and long-duration transients that are potentially detectable by ANITA without detection by Auger. We simulate the period between May 1st, 2008 to August 31st, 2018 which corresponds to the published exposure and effective curves in [93]. This corresponds to a total of exposure time $T_{\text{auger}} \sim 3700$ days during which ANITA-IV flew for 28 days starting in December 2016.

We use a dedicated Monte Carlo simulation to calculate the distribution of possible outcomes for the number of detected events for the ANITA ν_τ, ANITA Askaryan, and Auger channels. For a given transient duration ΔT and average full-sky event rate r, we throw $N \sim \text{Poisson}(rT_{\text{auger}})$ random sources on the sky throughout the ~ 10 years. For each source, we place a box-car (rectangular) time-dependent flux model at the time of each simulated event with the given transient duration, ΔT. We then calculate the total integrated exposure to each of these transients using ANITA-IV's ν_τ effective area (this work), ANITA-IV's Askaryan point source effective area [304], and Auger's upgoing ν_τ effective area [93]. While Auger has sensitivity to downgoing ν_τ via in-air neutrino showers, this is significantly subdominant to the Earth-skimming ν_τ channel and is therefore not included in this comparison. We calculate the total sensitivity across all sources visible by each experiment assuming that the underlying flux results in ANITA-IV observing N_{true} events, where N_{true} is sampled from Figure 4.2 and is typically ~ 3. Given N_{true} detections by ANITA-IV's ν_τ channel for this particular distribution of sources, we calculate corresponding limits on the fluence that would be set by ANITA-IV's Askaryan channel and Auger assuming that no events were detected in either observatory. This process is a single *realization* of ANITA-IV/Auger in the Monte Carlo simulation. This is repeated many times ($N_{\text{src}} \in [10^5, 10^6]$) to accurately sample the distribution of possible transient limits that each respective experiment may set. For a given underlying full-sky transient rate and duration, this Monte Carlo simulation accounts for fluctuations in the number and location of sources on the sky. The model independent limits on the fluence, calculated using this Monte Carlo, is shown in Figure 5.11 for two representative transient durations and rates.

For all simulated transient durations and full-sky rates, the observation of ~ 3 ν_τ events is in strong tension with Auger across the full simulated energy range, and is also in tension with ANITA-IV's Askaryan channel above $\sim 10^{18.8}$ eV. This tension with

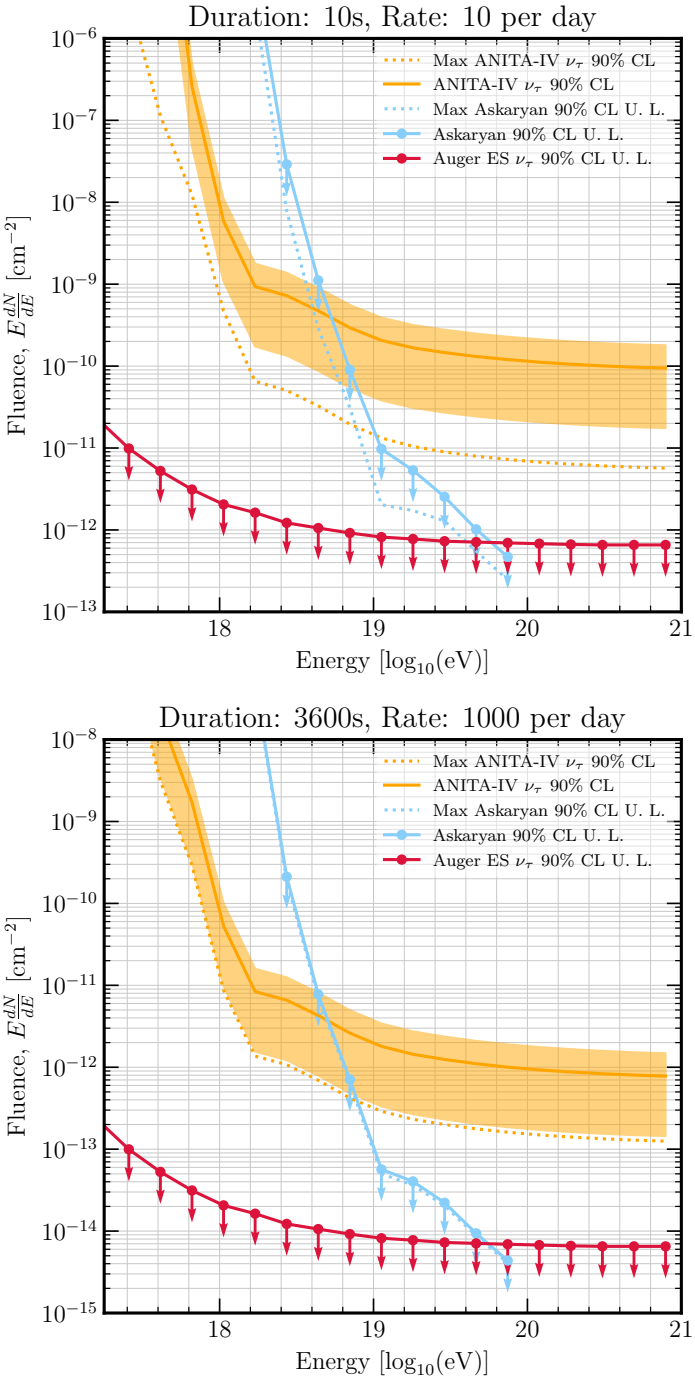

Figure 5.11: The fluence limits set by Auger ν_τ and the ANITA-IV Askaryan channel assuming ANITA-IV observed ~ 3 ν_τ events via the EAS channel. For both transient source duration and full-sky event rates simulated here, the range of ν_τ fluences consistent with our observation (orange band) are inconsistent with the limits set by Auger (red curve) across the entire simulated energy range and inconsistent with ANITA-IV's Askaryan limit (blue curve) above $\sim 10^{18}$ eV. All Auger results were calculated using the published effective areas from [93].

ANITA's Askaryan channel could potentially be resolved by a cut-off in the neutrino energy spectrum at or around $\sim 10^{19}$ eV but this would not eliminate the tension with Auger. As shown in Figure 5.10, ANITA-IV and Auger's Earth-skimming ν_τ channels have very similar instantaneous field-of-views so Auger immediately sets a stronger limit due to its $\sim 120\times$ longer livetime and larger effective area at lower energies (Figure 5.6). The strength of the fluence limit set by each detector can vary significantly with the transient duration and full-sky transient rate, but Auger always sets a stronger limit than the ANITA-IV ν_τ channel by an approximately constant factor due to the similarity of each observatories' fields-of-view and effective area. Above 10^{20} eV, ANITA-IV's Askaryan channel is able to set a stronger limit (in ~ 28 days) than Auger for all simulated transient durations and full-sky transient rates.

An important caveat to this tension between Auger and ANITA is the challenges associated with Auger's detection of Earth-skimming ν_τ compared to ANITA. Beside their anomalous polarity, these events are observed by ANITA as only a small part of a larger sample of air shower events that cover a range of solid angle immediately adjacent to the anomalous events both above and below the horizon. ANITA therefore has a large sample of similar, nearby events that can be used to understand the behaviour of these events, and they are only separated from well-understood UHECRs by one parameter (polarity). On the other hand, Auger *would* observe these events in a highly unusual geometry from a range of solid angle where they have never observed *any* events (of any kind) and that rely entirely on simulations for modeling the expected signal. Therefore, there remains the possibility that Auger's effective area may be over-estimated and therefore the corresponding limit may be overly strong, potentially resolving or reducing the tension with the ANITA-IV near horizon events.

Comparison with IceCube Unfortunately, at the time of writing, the IceCube collaboration does not publish the complete point-source ν_τ effective areas that are needed for a similar comparison as done with Auger. We look forward to a potential future follow-up by the IceCube collaboration for these events.

5.4 Discussion

The anomalous events found in ANITA-IV are significantly different from those found in the first and third flights in that they are closer to the horizon rather than being steeply

upgoing. While this makes them more consistent with a Standard Model ν_τ hypothesis as ANITA is maximally sensitive to ν_τ's in the region below the horizon, the limits imposed by other observatories makes this an unlikely explanation. For an in-depth discussion of backgrounds associated with these events, including ice surface and subsurface features, coherent backscattering, stopping radiation, and other effects, see the appendix of [257].

In this section we briefly discuss the potential origin of the low-frequency spectral discrepancies observed in several of the anomalous events and speculate on future investigations related to these events.

5.5 Potential Origin for the Low-Frequency Attenuation

In Figure 5.2, we showed that while the spectra of events 4098827 and 72164985 match the expected exponential distribution, events 19848917 and 50549772 show attenuation at frequencies below $\sim$ 500 MHz. We explore several possibilities for the origin of this low-frequency (LF) attenuation in two of the events: (1) geometries where ANITA simultaneously observes direct emission where an off-cone reflected emission whose inverted (from the reflection) waveform interferes with the direct pulse; and (2) atmospheric propagation effects, in particular tropospheric ducting, during the $\sim$600 km near-horizontal propagation of the electric field from the decay point to ANITA.

The "interfering" reflected hypothesis (1) can be further broken into two classes. In both classes, the direct radio signal from an Earth-skimming air shower is observed along with a reflected signal. While they both propagate close to the horizon, the two classes are distinguished by the particles that generate the air shower and their incoming angle. In class (a), a cosmic ray produces an elongated air shower above the horizon, in the stratosphere. In class (b), an upgoing τ lepton decay produces a skimming air shower originating from below the horizon. We consider both hypotheses by adding an inverted pulse – representing the reflected signal – to a non-inverted pulse – representing the direct signal. The inverted and non-inverted pulses are delayed and summed in the time-domain to match the observed time-domain waveforms. The three spectrally anomalous events reconstruct significantly below the horizon at the level of $\gtrsim 2\sigma$, therefore hypothesis (a) is strongly disfavored.

To recreate the observed waveforms, the delay between the direct and reflected pulse must be less than $\sim$1 ns, or $\lesssim$ 30 cm of total path length. An above-horizon cosmic ray geometry that allows for an off-axis reflection detectable by ANITA with a $\lesssim$30 cm path length must propagate extremely close to the ground and is therefore strongly suppressed by the near horizon radio propagation effects discussed in [257].

Furthermore, for each of the two events attenuated at low frequencies, the emergence angle at the Earth is $2^\circ - 3^\circ$. For a τ energy of $\mathcal{O}(1 - 10\ \mathrm{EeV})$, the average τ lepton decay point is several kilometers above the ground (the decay length for a 1 EeV τ is 47 km). With a $\lesssim$ 30 cm path length constraint, the relatively high-altitude of the τ decay rules out any possible geometry for a reflection.

The reflected signal must also be of similar strength to the direct pulse to create the observed waveforms shown in Fig. 5.2. As shown in [273], the total reflection coefficient including Fresnel, roughness, and curvature effects, approaches zero near the horizon significantly suppressing the strength of any reflection, further disfavoring any reflected explanation for the observed spectral attenuation below 250 MHz.

5.6 Limitations of simulations

The air shower simulation code used in this work, AIRES [64], makes several assumptions that may affect the simulation of near-horizontal cosmic ray showers from near-to or over-the horizon. In particular, AIRES, as well as the other major EAS simulation code CoREAS [305]: a) do not accurately simulate the curvature of the Earth and atmosphere at the 600 km scale of the ANITA events and therefore do not allow for "over the horizon" propagation; b) ignore the refraction of the radio emission from the shower during propagation to the receiving antennas; and c) use a *geometric optics* formalism that ignores any wave-like (diffraction, dispersion, ducting, etc.) effects that may occurs in real atmospheres and alter the propagation of the radio emission from the shower to the antenna. All of these effects are most dominant for events originating near the horizon (i.e. propagating close to the surface) where the Earth's curvature is most significant and many wave-like effects are possible (i.e. tropospheric ducting, Fresnel zone attenuation or diffraction, etc.) which are often strongly frequency-dependent and could potentially explain the anomalous low-frequency spectra observed in two of these ANITA events.

The authors of ZHAireS have investigated the effect of ray curvature for highly-inclined *reflected* UHECR showers (as might be seen by ANITA) and found that for showers with

zenith angles of 85°, the straight-ray approximation was valid up to $\sim$ 900 MHz above which several changes in the angular spectrum could be observed [231]. The four events discussed in this work were observed at frequencies well below this frequency. Furthermore, the τ-induced EAS events visible by ANITA are also less likely to be affected by these effects, compared to a high-zenith angle reflected EAS, since a τ lepton at these energies typically decays tens or hundreds of kilometers after leaving the Earth and therefore the shower typically develops far from the horizon and potentially several kilometers above the surface, away from the regions that are most affected by these approximations.

While this analysis has been performed using these existing tools as they are the best available at the time of writing, future efforts may help alleviate some (but not all) of these issues. The upcoming next-generation shower simulation tool CORSIKA 8 [66] allows for simulating showers in arbitrary 3D geometries so will allow for a correct treatment of Earth- and atmospheric curvature near the horizon. However, the current simulation programs of radio pulses in EAS based on superposition of contributions from particle sub-tracks (ZHS [306] and CoREAS [307]) do not currently account for the geometric refraction of rays during propagation. Future versions of these packages such as those planned to be implemented in CORSIKA 8 may be able to incorporate these effects and may significantly alter these results.

However, incorporating full-wave optic effects is a computationally challenging problem that will require the development of significantly new tools. The standard high-fidelity full-wave electromagnetics simulation tool is the finite-difference time-domain (FDTD) algorithm but this requires extremely large amounts of memory when simulating large volumes at high frequencies and simulating the propagation of ANITA's near horizon events is currently computationally intractable on even the world's largest supercomputers. Alternative methods, such as parabolic equation (PE) propagation, have the potential to provide more accurate wave-like simulations for EAS than current tools (ZHAireS, CoREAS) but are still computationally expensive and have so far primarily been developed for defense-related radar propagation and are only beginning to be employed for ultrahigh-energy neutrino physics [308].

5.7 Future Observations

Several current and future experiments are designed to search for upgoing tau neutrinos via the τ-induced air shower channel. PUEO, the follow-up mission to ANITA, has

significantly improved sensitivity to τ-induced EAS events and includes dedicated hardware to improve analysis and reduce backgrounds [111]. Experiments searching for air showers from high elevation mountains [309, 310, 311, 312], balloons [111], and satellites [62] are also sensitive to events with similar geometries and origins. Given that these events are challenging to interpret under a ν_τ hypothesis, it will be important to follow-up the ANITA observations in different locations (overlooking water, rock,) and from different altitudes (mountain, balloon, satellite) that will have different systematics and backgrounds.

The point-like ν_τ analysis by Auger used for this work also only includes the surface detectors. A tau search using Auger's fluorescence detectors was also performed but only considered events with exit elevation angles greater than 20° and so cannot be used to constrain these new ANITA-IV events [313, 314].

5.8 Conclusion

We have analyzed the plausibility that the upgoing near-horizon ANITA-IV events are explained by τ-lepton extensive air showers from skimming ν_τ interactions in the Earth. To achieve this, we have applied detailed models of the $\nu_\tau \rightarrow \tau$ propagation through the Earth, radio emission from air showers, and the ANITA-IV detector. We have found consistency in the elevation angles and radio-frequency impulsive signatures of these events, namely the polarity and spectral shape of the events, with reconstructed ν_τ energies in the 1 - 50 EeV range (depending upon assumptions regarding the underlying neutrino flux shape). We find that while these events are not observationally *inconsistent* with UHE ν_τ's, the implied fluence necessary for ANITA-IV to have observed ~ 3 of these events is in tension with Auger's existing ν_τ limits at all simulated energies and is also in tension with ANITA's Askaryan channel above $10^{18.8}$ eV.

Chapter Summary

1. We use a Markov-Chain Monte Carlo technique to reconstruct the posterior parameters of each near horizon event and find that they are consistent with ultrahigh energy neutrinos over a range of neutrino flux priors.

2. We find that the observed elevation angles of the near horizon events are not inconsistent with distributions simulated using `tapioca`.

3. Event 72164985 is a near-perfect match for simulated τ-induced waveforms and is highly aligned with the expected geomagnetic polarization angle. However, the other three events show varying degrees of anomalous low-frequency attenuation that impart a degree of bipolarity to each event, and are not as well aligned to the expected geomagnetic polarization as event 72164985. However, we find that the overall slope of the frequency spectra of the events is not inconsistent with distributions simulated with `tapioca`.

4. For a diffuse isotropic neutrino flux, both Auger and IceCube set *significantly* stronger limits on the flux than implied by ANITA-IV's observation of the near horizon events. The discrepancy with these limits strongly disfavors a isotropic flux model for these events.

5. Using another Monte Carlo, we also find that we are unable to avoid the limits set by Auger even with a generic population of *transient* neutrino sources that occur uniformly on the sky with varying rates and durations. Since Auger has roughly the same field of view and effective area as ANITA-IV's ν_τ channel, the 120x longer livetime of Auger is challenging to circumvent.

6 Searching for astrophysical sources coincident with the ANITA-IV near horizon events

In this chapter, we use the the ANITA-IV ν_τ simulations developed in the previous chapters to search for potential associations between any one of the ANITA-IV ν_τ candidate near horizon events and catalogs of known astrophysical sources with models of ultrahigh-energy neutrino production.

As shown in section 5.3 of the previous chapter, ANITA-IV's diffuse ν_τ exposure is orders of magnitude smaller than that of the Pierre Auger or IceCube observatories, principally due to the orders of magnitude longer livetimes of these experiments. In addition, ANITA-IV's ν_τ exposure is also exceeded by ANITA-IV's own Askaryan channel by an order of magnitude or more above 10^{19} eV. Therefore, modeling these events as from a *diffuse* ν_τ flux is phenomenologically challenging without violating the limits from Auger, IceCube, *and* ANITA-IV itself.

Unlike the full-sky Askaryan neutrino searches performed with previous flights of ANITA [304], and the full-sky point-source searches by Auger and IceCube [93, 315, 316], the extremely focused field-of-view of the ν_τ channel has the potential to be an exceptional powerful search for *point-like* neutrino sources. We focus our search for astrophysical objects on source classes that are inherently *transient* as any non-transient (i.e. "constantly emitting") source is ruled out with the same reasoning as for a diffuse neutrino flux (i.e. Auger/IceCube have orders of magnitude more exposure to it than ANITA-IV's ν_τ channel). A transient object, especially a rarer source class with an extremely short lifetime, may have the *potential* to be detected by ANITA-IV without violating the limits set by the Pierre Auger observatory, although as discussed in section 5.3, this is still phenomenologically challenging.

Section 1.3 discussed models of ultrahigh-energy neutrino and cosmic ray production from a variety of astrophysical sources. In particular, source classes that had inherently *transient* behavior along with an energy budget to produce a significant flux of neutrinos included:

1. Hypernovae and engine-driven supernovae (HNe/SNe)
2. Gamma-ray burst (GRB)
3. Tidal disruption events (TDE)
4. Flaring blazars

We perform our ANITA-IV transient source search over catalogs of these four event classes (SNe, GRB, TDE, and flaring blazars). In section 6.1, we present an introduction to the unbinned maximum likelihood technique used to perform the search; section 6.2 introduces the source classes and catalogs that we search over; section 6.3 develops the background and signal likelihoods needed for this technique; section 6.4 presents the theory and develops the models for the temporal likelihoods used for each different event class; and finally, section 6.5 presents the final results of the search.

6.1 Unbinned maximum likelihood method

We use an unbinned maximum likelihood search technique, following the formalism for this technique to be used for neutrino astronomy in [317], and further developed for time-dependent neutrino searches in [318]. Compared to a classical *binned* search, unbinned maximum likelihood searches are provably *at least* as statistically powerful, and have the potential to be orders of magnitude more sensitive [317].

In this application of the general unbinned maximum likelihood method, we attempt to distinguish between two distinct hypotheses: H_0 that the observed data consists only of *unwanted background*; and H_1, that the observed data consists of a mixture of some *wanted* signal and *unwanted* background. In our case, this technique provides a statistically rigorous method for determining whether the *observed data* contains a *statistically significant* contribution of "signal", at a specified significance level (typically 3σ or 5σ).

Following the prescription laid out in [318], we model the observed data (the four near-horizon events) as a weighted sum of a *signal probability distribution function* and a *background probability distribution function* (PDF) where the signal PDF describes the distribution of events under a pure-*signal* hypothesis and the background PDF describes the distribution of events under a pure-*background* hypothesis. We then construct and maximize a *log-likelihood test statistic* over the observed data to determine the best-fit weight for *signal* and *background*, and determine if there is a *statistically significant* fraction of *signal* in the data.

The total likelihood for observing N events, construct from a weighted sum of signal and background, is expressed as:

$$\mathcal{L}(n_s, \vec{\theta}_s, \vec{\theta}_b) = \prod_{i=1}^{N} \left[\frac{n_s}{N} S_i(\vec{\theta}_s) + \left(1 - \frac{n_s}{N}\right) B_i(\vec{\theta}_b) \right] \tag{6.1}$$

$$= \prod_{i=1}^{N} \left[\alpha S_i(\vec{\theta}_s) + (1-\alpha) B_i(\vec{\theta}_b) \right], \; \alpha = \frac{n_s}{N} \tag{6.2}$$

where

N = the total number of events observed (potentially signal + background),
n_s = the number of signal events observed,
α = the fraction of the total observed events that are signal,
$\vec{\theta}_s$ = the vector of parameters for the signal distribution,
$\vec{\theta}_b$ = the vector of parameters for the background distribution,
S_i = the probability density function of *signal* for event i,
B_i = the probability density function of *background* for event i.

Given the observed data, we *maximize* the likelihood, $\mathcal{L}$, by varying the parameters n_s, $\vec{\theta}_s$, and $\vec{\theta}_b$, to find the best-fit value of n_s, and the best-fit value of $\mathcal{L}$, $\mathcal{L}(\hat{n}_s, \hat{\theta}_s, \hat{\theta}_b)$. We use this best-fit likelihood to construct a *likelihood-ratio test-statistic*, λ, formed from the ratio between the best-fit likelihood under the signal hypothesis, $n_s > 0$, and the likelihood under the background hypothesis, $n_s = 0$.

$$\lambda = 2\log\left(\frac{\mathcal{L}(\hat{n}_s, \hat{\theta}_s, \hat{\theta}_b)}{\mathcal{L}(n_s = 0, \hat{\theta_{bg}}_s, \hat{\theta_{bg}}_b)}\right) \tag{6.3}$$

where

$\mathcal{L}(\hat{n}_s, \hat{\theta}_s, \hat{\theta}_b)$ = is the likelihood function evaluated at the parameters $\hat{n}_s$, $\hat{\theta}_s$, and $\hat{\theta}_b$ that *maximize* the likelihood function given $n_s > 0$ (i.e. the "best-fit" parameters),

$\mathcal{L}(n_s = 0, \hat{\theta}_{bg,s}, \hat{\theta}_{bg,b})$ = is the likelihood function evaluated at the *potentially different* parameters $\hat{\theta}_{bg,s}$, and $\hat{\theta}_{bg,b}$ that *maximize* the likelihood function given $n_s = 0$.

To determine the significance of a particular value of λ, we compare the observed test statistic, λ_{obs}, against the distribution of the test statistic under a sample of *background only* random trials. The significance of the observed value, λ_{obs}, is the empirically determined from the fraction of these *background only* that have a test statistic *at least as* large as the observed value.

$$\sigma = P(\lambda > \lambda_{obs}) \tag{6.4}$$

Since different source classes (SNe, GRB, etc.) may have different probability distribution functions for signal events from that source, we must specialize $\mathcal{L}$, and therefore λ, to each source class. We therefore write the total likelihood function as,

$$\mathcal{L}_K(n_s, \vec{\theta}_s, \vec{\theta}_b) = \prod_{i=1}^{N}\Big[\alpha S_{K,i}(\vec{\theta}_s) + (1-\alpha)B_i(\vec{\theta}_b)\Big],\ \alpha = \frac{n_s}{N} \tag{6.5}$$

where $\mathcal{L}_K$ is the likelihood for the K-th source class, and S_K is the distribution of signal events from the K-th source class. $\mathcal{L}_K$ is then also used to construct a source-class-specific test-statistic, λ_K.

Since a source class contains typically contains a large number of individual sources, $k \in K$, we must also specify a method for combining the signal probability density functions from each of the individual sources in the catalog. Since each source is independent, we can linearly combine the signal distributions from each individual source as follows

$$S_{K,i}(\vec{\theta}_s) = \frac{1}{\sum_k w_k} \sum_{k \in K} w_k S_{k,i}(\vec{\theta}_s) \tag{6.6}$$

where

$S_{K,i}$ = the combined signal probability distribution for the K-th source class,
k = an individual source in the source class K,
w_k = the *weight* for the k-th source,
$S_{k,i}$ = the signal PDF for the k-th source in the K-th source class for event i.

The weights, w_k, are chosen for a given search in order to maximize the potential search power and/or reduce the influence of backgrounds. However, since $S_{K,i}(\vec{\theta}_s)$ *must* be a true unit-norm probability density function, and $S_{k,i}(\vec{\theta}_s)$ are typically specified as unit-norm probability distributions, we must ensure that the *weighted* sum is also a unit-norm probability distribution by dividing by the sum of the weights.

All that remains to perform this search is to specify the signal and background probability density functions for each event and for each source class, $S_{k,i}$ and $B_{k,i}$, compute the source weights, w_k, find the best-fit likelihood ratio test-statistic, $\lambda_{k,obs}$, and calculate the significance of the observed events.

6.1.1 Maximum likelihood search over the near horizon events

We perform this search over the four observed near horizon events so we know *a priori* that $N = 4$, for this particular search. In our case, no additional parameters are needed to describe the signal and background ditributions used in our likelihood functions, so $\vec{\theta}_s = \vec{\theta}_b = \emptyset$.

Therefore, we use the following likelihood function

$$\mathcal{L}_K(n_s) = \prod_{i=1}^{N=4} [\alpha S_{K,i} + (1-\alpha) B_i], \quad \alpha = \frac{n_s}{N} \tag{6.7}$$

With this likelihood function, the likelihood ratio test statistic can be written as

$$\lambda_K = 2 \log\left(\frac{\mathcal{L}_K(\hat{n}_s)}{\mathcal{L}_K(n_s = 0)} \right) \tag{6.8}$$

6.2 Search & Catalog Selection

In the following sections, we lay out the parameter space over which we search for possible associations, and motivate the selection of astrophysical source catalogs, and sources, for each search.

6.2.1 Search region

For the unbinned maximum likelihood technique, we must choose the support of our search region over all the dimensions of our likelihood function—in particular, for our choice of $\mathcal{L}_K$, we must define a search region over the sky and over time. For time, we define our search region as the time of flight—approximately 28 days in duration. For the search region over the sky, since this is fundamentally a "near horizon" we wish to define an elevation band, from ANITA-IV's vantage point, that captures the bulk of the ν_τ effective area. Outside of the near horizon region, ANITA-IV has negigible (and rapidly decreasing) ν_τ effective area so the signal PDF is extremely small, and any spurious association is almost guaranteed to be a background event. Furthermore, due to the lack of a full empirical anthropogenic and UHECR background distribution over the full sky, it is challenging to estimate B_i far outside of the horizon, where our bootstrapping method breaks down. Therefore, we define our search region to be uniform in azimuth, and extending over the 3° band near the horizon. Nominally, this extends from $-5.9°$ to $-8.9°$, but the horizon location does change slightly as ANITA-IV's altitude changes over the flight (as well as the change in the observed ice thickness) and this is accounted for at any instance of time in the search.

As we are defining our search region in ANITA-IV's altitude-azimuth reference frame (altitude, azimuth, and time), our search region is a time-varying function over equatorial coordinates (right-ascension, declination, and time)—our search is nominally implemented in the altitude-azimuth reference frame, with conversions to equatorial coordinates as needed to compare against the known location of our astrophysical sources (specified in equatorial coordinates).

6.2.2 Supernovae catalog

For our supernovae search, we use the Open Supernova Catalog to find all supernova that occured in 2016 and the quarter of 2017 that also possess a valid redshift (in order

to discard spurious or low-significance supernova detections) [319]. This finds approximately 700 supernovae in 2016, and another 130 in the first three months of 2017. The distribution of this catalog over declination and over time is shown in Figure 6.1.

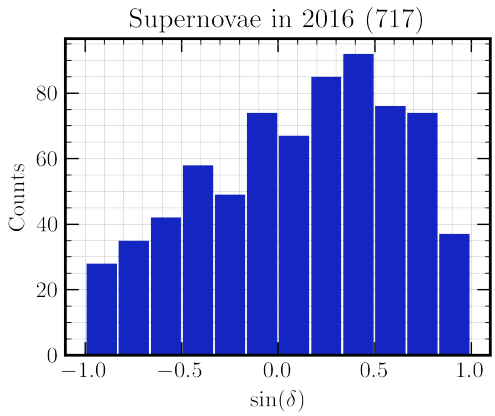

(a) The declination distribution of supernovae detected in 2016 in the catalog used in this work.

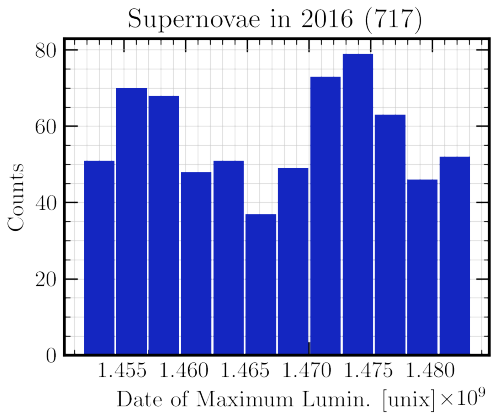

(b) The distribution of the date of maximum luminosity over supernovae in 2016 in the catalog used in this work.

Figure 6.1

6.2.3 Gamma-ray burst catalog

For our gamma-ray burst search, we use the IceCube GRBweb catalog that provides a complete list of identified GRBs using the Fermi space telescope and other gamma-ray observatories [320]—this is also the catalog used by recent IceCube GRB searches [315]. During 2016, nearly 300 gamma-ray bursts were identified in this catalog. This catalog provides the location of GRB in equatorial coordinates, as well as the "burst time" and an estimate of the T_{90} of the GRB (the time over which 90% of the gamma-ray flux was detected). The distribution of the declination and start time of each GRB in the catalog is shown in Figure 6.2, while the distribution of T_{90} is shown in Figure 6.3.

6.2.4 Tidal disruption event catalog

We use the Open TDE Catalog to identify all *potential* TDEs that occurred between 2014 and 2017, of which seven were identified [321]. This includes sources that were only *potentially* TDEs and also had possible classifications as AGNs, QSOs, and blazars.

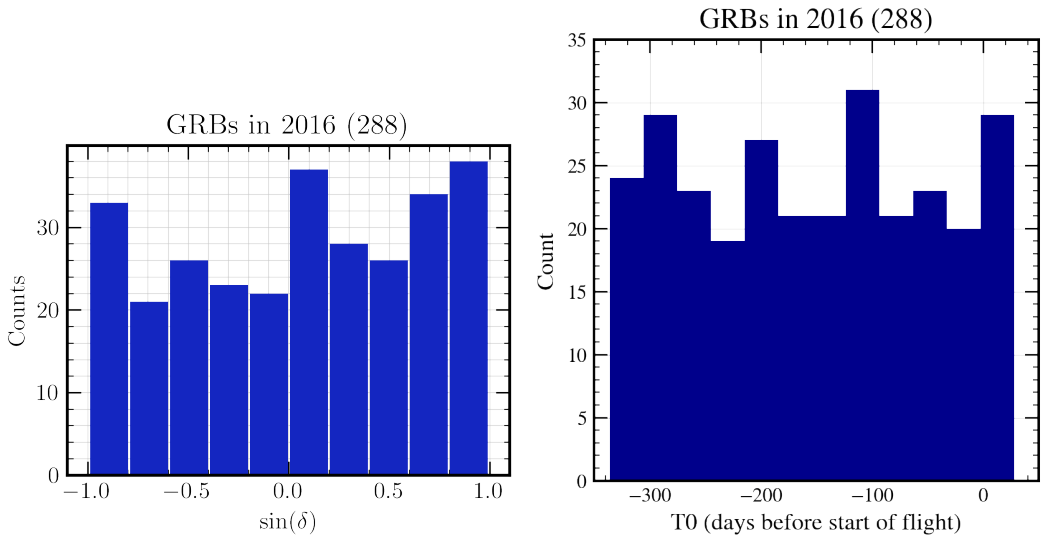

(a) The distribution of GRBs from the catalog used in this search as a function of declination.

(b) The distribution of the "burst time" of the GRBs in the catalog used in this search.

Figure 6.2

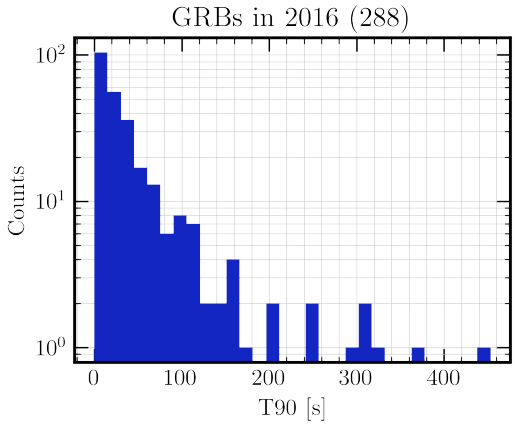

Figure 6.3: The distribution of T_{90} for the GRBs occurring in 2016 for the catalog used in this search. For this catalog, T_{90} is defined as the time period over which 90% of the GRBs total gamma-ray flux was detected.

The definitive identification of a tidal disruption event is observationally challenging and typically requires a large number of spectroscopic observations over time to identify the charactestic spectral characteristics, and the time decay of these properties [322].

Due to the extremely small tidal disruption event catalog, we did not produce distributions of the event times and declinations, as shown for previous catalogs, as we did not wish to potentially bias the "blinding" of the search by visualling recognizing if there were no sources in the region around our events.

6.2.5 Flaring blazar catalog

For our flaring blazar search, we use the Fermi space telescope Fermi All-sky Variability Analysis (FAVA) catalog that publishes a week-by-week list of different blazars that have been identified as flaring with at least 6σ significance [323]. The threshold for identification, 6σ, is the standard threshold (on the combined significance of the high energy and low energy γ flux) for the FAVA weekly flare announcement and was not modified for this search. A blazar that is flaring for multiple weeks shows up repeatedly in the catalog over each week that it was at least partially in a "flaring" state. Various data releases (versions) of this catalog have been used for past IceCube blazar searches. While typically we would prefer to use a published catalog of blazar flare durations, as has been used for past IceCube analyses, such a catalog does not exist for the ANITA-IV flight (the previous post-processed Fermi catalog includes flares up to six months mid-2016, roughly six months before the start of the flight) [324].

6.3 Near horizon signal likelihood models

In this section, we present the signal probability density functions, $S_{k,i}$, that we use for each source, $k \in K$, and for each event, i. This particular construction of the unbinned maximum likelihood technique *requires* that both $S_{k,i}$ and B_i are true unit-norm probability density functions over the *same support*.

To calculate our signal probability density function $S_{k,i}$, we decompose it into three *independent* probability distributions functions over different supports (we must ensure that when we construct B_i, it is also constructed over the same multi-dimensional support).

$$S_{k,i} = P_{spatial}(\Delta\phi_{k,i})\, P_{temporal}(\Delta t_{k,i})\, P_{elevation}(\theta_k, t_k) \tag{6.9}$$

where

$P_{spatial}$ = a PDF for the *spatial* separation between the k-th source and i-th event,
$\Delta\phi_{k,i}$ = is the angular distance on the sky between the k-th source and the i-th event,
$P_{temporal}$ = a PDF for the *temporal* separation between the k-th source and i-th event,
$\Delta t_{k,i}$ = is the temporal separation between the k-th source and the i-th event,
P_{sky} = a PDF for the *elevation* distribution, on the sky, of ν_τ from the k-th source,
θ_k = is the elevation angle of the k-th source (in ANITA-IV's reference frame) at time t_k.

This deconstruction is motivated by three intuitive heuristics: (i) that events *spatially* closer *on the sky* to a potential neutrino source are more probably (with an important caveat discussed below); (ii) that events that occur close *in time* to the peak of the time-dependent neutrino fluence from that source; and, (iii) that events closer to the horizon, where ANITA's ν_τ effective area is maximized, are more likely to be ν_τ's.

Since both $S_{k,i}$ and B_i must be true *probability distribution functions* over this support, they must satisfy the following normalization condition:

$$\int_{\Omega_{search}} \int_{T_{flight}} \int_{\theta_{search}} S_{K,i}\; d\theta\; dt\; d\Omega = 1 \tag{6.10}$$

$$\int_{\Omega_{search}} \int_{T_{flight}} \int_{\theta_{search}} B_i\; d\theta\; dt\; d\Omega = 1 \tag{6.11}$$

where:

Ω_{search} = is the solid angle on the sky over which the search is performed,
T_{flight} = is the time window for ANITA-IV's flight/livetime,
θ_{search} = is the elevation angle band near the horizon over which the search is performed,
θ = elevation angle,
t = time,
Ω = solid angle,

This normalization condition requires that both $S_{K,i}$ and B have units of $\mathrm{sr}^{-1}\ \mathrm{s}^{-1}\ \mathrm{rad}^{-1}$. In the following sections, we motivate and construct the various sub-components of $S_{K,i}$: *spatial*, *elevation*, and *temporal*.

6.3.1 Spatial probability density function

The *reconstructed* direction of ultrahigh-energy ν_τ observed from a point-like neutrino source by ANITA-IV are not expected to be *exactly* spatially coincident with the known location of the source for several reasons:

1. The event direction has an uncertainty due to measurement and reconstruction error, typically $\sim 0.2^\circ$ for ANITA-IV;

2. The "opening angle" of the radio emission (both Askaryan and geomagnetic), typically $\sim 1^\circ$, biases the observed direction of the radio emission (the "reconstructed direction" of the event), and the direction of the neutrino source. Since ANITA-IV only observes each shower from a *single location*, ANITA-IV cannot resolve the *azimuthal* ambiguity in the *azimuthal angle* that ANITA-IV observed the emission; this creates an annular region on the sky for neutrino source locations consistent with our observed geometry.

3. For certain classes of astrophysical objects, the reported catalog location can have significant position uncertainty—this is particularly true of short-lived non-repeating sources like gamma-ray bursts.

As shown in section 4.3, the `tapioca` simulation code can *forward model* the expected distribution of reconstruct event locations given the specific location of a point-like neutrino. An example of one of these two-dimensional angular distributions is shown in Figure 6.4, generated with `tapioca`, and is a full end-to-end neutrino-to-detection simulation including all relevant effects (neutrino absorption, tau decay ranges, shower energy distributions, etc.) This particular simulation included a 0.2° uncertainty in the reconstructed event direction but did not include any uncertainty in the location of the point source, which is located in the center of the "annulus". The "annulur"-part of this distribution is formed from the *expected* Cherenkov-angle beaming, discussed in section 3.1, of the geomagnetic emission from the shower. However, there is also a top-to-bottom

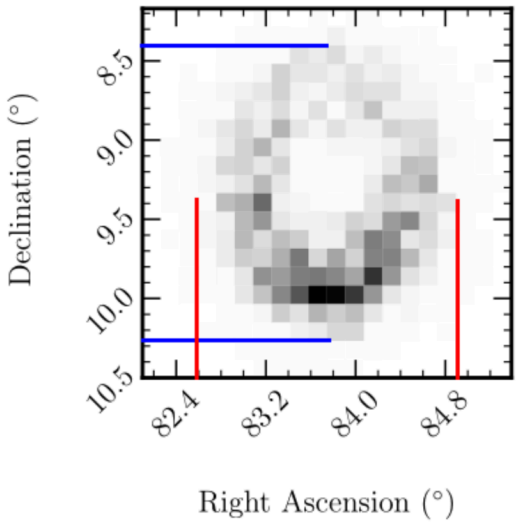

Figure 6.4: The 2D histogram of the point-like neutrino source directions consistent with observing an event whose incoming direction reconstructs to a point in the center of this "ring". This was produced using the `tapioca` simulation discussed in detail in Chapter 4.

assymmetry—this is due to the suppression of the tau neutrino flux as a function of elevation angle.

Since the strength and steepness of this suppression depend upon the *absolute* elevation angle of the ring, we decouple this into two components: (i) a pure spatial "ring" component centered around the location of the event; and, (ii) the elevation angle dependent sensitivity, multiplied vertically over the ring, to account for the different possible assymetries in these rings (the elevation angle component is discussed in detail in section 6.3.2).

It is possible to directly use this 2D angular histogram as the probability distribution function the spatial separation betwen a neutrino source and an event. However, there are several complex propagation effects that can *potentially* perturb the shape of this distribution over the nearly 600 km propagation of the radio emission from near-the-horizon to the ANITA-IV payload. As discussed in section 5.4, many of these effects are intractable to simulate and are a function of the *exact* unknown atmosphere at the time of event. Given these model-related uncertainties, there is the possibility that directly using this simulated distribution would be *over-specified* and may strongly disfavor events that could *potentially* be signal neutrinos.

Therefore, we "fill-in" the center of the ring with a uniform probability density—a Gaussian was explicitly not chosen as the center of the ring is *not* the most-likely origin and we did not want to enforce that by using a Gaussian PDF. To enable the probability density function to be evaluated analytically during the likelihood optimization, we fit

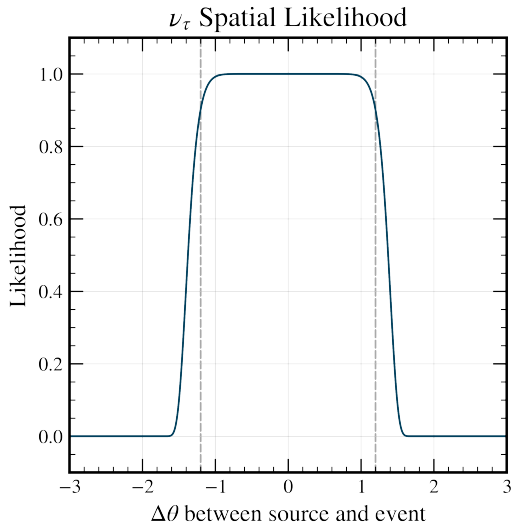

Figure 6.5: The "smooth" top-hat likelihood function used in the search to determine how likely a given angular separation between a source and event. This was generated by approximately fitting Equation 6.12 to Figure 6.4.

a top-hat function to the average radial cross-section of Figure 6.4; the region inside the "ring" is ignored during the fitting process in order to get an accurate fit between the two functions that differ strongly in shape in this region. The top-hat probability density function used is:

$$P_{spatial}(\Delta\theta; w, n) = e^{-2\left(\frac{\Delta\theta}{w}\right)^n} \quad w = 1.842,\ n = 6 \tag{6.12}$$

A plot of this fitted top-hat probability density function is shown in Figure 6.5. This is the *spatial* probability density function, $P_{spatial}$, over the separation between the k-th source and the i-th event, $\Delta\theta_{k,i}$ in Equation 6.9 and has units of inverse steradians (sr^{-}1).

6.3.2 Elevation probability density function

As discussed in section 6.3.1, the simulated Cherenkov ring has an asymmetry that changes based on the elevation angle of each differential area element on the sky. This is not included in Equation 6.12; however, it is included in the total likelihood, $\mathcal{L}_K$, through the use of the $P_{elevation}$ term. This probability density function, with units of inverse radians (rad^{-1}), is a rescaled version of ANITA-IV's ν_τ effective area and acts as an elevation angle dependent weight for "how likely" we are to detect a ν_τ air shower from that elevation angle on the sky. Since $P_{elevation}$ must be a *unit-norm* probability distribution function (so that $S_{K,i}$ is unit-norm), we take the elevation angle-dependent effective area of Figure 5.5, and renormalize it over the elevation angle band used in the likelihood search.

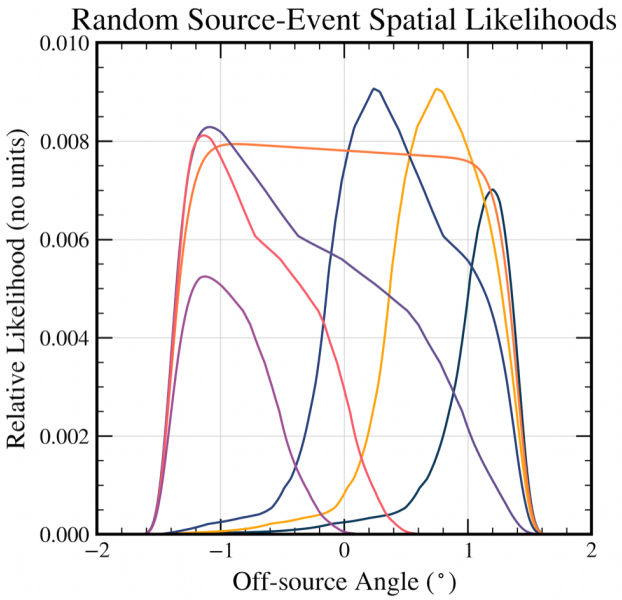

Figure 6.6: Various spatial likelihood functions, over the source-event angular separation, derived from the convolution of the off-axis tophat likelihood function with the elevation angle dependent effective area.

For each pair of directions for a neutrino source and an event, the combination of the "angular distance" PDF modeled with the top-hat, and the elevation angle dependence *over* that top-hat function, can construct variety of assymetrical likelihood functions similar to that shown in Figure 6.4—several examples of these likelihood functions, produced on an event-by-event basis, is shown in Figure 6.6. The exact shape produced for a given event depends upon the relative orientation of the event and the source: for an event-source pair separated only by azimuth, we expect almost no assymetry over angular separation as the ν_τ effective area is principally elevation dependent, not azimuth dependent; alternatively, for an event-source pair separated predominantly by elevation, we expect a significant amount of assymetry over the angular separation.

6.3.3 Temporal probability density functions

As motivated in section 5.4, this search is focused on *transient* astrophysical sources as steady-state sources are challenging to reconcile with limits from Auger and IceCube. Each of the chosen source classes has different (expected) timescales for the neutrino emission and this information allows us to reject background *spatial* associations if they are incompatible with the timescale of the given neutrino source.

Since different source classes have different timescales, we must specialize $P_{temporal}$ for each individual source class. We present these models, as well as their theoretical motivation, in section 6.4.

6.3.4 Source-specific weights

As shown in Equation 6.6, each source is multiplied by a source-specific weight, w_k, when summing the likelihood over the entire astrophysical catalog for a given search. The motivation for doing a *weighted sum* is that certain sources may be significantly *more* likely to produce a detectable signal than other sources which may be significantly *less* likely to produce a signal. A spatio-temporal association with a source from which we expect *more signal events* should be treated with higher significance than a source for which we expect *little to no signal*.

For this search, we make each weight directly proportional to the *time-integrated exposure* of ANITA-IV to ν_τ EASs from a point-like E^{-2} neutrino flux at each source location. Due to the extremely narrow field of view of the ν_τ channel ($\mathcal{O}(1^\circ)$), many catalog sources are extremely unlikely, or practically impossible, for ANITA-IV to detect a ν_τ from. For example, a source with a declination close to $+5^\circ$ is likely to spend significant time near ANITA-IV's horizon and can therefore accumulate significant ν_τ exposure. On the other hand, an identical source located at a declination of -30° will *never* approach the horizon for ANITA-IV and as such will have practically zero integrated exposure (the suppression of the neutrino flux via Earth absorption is orders of magnitude stronger away from the horizon than for skimming near-horizon trajectories).

To calculate w_k, we use

$$w_k \propto \int_{T_{flight}} \int_{\Omega_{sky}} \int_{E_{min}}^{E_{max}} \mathcal{A}(t, \vec{\omega}, E)\, \hat{\mathcal{F}}(t)\, E^{-2}\, dE\, d\Omega\, dt \tag{6.13}$$

where

T_{flight} = is the total time of the flight,
Ω_{sky} = is the total solid angle of the sky,
E_{min}, E_{max} = are the minimum and maximum neutrino energies used in the search,
$\mathcal{A}(t, \vec{\omega}, E)$ = is the effective area of ANITA-IV to ν_τ air showers at a given time t, in a given direction ω, at a given neutrino energy E,
$\hat{\mathcal{F}}(t)$ = is a unit-norm function with units of inverse time that models the neutrino fluence we expect from this object, i.e. $\hat{\mathcal{F}}(t) \propto P_{temporal}$ (see section 6.4 for more details).

We use $\propto$ here as after calculating the above-integral for each source in the catalog, we renormalize each w_k such that the *sum of all weights*, w_k, is one. This is to preserve the PDF-ness of $S_{K,i}$ when summing multiple PDF-like $S_{k,i}$ for all $k \in K$. While we use an E^{-2} flux assumption here, the *relative weights* between sources are only negligibly changed by changing this flux from E^{-1} to E^{-3} (the *absolute exposure* can change drastically, but since the weights are *renormalized* to have unit-sum, the *relative* weights are practically unchanged).

The use of these weights *significantly* improves the potential search significance by discounting sources for which we are extremely unlikely to detect a ν_τ air shower, so that we can reject associations with that search as *background*. The net effect is that the weights reduce our total catalog of sources down to an "effective catalog" that can have an order of magnitude or more *fewer* sources. For example, our GRB catalog contains nearly 300 total GRBs for 2016—when including these source specific weights, only six GRBs account for $(1 - 10^{-7})$ of the total integrated GRB exposure, nominally reducing the background chance association probability (in this example) by $\sim 6/300$.

6.3.5 Background Model

When searching for ν_τ-induced extensive air showers, there are several possibilities for other events that could possible "leak-in" to our event sample as "backgrounds". The three principal background classes, all considered in this analysis and discussed extensively in section 5.4, are

1. Anthropogenic sources of impulsive radio emission,

2. *Above*-horizon ultrahigh-energy cosmic rays whose (mis)-reconstructed direction points *below* the horizon,

3. *Below*-horizon "reflected" ultrahigh-energy cosmic rays whose polarity was (mis)-identified to be non-inverted (all "reflected" cosmic rays should have inverted polarity as discussed in section 3.1)

Typically, applications of the unbinned maximum likelihood technique for neutrino searches use Monte Carlo simulations of the various background possibilites or background-only sideband data to empirically construct a background probability density function. However, as discussed in section 3.1, there does not exist a full simulation pipeline of above-horizon and reflected UHECRs leaking into the ν_τ channel; this is principally due to the many challenges simulating events extremely close to the horizon, where propagation and surface effects can be extremely important. Therefore, we construct a semi-empirical background PDF using an analysis of each individual ANITA-IV event, previously-validated models for ANITA-IV's acceptance to cosmic rays, and some assumptions regarding the distribution of anthropogenics.

Each observed near-horizon event has a different chance of being in each of three classes; these chances depend on the probability that the event is anthropogenic, P_{anthro}, the probability that we (mis)-reconstructed the event direction to be below the horizon, $P_{hor,flip}$, and the probability that we (mis)-identified the polarity, $P_{pol,flip}$.

We construct a probability density function for the elevation angle dependence of these backgrounds in Equation 6.14 and justify the various assumptions in the following sections.

$$B(\theta_i) = \left(\frac{1}{T\,\Delta\theta}\right)\Big[\frac{\bar{P}_{anthro}}{\Omega} \tag{6.14}$$

$$+(1-\bar{P}_{anthro})\big(P_{pol,flip,i}\,P_{refl,CR}(\theta_i) \tag{6.15}$$

$$+(1-P_{pol,flip,i})\,P_{AH,CR}(\theta_i)\big)\Big] \tag{6.16}$$

where

$B(\theta_i)$	=	the probability density of background events as a function of elevation angle at the payload,
T	=	the total integrated time of the flight,
$\Delta\theta$	=	the span in elevation angle near the horizon over which the search is performed,
Ω	=	the total solid angle of the search region on the sky,
$\bar{P}_{anthro}$	=	the expected probability of having at least one anthropogenic background event in the near horizon sample,
$P_{pol,flip,i}$	=	the probability that the i-th event has (mis)-reconstructed polarity,
$P_{refl,CR}(\theta_i)$	=	the probability density function of reflected UHECRs detected by ANITA-IV as a function of elevation angle,
$P_{hor,flip,i}$	=	the probability that the i-th event flipped the horizon during reconstruction,
$P_{AH,CR}(\theta_i)$	=	the probability of an above-horizon UHECR flipping the horizon and being reconstructed to θ_i (where θ_i is *below* the horizon).

In order to properly construct $\mathcal{L}_K$, B_i must be unit-norm over the same support as S_K and therefore must have units of $\text{sr}^{-1}\,\text{s}^{-1}\,\text{rad}^{-1}$. The combined background PDF, $B(\theta_i)$, for an event with similar properties to event 721xx as a function of changing elevation angle is shown in Figure 6.7.

Anthropogenic background estimate

We are performing this search over a subset of the highly-selected ANITA-IV event sample, identified and selected by ANITA-IV analyst Andrew Ludwig [260] with follow-up analysis by Peter Gorham and others [257]. An estimate for the number of anthropogenic events that leaked into the final event sample was performed during this analysis using a variety of sideband channels. The distribution of the number of true signal events (i.e.

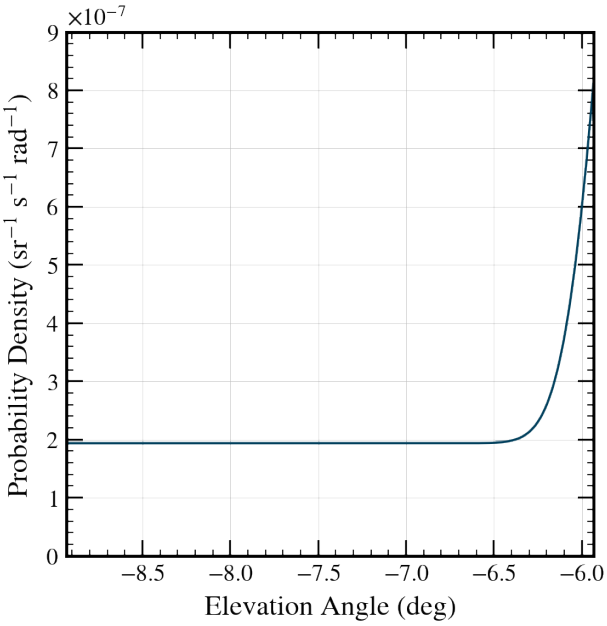

Figure 6.7: The total background probability density function used in this search for an event with parameters otherwise consistent with event 721xx, but with a changing elevation angle over the search elevation band.

four minus the number of anthropogenic events) expected in the event sample is shown in Figure 6.8.

Andrew's background estimate for the number of anthropogenic events in the sample can be constructed with the following statistical model

$$N_{bg} \sim \text{Poisson}\left(\text{Gamma}(2.5, 1)\frac{\text{Gamma}(32.5, 1)}{\text{Gamma}(207.5, 1)}\right) \approx \text{Poisson}(0.393\ldots) \quad (6.17)$$

where $\approx$ indicates that the full function is well approximated a standard Poisson distribution with $\mu = 0.393\ldots$. where

$\text{Gamma}(k, \theta) =$ is the probability density function of a gamma distribution with shape parameter, k, and scale parameter θ,

$\text{Poisson}(\mu) \quad =$ is the probablity density function of a Poisson distribution with mean mu.

The background PDF used in the likelihood search, B_i is *not* an estimate of the *number* of background events in the sample—B_i is the *probability density* of *where* we are more likely to see background *given* that the event in question *is* background. So, for $\bar{P}_{anthro}$, we need the probability that we got *at least* one background event (as opposed to the *number* of background events). We calculate this with a simple Poisson CDF

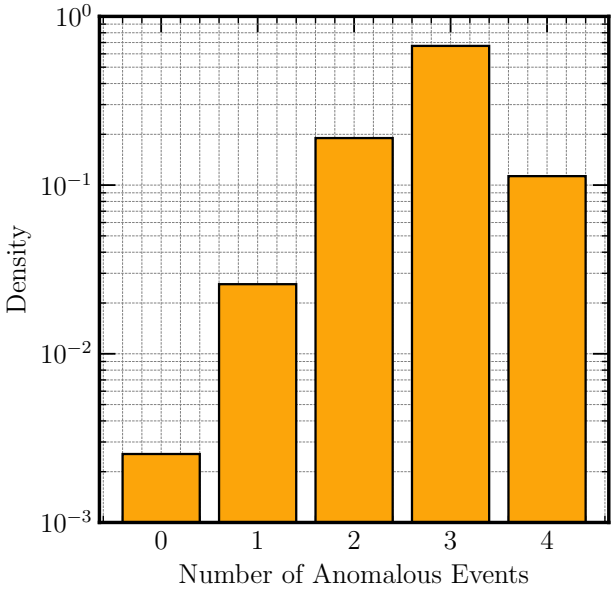

Figure 6.8: The probability density distribution (i.e. normalized event density) for the true number of near-horizon anomalous events observed by ANITA-IV under the assumptions of the toy Monte Carlo simulations described in [257]

$$\bar{P}_{anthro} = \frac{\Gamma(\lfloor 1+1 \rfloor, \mu)}{1!} = \Gamma(2,\mu) = 0.304\ldots, \quad \mu \approx 0.393\ldots \tag{6.18}$$

Therefore, we take the total probability of getting an anthropogenic event to be $\bar{P}_{anthro} \approx 0.304$—this is used in Equation 6.14 as the relative weight assigned to the anthropogenic vs. cosmic ray hypothesis.

While the true distribution of *post*-analysis anthropogenics on the sky is unknown, the ANITA-IV event analysis was highly selective, reducing $\mathcal{O}(100 \times 10^6)$ events down to the final sample of 28 UHECRs. This analysis focused on removing many of the primary time-varying sources of anthropogenic background events, such as Antarctic bases moving in-and-out of view, with extremely high efficiency. We assume that any single anthropogenic background event leaking into our event sample (with $\mu \approx 0.3$) is *approximately* equally likely to have "leaked in" at any point in the flight (i.e. that the distribution of falsely selected anthropogenic background events is *time-independent*)—this motivates the $1/T$ term used in Equation 6.14.

Since our search is perfomed only over a narrow region in elevation angle near the horizon ($\Delta\theta \approx 3°$), we assume that any *post*-analysis anthropgenics in the event sample are *approximately* uniformly distributed in solid angle *only over this narrow 3° band*. This

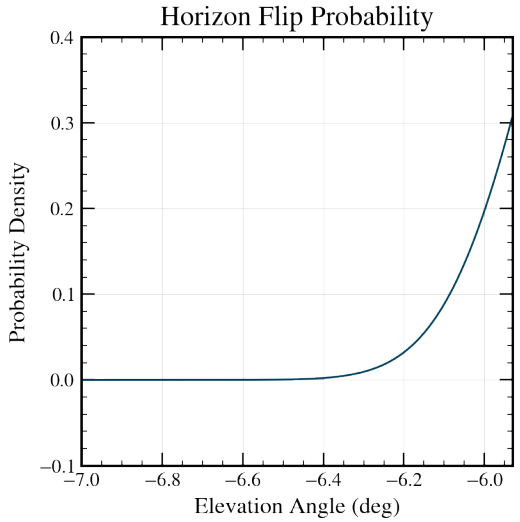

Figure 6.9: The probability density of an above-horizon UHECR "flipping" below the horizon to be reconstructed at the specified elevation angle.

assumption allows us to proceed with a search without a full knowledge and simulation of anthropogenics that leaked through the highly-efficient ANITA-IV analysis.

Probability of a "Horizon Flip"

We estimate the probability, $P_{hor,flip}$, that the event has flipped the horizon by calculating the integral probability that a Gaussian, centered at the elevation angle of the event, θ_{ev}, with a standard deviation equal to the event pointing uncertainty extends $> 0.1^\circ$ *above* the horizon; this is shown in Equation 6.19.

$$P_{hor,flip}(\theta_{ev}) = \int_{\theta_h+0.1^\circ}^{\infty} \mathcal{N}(\theta_{ev}, \sigma_\theta), \quad \sigma_\theta \sim 0.2^\circ \tag{6.19}$$

where

$\mathcal{N}(\mu, \sigma)$ = is a Normal PDF with mean, μ, and variance σ^2,
θ_{ev} = the reconstructed elevation angle of the event,
σ_θ = the estimated pointing uncertainty of this event (typically 0.2°),
θ_h = the elevation angle of the horizon at the time of this event

Equation 6.19 can be evaluated over a range of elevation angles to construct a probability density function over elevation angle for the probability that an event at this elevation angle is from above the horizon; this is shown in Figure 6.9 and is labeled as $P_{AH,CR}(\theta_i)$ in Equation 6.14.

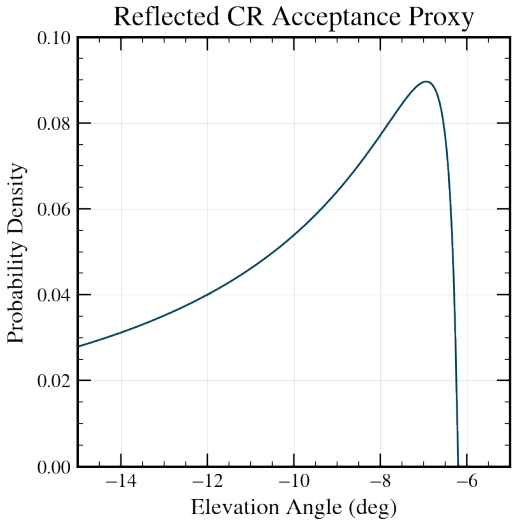

Figure 6.10: The (renormalized) UHECR effective area as a function of elevation angle used as a proxy for the distribution of reflected UHECRs that "flip" polarity and then be mistaken for an ν_τ event. Note, in this plot, the $P_{pol,flip}$ leading term has not been multipled through yet.

Probability of a "Polarity Flip"

There is also the possibility that the near horizon events are ordinary reflected UHECRs that have had their polarity (mis)-reconstructed. The chance for each observed event to have misreconstructed polarity was calculated in [257] as is typically $\mathcal{O}(10^{-4})$ for most of the events, with the exception of the 198xx which is $\mathcal{O}(10^{-3})$. This makes the polarity reconstruction possibility strongly sub-dominant compared to the anthropogenic and above-horizon possibilities. However, we still wish to correctly treat this class of background events.

We use ANITA's elevation angle effective area to reflected UHECRs as a proxy for the elevation angle distribution of polarity (mis)-reconstructed events—this was first calculated in [273] and is shown in Figure 6.10. This (renormalized) effective area is $P_{refl,CR}(\theta_i)$ in Equation 6.14.

6.3.6 Significance calculation of our search

As discussed in section 5.4, we do not currently have a Monte Carlo simulation capable of producing simulated background distributions from our three background possibilities (anthropogenic, above horizon UHECRs, reflected UHECRs). For this analysis, we also did not have access to a full sub-threshold background event sample that could be used as an empirical estimate of the distribution of background events.

Therefore, to generate the statistical sample of background events needed to evaluate the significance of our search, we use a bootstrapping approach. For every random trial we wish to generate, we sample $N = 4$ events from the near horizon sample (with replacement), scrambling the azimuth uniformly on $[0°, 360°]$ and scrambling the event time uniformly throughout the flight. Since ANITA-IV is nominally orbiting the South Pole, changes in azimuth are almost exclusively mapped into changes in right-ascension while changes in elevation are almost exclusively mapped into equivalent changes in declination. By scrambling azimuth, we are in effect scrambling the right-ascension of any potential event-source association but preserving the "near-horizon-ness" of the event sample. Similarly, by redistributing the time of events throughout the flight, we are scrambling any temporal association between an event and an astrophysical source.

The distribution of right-ascension and declination produced by this boostrapping process is shown in Figure 6.11. The "peaks" in the declination distribution are *not* due to the small event sample—they are the location of the "near-horizon" region when integrated over the multiple orbits that ANITA-IV made around the South Pole with distinctly different average latitudes. By changing the latitude of an orbit, you shift the declination band corresponding to ANITA-IV's "horizon" approximately by the same magnitude as the shift in latitude.

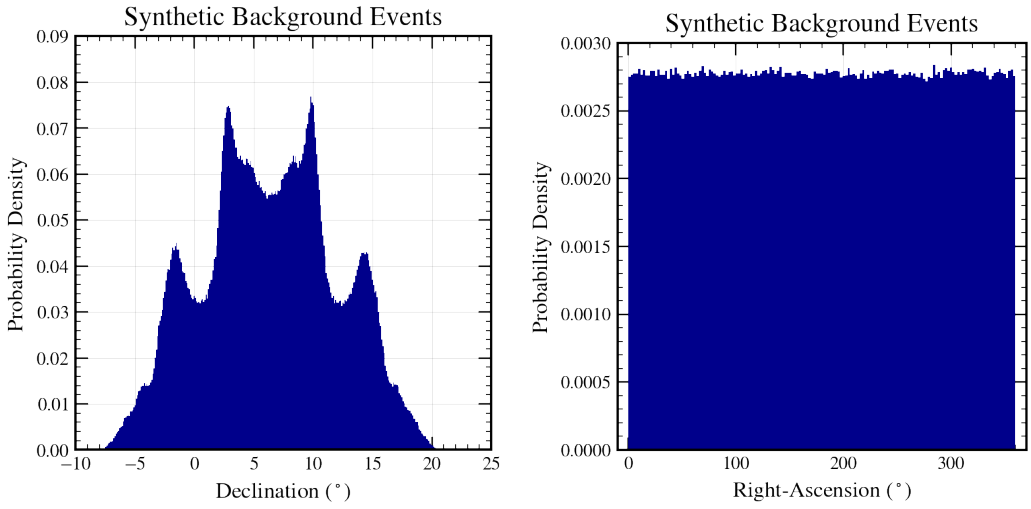

Figure 6.11: The distribution of right-ascension and declination from the bootstrapping process used to generate random background events for this search technique.

To calculate the significance of a specific search, each random "flight realization" in this bootstrapped event sample is input to our likelihood fitter and the resulting test statistic is observed (we typically repeat this process 20M–30M times in order to accumulate statistics at the 5σ level). To evaluate the significance of the data observed in the flight, we calculate the observed test statistic and determine what fraction of the bootstrapped samples had a test statistic at least as large as what was observed—this fraction is the p-value of the search and can be converted to a "sigma"-level using a standard normal CDF.

6.4 Astrophysically-motivated models for the time dependent neutrino fluence

In this section, we present some high-level models for the temporal probability distribution functions, $P_{temporal}$, for each source class that can significantly improve the power of our search. We do not claim that these various models represent the *actual neutrino fluence*—and that is not required by this technique— but they represent some reasonable assumptions about "how likely" we expect a neutrino with the corresponding time-delay to be "associated" with the sources. Wherever possible, we make conservative assumptions to avoid overly restricting our search (and potentially throwing away an actual source neutrino).

We must specify this independently for each source class as different classes are expected to have drastically different timescales and temporal probability density functions.

6.4.1 Supernovae temporal emission model

As discussed in section 1.3.2, it is phenomenologically challenging for ordinary supernovae to produce ultrahigh energy neutrinos. However, specific supernova subclasses, such as hypernovae or engine-driven supernovae, are potentially capable of producing such energetic neutrinos. Since there are no temporal models "unique" to these supernovae subclasses, we follow the methodology of other supernovae searches in assuming that the neutrino fluence approximately follows the total optical-and-ultraviolet (OUV) luminosity of the supernovae [163].

As we do not have access to individual light curves for most supernovae in our catalog, we use a sub-sample to construct an "average" *approximate* lightcurve that is explicitly conservative—this negatively impacts the possible significance of our search but allows

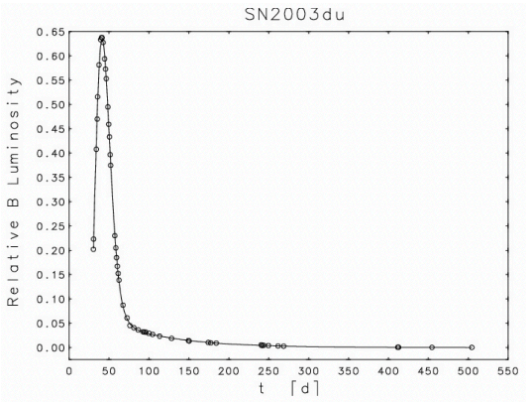

Figure 6.12: An example of a supernovae light curve, from SN2003du, fit to the sum of a Weibull and exponential model described in [325]. Figure from [325].

us to proceed without a full analysis of nearly 800 individual supernovae light curves recorded by multiple different supernova observatories.

We use the model and data of [325] that analyzed the total OUV luminosity of a population of supernovae and fit them to the sum of a Weibull and exponential distribution model. An example of one of these light curves fit with this Weibull+exponential combination is shown in Figure 6.12. A Weibull distribution is used to fit the turn on, peak, and initial decay of the superovae light curve; the exponential then "takes over" and softens the decay faster-than-exponential decay of the Weibull. We use this same model in our analysis, implemented using

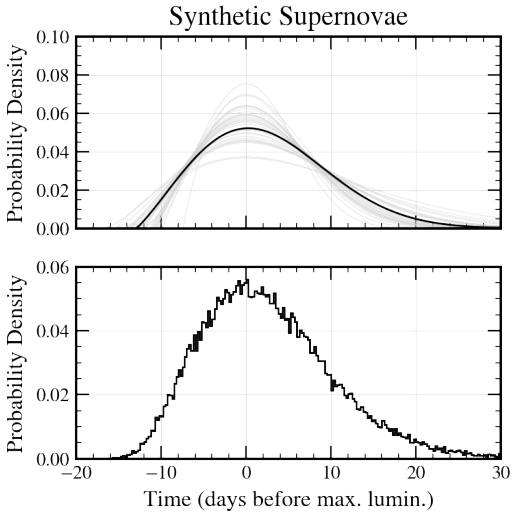

Figure 6.13: The distribution of light curves generated by resampling the parameters of [325] with their sample variance to produce a "population" of supernovae light curves.

$$\mathcal{L}_t(T_i; k, \lambda, \tau) \propto \alpha\,\text{Weibull}(T_i - T_{max} + \Delta T_{mode}; k, \lambda) + \beta\,\text{Exponential}(\max(0, T_i - T_{max}); \tau) \tag{6.20}$$

where

T_i	=	is the time of the i-th event,
$\text{Weibull}(t; k, \lambda)$	=	is the PDF of a two-parameter Weibull distribution over t with shape parameter, k, and scale parameter λ,
$\alpha,\ \beta$	=	are scale factors from [325] needed to "join" the Weibull and exponential terms in the right ratios,
$\text{Exponential}(t; \tau)$	=	is the PDF of an exponential distribution over t with time constant τ,
T_{max}	=	is the *absolute* time of maximum OUV supernovae luminosity,
ΔT_{mode}	=	is the time-delay between the start of the Weibull function and its *mode* (i.e. the delay between the "start" of the supernovae and the time of peak OUV luminosity).

By constructing the time delays following [325], and as in Equation 6.20, we place the time of maximum *measured* supernovae OUV luminosity at the peak (mode) of the Weibull distribution. [325] provides measured values for α, β, k, λ, and τ for a sample of supernovae. An example of various light curves re-sampled from this distribution using the mean and variance of each parameter is shown in Figure 6.13.

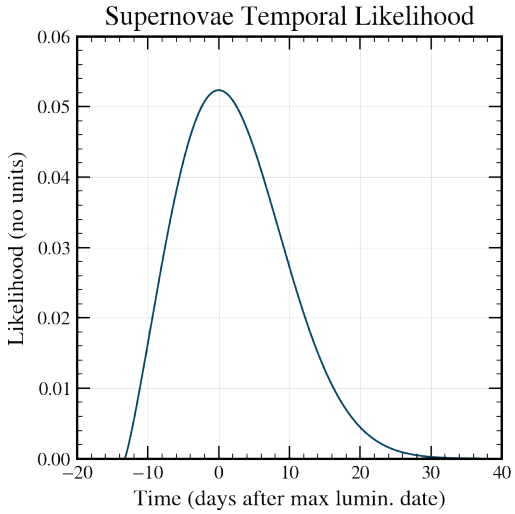

Figure 6.14: The un-normalized supernovae temporal likelihood function used in this search in linear units. This predominantly shows the Weibull function used for the prompt emission. The exponential tail begins to dominate after 20 days.

Since we do not have the light curves for the supernovae in our catalog (so we cannot specialize Equation 6.20 to each supernovae), we use the *average* values of these distributions as "fixed parameters" in Equation 6.20 to create an "average light curve". To ensure that our distribution is slightly conservative, we round up λ from 16.9 days to 18 days (scale parameter), and round up τ from 18.4 days to 20 days. This "average" light curve, shown in Figure 6.14, is used for each supernovae in the analysis, centered at the date of maximum OUV measured luminosity. As the temporal PDF for each supernovae must be a true PDF over the flight, and the light curves of these supernovae can have a support that is significant outside or larger than the flight, we must individually renormalize this average fluence model for each supernovae in our catalog such that it satisfies Equation 6.10.

6.4.2 Gamma-ray burst temporal emission model

Gamma-ray bursts (GRBs) are one of the promising sources of high-energy and ultrahigh-energy neutrinos (see section 1.2.2). There exist a plethora of models for the neutrino emission from gamma-ray bursts—some models focus on *prompt* emission, that occurs on short time-scales (typically seconds), and *late* emission that can occur on much longer timescales (potentially hours). Lacking any model constraints due to lack of significant GRB neutrino measurements at these energies, we perform two independent searches—one for *prompt* emission and one for *late* emission. In addition, GRBs are typically split into two sub-classes—short-lived GRBs (sGRBs) and long-lived (LL-GRBs)—based upon

the duration of their prompt emission. An example of the different timescales of GRB lightcurves for sGRBS and LL-GRBs is shown in Figure 6.15.

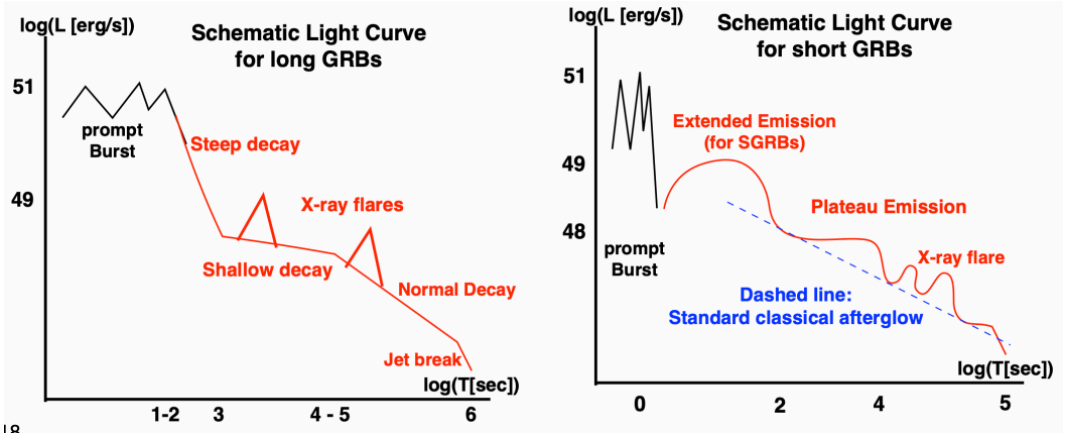

Figure 6.15: A schematic light curve of the overall timescales and fluences expected from a nominal short-lived gamma-ray burst (sGRB) versus a long-lived gamma-ray burst (LL-GRB). Figure from [326].

The observed gamma-ray fluence from a GRB can vary significantly in temporal shape—some are monotonically decaying while others can have complex multi-modal structure over the lifetime of the GRB. An Without a strong model-specific prediction for the time-dependence of the corresponding neutrino fluence, we use an exponential probability density function over time. An exponential distribution is the *maximum entropy distribution* over $[0, \infty)$ (i.e. time delays) with a finite mean (i.e. a convergent first-moment). A *maximum entropy distribution* is the probability distribution that contains the *least additional information* (i.e. maximum entropy) given the constraints—these are preferred in likelihood searches as they are the "least informative" distributions (i.e. those with the fewest assumptions). For our search, an exponential distribution assigns the most probability to events that are observed at the time of the GRB ignition, with a decreasing likelihood as the event moves later after the GRB.

To capture both types of GRB fluence models, we use two different time-constant, τ, for the exponential in each source.

For the *prompt* search, we use a time-constant equal to the T_{90} of the specific GRB (the time interval over which 90% of the gamma-ray counts were observed) provided by our catalog. For our catalog, $\langle T_{90} \rangle \approx 2\,\text{s}$, so we are typically searching for events that occur within a few seconds of the GRB ignition.

For the *late* search, we follow the model of [326] (shown in Figure 6.15) and use $\tau = 10^3$ for the *late* emission from *sGRBs* and use $\tau = 10^4$ for the *late* emission from *LL-GRBs*. As for all of the other source classes, we separately renormalize the temporal probability curve of each GRB over the flight to preserve the "PDF-ness" of $S_{k,i}$ and $S_{K,i}$.

6.4.3 Tidal disruption event temporal emission model

Tidal disruption events (TDEs) are considered a strong candidate for point-like neutrino fluence. Due to their extremely low rate, it is challenging for the population of TDEs to reproduce the majority of the observed UHECR and expected neutrino flux, but individually they have the potential to be extremely luminous point-like neutrino sources [145, 146, 148, 327]. This is complicated by the difficulty in separating TDEs from other astrophysical objects, such as blazars and AGNs, that can have similar observational signatures [148, 328, 329]

IceCube has claimed an association between three of the candidate neutrino events, IC191001A, IC200530A, and IC191119A, and three known tidal disruption events, AT2019dsg, AT2019fdr, and AT2019aalc [330]. These events were observed with significant time delays with respect to the tidal ignition—150 days for two of the detections, and 300 days for the other.

The currently most supported model for the delay between the *ignition* of the TDE and any subsequent neutrino emission is the "infrared dust echo" model [329]. In this model, constrained to both multi-messenger electromagnetic observations and the IceCube observations, the initial TDE ignition does not create sufficient density of high energy targets for efficient photo-hadronic production of high-energy and ultrahigh-energy neutrinos. Instead, the initial optical and ultraviolet emission radiatively heats the surrounding dust cloud left by the ignition over a period of several months. The infrared photons in the dense dust cloud then act as the targets for photohadronic production of neutrinos, instead of the prompt optical and ultraviolet emission, with a corresponding time delay between these two processes of $\mathcal{O}(\gtrsim 150\,\text{days})$ [329].

The OUV (red & green) and infrared (violet and purple) luminosity of these three TDEs along with the detection time of the "corresponding" IceCube neutrino is shown in Figure 6.16. In all three cases, the candidate neutrinos were detected at times around the peak of the infrared luminosity, not the OUV luminosity. These observations provide

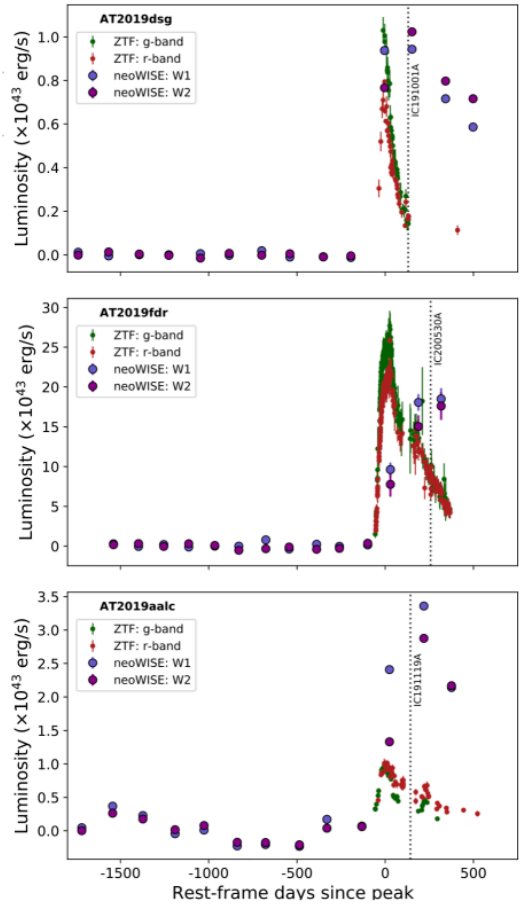

Figure 6.16: The measure OUV (red & green) and infrared (violet and purple) light curves of three suspected TDEs, along with the detection time of the "corresponding" IceCube neutrinos. Figure from [329].

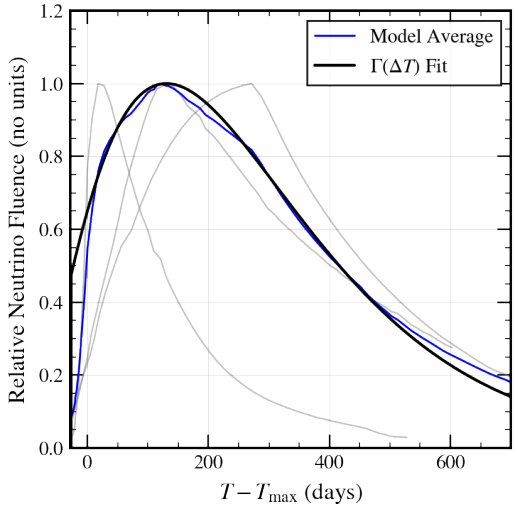

Figure 6.17: Three predictions (light grey) of the neutrino fluence from three TDEs from [329] along with a Gamma function fit (black) to their average luminosity (blue). The Gamma fit is used as the temporal likelihood/probability density function in this search.

the primary model constraints and evidence for the infrared dust echo model for neutrino emission from TDEs [329].

[329] uses these observations and infrared observations in an end-to-end model producing the (modeled) *time dependence* of the neutrino emission from each of these TDEs under the IR dust-echo model. To avoid over-constraining our search with an over-fitted PDF, we average the three modeled neutrino fluence curves together, and fit the average with a Gamma distribution. As seen in Figure 6.17, the Gamma distribution preserves the key behavior of the average neutrino fluence, with a peak around 150 days after TDE ignition—this fit results in Equation 6.21 and is used directly for all TDEs (with appropriate renormalization over the time of the flight as in other source classes)

$$P_{tde,temporal} \propto \text{Gamma}\left(\frac{\Delta T + \mu}{\sigma}; \alpha \sim 2.6, \theta \sim 1.45\right) \tag{6.21}$$

where

$\text{Gamma}(t; \alpha, \theta)$ = is a two-parameter Gamma distribution with shape parameter α and scale parameter θ,

ΔT = the time difference between the event and the maximum *OUV* luminosity,

μ, σ = are renormalization parameters to convert absolute time into the domain of the Gamma distribution,

6.4.4 Flaring blazar temporal emission model

Like gamma-ray bursts, the *time-dependence* of the neutrino fluence from flaring blazars is poorly understood and not measured with any significance, especially at our energy ranges [331, 332]. In addition, the OUV and gamma-ray luminosities are also challenging to approximate using a simple model, despite exceptional measurements from the Fermi space telescope and other instruments [324]. The gamma-ray luminosities during a "flaring state" regularly show complex multi-modal that is challenging to approximate [331]. An example of the gamma-ray fluence from a flaring blazar measured by the Fermi space telescope in December 2016 is shown in Figure 6.18.

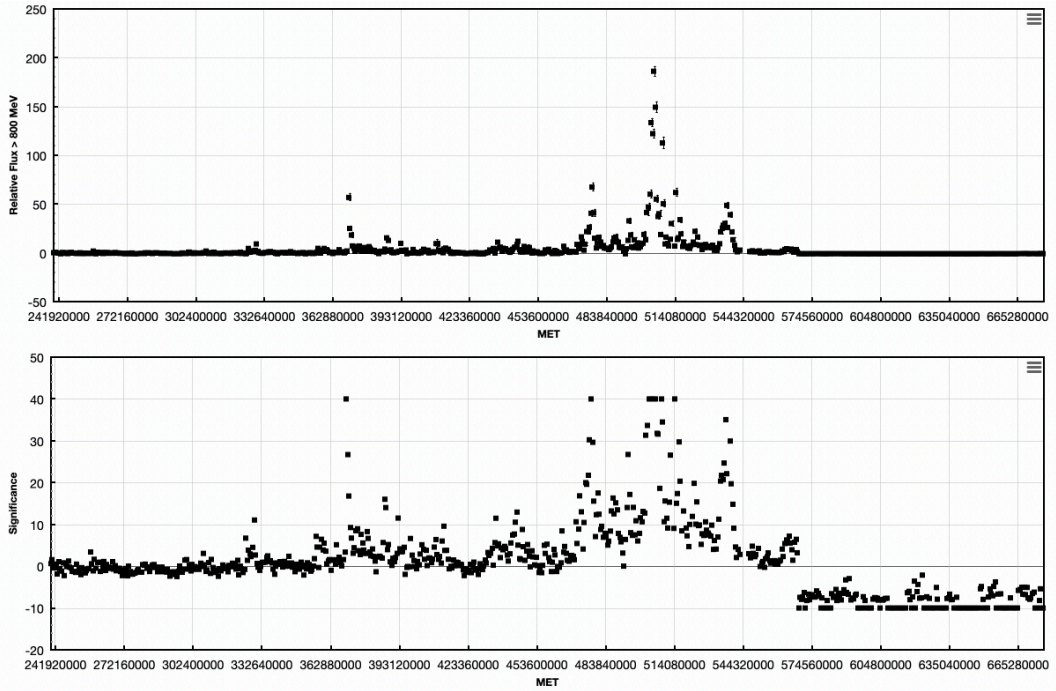

Figure 6.18: (Top): The high-energy (800 MeV–10 GeV) light curve of a blazar, located at $(338.18°,\ 11.73°)$, that was in a "flaring" state at some point during the ANITA-IV flight as measured by the Fermi space telescope. (Bottom): The corresponding significance of the "flare" state at any one time compared to the non-flaring variability of the blazar. Figure from [324].

The Fermi gamma-ray burst monitor (GBM) provides a list all blazars that are currently flaring with 6σ-or-better significance on a week-by-week basis (i.e. the same blazar can show up multiple weeks in a row if it is continually flaring over that time period). Due to the lack of reasonable models to use within each week, we use a simple Heaviside

step function—the likelihood is uniform over the week that Fermi declares that blazar to be "flaring", and zero otherwise. By adding in this simple temporal model, we have significantly reduced the background chance association compared to the full catalog of thousands of known blazars (i.e. if you don't know about the flare state).

6.5 Association between near horizon events and astrophysical sources

In this section, we unblind the results of our searches. We develop and perform each of these searches *blind* to whether there are any astrophysical associatons (of *any* significance). In each section, we present the distribution of the test statistic under the background hypothesis and then *unblind* the search by calculating the observed test statistic and comparing it to the background distribution.

An unbinned maximum likelihood search will always be *at least* as powerful as a corresponding binned analysis (as a binned analysis is equivalent to an unbinned analysis with binary probability density functions). For each search, we also provide significance estimates using a simple binned analysis to demonstrate the increase in search power by unbinned likelihood technique. The binned analysis assumes any event with 1.5° is "spatially coincident" (i.e. a binary likelihood function); temporal coincidence is determined specifically for each source class and is discussed in the sections below.

For each source class, we also use a simple generative model, based around our temporal and spatial likelihood functions, to produce an *estimate* of the distribution of the test statistic given a different number of signal vs. background events. For example, we generate a "synthetic" ANITA-IV flight by mixing one modeled supernovae neutrino with three events taken from our bootstrapped background event sample, or vice-versa (3 modeled supernovae neutrinos mixed with one background event). We use these synthetic distributions to estimate the possible significance achieved by the different searches.

Remark on Wilke's theorem and χ^2 tails

Before proceeding with the unblinding, we need to make one remark about the applicability of Wilke's theorem to the test statistic distributions produced in the below sections. In a standard application of the unbinned maximum likelihood technique, Wilke's theorem, which states that the distribution of the log-likelihood ratio test statistic, λ, under

the null hypothesis should asymptotically approach a χ^2 distribution as the number of parameters increases [333]. This is often used to motivate a χ^2 fit to the asymptotic tail of these distribution to "smooth" or "extend" the empirical histograms [315, 156, 334, 188].

Unfortunately, this theorem cannot be applied in the below searches due to the extremely low-background. The fundamental assumption used in deriving Wilke's theorems is that the best-fit parameter lies *strictly within* the parameter space—it must be an *interior* point [333]. As demonstrated in [335], and in the searches presented in this work, for low background searches, n_s is typically always *at* the boundary of $n_s = 0$ as the likelihood fitter is will only consider non-negative values for n_s—this is in direct violation of the first, and essential, assumption in the derivation of Wilke's theorem, and as such, the distribution of the test statistics below do not necessarily appear to have recognizable χ^2 tails. To be clear, this does not invalidate the statistical test—the log-likelihood ratio test does not require n_s to be an interior point, but if it *is* usually located on the boundary of the support, we no longer *expect* that it should be χ^2 distributed as the number of null hypothesis samples increases [333].

6.5.1 Sky direction reconstruction

To reconstruct the equatorial sky coordinates of the ANITA-IV event candidates (specified in [257] in altitude-azimuth coordinates), we use two independent methods as a cross-check:

1. `AstroPy`: The `AstroPy` library, for the Python programming language, is the currently standard toolkit in astronomy and provides routines for converting between all known astronomical coordinate systems [336, 337, 338].

2. NASA's `hor2eq` publically-available FORTRAN routine that converts a horizontal (alt-az) coordinate into the FK5 equatorial coordinate system [339].

We use the `AstroPy` library to convert the published altitude-azimuth-time of each ANITA-IV event into the International Celestial Reference System (ICRS) equatorial reference frame. We also independently use NASA's `hor2eq` routine to convert altitude-azimuth-time into the FK5 equatorial reference frame, and then use `AstroPy` to convert FK5 into ICRS (a correction on the scale of arcminutes or less). Both methods agree to

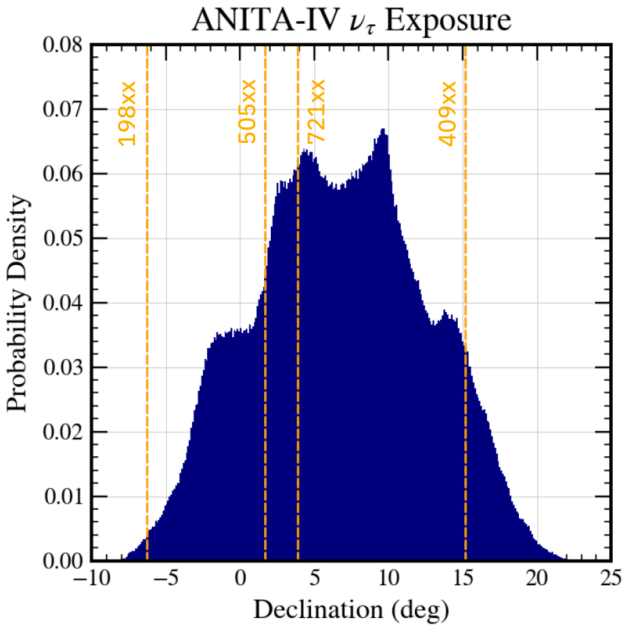

Figure 6.19: The declination of the four near-horizon events reconstructed using the `AstroPy` library against a normalized distribution of ANITA-IV's relative ν_τ exposure integrated over the entire flight.

within $\mathcal{O}$(arcseconds), after converting FK5–>ICRS, and we show reconstructed directions in Table 6.1 (within our pointing uncertainty, both methods give identical results).

Event	RA (deg)	Dec. (deg)
4098827	332.2	15.2
19848917	15.1	-6.3
50549772	232.2	1.7
72164985	223.8	3.9

Table 6.1: The reconstructed event coordinates for the four ANITA-IV near-horizon events.

We note that all four events point to distinct locations on the sky (considering our pointing resolution on the radio-frequency of 0.2° and a total neutrino uncertainty of $\mathcal{O}(1.4°)$). The location of each of these events on the accumulated ν_τ (renormalized) exposure, as a function of declination, is shown in Figure 6.19.

6.5.2 Supernovae search results

From the full catalog of over 800 supernovae detected in 2016 and the first quarter of 2017, our integrated exposure weights reduce the catalog to 44 supernovae for which ANITA-IV had any appreciable ν_τ exposure. However, the relatively long timescale of

our temporal likelihood function only provides a moderate boost in search power compared to a non-transient search.

The distribution of the background test statistic for the supernovae search, along with synthetic mixed-signal distributions, is shown in Figure 6.20. In Figure 6.20, the *grey* curve shows the distribution of the test statistic, λ, using random background samples—this is the distribution of the test statistic under the background-only hypothesis $n_s = 0$. When computing the significance of an observed association, this is the only curve in Figure 6.20 that is required. The fraction of the grey curve in Figure 6.20 that is greater than the observed value of the test statistic, λ_{obs}, is the p-value associated with this observation.

The series of blue curves in Figure 6.20 show the distribution of the test statistic expected under our model when some fraction of the $N = 4$ observed events are signal i.e. the $N_s = 1$ plot corresponds to the distribution of the test statistic that we *should* observe if *one* event was a *real* supernovae neutrino and the other three are background. These blue curves are used to study the sensitivity of our search, and are a useful diagnostic, but they are *not* required for calculating the significance of an observed association (which only requires the grey curve). These synthetic curves are calculated by repeatedly generating fake realizations of the near horizon events where *one, two, three, or all four* events are randomly drawn from our supernovae model while the other events are sampled from our background distributions. For our specific supernovae model, we expect that the observation of a single supernovae neutrino should be a 3σ association (as the majority of the light blue, $N_s = 1$ curve is above the vertical line corresponding to the 3σ quantile of the background distribution). Similarly, the observation of two supernovae neutrinos would *likely* be a 4σ or 5σ discovery. Since the vast majority of the dark blue $N_s = 4$ curve is well above the vertical 5σ quantile, we expect that *if* these four events *are* supernovae ν_τ, we should be able to make a $> 5\sigma$ discovery.

To ensure that our unbinned maximum likelihood distributions are sensible, we compare the unbinned likelihood curves in Figure 6.20 with a simple *classical* binned analysis that does not require any likelihood function. For a binned analysis, a serius of binary *cuts* are made in the search parameter space—any event inside *all* of the cuts is deemed to be a signal event while any event outside *any* of the cuts is deemed to be a background event. A simple binned analysis comparison for the supernovae search that uses any association within 1.5° on the sky and after five days before maximum luminosity and up to twenty days after as "significant", finds that a single supernova association should be an approximately 1.2σ association, with 1.9σ and 2.7σ for two and three event-GRB associations,

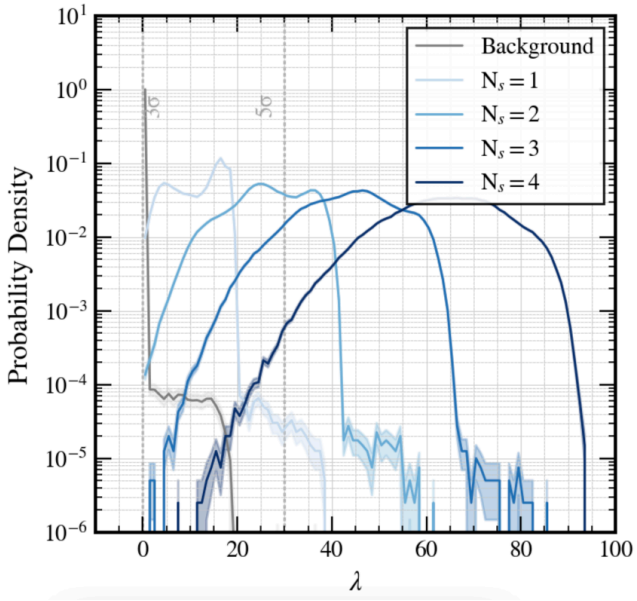

Figure 6.20: The distribution of the test statistic for the supernovae search under the null (background-only) hypothesis (gray) and for synthetic datasets with varying amounts of injected forward modeled signals (blue curves).

respectively. In this case, the use of a continuous temporal probability density function, as opposed to the binary selector used in a binned search, can *significantly* increase the potential significance.

After unblinding, *no significant assocations were identified* with an observed test statistic of $\lambda_{sne} \sim 0$. The closest spatial association with a source in our effective catalog was 3.5° for event 409xx with a supernovae maximum luminosity $\sim$ 100 days prior (which was not significant under this search). Against the full catalog, the closest spatial association was 1.1° for event 721xx with SNE2016bli; while this spatially signicant, SNE2016bli had maximum luminosity over 300 days prior to the event which is strongly disfavored (by many orders of magnitude) under our temporal model. Historically, all four events had strong spatial associations with at least one supernovae over the last 10 years, but these timescales are not consistent with current models or experimental limits. We also confirmed that none of these historical supernovae that were spatially associated with the near horizon events was SN2014dz that had the 2.7σ association with the ANITA-III anomalous event 157xx.

6.5.3 Gamma-ray burst search results

From our full catalog of nearly 300 gamma-ray bursts detected in 2016, our integrated exposure weights reduce the catalog down to only three GRBs for our prompt emission

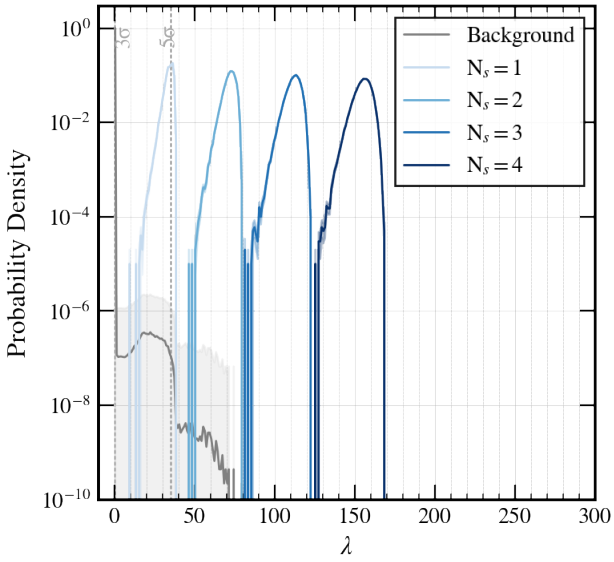

Figure 6.21: The distribution of the test statistic for the prompt gamma-ray burst search under the null (background-only) hypothesis (gray) and for synthetic datasets with varying amounts of injected forward modeled signals (blue curves).

search, and only six GRBs for our late emission search. This significant catalog reduction is due to the extremely short timescales over which we consider a neutrino to be "temporally coincident" with a corresponding GRB. This short timescale (a few seconds for the prompt search, and a few hours for the late search) is the most powerful component of our GRB search and makes this specific source class the most sensitive of all of our searches.

The distribution of the background test statistic for the gamma-ray burst search, along with synthetic mixed-signal distributions, is shown in Figure 6.21 for our prompt search, and Figure 6.22 for our late search. A simple binned analysis that uses any association within ten exponential time constants as "significant", finds that a single GRB association should be 4.7σ association, with 6.5σ and 7.8σ for two and three event-GRB associations, respectively. For our unbinned maximum likelihood technique, we similarly find that almost all one event associations should have a significance of $> 5\sigma$, with two and three event-GRB associations having typical significances in excess of $> 7\sigma$ and 8σ, respectively.

This search is extremely powerful compared to all of our other search classes, and compared to other gamma-ray searches performed by other experiments due to the unique "near-horizon geometry" of the ν_τ channel [304, 315]. For other neutrino observatories like IceCube or Auger, the significance is principally determined by the background chance association between an event and a GRB occuring over a significant fraction of the

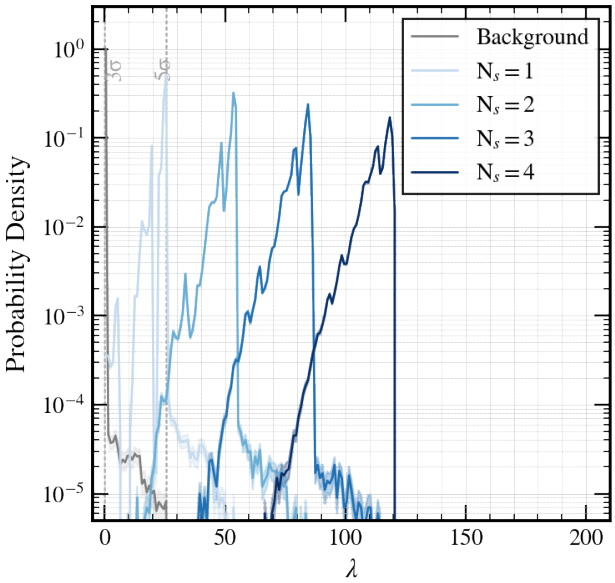

Figure 6.22: The distribution of the test statistic for the late gamma-ray burst search under the null (background-only) hypothesis (gray) and for synthetic datasets with varying amounts of injected forward modeled signals (blue curves).

sky (approaching 4π steradians for some searches). While ANITA-IV may have a similar "full sky" background chance association (and corresponding significance), the narrow ν_τ field-of-view adds an additional restriction in that any event-GRB association must occur within a few degrees of the horizon. The nominal area of ANITA-IV's ν_τ field-of-view is <2% of the total solid angle of the sky, decreasing ANITA-IV's background chance probability by $\sim\frac{1.7}{100}$, with a corresponding increase the possible significance of a given search.

After unblinding, *no significant assocations were identified* with an observed test statistic of $\lambda_{grb} \sim 0$. The closest spatial association with a source in our effective catalog was 17° for event 198xx—this is spatially not significant under our search. Against the full GRB catalog, the closest spatial association was 2° for event 721xx a GRB that occurred 185 days prior; with current models predicting timescales in the few-hour range, a 185 day separation is not found to be significant. Historically, all four events had strong spatial associations with at least one gamma-ray bursts over the last 10 years, but these timescales are not consistent with current models or experimental limits.

6.5.4 Tidal disruption event search results

As discussed in section 1.2.2, the identification of TDEs is currently challenging as they share many signatures with other astrophysical sources. From our full catalog of 7 TDEs

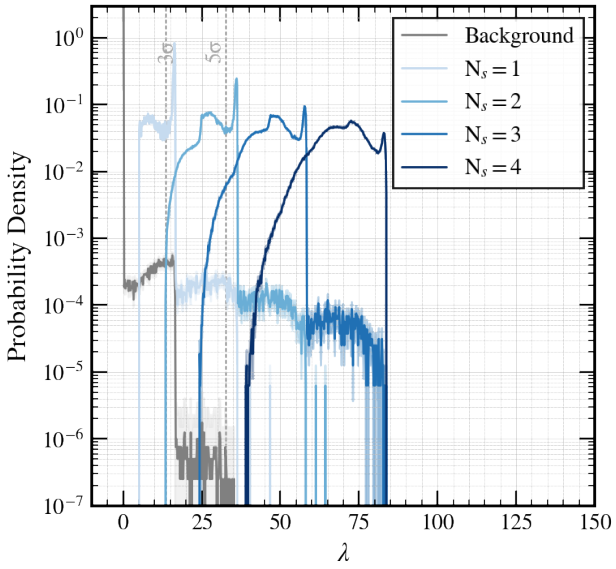

Figure 6.23: The distribution of the test statistic for the tidal disruption event (TDE) search under the null (background-only) hypothesis (gray) and for synthetic datasets with varying amounts of injected forward modeled signals (blue curves).

identified between 2014 and 2017, only two TDEs accumulate any ν_τ exposure with ANITA-IV. Of those two TDEs, one TDE in particular accounts for $\gtrsim 90\%$ of the total integrated TDE exposure. The distribution of the background test statistic for the TDE search, along with synthetic mixed-signal distributions, is shown in Figure 6.23. Since we know that the sky locations of each source are distinct, it is impossible for us to have more than two event-TDE associations from our effective catalog (as there are only two sources with non-zero weights), so Figure 6.23 only shows synthetic curves with a maximum of two signal events out of four total events.

After unblinding, *no significant assocations were identified* with an observed test statistic of $\lambda_{tde} \sim 0$. The closest spatial association with a source in our effective catalog was 15.3° for event 198xx with a TDE with maximum luminosity $\sim$ 73 days prior (which was not significant under this search). This was also the closest association for the events under the full and historical catalogs, which are extremely small for TDEs, due to the aforementioned difficulties with identifying them and separating them from other astrophysical objects, as well as their (expected) low fundamental rates in the universe.

6.5.5 Flaring blazar search results

From the full catalog of over $\sim$ 3800 known blazars, only $\sim$ 40 were detected as "flaring" by the Fermi space telescope during some portion of the ANITA-IV flight [323]. Of

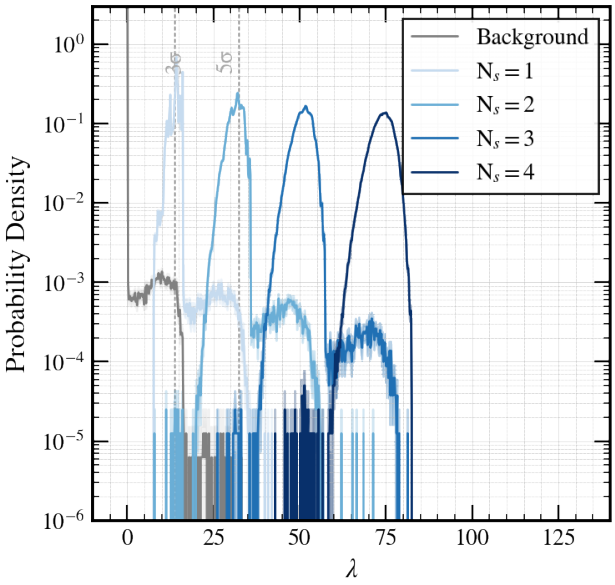

Figure 6.24: The distribution of the test statistic for the flaring blazar search under the null (background-only) hypothesis (gray) and for synthetic datasets with varying amounts of injected forward modeled signals (blue curves).

those $\sim$ 40 flaring blazars, only 12 had any significant ν_τ exposure and constituted our effective catalog. The distribution of the background test statistic for the flaring blazar search, along with synthetic mixed-signal distributions, is shown in Figure 6.24.

Since our "time-resolution" for each blazar flare was 7 days, we only observe a moderate increase in search power due to the temporal likelihood. However, the integrated ν_τ exposure weights, which reduce our total catalog by $\frac{12}{3800}$, act to make this a reasonably powerful search compared to one with no transient information. For our flaring blazar search, our synthetic distributions predict that a single GRB-flaring blazar association should typically be a 3σ result, while two or more GRB-flaring blazar associations should exceed 5σ. A binned search using the 7-day search window as the binning function finds a potential significance of that is only slightly weaker (as expected) than that shown in Figure 6.24—2.8σ for one flare-event association, 3.3σ for two associations, and 4.7σ for three associations.

After unblinding, *no significant assocations were identified* with an observed test statistic of $\lambda_{blazar} \sim 0$. The closest spatial association with a source in our effective catalog was 6.8° for event 721xx with a blazar that was in a flaring state between 10 days and 7 days prior and which is not significant under this search. Historically, all four events have associations with one of the several thousand known blazars with separations less than 1.1°, but not while they were in a flaring state (this is consistent with background expectations due to the large number of known blazars on the sky).

Conclusions

As we saw in Chapter 1, the search for ultrahigh energy neutrinos is motivated by their fundamentally weakly interacting nature—they have the potential to travel cosmological distances, from sources far beyond the GZK horizon, without being disturbed by turbulent galactic and extragalactic magnetic fields, and therefore act as probes into hadronic and leptonic processes in the extreme astrophysical environments that produced them. Unfortunately, the neutrino's greatest advantage, its neutral weakly-interacting nature, is also what makes it so challenging to detect; we need to instrument extremely large volumes for long periods of time in order to have a reasonable chance of detecting them.

The fourth flight of ANITA, described in Chapter 3, set the strongest limits on the ultrahigh energy neutrino flux above 3×10^{19} eV with one candidate event on an expected background of $0.64^{+0.69}_{-0.45}$. However, the detection of four anomalous near horizon events opened the possibility that ANITA-IV may have made the first detection of ultrahigh energy tau neutrinos via the near horizon "air shower channel". While we showed that these events are not *observationally inconsistent* with tau neutrinos in Chapter 5, the implied (diffuse) flux and (point-like) fluence are in strong tension with limits set by other observatories, casting doubt on their interpretation as ultrahigh energy tau neutrinos.

As we saw in Chapter 5, the narrow field-of-view of the τ air shower channel decreases significantly the sensitivity to *diffuse* neutrino fluxes. However, this narrow field-of-view can significantly improve searches for *point-like* transient neutrino sources that happen to be neutrino-bright while the source is within this field-of-view. We used this technique in Chapter 6 to search for associations between the four near horizon events and known astrophysical objects. Unfortunately, no associations were identified, implying that these sources likely do not come from any known astrophysical object in current catalogs.

The next generation of the ANITA experiment, the Payload for Ultrahigh Energy Observations (PUEO), has been designed to have at least an order of magnitude more sensitivity to near horizon air showers events—both by doubling the number of antennas on the main instrument, *and* adding a dedicated low-frequency antenna array specifically

designed to detect extensive air showers. Hopefully, with its significantly larger effective area, PUEO may be able to complete the search started by ANITA-IV and definitively detect an Earth-skimming tau neutrino extensive air shower near the horizon.

Bibliography

[1] V. F. Hess. "Cosmic Rays". In: *Thought* 15.1 (1940), pp. 182–184. ISSN: 0040-6457. DOI: 10.5840/thought1940151247. URL: http://dx.doi.org/10.5840/thought1940151247.

[2] B. P. Abbott et al. "GW170817: Observation of Gravitational Waves from a Binary Neutron Star Inspiral". In: *Phys. Rev. Lett.* 119 (16 Oct. 2017), p. 161101. DOI: 10.1103/PhysRevLett.119.161101. URL: https://link.aps.org/doi/10.1103/PhysRevLett.119.161101.

[3] M. G. Aartsen et al. "Multimessenger observations of a flaring blazar coincident with high-energy neutrino IceCube-170922A". In: *Science* 361.6398 (2018), eaat1378. DOI: 10.1126/science.aat1378. arXiv: 1807.08816 [astro-ph.HE].

[4] L. Miroshnichenko. "Solar Cosmic Rays at High Energies". In: *Astrophysics and Space Science Library* (Aug. 2014), pp. 91–118. ISSN: 2214-7985. DOI: 10.1007/978-3-319-09429-8_4. URL: http://dx.doi.org/10.1007/978-3-319-09429-8_4.

[5] P. Zyla et al. "Review of Particle Physics". In: *PTEP* 2020.8 (2020), p. 083C01. DOI: 10.1093/ptep/ptaa104.

[6] D. Caprioli. "Cosmic-ray acceleration and propagation". In: *Proceedings of The 34th International Cosmic Ray Conference — PoS(ICRC2015)* (Aug. 2016). DOI: 10.22323/1.236.0008. URL: http://dx.doi.org/10.22323/1.236.0008.

[7] C. Ding, N. Globus, and G. R. Farrar. "On the origin of ultra-high energy cosmic ray anisotropy". In: *Proceedings of 36th International Cosmic Ray Conference — PoS(ICRC2019)* (Sept. 2019). DOI: 10.22323/1.358.0243. URL: http://dx.doi.org/10.22323/1.358.0243.

[8] G. Giacinti et al. "Cosmic ray anisotropy as signature for the transition from galactic to extragalactic cosmic rays". In: *Journal of Cosmology and Astroparticle Physics* 2012.07 (July 2012), pp. 031–031. ISSN: 1475-7516. DOI: 10.1088/1475-7516/2012/07/031. URL: http://dx.doi.org/10.1088/1475-7516/2012/07/031.

[9] A. Aab et al. "An Indication of Anisotropy in Arrival Directions of Ultra-high-energy Cosmic Rays through Comparison to the Flux Pattern of Extragalactic Gamma-Ray Sources". In: *The Astrophysical Journal* 853.2 (Feb. 2018), p. L29. ISSN: 2041-8213. DOI: 10.3847/2041-8213/aaa66d. URL: http://dx.doi.org/10.3847/2041-8213/aaa66d.

[10] G. R. Farrar, M. Unger, and L. A. Anchordoqui. "The origin of the ankle in the UHECR spectrum, and of the extragalactic protons below it". In: *Proceedings of The 34th International Cosmic Ray Conference — PoS(ICRC2015)* (Aug. 2016). DOI: 10.22323/1.236.0513. URL: http://dx.doi.org/10.22323/1.236.0513.

[11] S. Das, S. Razzaque, and N. Gupta. "Combined fit of UHECR spectrum and composition with two extragalactic source populations". In: *Proceedings of 37th International Cosmic Ray Conference — PoS(ICRC2021)* (June 2021). DOI: 10.22323/1.395.0460. URL: http://dx.doi.org/10.22323/1.395.0460.

[12] A. di Matteo. "Astrophysical interpretation of Pierre Auger Observatory measurements of the UHECR energy spectrum and mass composition". In: *EPJ Web of Conferences* 136 (2017). Ed. by A. Morselli, A. Capone, and G. Rodriguez Fernandez, p. 02002. ISSN: 2100-014X. DOI: 10.1051/epjconf/201713602002. URL: http://dx.doi.org/10.1051/epjconf/201713602002.

[13] M. S. Muzio, M. Unger, and G. R. Farrar. "Constraints on UHECR sources and their environments, from fitting UHECR spectrum and composition, and neutrinos and gammas." In: *Proceedings of 36th International Cosmic Ray Conference — PoS(ICRC2019)* (Aug. 2019). DOI: 10.22323/1.358.0364. URL: http://dx.doi.org/10.22323/1.358.0364.

[14] D. Ivanov. "Energy Spectrum Measured by the Telescope Array". In: *Proceedings of 36th International Cosmic Ray Conference — PoS(ICRC2019)* (July 2019).

DOI: 10.22323/1.358.0298. URL: http://dx.doi.org/10.22323/1.358.0298.

[15] "Overview of the Pierre Auger observatory dedicated to the study of cosmic rays". In: (2019). DOI: 10.1063/1.5091635. URL: http://dx.doi.org/10.1063/1.5091635.

[16] T. T. A. Collaboration and T. P. A. Collaboration. *Pierre Auger Observatory and Telescope Array: Joint Contributions to the 35th International Cosmic Ray Conference (ICRC 2017)*. 2018. arXiv: 1801.01018 [astro-ph.HE].

[17] T. AbuZayyad et al. "Auger-TA energy spectrum working group report". In: *EPJ Web of Conferences* 210 (2019). Ed. by I. Lhenry-Yvon et al., p. 01002. ISSN: 2100-014X. DOI: 10.1051/epjconf/201921001002. URL: http://dx.doi.org/10.1051/epjconf/201921001002.

[18] D. Ivanov. "Report of the Telescope Array - Pierre Auger Observatory Working Group on Energy Spectrum". In: *Proceedings of 35th International Cosmic Ray Conference — PoS(ICRC2017)* (Sept. 2017). DOI: 10.22323/1.301.0498. URL: http://dx.doi.org/10.22323/1.301.0498.

[19] P. Abreu et al. "Constraints on the Origin Of Cosmic Rays Above 10^{18} eV From Large-Scale Anisotropy Searches In Data of the Pierre Auger Observatory". In: *The Astrophysical Journal* 762.1 (Dec. 2012), p. L13. ISSN: 2041-8213. DOI: 10.1088/2041-8205/762/1/l13. URL: http://dx.doi.org/10.1088/2041-8205/762/1/L13.

[20] R. Abbasi et al. "The energy spectrum of cosmic rays above $10^{17.2}$ eV measured by the fluorescence detectors of the Telescope Array experiment in seven years". In: *Astroparticle Physics* 80 (2016), pp. 131–140. ISSN: 0927-6505. DOI: https://doi.org/10.1016/j.astropartphys.2016.04.002. URL: https://www.sciencedirect.com/science/article/pii/S0927650516300445.

[21] B. Dawson. "The Energy Scale of the Pierre Auger Observatory". In: *Proceedings of 36th International Cosmic Ray Conference — PoS(ICRC2019)* (July 2019). DOI: 10.22323/1.358.0231. URL: http://dx.doi.org/10.22323/1.358.0231.

[22] M. C. Beck et al. "New constraints on modelling the random magnetic field of the MW". In: *Journal of Cosmology and Astroparticle Physics* 2016.05 (May 2016), pp. 056–056. ISSN: 1475-7516. DOI: 10.1088/1475-7516/2016/05/056. URL: http://dx.doi.org/10.1088/1475-7516/2016/05/056.

[23] G. Giacinti, M. Kachelrieß, and D. V. Semikoz. "Explaining the spectra of cosmic ray groups above the knee by escape from the Galaxy". In: *Phys. Rev. D* 90 (4 Aug. 2014), p. 041302. DOI: 10.1103/PhysRevD.90.041302. URL: https://link.aps.org/doi/10.1103/PhysRevD.90.041302.

[24] A. Codino. "The Ankle, the Knee and the Principle of Constant Spectral Indices in Cosmic Ray Physics". In: *Proceedings of The 34th International Cosmic Ray Conference — PoS(ICRC2015)* (Aug. 2016). DOI: 10.22323/1.236.0465. URL: http://dx.doi.org/10.22323/1.236.0465.

[25] "Acceleration of petaelectronvolt protons in the Galactic Centre". In: *Nature* 531.7595 (Mar. 2016), pp. 476–479. ISSN: 1476-4687. DOI: 10.1038/nature17147. URL: http://dx.doi.org/10.1038/nature17147.

[26] A. R. Bell et al. "Cosmic-ray acceleration and escape from supernova remnants". In: *Monthly Notices of the Royal Astronomical Society* 431.1 (Feb. 2013), pp. 415–429. ISSN: 1365-2966. DOI: 10.1093/mnras/stt179. URL: http://dx.doi.org/10.1093/mnras/stt179.

[27] Y. Fujita, K. Murase, and S. S. Kimura. "Sagittarius A* as an origin of the Galactic PeV cosmic rays?" In: *Journal of Cosmology and Astroparticle Physics* 2017.04 (Apr. 2017), pp. 037–037. ISSN: 1475-7516. DOI: 10.1088/1475-7516/2017/04/037. URL: http://dx.doi.org/10.1088/1475-7516/2017/04/037.

[28] "Acceleration of petaelectronvolt protons in the Galactic Centre". In: *Nature* 531.7595 (Mar. 2016), pp. 476–479. ISSN: 1476-4687. DOI: 10.1038/nature17147. URL: http://dx.doi.org/10.1038/nature17147.

[29] J. Vink. "Cosmic-Ray Acceleration by Supernova Remnants: Introduction and Theory". In: *Physics and Evolution of Supernova Remnants* (2020), pp. 277–321. ISSN: 2196-9698. DOI: 10.1007/978-3-030-55231-2_11. URL: http://dx.doi.org/10.1007/978-3-030-55231-2_11.

[30] D. Caprioli. "Cosmic-ray acceleration in supernova remnants: non-linear theory revised". In: *Journal of Cosmology and Astroparticle Physics* 2012.07 (July 2012), pp. 038–038. ISSN: 1475-7516. DOI: 10.1088/1475-7516/2012/07/038. URL: http://dx.doi.org/10.1088/1475-7516/2012/07/038.

[31] R. Alves Batista et al. "Open Questions in Cosmic-Ray Research at Ultrahigh Energies". In: *Front. Astron. Space Sci.* 6 (2019), p. 23. DOI: 10.3389/fspas.2019.00023. arXiv: 1903.06714 [astro-ph.HE].

[32] A. R. Bell. "The acceleration of cosmic rays in shock fronts - I". In: *Monthly Notices of the Royal Astronomical Society* 182.2 (Feb. 1978), pp. 147–156. ISSN: 1365-2966. DOI: 10.1093/mnras/182.2.147. URL: http://dx.doi.org/10.1093/mnras/182.2.147.

[33] A. R. Bell. "The acceleration of cosmic rays in shock fronts - II". In: *Monthly Notices of the Royal Astronomical Society* 182.3 (Mar. 1978), pp. 443–455. ISSN: 1365-2966. DOI: 10.1093/mnras/182.3.443. URL: http://dx.doi.org/10.1093/mnras/182.3.443.

[34] J. R. Hörandel. "The composition of cosmic rays at the knee". In: (2013). DOI: 10.1063/1.4792566. URL: http://dx.doi.org/10.1063/1.4792566.

[35] A. Coleman. "Measurement of the Cosmic Ray Flux near the Second Knee with the Pierre Auger Observatory". In: *Proceedings of 36th International Cosmic Ray Conference — PoS(ICRC2019)* (July 2019). DOI: 10.22323/1.358.0225. URL: http://dx.doi.org/10.22323/1.358.0225.

[36] V. Novotný. "Measurement of the spectrum of cosmic rays above $10^{16.5}$ eV with Cherenkov-dominated events at the Pierre Auger Observatory". In: *Proceedings of 36th International Cosmic Ray Conference — PoS(ICRC2019)* (July 2019). DOI: 10.22323/1.358.0374. URL: http://dx.doi.org/10.22323/1.358.0374.

[37] W. D. Apel et al. "Kneelike Structure in the Spectrum of the Heavy Component of Cosmic Rays Observed with KASCADE-Grande". In: *Physical Review Letters* 107.17 (Oct. 2011). ISSN: 1079-7114. DOI: 10.1103/physrevlett.107.171104. URL: http://dx.doi.org/10.1103/PhysRevLett.107.171104.

[38] E. Kido. "Implications of the cosmic ray spectrum from the second knee to the ankle region observed by the TA and TALE experiment for the cosmic ray proton sources". In: *Proceedings of 36th International Cosmic Ray Conference — PoS(ICRC2019)* (July 2019). DOI: 10.22323/1.358.0313. URL: http://dx.doi.org/10.22323/1.358.0313.

[39] T. Abu-Zayyad et al. "The Knee and the Second Knee of the Cosmic-Ray Energy Spectrum". In: (Mar. 2018). arXiv: 1803.07052 [astro-ph.HE].

[40] J. Abraham et al. "Observation of the Suppression of the Flux of Cosmic Rays above 4×10^{19} eV". In: *Phys. Rev. Lett.* 101 (6 Aug. 2008), p. 061101. DOI: 10.1103/PhysRevLett.101.061101. URL: https://link.aps.org/doi/10.1103/PhysRevLett.101.061101.

[41] G. T. Zatsepin and V. A. Kuz'min. "Upper Limit of Spectrum of Cosmic Rays". In: *JETP Lett. (USSR) (Engl. Transl.)* 4 (Aug. 1966). URL: https://www.osti.gov/biblio/4515382.

[42] K. Greisen. "End to the Cosmic-Ray Spectrum?" In: *Phys. Rev. Lett.* 16 (17 Apr. 1966), pp. 748–750. DOI: 10.1103/PhysRevLett.16.748. URL: https://link.aps.org/doi/10.1103/PhysRevLett.16.748.

[43] V. Verzi, D. Ivanov, and Y. Tsunesada. "Measurement of energy spectrum of ultra-high energy cosmic rays". In: *Progress of Theoretical and Experimental Physics* 2017.12 (Nov. 2017). ISSN: 2050-3911. DOI: 10.1093/ptep/ptx082. URL: http://dx.doi.org/10.1093/ptep/ptx082.

[44] R. Aloisio, V. Berezinsky, and P. Blasi. "Ultra high energy cosmic rays: implications of Auger data for source spectra and chemical composition". In: *Journal of Cosmology and Astroparticle Physics* 2014.10 (Oct. 2014), pp. 020–020. ISSN: 1475-7516. DOI: 10.1088/1475-7516/2014/10/020. URL: http://dx.doi.org/10.1088/1475-7516/2014/10/020.

[45] A. Aab et al. "Combined fit of spectrum and composition data as measured by the Pierre Auger Observatory". In: *Journal of Cosmology and Astroparticle Physics* 2017.04 (Apr. 2017), pp. 038–038. ISSN: 1475-7516. DOI: 10.1088/1475-7516/2017/04/038. URL: http://dx.doi.org/10.1088/1475-7516/2017/04/038.

[46] A. Romero-Wolf and M. Ave. "Bayesian inference constraints on astrophysical production of ultra-high energy cosmic rays and cosmogenic neutrino flux predictions". In: *Journal of Cosmology and Astroparticle Physics* 2018.07 (July 2018), pp. 025–025. ISSN: 1475-7516. DOI: 10.1088/1475-7516/2018/07/025. URL: http://dx.doi.org/10.1088/1475-7516/2018/07/025.

[47] D. Wittkowski. "Reconstructed properties of the sources of UHECR and their dependence on the extragalactic magnetic field". In: *Proceedings of 35th International Cosmic Ray Conference — PoS(ICRC2017)* (Aug. 2017). DOI: 10.22323/1.301.0563. URL: http://dx.doi.org/10.22323/1.301.0563.

[48] X. Rodrigues et al. "Neutrinos and Ultra-high-energy Cosmic-ray Nuclei from Blazars". In: *The Astrophysical Journal* 854.1 (Feb. 2018), p. 54. ISSN: 1538-4357. DOI: 10.3847/1538-4357/aaa7ee. URL: http://dx.doi.org/10.3847/1538-4357/aaa7ee.

[49] S. Das, S. Razzaque, and N. Gupta. "Combined fit of UHECR spectrum and composition with two extragalactic source populations". In: *Proceedings of 37th International Cosmic Ray Conference — PoS(ICRC2021)* (June 2021). DOI: 10.22323/1.395.0460. URL: http://dx.doi.org/10.22323/1.395.0460.

[50] R. Alves Batista et al. "CRPropa 3.2: a framework for high-energy astroparticle propagation". In: *Proceedings of 37th International Cosmic Ray Conference — PoS(ICRC2021)* (July 2021). DOI: 10.22323/1.395.0978. URL: http://dx.doi.org/10.22323/1.395.0978.

[51] R. A. Batista et al. "Cosmic ray propagation with CRPropa 3". In: *Journal of Physics: Conference Series* 608 (May 2015), p. 012076. ISSN: 1742-6596. DOI: 10.1088/1742-6596/608/1/012076. URL: http://dx.doi.org/10.1088/1742-6596/608/1/012076.

[52] R. A. Batista et al. "Effects of uncertainties in simulations of extragalactic UHECR propagation, using CRPropa and SimProp". In: *Journal of Cosmology and Astroparticle Physics* 2015.10 (Oct. 2015), pp. 063–063. ISSN: 1475-7516. DOI: 10.1088/1475-7516/2015/10/063. URL: http://dx.doi.org/10.1088/1475-7516/2015/10/063.

[53] C. D. Dermer and S. Razzaque. "Acceleration of Ultra-High-Energy Cosmic Rays in the Colliding Shells of Blazars and Gamma-Ray Bursts: Constraints from the Fermi Gamma-Ray Space Telescope". In: *The Astrophysical Journal* 724.2 (Nov. 2010), pp. 1366–1372. ISSN: 1538-4357. DOI: 10.1088/0004-637x/724/2/1366. URL: http://dx.doi.org/10.1088/0004-637X/724/2/1366.

[54] R.-Y. Liu, X.-Y. Wang, and Z.-G. Dai. "Nearby low-luminosity gamma-ray bursts as the sources of ultra-high-energy cosmic rays revisited". In: *Monthly Notices of the Royal Astronomical Society* 418.2 (Sept. 2011), pp. 1382–1391. ISSN: 0035-8711. DOI: 10.1111/j.1365-2966.2011.19590.x. URL: http://dx.doi.org/10.1111/j.1365-2966.2011.19590.x.

[55] M. Vietri. "The Acceleration of Ultra–High-Energy Cosmic Rays in Gamma-Ray Bursts". In: *The Astrophysical Journal* 453 (Nov. 1995), p. 883. ISSN: 1538-4357. DOI: 10.1086/176448. URL: http://dx.doi.org/10.1086/176448.

[56] E. Waxman. "Cosmological Gamma-Ray Bursts and the Highest Energy Cosmic Rays". In: *Physical Review Letters* 75.3 (July 1995), pp. 386–389. ISSN: 1079-7114. DOI: 10.1103/physrevlett.75.386. URL: http://dx.doi.org/10.1103/PhysRevLett.75.386.

[57] E. Resconi et al. "Connecting blazars with ultrahigh-energy cosmic rays and astrophysical neutrinos". In: *Monthly Notices of the Royal Astronomical Society* 468.1 (Feb. 2017), pp. 597–606. ISSN: 1365-2966. DOI: 10.1093/mnras/stx498. URL: http://dx.doi.org/10.1093/mnras/stx498.

[58] L. Caccianiga. "Anisotropies of the Highest Energy Cosmic-ray Events Recorded by the Pierre Auger Observatory in 15 years of Operation". In: *Proceedings of 36th International Cosmic Ray Conference — PoS(ICRC2019)* (July 2019). DOI: 10.22323/1.358.0206. URL: http://dx.doi.org/10.22323/1.358.0206.

[59] A. Aab et al. "Combined fit of spectrum and composition data as measured by the Pierre Auger Observatory". In: *Journal of Cosmology and Astroparticle Physics* 2017.04 (Apr. 2017), pp. 038–038. ISSN: 1475-7516. DOI: 10.1088/1475-7516/2017/04/038. URL: http://dx.doi.org/10.1088/1475-7516/2017/04/038.

[60] P. M. Hansen. "Tests of hadronic interactions using the Pierre Auger Observatory". In: *Proceedings of The 39th International Conference on High Energy Physics — PoS(ICHEP2018)* (Aug. 2019). DOI: 10.22323/1.340.0206. URL: http://dx.doi.org/10.22323/1.340.0206.

[61] K. Arisaka et al. "Composition of UHECR and the Pierre Auger Observatory spectrum". In: *Journal of Cosmology and Astroparticle Physics* 2007.12 (Dec. 2007), pp. 002–002. ISSN: 1475-7516. DOI: 10.1088/1475-7516/2007/12/002. URL: http://dx.doi.org/10.1088/1475-7516/2007/12/002.

[62] A. V. Olinto et al. "The POEMMA (Probe of Extreme Multi-MessengerAstrophysics) mission". In: *Proceedings of 36th International Cosmic Ray Conference — PoS(ICRC2019)* (July 2019). DOI: 10.22323/1.358.0378. URL: http://dx.doi.org/10.22323/1.358.0378.

[63] L. Wiencke. "The Extreme Universe Space Observatory on a Super-Pressure Balloon II Mission". In: *Proceedings of 36th International Cosmic Ray Conference — PoS(ICRC2019)* (July 2019). DOI: 10.22323/1.358.0466. URL: http://dx.doi.org/10.22323/1.358.0466.

[64] S. J. Sciutto. "AIRES: A system for air shower simulations". In: (Nov. 1999). DOI: 10.13140/RG.2.2.12566.40002. arXiv: astro-ph/9911331.

[65] D. Heck. "Extensive air shower simulations with CORSIKA and the influence of high energy hadronic interaction models". In: *30th International Symposium on Multiparticle Dynamics*. Oct. 2000, pp. 252–259. arXiv: astro-ph/0103073.

[66] M. Reininghaus and R. Ulrich. "CORSIKA 8 – Towards a modern framework for the simulation of extensive air showers". In: *EPJ Web of Conferences* 210 (2019). Ed. by I. Lhenry-Yvon et al., p. 02011. ISSN: 2100-014X. DOI: 10.1051/epjconf/201921002011. URL: http://dx.doi.org/10.1051/epjconf/201921002011.

[67] F. Riehn et al. "Hadronic interaction model SIBYLL 2.3d and extensive air showers". In: *Physical Review D* 102.6 (Sept. 2020). ISSN: 2470-0029. DOI: 10.1103/physrevd.102.063002. URL: http://dx.doi.org/10.1103/PhysRevD.102.063002.

[68] S. Ostapchenko. "QGSJET-II: towards reliable description of very high energy hadronic interactions". In: *Nuclear Physics B - Proceedings Supplements* 151.1 (Jan. 2006), pp. 143–146. ISSN: 0920-5632. DOI: 10.1016/j.nuclphysbps.2005.07.026. URL: http://dx.doi.org/10.1016/j.nuclphysbps.2005.07.026.

[69] T. Pierog et al. "EPOS LHC: Test of collective hadronization with data measured at the CERN Large Hadron Collider". In: *Physical Review C* 92.3 (Sept. 2015). ISSN: 1089-490X. DOI: 10.1103/physrevc.92.034906. URL: http://dx.doi.org/10.1103/PhysRevC.92.034906.

[70] J. Bellido. "Depth of maximum of air-shower profiles at the Pierre Auger Observatory: Measurements above $10^{17.2}$ eV and Composition Implications". In: *Proceedings of 35th International Cosmic Ray Conference — PoS(ICRC2017)* (Aug. 2017). DOI: 10.22323/1.301.0506. URL: http://dx.doi.org/10.22323/1.301.0506.

[71] A. Aab et al. "Inferences on mass composition and tests of hadronic interactions from 0.3 to 100 EeV using the water-Cherenkov detectors of the Pierre Auger Observatory". In: *Physical Review D* 96.12 (Dec. 2017). ISSN: 2470-0029. DOI: 10.1103/physrevd.96.122003. URL: http://dx.doi.org/10.1103/PhysRevD.96.122003.

[72] R. U. Abbasi et al. "Depth of Ultra High Energy Cosmic Ray Induced Air Shower Maxima Measured by the Telescope Array Black Rock and Long Ridge FADC Fluorescence Detectors and Surface Array in Hybrid Mode". In: *The Astrophysical Journal* 858.2 (May 2018), p. 76. ISSN: 1538-4357. DOI: 10.3847/1538-4357/aabad7. URL: http://dx.doi.org/10.3847/1538-4357/aabad7.

[73] J. M. Carceller. "Studies of the UHECR Mass Composition and Hadronic Interactions with the FD and SD of the Pierre Auger Observatory". In: *EPJ Web of Conferences* 209 (2019). Ed. by M. De Vincenzi, A. Capone, and A. Morselli, p. 01042. ISSN: 2100-014X. DOI: 10.1051/epjconf/201920901042. URL: http://dx.doi.org/10.1051/epjconf/201920901042.

[74] B. Keilhauer. "The Fluorescence Detector of the Pierre Auger Observatory — a Calorimeter for UHECR". In: *AIP Conference Proceedings* (2006). ISSN: 0094-

243X. DOI: 10.1063/1.2396952. URL: http://dx.doi.org/10.1063/1.2396952.

[75] P. Sanchez-Lucas. "$\langle X_{max} \rangle$ measurements and tests of hadronic models using the surface detector of the Pierre Auger Observatory". In: *Proceedings of 35th International Cosmic Ray Conference — PoS(ICRC2017)* (Aug. 2017). DOI: 10.22323/1.301.0495. URL: http://dx.doi.org/10.22323/1.301.0495.

[76] S. J. Sciutto. "Air showers, hadronic models, and muon production". In: *EPJ Web of Conferences* 210 (2019). Ed. by I. Lhenry-Yvon et al., p. 02007. ISSN: 2100-014X. DOI: 10.1051/epjconf/201921002007. URL: http://dx.doi.org/10.1051/epjconf/201921002007.

[77] F. Riehn. "Measurement of the fluctuations in the number of muons in inclined air showers with the Pierre Auger Observatory". In: *Proceedings of 36th International Cosmic Ray Conference — PoS(ICRC2019)* (July 2019). DOI: 10.22323/1.358.0404. URL: http://dx.doi.org/10.22323/1.358.0404.

[78] A. Aab et al. "Depth of maximum of air-shower profiles at the Pierre Auger Observatory. II. Composition implications". In: *Physical Review D* 90.12 (Dec. 2014). ISSN: 1550-2368. DOI: 10.1103/physrevd.90.122006. URL: http://dx.doi.org/10.1103/PhysRevD.90.122006.

[79] D. Hooper, A. Taylor, and S. Sarkar. "The impact of heavy nuclei on the cosmogenic neutrino flux". In: *Astroparticle Physics* 23.1 (Feb. 2005), pp. 11–17. ISSN: 0927-6505. DOI: 10.1016/j.astropartphys.2004.11.002. URL: http://dx.doi.org/10.1016/j.astropartphys.2004.11.002.

[80] L. A. Anchordoqui et al. "High energy neutrinos from astrophysical accelerators of cosmic ray nuclei". In: *Astroparticle Physics* 29.1 (Feb. 2008), pp. 1–13. ISSN: 0927-6505. DOI: 10.1016/j.astropartphys.2007.10.006. URL: http://dx.doi.org/10.1016/j.astropartphys.2007.10.006.

[81] K. Kotera, D. Allard, and A. Olinto. "Cosmogenic neutrinos: parameter space and detectabilty from PeV to ZeV". In: *Journal of Cosmology and Astroparticle Physics* 2010.10 (Oct. 2010), pp. 013–013. ISSN: 1475-7516. DOI: 10.1088/1475-7516/2010/10/013. URL: http://dx.doi.org/10.1088/1475-7516/2010/10/013.

[82] H. Takami et al. "Cosmogenic neutrinos as a probe of the transition from Galactic to extragalactic cosmic rays". In: *Astroparticle Physics* 31.3 (Apr. 2009), pp. 201–211. ISSN: 0927-6505. DOI: 10.1016/j.astropartphys.2009.01.006. URL: http://dx.doi.org/10.1016/j.astropartphys.2009.01.006.

[83] P. Ruehl et al. "Predicting the UHE photon flux from GZK-interactions of hadronic cosmic rays using CRPropa 3". In: *Proceedings of 37th International Cosmic Ray Conference — PoS(ICRC2021)* (July 2021). DOI: 10.22323/1.395.0449. URL: http://dx.doi.org/10.22323/1.395.0449.

[84] G. Gelmini, O. Kalashev, and D. V. Semikoz. "GZK photons in the minimal ultra-high energy cosmic rays model". In: *Astroparticle Physics* 28.4-5 (Dec. 2007), pp. 390–396. ISSN: 0927-6505. DOI: 10.1016/j.astropartphys.2007.08.006. URL: http://dx.doi.org/10.1016/j.astropartphys.2007.08.006.

[85] J. Rautenberg. "Limits on ultra-high energy photons with the Pierre Auger Observatory". In: *Proceedings of 36th International Cosmic Ray Conference — PoS(ICRC2019)* (Sept. 2019). DOI: 10.22323/1.358.0398. URL: http://dx.doi.org/10.22323/1.358.0398.

[86] M. Kachelrieß, E. Parizot, and D. V. Semikoz. "The GZK horizon and constraints on the cosmic ray source spectrum from observations in the GZK regime". In: *JETP Letters* 88.9 (Jan. 2009), pp. 553–557. ISSN: 1090-6487. DOI: 10.1134/s0021364008210017. URL: http://dx.doi.org/10.1134/s0021364008210017.

[87] P. W. Gorham et al. "Constraints on the ultrahigh-energy cosmic neutrino flux from the fourth flight of ANITA". In: *Physical Review D* 99.12 (June 2019). ISSN: 2470-0029. DOI: 10.1103/physrevd.99.122001. URL: http://dx.doi.org/10.1103/PhysRevD.99.122001.

[88] A. Connolly, R. S. Thorne, and D. Waters. "Calculation of high energy neutrino-nucleon cross sections and uncertainties using the Martin-Stirling-Thorne-Watt parton distribution functions and implications for future experiments". In: *Physical Review D* 83.11 (June 2011). ISSN: 1550-2368. DOI: 10.1103/physrevd.83.113009. URL: http://dx.doi.org/10.1103/physrevd.83.113009.

[89] P. W. GORHAM. "THE ANITA COSMOGENIC NEUTRINO EXPERIMENT". In: *Acoustic and Radio EeV Neutrino Detection Activities* (Apr. 2006). DOI: 10.1142/9789812773791_0029. URL: http://dx.doi.org/10.1142/9789812773791_0029.

[90] E. Zas. "Searches for neutrino fluxes in the EeV regime with the Pierre Auger Observatory". In: *Proceedings of 35th International Cosmic Ray Conference — PoS(ICRC2017)* (Aug. 2017). DOI: 10.22323/1.301.0972. URL: http://dx.doi.org/10.22323/1.301.0972.

[91] M. G. Aartsen et al. "Differential limit on the extremely-high-energy cosmic neutrino flux in the presence of astrophysical background from nine years of IceCube data". In: *Phys. Rev. D* 98 (6 Sept. 2018), p. 062003. DOI: 10.1103/PhysRevD.98.062003. URL: https://link.aps.org/doi/10.1103/PhysRevD.98.062003.

[92] D. Veberic, ed. *The Pierre Auger Observatory: Contributions to the 35th International Cosmic Ray Conference (ICRC 2017)*. Aug. 2017. arXiv: 1708.06592 [astro-ph.HE].

[93] A. Aab et al. "Limits on point-like sources of ultra-high-energy neutrinos with the Pierre Auger Observatory". In: *Journal of Cosmology and Astroparticle Physics* 2019.11 (Nov. 2019), pp. 004–004. ISSN: 1475-7516. DOI: 10.1088/1475-7516/2019/11/004. URL: http://dx.doi.org/10.1088/1475-7516/2019/11/004.

[94] A. Castellina. "Highlights from the Pierre Auger Observatory". In: *Proceedings of 36th International Cosmic Ray Conference — PoS(ICRC2019)* (Oct. 2019). DOI: 10.22323/1.358.0004. URL: http://dx.doi.org/10.22323/1.358.0004.

[95] A. Fedynitch et al. "A New View on Auger Data and Cosmogenic Neutrinos in Light of Different Nuclear Disintegration and Air-shower Models". In: *Proceedings of 36th International Cosmic Ray Conference — PoS(ICRC2019)* (July 2019). DOI: 10.22323/1.358.0249. URL: http://dx.doi.org/10.22323/1.358.0249.

[96] D. Bergman. "Combined Fit of the Spectrum and Composition from Telescope Array". In: *Proceedings of 36th International Cosmic Ray Conference — PoS(ICRC2019)* (July 2019). DOI: 10.22323/1.358.0190. URL: http://dx.doi.org/10.22323/1.358.0190.

[97] A. van Vliet, R. A. Batista, and J. R. Hörandel. "Determining the fraction of cosmic-ray protons at ultrahigh energies with cosmogenic neutrinos". In: *Physical Review D* 100.2 (July 2019). ISSN: 2470-0029. DOI: 10.1103/physrevd.100.021302. URL: http://dx.doi.org/10.1103/physrevd.100.021302.

[98] O. E. Kalashev et al. "Ultrahigh-energy neutrino fluxes and their constraints". In: *Physical Review D* 66.6 (Sept. 2002). ISSN: 1089-4918. DOI: 10.1103/physrevd.66.063004. URL: http://dx.doi.org/10.1103/physrevd.66.063004.

[99] C. Righi et al. "EeV astrophysical neutrinos from flat spectrum radio quasars". In: *Astronomy & Astrophysics* 642 (Oct. 2020), A92. ISSN: 1432-0746. DOI: 10.1051/0004-6361/202038301. URL: http://dx.doi.org/10.1051/0004-6361/202038301.

[100] X. Rodrigues et al. "Active Galactic Nuclei Jets as the Origin of Ultrahigh-Energy Cosmic Rays and Perspectives for the Detection of Astrophysical Source Neutrinos at EeV Energies". In: *Physical Review Letters* 126.19 (May 2021). ISSN: 1079-7114. DOI: 10.1103/physrevlett.126.191101. URL: http://dx.doi.org/10.1103/physrevlett.126.191101.

[101] S. Razzaque and L. Yang. "PeV-EeV neutrinos from GRB blast waves in IceCube and future neutrino telescopes". In: *Physical Review D* 91.4 (Feb. 2015). ISSN: 1550-2368. DOI: 10.1103/physrevd.91.043003. URL: http://dx.doi.org/10.1103/physrevd.91.043003.

[102] K. Fang et al. "Testing the newborn pulsar origin of ultrahigh energy cosmic rays with EeV neutrinos". In: *Physical Review D* 90.10 (Nov. 2014). ISSN: 1550-2368. DOI: 10.1103/physrevd.90.103005. URL: http://dx.doi.org/10.1103/physrevd.90.103005.

[103] K. Fang et al. "Erratum: Testing the newborn pulsar origin of ultrahigh energy cosmic rays with EeV neutrinos [Phys. Rev. D90, 103005 (2014)]". In: *Physical Review D* 92.12 (Dec. 2015). ISSN: 1550-2368. DOI: 10.1103/physrevd.92.129901. URL: http://dx.doi.org/10.1103/physrevd.92.129901.

[104] J. Stettner. "Measurement of the diffuse astrophysical muon-neutrino spectrum with ten years of IceCube data". In: *Proceedings of 36th International Cosmic Ray Conference — PoS(ICRC2019)* (July 2019). DOI: 10.22323/1.358.1017. URL: http://dx.doi.org/10.22323/1.358.1017.

[105] T. J. Weiler. "Relic neutrinos, Z bursts, and cosmic rays above 10^{20} eV." In: *2nd International Conference Physics Beyond the Standard Model: Beyond the Desert 99: Accelerator, Nonaccelerator and Space Approaches*. June 1999, pp. 1085–1106. arXiv: hep-ph/9910316.

[106] O. E. Kalashev et al. "Ultrahigh-energy neutrino fluxes and their constraints". In: *Physical Review D* 66.6 (Sept. 2002). ISSN: 1089-4918. DOI: 10.1103/physrevd.66.063004. URL: http://dx.doi.org/10.1103/PhysRevD.66.063004.

[107] P. W. Gorham et al. "New Limits on the Ultra-high Energy Cosmic Neutrino Flux from the ANITA Experiment". In: *Phys. Rev. Lett.* 103 (2009), p. 051103. DOI: 10.1103/PhysRevLett.103.051103. arXiv: 0812.2715 [astro-ph].

[108] D. Biehl et al. "Astrophysical neutrino production and impact of associated uncertainties in photo-hadronic interactions of UHECRs". In: *EPJ Web of Conferences* 208 (2019). Ed. by B. Pattison et al., p. 04002. ISSN: 2100-014X. DOI: 10.1051/epjconf/201920804002. URL: http://dx.doi.org/10.1051/epjconf/201920804002.

[109] S. Zhou. "Cosmic Flavor Hexagon for Ultrahigh-energy Neutrinos and Antineutrinos at Neutrino Telescopes". In: (June 2020). arXiv: 2006.06181 [hep-ph]. URL: https://arxiv.org/pdf/2006.06181.pdf.

[110] E. Waxman and J. Bahcall. "High energy neutrinos from astrophysical sources: An upper bound". In: *Physical Review D* 59.2 (Dec. 1998). ISSN: 1089-4918. DOI: 10.1103/physrevd.59.023002. URL: http://dx.doi.org/10.1103/physrevd.59.023002.

[111] Q. Abarr et al. "The Payload for Ultrahigh Energy Observations (PUEO): a white paper". In: *Journal of Instrumentation* 16.08 (Aug. 2021), P08035. ISSN: 1748-0221. DOI: 10.1088/1748-0221/16/08/p08035. URL: http://dx.doi.org/10.1088/1748-0221/16/08/P08035.

[112] S. L. Glashow. "Resonant Scattering of Antineutrinos". In: *Physical Review* 118.1 (Apr. 1960), pp. 316–317. ISSN: 0031-899X. DOI: 10.1103/physrev.118.316. URL: http://dx.doi.org/10.1103/physrev.118.316.

[113] F. Suekane. "Neutrino Oscillation: Relativistic Oscillation of Three-Flavor System". In: *Lecture Notes in Physics* (2021), pp. 145–160. ISSN: 1616-6361. DOI: 10.1007/978-3-030-70527-5_12. URL: http://dx.doi.org/10.1007/978-3-030-70527-5_12.

[114] E. Catano Mur. "Constraints on neutrino oscillation parameters with the NOvA experiment". In: (Jan. 2018). DOI: 10.2172/1498546. URL: http://dx.doi.org/10.2172/1498546.

[115] X.-Y. Wang et al. "High-energy cosmic rays and neutrinos from semirelativistic hypernovae". In: *Physical Review D* 76.8 (Oct. 2007). ISSN: 1550-2368. DOI: 10.1103/physrevd.76.083009. URL: http://dx.doi.org/10.1103/PhysRevD.76.083009.

[116] G. E. Romero, A. L. Müller, and M. Roth. "Particle acceleration in the superwinds of starburst galaxies". In: *Astronomy & Astrophysics* 616 (Aug. 2018), A57. ISSN: 1432-0746. DOI: 10.1051/0004-6361/201832666. URL: http://dx.doi.org/10.1051/0004-6361/201832666.

[117] S. Hümmer et al. "Energy dependent neutrino flavor ratios from cosmic accelerators on the Hillas plot". In: *Astroparticle Physics* 34.4 (Nov. 2010), pp. 205–224. ISSN: 0927-6505. DOI: 10.1016/j.astropartphys.2010.07.003. URL: http://dx.doi.org/10.1016/j.astropartphys.2010.07.003.

[118] N. Sahakyan. "Lepto-hadronic γ-Ray and Neutrino Emission from the Jet of TXS 0506+056". In: *The Astrophysical Journal* 866.2 (Oct. 2018), p. 109. ISSN: 1538-4357. DOI: 10.3847/1538-4357/aadade. URL: http://dx.doi.org/10.3847/1538-4357/aadade.

[119] J. Arteaga-Velázquez. "Neutrino production from photo-hadronic interactions of the gamma flux from Active Galactic Nuclei with their gas content". In: *Astroparticle Physics* 37 (Sept. 2012), pp. 40–50. ISSN: 0927-6505. DOI: 10.1016/j.astropartphys.2012.07.002. URL: http://dx.doi.org/10.1016/j.astropartphys.2012.07.002.

[120] K. Fang et al. "Multimessenger Implications of AT2018cow: High-energy Cosmic-Ray and Neutrino Emissions from Magnetar-powered Superluminous Transients". In: *The Astrophysical Journal* 878.1 (June 2019), p. 34. ISSN: 1538-4357. DOI: 10.3847/1538-4357/ab1b72. URL: http://dx.doi.org/10.3847/1538-4357/ab1b72.

[121] T. M. Venters et al. "POEMMA's target-of-opportunity sensitivity to cosmic neutrino transient sources". In: *Physical Review D* 102.12 (Dec. 2020). ISSN: 2470-0029. DOI: 10.1103/physrevd.102.123013. URL: http://dx.doi.org/10.1103/physrevd.102.123013.

[122] X. Rodrigues et al. "Neutrinos and UHECR nuclei from blazars: from a single-source model to a population study". In: *Proceedings of 36th International Cosmic Ray Conference — PoS(ICRC2019)* (July 2019). DOI: 10.22323/1.358.0991. URL: http://dx.doi.org/10.22323/1.358.0991.

[123] A. Aab et al. "Improved limit to the diffuse flux of ultrahigh energy neutrinos from the Pierre Auger Observatory". In: *Physical Review D* 91.9 (May 2015). ISSN: 1550-2368. DOI: 10.1103/physrevd.91.092008. URL: http://dx.doi.org/10.1103/PhysRevD.91.092008.

[124] A. Plavin et al. "Observational Evidence for the Origin of High-energy Neutrinos in Parsec-scale Nuclei of Radio-bright Active Galaxies". In: *The Astrophysical Journal* 894.2 (May 2020), p. 101. ISSN: 1538-4357. DOI: 10.3847/1538-4357/ab86bd. URL: http://dx.doi.org/10.3847/1538-4357/ab86bd.

[125] R. Aloisio et al. "Cosmogenic neutrinos and ultra-high energy cosmic ray models". In: *Journal of Cosmology and Astroparticle Physics* 2015.10 (Oct. 2015), pp. 006–006. ISSN: 1475-7516. DOI: 10.1088/1475-7516/2015/10/006. URL: http://dx.doi.org/10.1088/1475-7516/2015/10/006.

[126] A. Palladino. "The flavor composition of astrophysical neutrinos after 8 years of IceCube: an indication of neutron decay scenario?" In: *The European Physical Journal C* 79.6 (June 2019). ISSN: 1434-6052. DOI: 10.1140/epjc/s10052-019-7018-7. URL: http://dx.doi.org/10.1140/epjc/s10052-019-7018-7.

[127] X.-J. Xu, H.-J. He, and W. Rodejohann. "Constraining astrophysical neutrino flavor composition from leptonic unitarity". In: *Journal of Cosmology and Astroparticle Physics* 2014.12 (Dec. 2014), pp. 039–039. ISSN: 1475-7516. DOI: 10.1088/1475-7516/2014/12/039. URL: http://dx.doi.org/10.1088/1475-7516/2014/12/039.

[128] L. A. Anchordoqui et al. "Galactic point sources of TeV antineutrinos". In: *Physics Letters B* 593.1-4 (July 2004), pp. 42–47. ISSN: 0370-2693. DOI: 10.1016/j.physletb.2004.04.054. URL: http://dx.doi.org/10.1016/j.physletb.2004.04.054.

[129] D. Hooper, D. Morgan, and E. Winstanley. "Probing quantum decoherence with high-energy neutrinos". In: *Physics Letters B* 609.3-4 (Mar. 2005), pp. 206–211. ISSN: 0370-2693. DOI: 10.1016/j.physletb.2005.01.034. URL: http://dx.doi.org/10.1016/j.physletb.2005.01.034.

[130] P. D. Serpico. "High energy neutrino flavor ratios, neutrino mixing angles, and astrophysical diagnostics". In: *Nuclear Physics B - Proceedings Supplements* 221 (Dec. 2011), p. 397. ISSN: 0920-5632. DOI: 10.1016/j.nuclphysbps.2011.10.045. URL: http://dx.doi.org/10.1016/j.nuclphysbps.2011.10.045.

[131] G.-L. Lin. "Determination of the Neutrino Flavor Ratio at the Astrophysical Source". In: *Proceedings of European Physical Society Europhysics Conference on High Energy Physics — PoS(EPS-HEP 2009)* (June 2010). DOI: 10.22323/1.084.0103. URL: http://dx.doi.org/10.22323/1.084.0103.

[132] K.-C. Lai, G.-L. Lin, and T.-C. Liu. "Probing neutrino flavor transition mechanism with ultrahigh energy astrophysical neutrinos". In: *Physical Review D* 89.3 (Feb. 2014). ISSN: 1550-2368. DOI: 10.1103/physrevd.89.033002. URL: http://dx.doi.org/10.1103/physrevd.89.033002.

[133] N. Song et al. "The Future of High-Energy Astrophysical Neutrino Flavor Measurements". In: *Proceedings of 37th International Cosmic Ray Conference — PoS(ICRC2021)* (July 2021). DOI: 10.22323/1.395.1178. URL: http://dx.doi.org/10.22323/1.395.1178.

[134] A. M. Hillas. "The Origin of Ultra-High-Energy Cosmic Rays". In: *Annual Review of Astronomy and Astrophysics* 22.1 (1984), pp. 425–444. DOI: 10.1146/annurev.aa.22.090184.002233. eprint: https://doi.org/10.1146/annurev.aa.22.090184.002233. URL: https://doi.org/10.1146/annurev.aa.22.090184.002233.

[135] M. Hussein and A. Shalchi. "Detailed Numerical Investigation of the Bohm Limit in Cosmic Ray Diffusion Theory". In: *The Astrophysical Journal* 785.1 (Mar. 2014), p. 31. ISSN: 1538-4357. DOI: 10.1088/0004-637x/785/1/31. URL: http://dx.doi.org/10.1088/0004-637x/785/1/31.

[136] A. de la Chevrotière, N. St-Louis, and A. F. J. Moffat. "Searching For Magnetic Fields in 11 Wolf-Rayet Stars: Analysis of Circular Polarization Measurements From ESPaDOnS". In: *The Astrophysical Journal* 781.2 (Jan. 2014), p. 73. ISSN: 1538-4357. DOI: 10.1088/0004-637x/781/2/73. URL: http://dx.doi.org/10.1088/0004-637X/781/2/73.

[137] S. P. Reynolds, B. M. Gaensler, and F. Bocchino. "Magnetic fields in supernova remnants and pulsar-wind nebulae". In: *Space Sci. Rev.* 166 (2012), pp. 231–261. DOI: 10.1007/s11214-011-9775-y. arXiv: 1104.4047 [astro-ph.GA].

[138] T. A. Thompson, E. Quataert, and N. Murray. "Radio emission from supernova remnants: implications for post-shock magnetic field amplification & the magnetic fields of galaxies". In: *Monthly Notices of the Royal Astronomical Society* 397.3 (July 2009), pp. 1410–1419. ISSN: 0035-8711. DOI: 10.1111/j.1365-2966.2009.14889.x. eprint: https://academic.oup.com/mnras/article-pdf/397/3/1410/3738296/mnras0397-1410.pdf. URL: https://doi.org/10.1111/j.1365-2966.2009.14889.x.

[139] J. Arons. "Magnetars in the Metagalaxy: An Origin for Ultra–High-Energy Cosmic Rays in the Nearby Universe". In: *The Astrophysical Journal* 589.2 (June 2003), pp. 871–892. ISSN: 1538-4357. DOI: 10.1086/374776. URL: http://dx.doi.org/10.1086/374776.

[140] X. Rodrigues et al. "Active Galactic Nuclei Jets as the Origin of Ultrahigh-Energy Cosmic Rays and Perspectives for the Detection of Astrophysical Source Neutrinos at EeV Energies". In: *Physical Review Letters* 126.19 (May 2021). ISSN: 1079-

7114. DOI: 10.1103/physrevlett.126.191101. URL: http://dx.doi.org/10.1103/physrevlett.126.191101.

[141] R. Mbarek, D. Caprioli, and K. Murase. "Ultra-High-Energy Cosmic Rays and Neutrinos from relativistic jets of Active Galactic Nuclei". In: *Proceedings of 37th International Cosmic Ray Conference — PoS(ICRC2021)* (July 2021). DOI: 10.22323/1.395.0481. URL: http://dx.doi.org/10.22323/1.395.0481.

[142] K. Murase et al. "High-energy cosmic-ray nuclei from high- and low-luminosity gamma-ray bursts and implications for multimessenger astronomy". In: *Phys. Rev. D* 78 (2 July 2008), p. 023005. DOI: 10.1103/PhysRevD.78.023005. URL: https://link.aps.org/doi/10.1103/PhysRevD.78.023005.

[143] K. Murase et al. "High-Energy Neutrinos and Cosmic Rays from Low-Luminosity Gamma-Ray Bursts?" In: *The Astrophysical Journal* 651.1 (Oct. 2006), pp. L5–L8. ISSN: 1538-4357. DOI: 10.1086/509323. URL: http://dx.doi.org/10.1086/509323.

[144] L. A. Anchordoqui. "Acceleration of ultrahigh-energy cosmic rays in starburst superwinds". In: *Physical Review D* 97.6 (Mar. 2018). ISSN: 2470-0029. DOI: 10.1103/physrevd.97.063010. URL: http://dx.doi.org/10.1103/PhysRevD.97.063010.

[145] G. Farrar. "Tidal disruption flares as the source of ultra-high energy cosmic rays". In: *EPJ Web of Conferences* 39 (2012). Ed. by R. Saxton and S. Komossa, p. 07005. ISSN: 2100-014X. DOI: 10.1051/epjconf/20123907005. URL: http://dx.doi.org/10.1051/epjconf/20123907005.

[146] D. N. Pfeffer, E. D. Kovetz, and M. Kamionkowski. "Ultrahigh-energy cosmic ray hotspots from tidal disruption events". In: *Monthly Notices of the Royal Astronomical Society* 466.3 (Dec. 2016), pp. 2922–2926. ISSN: 1365-2966. DOI: 10.1093/mnras/stw3337. URL: http://dx.doi.org/10.1093/mnras/stw3337.

[147] D. N. Burrows et al. "Relativistic jet activity from the tidal disruption of a star by a massive black hole". In: *Nature* 476.7361 (Aug. 2011), pp. 421–424. ISSN: 1476-4687. DOI: 10.1038/nature10374. URL: http://dx.doi.org/10.1038/nature10374.

[148] N. Senno, K. Murase, and P. Mészáros. "High-energy Neutrino Flares from X-Ray Bright and Dark Tidal Disruption Events". In: 838.1 (Mar. 2017), p. 3. DOI: 10.3847/1538-4357/aa6344. URL: https://doi.org/10.3847/1538-4357/aa6344.

[149] G. F. Krymskii. "A regular mechanism for the acceleration of charged particles on the front of a shock wave". In: *Akademiia Nauk SSSR Doklady* 234 (June 1977), pp. 1306–1308.

[150] E. Fermi. "On the Origin of the Cosmic Radiation". In: *Phys. Rev.* 75 (8 Apr. 1949), pp. 1169–1174. DOI: 10.1103/PhysRev.75.1169. URL: https://link.aps.org/doi/10.1103/PhysRev.75.1169.

[151] M. G. Baring. "Diffusive Shock Acceleration : the Fermi Mechanism." In: *Very High Energy Phenomena in the Universe; Moriond Workshop*. Ed. by Y. Giraud-Heraud and J. Tran Thanh van. Jan. 1997, p. 97. arXiv: astro-ph/9711177 [astro-ph].

[152] T. P. A. collaboration. "Bounds on the density of sources of ultra-high energy cosmic rays from the Pierre Auger Observatory". In: *Journal of Cosmology and Astroparticle Physics* 2013.05 (May 2013), pp. 009–009. ISSN: 1475-7516. DOI: 10.1088/1475-7516/2013/05/009. URL: http://dx.doi.org/10.1088/1475-7516/2013/05/009.

[153] H. Gao and P. Mészáros. "Reverse Shock Emission in Gamma-Ray Bursts Revisited". In: *Advances in Astronomy* 2015 (2015), pp. 1–16. ISSN: 1687-7977. DOI: 10.1155/2015/192383. URL: http://dx.doi.org/10.1155/2015/192383.

[154] A. Panaitescu and P. Meszaros. "Simulations of Gamma-Ray Bursts from External Shocks: Time Variability and Spectral Correlations". In: *The Astrophysical Journal* 492.2 (Jan. 1998), pp. 683–695. ISSN: 1538-4357. DOI: 10.1086/305056. URL: http://dx.doi.org/10.1086/305056.

[155] M. Honda et al. "Calculation of atmospheric neutrino flux using the interaction model calibrated with atmospheric muon data". In: *Physical Review D* 75.4 (Feb. 2007). ISSN: 1550-2368. DOI: 10.1103/physrevd.75.043006. URL: http://dx.doi.org/10.1103/physrevd.75.043006.

[156] "Evidence for High-Energy Extraterrestrial Neutrinos at the IceCube Detector". In: *Science* 342.6161 (Nov. 2013). ISSN: 1095-9203. DOI: 10.1126/science.1242856. URL: http://dx.doi.org/10.1126/science.1242856.

[157] "An absence of neutrinos associated with cosmic-ray acceleration in γ-ray bursts". In: *Nature* 484.7394 (Apr. 2012), pp. 351–354. ISSN: 1476-4687. DOI: 10.1038/nature11068. URL: http://dx.doi.org/10.1038/nature11068.

[158] M. Mottram. "An observational limit on the UHE cosmic neutrino flux from the second flight of the ANITA experiment". In: *Nuclear Instruments and Methods in Physics Research Section A: Accelerators, Spectrometers, Detectors and Associated Equipment* 662 (Jan. 2012), S59–S65. ISSN: 0168-9002. DOI: 10.1016/j.nima.2010.11.158. URL: http://dx.doi.org/10.1016/j.nima.2010.11.158.

[159] I. Kravchenko et al. "Updated results from the RICE experiment and future prospects for ultra-high energy neutrino detection at the south pole". In: *Physical Review D* 85.6 (Mar. 2012). ISSN: 1550-2368. DOI: 10.1103/physrevd.85.062004. URL: http://dx.doi.org/10.1103/PhysRevD.85.062004.

[160] G. Nir et al. "Ultra-High Energy Neutrinos from Gamma-Ray Burst Afterglows using the Swift-UVOT Data". In: *The Astrophysical Journal* 817.2 (Jan. 2016), p. 142. ISSN: 1538-4357. DOI: 10.3847/0004-637x/817/2/142. URL: http://dx.doi.org/10.3847/0004-637x/817/2/142.

[161] S. Chakraborti et al. "Ultra-high-energy cosmic ray acceleration in engine-driven relativistic supernovae". In: *Nature Communications* 2.1 (Feb. 2011). ISSN: 2041-1723. DOI: 10.1038/ncomms1178. URL: http://dx.doi.org/10.1038/ncomms1178.

[162] R.-Y. Liu and X.-Y. Wang. "Energy Spectrum and Chemical Composition of Ultrahigh Energy Cosmic Rays from Semi-Relativistic Hypernovae". In: 746.1 (Jan. 2012), p. 40. DOI: 10.1088/0004-637x/746/1/40. URL: https://doi.org/10.1088/0004-637x/746/1/40.

[163] B. T. Zhang and K. Murase. "Ultrahigh-energy cosmic-ray nuclei and neutrinos from engine-driven supernovae". In: *Physical Review D* 100.10 (Nov. 2019). ISSN: 2470-0029. DOI: 10.1103/physrevd.100.103004. URL: http://dx.doi.org/10.1103/PhysRevD.100.103004.

[164] K. Murase and K. Ioka. "TeV–PeV Neutrinos from Low-Power Gamma-Ray Burst Jets inside Stars". In: *Physical Review Letters* 111.12 (Sept. 2013). ISSN: 1079-7114. DOI: 10.1103/physrevlett.111.121102. URL: http://dx.doi.org/10.1103/physrevlett.111.121102.

[165] S. Gabici and F. A. Aharonian. "Pointlike Gamma Ray Sources as Signatures of Distant Accelerators of Ultrahigh Energy Cosmic Rays". In: *Physical Review Letters* 95.25 (Dec. 2005). ISSN: 1079-7114. DOI: 10.1103/physrevlett.95.251102. URL: http://dx.doi.org/10.1103/PhysRevLett.95.251102.

[166] K. Murase et al. "Blazars as Ultra-High-Energy Cosmic-Ray Sources: Implications for TeV Gamma-Ray Observations". In: *The Astrophysical Journal* 749.1 (Mar. 2012), p. 63. ISSN: 1538-4357. DOI: 10.1088/0004-637x/749/1/63. URL: http://dx.doi.org/10.1088/0004-637X/749/1/63.

[167] K. Kotera, D. Allard, and M. Lemoine. "Detectability of ultrahigh energy cosmic-ray signatures in gamma-rays". In: *Astronomy & Astrophysics* 527 (Jan. 2011), A54. ISSN: 1432-0746. DOI: 10.1051/0004-6361/201015259. URL: http://dx.doi.org/10.1051/0004-6361/201015259.

[168] S. S. Kimura, K. Murase, and B. T. Zhang. "Ultrahigh-energy cosmic-ray nuclei from black hole jets: Recycling galactic cosmic rays through shear acceleration". In: *Phys. Rev. D* 97 (2 Jan. 2018), p. 023026. DOI: 10.1103/PhysRevD.97.023026. URL: https://link.aps.org/doi/10.1103/PhysRevD.97.023026.

[169] A. Meli and P. L. Biermann. "Active galactic nuclei jets and multiple oblique shock acceleration: starved spectra". In: *Astronomy & Astrophysics* 556 (Aug. 2013), A88. ISSN: 1432-0746. DOI: 10.1051/0004-6361/201016299. URL: http://dx.doi.org/10.1051/0004-6361/201016299.

[170] Q. Xu et al. "Understanding the Puzzling Acceleration of Jets of Active Galactic Nuclei". In: *The Astrophysical Journal Supplement Series* 252.2 (Feb. 2021), p. 25. ISSN: 1538-4365. DOI: 10.3847/1538-4365/abc9b2. URL: http://dx.doi.org/10.3847/1538-4365/abc9b2.

[171] D. Caprioli. ""ESPRESSO" Acceleration of Ultra-High-Energy Cosmic Rays". In: *The Astrophysical Journal* 811.2 (Sept. 2015), p. L38. ISSN: 2041-8213. DOI:

10.1088/2041-8205/811/2/l38. URL: http://dx.doi.org/10.1088/2041-8205/811/2/L38.

[172] A. Mignone et al. "PLUTO: A Numerical Code for Computational Astrophysics". In: *Astrophysical Journal, Supplement* 170.1 (May 2007), pp. 228–242. DOI: 10.1086/513316. arXiv: astro-ph/0701854 [astro-ph].

[173] F. Tavecchio et al. "TeV BL Lac objects at the dawn of the Fermi era". In: *Monthly Notices of the Royal Astronomical Society* 401.3 (Jan. 2010), pp. 1570–1586. ISSN: 1365-2966. DOI: 10.1111/j.1365-2966.2009.15784.x. URL: http://dx.doi.org/10.1111/j.1365-2966.2009.15784.x.

[174] B. Zhang, X. Zhao, and Z. Cao. "TeV Blazars as the Sources of Ultra High Energy Cosmic Rays". In: *International Journal of Astronomy and Astrophysics* 04.03 (2014), pp. 499–509. ISSN: 2161-4725. DOI: 10.4236/ijaa.2014.43046. URL: http://dx.doi.org/10.4236/ijaa.2014.43046.

[175] M. Ajello et al. "The Luminosity Function of Fermi-Detected Flat-Spectrum Radio Quasars". In: *The Astrophysical Journal* 751.2 (May 2012), p. 108. ISSN: 1538-4357. DOI: 10.1088/0004-637x/751/2/108. URL: http://dx.doi.org/10.1088/0004-637x/751/2/108.

[176] M. Ajello et al. "The Cosmic Evolution of Fermi BL Lacertae Objects". In: *The Astrophysical Journal* 780.1 (Dec. 2013), p. 73. ISSN: 1538-4357. DOI: 10.1088/0004-637x/780/1/73. URL: http://dx.doi.org/10.1088/0004-637X/780/1/73.

[177] O. Hervet, C. Boisson, and H. Sol. "An innovative blazar classification based on radio jet kinematics". In: *Astronomy & Astrophysics* 592 (July 2016), A22. ISSN: 1432-0746. DOI: 10.1051/0004-6361/201628117. URL: http://dx.doi.org/10.1051/0004-6361/201628117.

[178] K. Murase and M. Fukugita. "Energetics of high-energy cosmic radiations". In: *Physical Review D* 99.6 (Mar. 2019). ISSN: 2470-0029. DOI: 10.1103/physrevd.99.063012. URL: http://dx.doi.org/10.1103/physrevd.99.063012.

[179] L. A. Anchordoqui, G. E. Romero, and J. A. Combi. "Heavy nuclei at the end of the cosmic-ray spectrum?" In: *Physical Review D* 60.10 (Oct. 1999). ISSN: 1089-4918. DOI: 10.1103/physrevd.60.103001. URL: http://dx.doi.org/10.1103/PhysRevD.60.103001.

[180] R. U. Abbasi et al. "Testing a Reported Correlation between Arrival Directions of Ultra-high-energy Cosmic Rays and a Flux Pattern from nearby Starburst Galaxies using Telescope Array Data". In: *The Astrophysical Journal* 867.2 (Nov. 2018), p. L27. ISSN: 2041-8213. DOI: 10.3847/2041-8213/aaebf9. URL: http://dx.doi.org/10.3847/2041-8213/aaebf9.

[181] K. Fang et al. "Is the Ultra-High Energy Cosmic-Ray Excess Observed by the Telescope Array Correlated with Icecube Neutrinos?" In: *The Astrophysical Journal* 794.2 (Oct. 2014), p. 126. ISSN: 1538-4357. DOI: 10.1088/0004-637x/794/2/126. URL: http://dx.doi.org/10.1088/0004-637x/794/2/126.

[182] H.-N. He et al. "Monte Carlo Bayesian search for the plausible source of the Telescope Array hotspot". In: *Physical Review D* 93.4 (Feb. 2016). ISSN: 2470-0029. DOI: 10.1103/physrevd.93.043011. URL: http://dx.doi.org/10.1103/physrevd.93.043011.

[183] A. Ambrosone et al. "Could Nearby Star-forming Galaxies Light Up the Point-like Neutrino Sky?" In: *The Astrophysical Journal Letters* 919.2 (Oct. 2021), p. L32. ISSN: 2041-8213. DOI: 10.3847/2041-8213/ac25ff. URL: http://dx.doi.org/10.3847/2041-8213/ac25ff.

[184] E. Peretti et al. *Particle acceleration and multi-messenger emission from starburst-driven galactic winds*. 2021. arXiv: 2104.10978 [astro-ph.HE].

[185] A. Marinelli et al. "A novel multimessenger study of Starburst galaxies: implications for neutrino astronomy". In: *Proceedings of 37th International Cosmic Ray Conference — PoS(ICRC2021)* (Aug. 2021). DOI: 10.22323/1.395.1232. URL: http://dx.doi.org/10.22323/1.395.1232.

[186] I. Tamborra, S. Ando, and K. Murase. "Star-forming galaxies as the origin of diffuse high-energy backgrounds: gamma-ray and neutrino connections, and implications for starburst history". In: *Journal of Cosmology and Astroparticle Physics* 2014.09 (Sept. 2014), pp. 043–043. ISSN: 1475-7516. DOI: 10.1088/1475-7516/2014/09/043. URL: http://dx.doi.org/10.1088/1475-7516/2014/09/043.

[187] K. Murase, M. Ahlers, and B. C. Lacki. "Testing the hadronuclear origin of PeV neutrinos observed with IceCube". In: *Physical Review D* 88.12 (Dec. 2013).

ISSN: 1550-2368. DOI: 10.1103/physrevd.88.121301. URL: http://dx.doi.org/10.1103/PhysRevD.88.121301.

[188] M. G. Aartsen et al. "Time-Integrated Neutrino Source Searches with 10 Years of IceCube Data". In: *Physical Review Letters* 124.5 (Feb. 2020). ISSN: 1079-7114. DOI: 10.1103/physrevlett.124.051103. URL: http://dx.doi.org/10.1103/PhysRevLett.124.051103.

[189] C. Lunardini et al. "Are starburst galaxies a common source of high energy neutrinos and cosmic rays?" In: *Journal of Cosmology and Astroparticle Physics* 2019.10 (Oct. 2019), pp. 073–073. ISSN: 1475-7516. DOI: 10.1088/1475-7516/2019/10/073. URL: http://dx.doi.org/10.1088/1475-7516/2019/10/073.

[190] A. Ambrosone et al. "Starburst galaxies strike back: a multi-messenger analysis with Fermi-LAT and IceCube data". In: *Monthly Notices of the Royal Astronomical Society* 503.3 (Mar. 2021), pp. 4032–4049. ISSN: 1365-2966. DOI: 10.1093/mnras/stab659. URL: http://dx.doi.org/10.1093/mnras/stab659.

[191] J. Alvarez-Muñiz and E. Zas. "EeV Hadronic Showers in Ice: The LPM effect". In: (1999). arXiv: astro-ph/9906347v1. URL: http://arxiv.org/abs/astro-ph/9906347v1.

[192] J. Knapp et al. "Extensive Air Shower Simulations at the Highest Energies". In: *Astropart.Phys. 19 (2003) 77-99* (2002). DOI: 10.1016/S0927-6505(02)00187-1. arXiv: astro-ph/0206414v1. URL: http://arxiv.org/abs/astro-ph/0206414v1.

[193] M. Hauschild. "The Large Hadron Collider (LHC)". In: *essentials* (2021), pp. 43–55. ISSN: 2197-6716. DOI: 10.1007/978-3-658-32726-2_6. URL: http://dx.doi.org/10.1007/978-3-658-32726-2_6.

[194] A. Abada and et al. "Future Circular Collider Study". In: (Dec. 2018). DOI: 10.2172/1527436. URL: http://dx.doi.org/10.2172/1527436.

[195] J. Espadanal. "Measurement of the Muon content of Extensive Air Showers with the Pierre Auger Observatory". In: (2015). arXiv: 1505.05527v1. URL: http://arxiv.org/abs/1505.05527v1.

[196] S. H oche. "Introduction to parton-shower event generators". In: (2014). arXiv: 1411.4085v2. URL: http://arxiv.org/abs/1411.4085v2.

[197] D. d'Enterria. "Experimental QCD summary (ICHEP 2020)". In: (2020). arXiv: 2012.06616v1. URL: http://arxiv.org/abs/2012.06616v1.

[198] G. Battistoni et al. "The hadronic models for cosmic ray physics: the FLUKA code solutions". In: *Nucl.Phys.Proc.Suppl.175:88-95,2008* (2006). DOI: 10.1016/j.nuclphysbps.2007.10.013. arXiv: hep-ph/0612075v1. URL: http://arxiv.org/abs/hep-ph/0612075v1.

[199] M. Bleicher et al. "Relativistic Hadron-Hadron Collisions in the Ultra-Relativistic Quantum Molecular Dynamics Model (UrQMD)". In: *J.Phys.G25:1859-1896,1999* (1999). DOI: 10.1088/0954-3899/25/9/308. arXiv: hep-ph/9909407v1. URL: http://arxiv.org/abs/hep-ph/9909407v1.

[200] I. C. Maris et al. "Influence of Low Energy Hadronic Interactions on Air-shower Simulations". In: *Nucl.Phys.Proc.Suppl.196:86-89,2009* (2009). DOI: 10.1016/j.nuclphysbps.2009.09.013. arXiv: 0907.0409v1. URL: http://arxiv.org/abs/0907.0409v1.

[201] I. Valino et al. "Characterisation of the electromagnetic component in ultra-high energy inclined air showers". In: *Astropart.Phys.32:304-317,2010* (2009). DOI: 10.1016/j.astropartphys.2009.09.008. arXiv: 0910.2873v1. URL: http://arxiv.org/abs/0910.2873v1.

[202] H. Bether and W. Heitler. "On the stopping of fast particles and on the creation of positive electrons". In: *Proceedings of the Royal Society of London. Series A, Containing Papers of a Mathematical and Physical Character* 146.856 (Aug. 1934), pp. 83–112. ISSN: 2053-9150. DOI: 10.1098/rspa.1934.0140. URL: http://dx.doi.org/10.1098/rspa.1934.0140.

[203] D. Saltzberg et al. "Observation of the Askaryan Effect: Coherent Microwave Cherenkov Emission from Charge Asymmetry in High Energy Particle Cascades". In: *Phys.Rev.Lett. 86 (2001) 2802-2805* (2000). DOI: 10.1103/PhysRevLett.86.2802. arXiv: hep-ex/0011001v1. URL: http://arxiv.org/abs/hep-ex/0011001v1.

[204] V. N. Baier and V. M. Katkov. "Variation of radiation length due to LPM effect". In: *Phys.Lett. A327 (2004) 202-209* (2004). DOI: 10.1016/j.physleta.2004.04.080. arXiv: hep-ph/0403132v1. URL: http://arxiv.org/abs/hep-ph/0403132v1.

[205] A. N. Cillis et al. "LPM effect and dielectric suppression in air showers". In: (1998). arXiv: astro-ph/9807062v1. URL: http://arxiv.org/abs/astro-ph/9807062v1.

[206] J. A. Formaggio and G. P. Zeller. "From eV to EeV: Neutrino Cross Sections Across Energy Scales". In: *Rev. Mod. Phys. 84, 1307 (2012)* (2013). DOI: 10.1103/RevModPhys.84.1307. arXiv: 1305.7513v1. URL: http://arxiv.org/abs/1305.7513v1.

[207] A. Garcia et al. "Complete predictions for high-energy neutrino propagation in matter". In: *JCAP 09 (2020) 025* (2020). DOI: 10.1088/1475-7516/2020/09/025. arXiv: 2004.04756v2. URL: http://arxiv.org/abs/2004.04756v2.

[208] J. Alvarez-Muñiz, R. A. Vázquez, and E. Zas. "Radiodetection of neutrino interactions in ice". In: (1999). arXiv: astro-ph/9906348v1. URL: http://arxiv.org/abs/astro-ph/9906348v1.

[209] D. García-Fernández, C. Glaser, and A. Nelles. "The signatures of secondary leptons in radio-neutrino detectors in ice". In: *Phys. Rev. D 102, 083011 (2020)* (2020). DOI: 10.1103/PhysRevD.102.083011. arXiv: 2003.13442v2. URL: http://arxiv.org/abs/2003.13442v2.

[210] S. Bevan et al. "Simulation of Ultra High Energy Neutrino Interactions in Ice and Water". In: *Astropart.Phys.28:366-379,2007* (2007). DOI: 10.1016/j.astropartphys.2007.08.001. arXiv: 0704.1025v1. URL: http://arxiv.org/abs/0704.1025v1.

[211] I. Allekotte et al. "The Surface Detector System of the Pierre Auger Observatory". In: *Nucl.Instrum.Meth.A586:409-420,2008* (2007). DOI: 10.1016/j.nima.2007.12.016. arXiv: 0712.2832v1. URL: http://arxiv.org/abs/0712.2832v1.

[212] S. Palomares-Ruiz, A. Irimia, and T. J. Weiler. "Acceptances for Space-Based and Ground-Based Fluorescence Detectors, and Inference of the Neutrino-Nucleon Cross-Section above 10^19 eV". In: *Phys.Rev.D73:083003,2006* (2005). DOI: 10.1103/PhysRevD.73.083003. arXiv: astro-ph/0512231v1. URL: http://arxiv.org/abs/astro-ph/0512231v1.

[213] J. Linsley. "The cosmic ray spectrum above 10(19) EV at Volcano Ranch and Haverah Park". In: *19th International Cosmic Ray Conference (ICRC19), Volume 9*. Vol. 9. International Cosmic Ray Conference. Aug. 1985, p. 475.

[214] G. Cassiday. "Observatory for Ultra High-Energy Processes: The Fly's Eye". In: *Annual Review of Nuclear and Particle Science* 35 (Nov. 2003), pp. 321–349. DOI: 10.1146/annurev.ns.35.120185.001541.

[215] P. Sokolsky. "Final Results from the High Resolution Fly's Eye (HiRes) Experiment". In: (2010). DOI: 10.1016/j.nuclphysbps.2011.03.010. arXiv: 1010.2690v2. URL: http://arxiv.org/abs/1010.2690v2.

[216] D. J. Bird et al. "Evidence for correlated changes in the spectrum and composition of cosmic rays at extremely high energies". In: *Phys. Rev. Lett.* 71 (21 Nov. 1993), pp. 3401–3404. DOI: 10.1103/PhysRevLett.71.3401. URL: https://link.aps.org/doi/10.1103/PhysRevLett.71.3401.

[217] T. Huege and D. Besson. "Radiowave Detection of Ultra-High Energy Neutrinos and Cosmic Rays". In: *Prog. Theor. Exp. Phys. 12 (2017) 12A106* (2017). DOI: 10.1093/ptep/ptx009. arXiv: 1701.02987v1. URL: http://arxiv.org/abs/1701.02987v1.

[218] H. R. ALLAN and J. K. JONES. "Radio Pulses from Extensive Air Showers". In: *Nature* 212.5058 (Oct. 1966), pp. 129–131. ISSN: 1476-4687. DOI: 10.1038/212129a0. URL: http://dx.doi.org/10.1038/212129a0.

[219] P. R. Barker, W. E. Hazen, and A. Z. Hendel. "Radio Pulses from Cosmic-Ray Air Showers". In: *Physical Review Letters* 18.2 (Jan. 1967), pp. 51–54. ISSN: 0031-9007. DOI: 10.1103/physrevlett.18.51. URL: http://dx.doi.org/10.1103/PhysRevLett.18.51.

[220] J. V. JELLEY et al. "Radio Pulses from Extensive Cosmic-Ray Air Showers". In: *Nature* 205.4969 (Jan. 1965), pp. 327–328. ISSN: 1476-4687. DOI: 10.1038/205327a0. URL: http://dx.doi.org/10.1038/205327a0.

[221] H. R. ALLAN, K. P. NEAT, and J. K. JONES. "Mechanism of Radio Emission from Extensive Air Showers". In: *Nature* 215.5098 (July 1967), pp. 267–268. ISSN: 1476-4687. DOI: 10.1038/215267a0. URL: http://dx.doi.org/10.1038/215267a0.

[222] G. A. Askar'yan. "Excess negative charge of an electron-photon shower and its coherent radio emission". In: *Zh. Eksp. Teor. Fiz.* 41 (1961), pp. 616–618.

[223] P. A. Cherenkov. "Visible emission of clean liquids by action of γ radiation". In: *Doklady Akademii Nuak SSSR* 451 (1934).

[224] I. M. Frank and I. E. Tamm. "Coherent visible radiation of fast electrons passing through matter". In: *Compt. Rend. Acad. Sci. URSS* 14.3 (1937), pp. 109–114. DOI: 10.3367/UFNr.0093.196710o.0388.

[225] T. M. Shaffer, E. C. Pratt, and J. Grimm. "Utilizing the power of Cerenkov light with nanotechnology". In: *Nature Nanotechnology* 12.2 (Feb. 2017), pp. 106–117. ISSN: 1748-3395. DOI: 10.1038/nnano.2016.301. URL: http://dx.doi.org/10.1038/nnano.2016.301.

[226] P. W. Gorham et al. "Accelerator Measurements of the Askaryan effect in Rock Salt: A Roadmap Toward Teraton Underground Neutrino Detectors". In: *Phys.Rev. D72 (2005) 023002* (2004). DOI: 10.1103/PhysRevD.72.023002. arXiv: astro-ph/0412128v2. URL: http://arxiv.org/abs/astro-ph/0412128v2.

[227] P. Miocinovic et al. "Time-Domain Measurement of Broadband Coherent Cherenkov Radiation". In: *Phys.Rev. D74 (2006) 043002* (2006). DOI: 10.1103/PhysRevD.74.043002. arXiv: hep-ex/0602043v2. URL: http://arxiv.org/abs/hep-ex/0602043v2.

[228] A. collaboration et al. "Observations of the Askaryan Effect in Ice". In: *Phys.Rev.Lett.99:171101,2007* (2006). DOI: 10.1103/PhysRevLett.99.171101. arXiv: hep-ex/0611008v2. URL: http://arxiv.org/abs/hep-ex/0611008v2.

[229] P. W. Gorham et al. "Picosecond timing of Microwave Cherenkov Impulses from High-Energy Particle Showers Using Dielectric-loaded Waveguides". In: *Phys. Rev. Accel. Beams 21, 072901 (2018)* (2017). DOI: 10.1103/PhysRevAccelBeams.21.072901. arXiv: 1708.01798v2. URL: http://arxiv.org/abs/1708.01798v2.

[230] P. Schellart et al. "Polarized radio emission from extensive air showers measured with LOFAR". In: (2014). DOI: 10.1088/1475-7516/2014/10/014. arXiv: 1406.1355v2. URL: http://arxiv.org/abs/1406.1355v2.

[231] J. Alvarez-Muñiz et al. "Simulations of reflected radio signals from cosmic ray induced air showers". In: *Astroparticle Physics 66 (2015) 31-38* (2015). DOI: 10.1016/j.astropartphys.2014.12.005. arXiv: 1502.02117v1. URL: http://arxiv.org/abs/1502.02117v1.

[232] J. Alvarez-Muñiz, A. Romero-Wolf, and E. Zas. "Practical and accurate calculations of Askaryan radiation". In: *Phys. Rev. D 84, 103003 (2011)* (2011). DOI: 10.1103/PhysRevD.84.103003. arXiv: 1106.6283v3. URL: http://arxiv.org/abs/1106.6283v3.

[233] A. Collaboration et al. "Probing the angular and polarization reconstruction of the ARIANNA detector at the South Pole". In: *Journal of Instrumentation JINST 15 (2020) P09039* (2020). DOI: 10.1088/1748-0221/15/09/P09039. arXiv: 2006.03027v2. URL: http://arxiv.org/abs/2006.03027v2.

[234] P. Allison et al. "Design and Initial Performance of the Askaryan Radio Array Prototype EeV Neutrino Detector at the South Pole". In: (2011). DOI: 10.1016/j.icarus.2012.05.028. arXiv: 1105.2854v2. URL: http://arxiv.org/abs/1105.2854v2.

[235] A. Anker et al. "Targeting ultra-high energy neutrinos with the ARIANNA experiment". In: *Advances in Space Research 64 (2019) 2595-2609* (2019). DOI: 10.1016/j.asr.2019.06.016. arXiv: 1903.01609v2. URL: http://arxiv.org/abs/1903.01609v2.

[236] M. G. Aartsen et al. "IceCube-Gen2: the window to the extreme Universe". In: *J. Phys. G* 48.6 (2021), p. 060501. DOI: 10.1088/1361-6471/abbd48. arXiv: 2008.04323 [astro-ph.HE].

[237] J. A. Aguilar et al. "Design and Sensitivity of the Radio Neutrino Observatory in Greenland (RNO-G)". In: *JINST 16 P03025 2021* (2020). DOI: 10.1088/1748-0221/16/03/P03025. arXiv: 2010.12279v3. URL: http://arxiv.org/abs/2010.12279v3.

[238] C. Glaser. "Neutrino direction and energy resolution of Askaryan detectors". In: *36th International Cosmic Ray Conference (ICRC2019)*. Vol. 36. International Cosmic Ray Conference. July 2019, 899, p. 899. arXiv: 1911.02093 [astro-ph.IM].

[239] P. W. Gorham. "Particle Astrophysics in NASA's Long Duration Balloon Program". In: (2013). DOI: 10.1016/j.nuclphysbps.2013.09.012. arXiv: 1308.4700v2. URL: http://arxiv.org/abs/1308.4700v2.

[240] R. Prechelt et al. "Analysis of a Tau Neutrino Origin for the Near-Horizon Air Shower Events Observed by the Fourth Flight of the Antarctic Impulsive Transient Antenna (ANITA)". In: (2021). arXiv: 2112.07069v1. URL: http://arxiv.org/abs/2112.07069v1.

[241] L. Wiencke and A. Olinto. "The Extreme Universe Space Observatory on a Super-Pressure Balloon II Mission". In: (2019). arXiv: 1909.12835v1. URL: http://arxiv.org/abs/1909.12835v1.

[242] J. Alvarez-Muñiz et al. "Radio pulses from ultra-high energy atmospheric showers as the superposition of Askaryan and geomagnetic mechanisms". In: *Astroparticle Physics 59 (2014) 29-38* (2014). DOI: 10.1016/j.astropartphys.2014.04.004. arXiv: 1402.3504v2. URL: http://arxiv.org/abs/1402.3504v2.

[243] T. Huege, M. Ludwig, and C. W. James. "Simulating radio emission from air showers with CoREAS". In: (2013). DOI: 10.1063/1.4807534. arXiv: 1301.2132v1. URL: http://arxiv.org/abs/1301.2132v1.

[244] V. Decoene et al. "Radio-detection of neutrino-induced air showers: The influence of topography". In: *Nuclear Instruments and Methods in Physics Research Section A: Accelerators, Spectrometers, Detectors and Associated Equipment* 986 (Jan. 2021), p. 164803. ISSN: 0168-9002. DOI: 10.1016/j.nima.2020.164803. URL: http://dx.doi.org/10.1016/j.nima.2020.164803.

[245] J. Alvarez-Muñiz et al. "Ultra high frequency geomagnetic radiation from extensive air showers". In: *AIP Conference Proceedings* (2013). ISSN: 0094-243X. DOI: 10.1063/1.4807537. URL: http://dx.doi.org/10.1063/1.4807537.

[246] A. Nelles et al. "Detecting Radio Emission from Air Showers with LOFAR". In: (2013). DOI: 10.1063/1.4807530. arXiv: 1304.0976v1. URL: http://arxiv.org/abs/1304.0976v1.

[247] A. Horneffer et al. "Air Shower Measurements with LOFAR". In: *Nucl.Instrum.Meth.A604:S20-S23,2009* (2009). DOI: 10.1016/j.nima.2009.03.027. arXiv: 0903.2398v1. URL: http://arxiv.org/abs/0903.2398v1.

[248] T. Huege. "Radio detection of cosmic rays with the Auger Engineering Radio Array". In: (2019). DOI: 10.1051/epjconf/201921005011. arXiv: 1905.04986v1. URL: http://arxiv.org/abs/1905.04986v1.

[249] H. Schoorlemmer and W. R. C. Jr. "Radio interferometry applied to the observation of cosmic-ray induced extensive air showers". In: (2020). arXiv: 2006.10348v1. URL: http://arxiv.org/abs/2006.10348v1.

[250] J. Alvarez-Muñiz et al. "A Comprehensive Approach to Tau-Lepton Production by High-Energy Tau Neutrinos Propagating Through Earth". In: *Phys. Rev. D 97, 023021 (2018)* (2017). DOI: 10.1103/PhysRevD.97.023021. arXiv: 1707.00334v4. URL: http://arxiv.org/abs/1707.00334v4.

[251] S. Wissel et al. "Prospects for High-Elevation Radio Detection of >100 PeV Tau Neutrinos". In: (2020). DOI: 10.1088/1475-7516/2020/11/065. arXiv: 2004.12718v3. URL: http://arxiv.org/abs/2004.12718v3.

[252] A. Cummings et al. "A More Complete Phenomenology of Tau Lepton Induced Air Showers". In: *PoS(ICRC2019)862* (2019). arXiv: 1910.01021v1. URL: http://arxiv.org/abs/1910.01021v1.

[253] A. M. Brown et al. "Trinity: An Imaging Air Cherenkov Telescope to Search for Ultra-High-Energy Neutrinos". In: (2021). arXiv: 2109.03125v1. URL: http://arxiv.org/abs/2109.03125v1.

[254] A. Romero-Wolf et al. "An Andean Deep-Valley Detector for High-Energy Tau Neutrinos". In: (2020). arXiv: 2002.06475v1. URL: http://arxiv.org/abs/2002.06475v1.

[255] R. Abbasi et al. "Measurement of Astrophysical Tau Neutrinos in IceCube's High-Energy Starting Events". In: *arXiv e-prints*, arXiv:2011.03561 (Nov. 2020), arXiv:2011.03561. arXiv: 2011.03561 [hep-ex].

[256] S. Hoover et al. "Observation of Ultrahigh-Energy Cosmic Rays with the ANITA Balloon-Borne Radio Interferometer". In: *Physical Review Letters* 105.15, 151101 (Oct. 2010), p. 151101. DOI: 10.1103/PhysRevLett.105.151101. arXiv: 1005.0035 [astro-ph.HE].

[257] P. W. Gorham et al. "Unusual Near-Horizon Cosmic-Ray-like Events Observed by ANITA-IV". In: *Phys. Rev. Lett.* 126.7 (2021), p. 071103. DOI: 10.1103/PhysRevLett.126.071103. arXiv: 2008.05690 [astro-ph.HE].

[258] P. W. Gorham et al. "Characteristics of Four Upward-pointing Cosmic-ray-like Events Observed with ANITA". In: *Phys. Rev. Lett.* 117.7 (2016), p. 071101. DOI: 10.1103/PhysRevLett.117.071101. arXiv: 1603.05218 [astro-ph.HE].

[259] A. Romero-Wolf et al. "Comprehensive analysis of anomalous ANITA events disfavors a diffuse tau-neutrino flux origin". In: *Phys. Rev. D* 99.6 (2019), p. 063011. DOI: 10.1103/PhysRevD.99.063011. arXiv: 1811.07261 [astro-ph.HE].

[260] A. Ludwig. "Radio Detection of Ultra-High Energy Neutrinos". PhD thesis. University of Chicago, 2019.

[261] R. Manning and G. A. Dulk. "The Galactic background radiation from 0.2 to 13.8 MHz". In: *Astronomy and Astrophysics* 372 (June 2001), pp. 663–666. DOI: 10.1051/0004-6361:20010516.

[262] P. Allison et al. "Dynamic tunable notch filters for the Antarctic Impulsive Transient Antenna (ANITA)". In: *Nuclear Instruments and Methods in Physics Research A* 894 (June 2018), pp. 47–56. DOI: 10.1016/j.nima.2018.03.059. arXiv: 1709.04536 [astro-ph.IM].

[263] B. Rotter. "Cosmic Ray and Neutrino Astrophysics with the ANITA-III Telescope". PhD thesis. University of Hawai'i Manoa, 2017.

[264] L. Cremonesi et al. "The simulation of the sensitivity of the Antarctic Impulsive Transient Antenna (ANITA) to Askaryan radiation from cosmogenic neutrinos interacting in the Antarctic Ice". In: *Journal of Instrumentation* 14.8 (Aug. 2019), P08011. DOI: 10.1088/1748-0221/14/08/P08011. arXiv: 1903.11043 [astro-ph.IM].

[265] G. S. Varner et al. "The large analog bandwidth recorder and digitizer with ordered readout (LABRADOR) ASIC". In: *Nuclear Instruments and Methods in Physics Research A* 583.2-3 (Dec. 2007), pp. 447–460. DOI: 10.1016/j.nima.2007.09.013. arXiv: physics/0509023 [physics.ins-det].

[266] S. W. Barwick et al. "Constraints on cosmic neutrino fluxes from the ANITA experiment". In: *Phys. Rev. Lett.* 96 (2006), p. 171101. DOI: 10.1103/PhysRevLett.96.171101. arXiv: astro-ph/0512265.

[267] T. Weiler. "Resonant Absorption of Cosmic-Ray Neutrinos by the Relic-Neutrino Background". In: *Phys. Rev. Lett.* 49 (3 July 1982), pp. 234–237. DOI: 10.1103/PhysRevLett.49.234. URL: https://link.aps.org/doi/10.1103/PhysRevLett.49.234.

[268] T. J. Weiler. "Relic neutrinos, Z bursts, and cosmic rays above 10^{20}-eV". In: *2nd International Conference Physics Beyond the Standard Model: Beyond the Desert 99: Accelerator, Nonaccelerator and Space Approaches*. June 1999, pp. 1085–1106. arXiv: hep-ph/9910316.

[269] N. G. Lehtinen et al. "FORTE satellite constraints on ultra-high energy cosmic particle fluxes". In: *Phys. Rev. D* 69 (2004), p. 013008. DOI: 10.1103/PhysRevD.69.013008. arXiv: astro-ph/0309656.

[270] R. Engel, D. Seckel, and T. Stanev. "Neutrinos from propagation of ultrahigh energy protons". In: *Phys. Rev. D* 64 (9 Oct. 2001), p. 093010. DOI: 10.1103/PhysRevD.64.093010. URL: https://link.aps.org/doi/10.1103/PhysRevD.64.093010.

[271] R. Protheroe and P. Johnson. "Propagation of ultra high energy protons and gamma rays over cosmological distances and implications for topological defect models". In: *Astroparticle Physics* 4.3 (Feb. 1996), pp. 253–269. ISSN: 0927-6505. DOI: 10.1016/0927-6505(95)00039-9. URL: http://dx.doi.org/10.1016/0927-6505(95)00039-9.

[272] L. A. Anchordoqui et al. "Neutrino bounds on astrophysical sources and new physics". In: *Phys. Rev. D* 66 (10 Nov. 2002), p. 103002. DOI: 10.1103/PhysRevD.66.103002. URL: https://link.aps.org/doi/10.1103/PhysRevD.66.103002.

[273] H. Schoorlemmer et al. "Energy and Flux Measurements of Ultra-High Energy Cosmic Rays Observed During the First ANITA Flight". In: *Astropart. Phys.* 77 (2016), pp. 32–43. DOI: 10.1016/j.astropartphys.2016.01.001. arXiv: 1506.05396 [astro-ph.HE].

[274] I. M. Shoemaker et al. "Reflections On the Anomalous ANITA Events: The Antarctic Subsurface as a Possible Explanation". In: *Annals Glaciol.* 61.81 (2020), pp. 92–98. DOI: 10.1017/aog.2020.19. arXiv: 1905.02846 [astro-ph.HE].

[275] D. Smith et al. "Experimental tests of sub-surface reflectors as an explanation for the ANITA anomalous events". In: *JCAP* 04 (2021), p. 016. DOI: 10.1088/1475-7516/2021/04/016. arXiv: 2009.13010 [astro-ph.HE].

[276] K. D. de Vries and S. Prohira. "Coherent transition radiation from the geomagnetically-induced current in cosmic-ray air showers: Implications for the anomalous events observed by ANITA". In: *Phys. Rev. Lett.* 123.9 (2019), p. 091102. DOI: 10.1103/PhysRevLett.123.091102. arXiv: 1903.08750 [astro-ph.HE].

[277] D. Borah et al. "Connecting ANITA Anomalous Events to a Non-thermal Dark Matter Scenario". In: (2019). arXiv: 1907.02740v1. URL: http://arxiv.org/abs/1907.02740v1.

[278] B. Chauhan and S. Mohanty. "Leptoquark solution for both the flavor and ANITA anomalies". In: *Phys. Rev. D 99, 095018 (2019)* (2018). DOI: 10.1103/PhysRevD.99.095018. arXiv: 1812.00919v3. URL: http://arxiv.org/abs/1812.00919v3.

[279] J. H. Collins, P. S. B. Dev, and Y. Sui. "R-parity Violating Supersymmetric Explanation of the Anomalous Events at ANITA". In: *Phys. Rev. D 99, 043009 (2019)* (2018). DOI: 10.1103/PhysRevD.99.043009. arXiv: 1810.08479v2. URL: http://arxiv.org/abs/1810.08479v2.

[280] I. Esteban et al. "Looking at the axionic dark sector with ANITA". In: (2019). arXiv: 1905.10372v3. URL: http://arxiv.org/abs/1905.10372v3.

[281] A. Esmaili and Y. Farzan. "Explaining the ANITA events by a $L_e - L$ gauge model". In: *JCAP12(2019)017* (2019). DOI: 10.1088/1475-7516/2019/12/017. arXiv: 1909.07995v2. URL: http://arxiv.org/abs/1909.07995v2.

[282] D. B. Fox et al. "The ANITA Anomalous Events as Signatures of a Beyond Standard Model Particle, and Supporting Observations from IceCube". In: (2018). arXiv: 1809.09615v1. URL: http://arxiv.org/abs/1809.09615v1.

[283] L. Heurtier, Y. Mambrini, and M. Pierre. "A Dark Matter Interpretation of the ANITA Anomalous Events". In: *Phys. Rev. D 99, 095014 (2019)* (2019). DOI: 10.1103/PhysRevD.99.095014. arXiv: 1902.04584v2. URL: http://arxiv.org/abs/1902.04584v2.

[284] L. Heurtier et al. "Explaining the ANITA Anomaly with Inelastic Boosted Dark Matter". In: *Phys. Rev. D 100, 055004 (2019)* (2019). DOI: 10.1103/PhysRevD.100.055004. arXiv: 1905.13223v2. URL: http://arxiv.org/abs/1905.13223v2.

[285] D. Hooper et al. "Superheavy Dark Matter and ANITA's Anomalous Events". In: *Phys. Rev. D 100, 043019 (2019)* (2019). DOI: 10.1103/PhysRevD.100.043019. arXiv: 1904.12865v1. URL: http://arxiv.org/abs/1904.12865v1.

[286] P. W. Gorham et al. "Constraints on the diffuse high-energy neutrino flux from the third flight of ANITA". In: *Physical Review D* 98.2, 022001 (July 2018), p. 022001. DOI: 10.1103/PhysRevD.98.022001. arXiv: 1803.02719 [astro-ph.HE].

[287] M. G. Aartsen et al. "A Search for IceCube Events in the Direction of ANITA Neutrino Candidates". In: *The Astrophysical Journal* 892.1 (Mar. 2020), p. 53. DOI: 10.3847/1538-4357/ab791d. URL: https://doi.org/10.3847/1538-4357/ab791d.

[288] J. Alvarez-Muñiz et al. "Erratum: Comprehensive approach to tau-lepton production by high-energy tau neutrinos propagating through the Earth [Phys. Rev. D 97, 023021 (2018)]". In: *Phys. Rev. D* 99 (6 Mar. 2019), p. 069902. DOI: 10.1103/PhysRevD.99.069902. URL: https://link.aps.org/doi/10.1103/PhysRevD.99.069902.

[289] M. G. Aartsen et al. "Constraints on Ultrahigh-Energy Cosmic-Ray Sources from a Search for Neutrinos above 10 PeV with IceCube". In: *Physical Review Letters* 117.24, 241101 (Dec. 2016), p. 241101. DOI: 10.1103/PhysRevLett.117.241101. arXiv: 1607.05886 [astro-ph.HE].

[290] S. Wissel et al. "Comprehensive estimate of the sensitivity of ANITA to tau neutrinos". In: *Proceedings of 36th International Cosmic Ray Conference — PoS(ICRC2019)* (July 2019). DOI: 10.22323/1.358.1034. URL: http://dx.doi.org/10.22323/1.358.1034.

[291] J. Alvarez-Muñiz et al. "Coherent radiation from extensive air showers in the ultrahigh frequency band". In: *Phys. Rev. D* 86 (12 Dec. 2012), p. 123007. DOI: 10.1103/PhysRevD.86.123007. URL: https://link.aps.org/doi/10.1103/PhysRevD.86.123007.

[292] J. Sullivan. "Geometric factor and directional response of single and multi-element particle telescopes". In: *Nuclear Instruments and Methods* 95.1 (Aug. 1971), pp. 5–11. ISSN: 0029-554X. DOI: 10.1016/0029-554x(71)90033-4. URL: http://dx.doi.org/10.1016/0029-554x(71)90033-4.

[293] J. Alvarez-Muñiz, W. R. Carvalho, and E. Zas. "Monte Carlo simulations of radio pulses in atmospheric showers using ZHAireS". In: *Astroparticle Physics* 35.6 (Jan. 2012), pp. 325–341. DOI: 10.1016/j.astropartphys.2011.10.005. arXiv: 1107.1189 [astro-ph.HE].

[294] S. Patel et al. "Monte Carlo simulations of neutrino and charged lepton propagation in the Earth with nuPyProp". In: *PoS* ICRC2021 (2021), p. 1203. DOI: 10.22323/1.395.1203. arXiv: 2109.08198 [hep-ph].

[295] J.-H. Koehne et al. "PROPOSAL: A tool for propagation of charged leptons". In: *Computer Physics Communications* 184.9 (Sept. 2013), pp. 2070–2090. ISSN: 0010-4655. DOI: 10.1016/j.cpc.2013.04.001. URL: http://dx.doi.org/10.1016/j.cpc.2013.04.001.

[296] H. Abramowicz and A. Levy. "The ALLM parameterization of sigma(tot)(gamma* p): An Update". In: (Dec. 1997). arXiv: hep-ph/9712415.

[297] A. M. Dziewonski and D. L. Anderson. "Preliminary reference Earth model". In: *Physics of the Earth and Planetary Interiors* 25.4 (June 1981), pp. 297–356. ISSN: 0031-9201. DOI: 10.1016/0031-9201(81)90046-7. URL: http://dx.doi.org/10.1016/0031-9201(81)90046-7.

[298] H. L. Lai et al. "Global QCD analysis of parton structure of the nucleon: CTEQ5 parton distributions". In: *Eur. Phys. J. C* 12 (2000), pp. 375–392. DOI: 10.1007/s100529900196. arXiv: hep-ph/9903282.

[299] M. Chrzaszcz et al. "TAUOLA of τ lepton decays—framework for hadronic currents, matrix elements and anomalous decays". In: *Comput. Phys. Commun.* 232 (2018), pp. 220–236. DOI: 10.1016/j.cpc.2018.05.017. arXiv: 1609.04617 [hep-ph].

[300] T. Sjöstrand et al. "An introduction to PYTHIA 8.2". In: *Computer Physics Communications* 191 (June 2015), pp. 159–177. DOI: 10.1016/j.cpc.2015.01.024. arXiv: 1410.3012 [hep-ph].

[301] P. Fretwell et al. "Bedmap2: improved ice bed, surface and thickness datasets for Antarctica". In: *The Cryosphere* 7.1 (2013), pp. 375–393. DOI: 10.5194/tc-7-375-2013. URL: https://tc.copernicus.org/articles/7/375/2013/.

[302] D. Foreman-Mackey et al. "emcee: The MCMC Hammer". In: *Publications of the ASP* 125.925 (Mar. 2013), p. 306. DOI: 10.1086/670067. arXiv: 1202.3665 [astro-ph.IM].

[303] J. Goodman and J. Weare. "Ensemble samplers with affine invariance". In: *Communications in Applied Mathematics and Computational Science* 5.1 (Jan. 2010), pp. 65–80. DOI: 10.2140/camcos.2010.5.65.

[304] Anita Collaboration et al. "A search for ultrahigh-energy neutrinos associated with astrophysical sources using the third flight of ANITA". In: *Journal of Cosmology and Astroparticle Physics* 2021.4, 017 (Apr. 2021), p. 017. DOI: 10.1088/1475-7516/2021/04/017. arXiv: 2010.02869 [astro-ph.HE].

[305] D. Heck et al. *CORSIKA: a Monte Carlo code to simulate extensive air showers.* 1998.

[306] E. Zas, F. Halzen, and T. Stanev. "Electromagnetic pulses from high-energy showers: Implications for neutrino detection". In: *Phys. Rev. D* 45 (1992), pp. 362–376. DOI: 10.1103/PhysRevD.45.362.

[307] T. Huege. "The endpoint formalism for the calculation of electromagnetic radiation and its applications in astroparticle physics". In: *Proceedings of the 32nd International Cosmic Ray Conference, ICRC 2011*. International Cosmic Ray Conference 4 (Jan. 2011), p. 308. DOI: 10.7529/ICRC2011/V04/0653. arXiv: 1112.2126 [astro-ph.HE].

[308] S. Prohira et al. "Modeling in-ice radio propagation with parabolic equation methods". In: *Phys. Rev. D* 103.10 (2021), p. 103007. DOI: 10.1103/PhysRevD.103.103007. arXiv: 2011.05997 [astro-ph.IM].

[309] J. W. Nam et al. "Design and implementation of the TAROGE experiment". In: *Int. J. Mod. Phys. D* 25.13 (2016), p. 1645013. DOI: 10.1142/S0218271816450139.

[310] S. Wissel et al. "Prospects for high-elevation radio detection of >100 PeV tau neutrinos". In: *JCAP* 11 (2020), p. 065. DOI: 10.1088/1475-7516/2020/11/065. arXiv: 2004.12718 [astro-ph.IM].

[311] A. N. Otte et al. "Trinity: An Air-Shower Imaging System for the Detection of Ultrahigh Energy Neutrinos". In: *Proceedings of 36th International Cosmic Ray Conference — PoS(ICRC2019)* (July 2019). DOI: 10.22323/1.358.0976. URL: http://dx.doi.org/10.22323/1.358.0976.

[312] J. Álvarez-Muñiz et al. "The Giant Radio Array for Neutrino Detection (GRAND): Science and Design". In: *Sci. China Phys. Mech. Astron.* 63.1 (2020), p. 219501. DOI: 10.1007/s11433-018-9385-7. arXiv: 1810.09994 [astro-ph.HE].

[313] M. Mastrodicasa et al. "Search for upward-going showers with the Fluorescence Detector of the Pierre Auger Observatory". In: *Proceedings of 37th International Cosmic Ray Conference — PoS(ICRC2021)* (July 2021). DOI: 10.22323/1.395.1140. URL: http://dx.doi.org/10.22323/1.395.1140.

[314] I. A. Caracas et al. "A tau scenario application to a search for upward-going showers with the Fluorescence Detector of the Pierre Auger Observatory". In: *Proceedings of 37th International Cosmic Ray Conference — PoS(ICRC2021)* (Oct. 2021). DOI: 10.22323/1.395.1145. URL: http://dx.doi.org/10.22323/1.395.1145.

[315] R. Abbasi et al. "Searches for Neutrinos from Gamma-Ray Bursts using the IceCube Neutrino Observatory". In: (2022). DOI: 10.48550/ARXIV.2205.11410. URL: https://arxiv.org/abs/2205.11410.

[316] R. Abbasi et al. "Search for Astrophysical Neutrinos from 1FLE Blazars with IceCube". In: (2022). DOI: 10.48550/ARXIV.2207.04946. URL: https://arxiv.org/abs/2207.04946.

[317] J. Braun et al. "Methods for point source analysis in high energy neutrino telescopes". In: *Astroparticle Physics* 29 (May 2008), pp. 299–305. DOI: 10.1016/j.astropartphys.2008.02.007.

[318] J. Braun et al. "Time-Dependent Point Source Search Methods in High Energy Neutrino Astronomy". In: *Astroparticle Physics* 33 (Apr. 2010), pp. 175–181. DOI: 10.1016/j.astropartphys.2010.01.005.

[319] J. Guillochon. *Open Supernova Catalog*. URL: https://sne.space/.

[320] P. Coppin. *GRBWeb*. URL: https://user-web.icecube.wisc.edu/~grbweb_public.

[321] J. Guillochon. *Open TDE Catalog*. URL: https://tde.space/.

[322] G. Lodato and E. M. Rossi. "Multiband light curves of tidal disruption events". In: *Monthly Notices of the Royal Astronomical Society* 410.1 (Dec. 2010), pp. 359–367. ISSN: 0035-8711. DOI: 10.1111/j.1365-2966.2010.17448.x. eprint: https://academic.oup.com/mnras/article-pdf/410/1/359/18446097/mnras0410-0359.pdf. URL: https://doi.org/10.1111/j.1365-2966.2010.17448.x.

[323] F. S. T. .-. S. 1.-4. for complete author list. *Fermi All-Sky Variability Analysis*. URL: https://fermi.gsfc.nasa.gov/ssc/data/access/lat/FAVA/index.php.

[324] S. Abdollahi et al. "The Second Catalog of Flaring Gamma-Ray Sources from the Fermi All-sky Variability Analysis". In: *The Astrophysical Journal* 846.1, 34 (Sept. 2017), p. 34. DOI: 10.3847/1538-4357/aa8092. arXiv: 1612.03165 [astro-ph.HE].

[325] B. Rust, D. O'Leary, and K. Mullen. "Modelling Type Ia Supernova Light Curves". en. In: Exponential Data Fitting and its Applications, Bentham Science Publishers, Oak Park, IL, Sept. 2010. URL: https://tsapps.nist.gov/publication/get_pdf.cfm?pub_id=903019.

[326] S. S. Kimura. "Neutrinos from Gamma-ray Bursts". In: (2022). DOI: 10.48550/ARXIV.2202.06480. URL: https://arxiv.org/abs/2202.06480.

[327] D. Biehl et al. "Tidally disrupted stars as a possible origin of both cosmic rays and neutrinos at the highest energies". In: *Scientific Reports* 8.1 (July 2018). DOI: 10.1038/s41598-018-29022-4. URL: https://doi.org/10.1038/s41598-018-29022-4.

[328] H.-J. Wu et al. "Could TDE outflows produce the PeV neutrino events?" In: *Monthly Notices of the Royal Astronomical Society* 514.3 (June 2022), pp. 4406–4412. DOI: 10.1093/mnras/stac1621. URL: https://doi.org/10.1093%2Fmnras%2Fstac1621.

[329] W. Winter and C. Lunardini. "Time-dependent interpretation of the neutrino emission from Tidal Disruption Events". In: (2022). DOI: 10.48550/ARXIV.2205.11538. URL: https://arxiv.org/abs/2205.11538.

[330] R. Stein et al. "A tidal disruption event coincident with a high-energy neutrino". In: *Nature Astronomy* 5.5 (Feb. 2021), pp. 510–518. DOI: 10.1038/s41550-020-01295-8. URL: https://doi.org/10.1038/s41550-020-01295-8.

[331] E. O'Sullivan and C. Finley. "Searching for Time-Dependent Neutrino Emission from Blazars with IceCube". In: (2019). DOI: 10.48550/ARXIV.1908.05526. URL: https://arxiv.org/abs/1908.05526.

[332] Das, Saikat, Razzaque, Soebur, and Gupta, Nayantara. "Cosmogenic gamma-ray and neutrino fluxes from blazars associated with IceCube events". In: *A&A* 658 (2022), p. L6. DOI: 10.1051/0004-6361/202142123. URL: https://doi.org/10.1051/0004-6361/202142123.

[333] S. S. Wilks. "The Large-Sample Distribution of the Likelihood Ratio for Testing Composite Hypotheses". In: *The Annals of Mathematical Statistics* 9.1 (Mar. 1938), pp. 60–62. DOI: 10.1214/aoms/1177732360. URL: https://doi.org/10.1214/aoms/1177732360.

[334] M. G. Aartsen et al. "The Contribution of Fermi-2LAC Blazars To Diffuse TeV–PeV Neutrino Flux". In: *The Astrophysical Journal* 835.1 (Jan. 2017), p. 45. ISSN: 1538-4357. DOI: 10.3847/1538-4357/835/1/45. URL: http://dx.doi.org/10.3847/1538-4357/835/1/45.

[335] IceCube Collaboration et al. "The IceCube Neutrino Observatory – Contributions to the 36th International Cosmic Ray Conference (ICRC2019)". In: (2019). DOI: 10.48550/ARXIV.1907.11699. URL: https://arxiv.org/abs/1907.11699.

[336] Astropy Collaboration et al. "Astropy: A community Python package for astronomy". In: *Astronomy & Astrophysics* 558, A33 (Oct. 2013), A33. DOI: 10.1051/0004-6361/201322068. arXiv: 1307.6212 [astro-ph.IM].

[337] Astropy Collaboration et al. "The Astropy Project: Building an Open-science Project and Status of the v2.0 Core Package". In: *The Astrophysical Journal* 156.3, 123 (Sept. 2018), p. 123. DOI: 10.3847/1538-3881/aabc4f. arXiv: 1801.02634 [astro-ph.IM].

[338] Astropy Collaboration et al. “The Astropy Project: Sustaining and Growing a Community-oriented Open-source Project and the Latest Major Release (v5.0) of the Core Package”. In: *Astrophysical Journal* 935.2, 167 (Aug. 2022), p. 167. DOI: 10.3847/1538-4357/ac7c74. arXiv: 2206.14220 [astro-ph.IM].

[339] NASA. *NASA's `hor2eq` FORTRAN routine*. URL: https://idlastro.gsfc.nasa.gov/ftp/pro/astro/hor2eq.pro.